

Valorization of Side Streams in Vegetable Oil Processing: From Molecular Catalysis to Process Design

Alexandra Bouriakova

Doctoral dissertation submitted to obtain the academic degree of
Doctor of Chemical Engineering

Supervisors

Prof. Joris Thybaut, PhD* - Prof. Jeriffa De Clercq, PhD* - Benjamin Katryniok, PhD**

* Department of Materials, Textiles and Chemical Engineering
Faculty of Engineering and Architecture, Ghent University

** Chemistry and Materials Department
Faculty of Engineering, Centrale Lille Institute, France

October 2021



**Valorization of Side Streams in Vegetable Oil Processing:
From Molecular Catalysis to Process Design**

Alexandra Bouriakova

Doctoral dissertation submitted to obtain the academic degree of
Doctor of Chemical Engineering

Supervisors

Prof. Joris Thybaut, PhD* - Prof. Jeriffa De Clercq, PhD* - Benjamin Katryniok, PhD**

* Department of Materials, Textiles and Chemical Engineering
Faculty of Engineering and Architecture, Ghent University

** Chemistry and Materials Department
Faculty of Engineering, Centrale Lille Institute, France

October 2021



ISBN 978-94-6355-529-6

NUR 952

Wettelijk depot: D/2021/10.500/77

Members of the Examination Board

Chair

Prof. Gert De Cooman, PhD, Ghent University

Other members entitled to vote

Kathy Elst, PhD, VITO

Eleni Heracleous, PhD, International Hellenic University, Greece

Hilde Poelman, PhD, Ghent University

Prof. Paul Van der Meeren, PhD, Ghent University

Supervisors

Prof. Joris Thybaut, PhD, Ghent University

Prof. Jeriffa De Clercq, PhD, Ghent University

Benjamin Katryniok, PhD, Centrale Lille Institute, France

ACKNOWLEDGMENTS

“Don’t cry because it’s over, smile because it happened” – dr. Seuss

Acknowledgments

Van september 2009 tot juni 2021 heb ik deel mogen uitmaken van Universiteit Gent. Eerst als student, vervolgens als onderzoeker en assistent. Ik heb zoveel nieuwe, gelijkgestemde mensen kunnen en mogen ontmoeten. Naast vele wetenschappelijke inzichten, heeft het mij ook persoonlijke inzichten opgeleverd. Ik heb geleerd hoe personen een verschillende aanpak kunnen hebben, maar toch hetzelfde doel kunnen nastreven. Maar vooral, heb ik ontdekt waarvoor ik sta en wat ik wil bereiken in het leven. Daarom wil ik heel wat mensen bedanken die hebben bijgedragen tot het UGent-hoofdstuk van mijn leven.

First and foremost, I would like to thank my supervisors prof. Joris W. Thybaut, prof. Jeriffa De Clercq and dr. Benjamin Katryniok for their guidance during all these years, the valuable discussions and the constructive feedback on this work. You helped me think more critically, which took my work to the next level. Jeriffa en Joris, door jullie heb ik de kans gekregen om op alle niveau's aan wetenschapscommunicatie te doen, zowel op wetenschappelijke conferenties als door middel van de STEM-workshops "Glaasje Vol" en "Ter land, ter zee en in de lucht". Jullie deur, of het laatste jaar jullie Teams-chat, stond altijd open als luisterend oor en voor een aanmoedigend woord, waarvoor dank. Benjamin, thank you for the collaboration and the hospitality of the whole group from Unité de Catalyse et Chimie du Solide. Natuurlijk gaat ook een woord van dank uit naar mijn coaches. dr. Kenneth Toch, niet alleen bedankt voor de begeleiding in mijn eerste PhD jaar (en bachelorproef), maar ook voor alle levenswijsheden tijdens mijn masterjaren. dr. Pedro S.F. Mendes, thank you for coaching me during the majority of my PhD. Your constructive input into the interpretation and analysis of the research results and the feedback on the reporting of these results in the form of presentations and articles was always appreciated. Thank you for being there when needed. I wish you all the best in your future career!

Next, I would like to thank my examination committee prof. Gert De Cooman, prof. Paul Van der Meeren, dr. Eleni Heracleous, dr. Hilde Poelman and dr. Kathy Elst for the time you dedicated in reading this thesis.

I would like to acknowledge some researchers who contributed to the characterization of the catalysts: dr. Els Bruneel (Department of Chemistry, UGent) for the TGA, Oliver Janssens (Department of Solid State Sciences, UGent) for the XRD and prof. Christophe Detavernier for providing access to the *in situ* XRD setup, dr. Lukas Buelens (Laboratory for Chemical Technology, UGent) for the STEM-EDX, dr. Pardis Simon and dr. Robert Wojcieszak (Unité de Catalyse et Chimie du Solide, Lille University) for the XPS measurements.

Een woord van dank aan mijn masterthesisstudenten voor hun bijdragen tot dit werk: Karel Vandenbroele, Daniel Rico, Charlotte De Vuyst, Marjon Willekens, Pieter Deconinck. Het was een genoegen om jullie te begeleiden en te zien groeien als persoon doorheen jullie masterthesis.

Een speciale dankbetuiging aan het administratief en technisch team van LCT. Bert Depuydt, Brecht Vervust, Erwin Turtelboom, Hans Heene, Lambert Peka Tchokam, Marcel Vervust, Michaël Lottin, Tom Verspeelt en Wim Rogiers, bedankt voor alle technische ondersteuning en interventies voor de

Acknowledgments

HTK-1! Natuurlijk mag de administratieve ondersteuning van Annelies Holvoet, Heidi De Pauw, Jarah Van Acoleyen, Kim Verbeeck, Sarah Verschooren, Paulien Baeyens en Petra Vereecken en de IT-ondersteuning van Georges Verenghen, Pieter Reyniers en Cato Papijn niet onderschat worden.

Over the past six years, I had the honor and pleasure of sharing my office with many talented researchers: Aditya Dharanipragada, Ana Rita Cruz, Beruk Bekele, Carlos Camacho, Chetan Raghuvver, Fabio Cavalcanti, Jiawei Hu, Lukas Buelens, Maëli Lissens, Matthias Filez, Maria Manzano, Rakesh Batchu, Reza Monjezi and Rusydi Fatahillah. Matthias, miraculously the sanseveria you left is still alive, even though it got more caffeine than water! I pass it over to the next generation in the office. Thank you to Aditya, Jiawei, Lucas and Maëli for the liters of tea, and to Beruk, Lukas and Reza for sharing my coffee addiction. Aditya, Chetan and Rakesh, thank you for introducing me great Indian food! Ana Rita and Maria, thank you for sharing your cookies and cakes with me (in times of despair). Carlos, Fabio and Rusydi, due to COVID we haven't had the change to see each other that often, but thank you for the talks we had in the (e-)breaks. Thank you all for moments in the office!

Dit brengt me tot de bedanking van de CaRE-groep. Eerst en vooral zou ik de HTK-buddies willen bedanken voor de uren sleutelplezier. Daria Otuyskaya, thanks for being my master coach and inspiring me to pursue my PhD. Tapas Rajkhowa, thank you for the tips and tricks for handling glycerol in the HTK. Anton De Vylder, Jolien De Waele, Maëli Lissens, Nebojsa Korica, thank you for the many hours in the lab. We laughed, we cried, we discussed, but most importantly, we helped each other in any way possible. I wish all the best luck to the newest generation of HTK-users, Geovani De Freitas, Maria Manzano, Reza Monjezi and Tom Vandevyvere. Graag zou ik ook Arno De Revière, Anton, Bert Biesemans, Maëli en Tom willen bedanken voor het opvangen van een deel van mijn labo-werk tijdens mijn zwangerschap. Daarnaast zou ik alle CaRE-leden willen bedanken voor de gezellige koffiepauzes en de vele activiteiten naast de werkvloer: van de vele ribbetjes-avonden tot de kerstmarkten, de fietsen wandeltochten, de (online) escape rooms en game nights, bowlingavonden en natuurlijk de onvergetelijke mol-dag. Jeroen Poissonnier en Maëli, niet alleen bedankt voor de CaRE-mol-dag, maar ook voor de zondaagse mol-zoektocht.

Ik had het genoegen om niet alleen deel uit te maken van de CaRE-groep, maar ook van de INKAT-groep op Schoonmeersen. Ik wil een bijzonder woord van dank uitspreken aan dr. Jeroen Lauwaert, dr. Maarten Sabbe en prof. Marie-Françoise Reyniers voor het vertrouwen in mij als assistent in respectievelijk Onderzoeksmethodiek en Algemene Chemie. Elien Laforce, wie had ooit gedacht dat we na het delen van de HTK-user room als studenten ooit samen zouden samen lesgeven? Katrien Maertens, Dieter Gunst, Arno de Reviere, Louis Naeyaert, Anna Tsibart en Hengameh Farahmandazad bedankt voor de vele uren Algemene Chemie! Ingeborg Stals, bedankt voor het doorgeven van de naaikriebels. INKATers, bedankt voor de gezellige pauzes, de kerstfeestjes, de zomerdrinks, de INKAT-spelletjes momenten,....

Ik had het geluk om niet alleen aan het PhD-avontuur te beginnen, maar met “de bende van tien”. Anton De Vylder, Alexander Vervust, Brigitte De Vocht, Florence Vermeire, Jenoff De Vrieze, Jens Dedeayne, Lies De Keer, Steffen Symoens en Yoshi Marien, jullie maakten het PhD-avontuur onvergetelijk. Ik zou jullie willen bedanken voor de koffie- en middagpauzes, de vrijdag-taartdag en de ribbetjes-avonden. Jullie stonden niet alleen klaar voor een babbel, maar waren ook een uitlaatklep. Ik weet zeker dat elk van jullie een prachtige toekomst tegemoet gaat.

Wetenschapscommunicatie heeft een belangrijke rol gespeeld de afgelopen jaren. Als assistent trachtte ik de studenten mijn liefde voor Chemie over te brengen. Het deed me dan ook altijd veel plezier om de 1^{ste} jaarstudenten te zien terugkeren in de latere jaren, of VOP'ers te zien terugkomen als thesisstudenten. De talrijke “Glaasje vol”-workshops op het LCT, in het kader van De Dag van De Wetenschap of van de Kinderuniversiteit, samen met Anton De Vylder, Bert Biesemans, Brigitte De Vocht, Jenoff De Vrieze, Maëli Lissens en Lies De Keer, toverden telkens pretoogjes bij de kinderen tijdens het verhaal van de dinosaurussen en bij de jongeren tijdens het uittesten van het autootje of het “echt” labo-werk. Hopelijk hebben we zo een nieuwe generatie kinderen en jongeren warm gemaakt voor een STEM-richting! Het was ook een genoeg om deel uit te maken van het organiserend comité bij twee edities van het jaarlijks symposium van onze faculteit, FEARS, georganiseerd door en voor de onderzoekers.

Ik zal ook altijd met plezier terugdenken aan vele niet-ribbetjes-avonden met de LCT-girls: Ana Rita Cruz, Annelies Holvoet, Brigitte De Vocht, Cato Papijn, Chitrakshi Goel, Daria Otuyasaka, Diana Vargas, Florence Vermeire, Jia Zhang, Jolien De Waele, Laura Pirro, Laurien Vandewalle, Lies De Keer, Maëli Lissens, Marian Flores, Marita Torregrosa, Naghmeh Fatemi, Natalia Lilka, Paulien Baeyens, Richa Sharma, Roxanne Hubesch, Sara Santon, Sri Bala, Stephanie Saerens, en de “aanhang”, Ana Sofia, Annelies, Audrey, Hadeel, Patricia, Roshanak, ... Girls, you rock!

Over the years at the LCT, I had the opportunity to get acquainted with the staff and almost three generations of PhD students. I was lucky to make memories that I will cherish because of you. Thank you for your kindness, your sense of humor, small talks, the international dinners, ...: Alejandro L., Ana B., Andres M., Anoop C., Arturo G., Azd Z., Bart V., Bram V.W., César B., César P., Chanakya R., David V.C., Dries D., Eli M., Elnaz Z., Fransisco H., Geraldine H., Gilles D.S., Guillermo R., Hilde P., Isabelle A., Ismaël A., Javier I., Jonas V.B., Juan S., Kasun K., Kevin D.R., Kristof V., Kyann D.S., Kristina F., Luis L., Manuel O., Marko D., Martin P., Marvin K., Max F., Moreno G., Mostafa A., Nenad R., Nils D.R., Olivier S., Onur D., Pablo I., Pieter D., Pieter J., Pieter N., Pieter P., Pieter V., Robert C., Ruben V., Saashwath T., Sebastien S., Sepehr M., Shekhar K., Shiwen L., Simon D., Srinath N., Stamatis S., Stavros T., Stijn F., Stijn V., Vaios O., Valentijn D., Varun S., Vladimir G., Yonggang C. and many others that I have failed to mention. Lukas Buelens, Pieter Reyniers en Stephanie Saerens, hoewel we het allemaal druk hebben, vind ik het fantastisch dat we af en toe tijd vrij maken voor een gezellig etentje (of een wandeling het afgelopen jaar).

Acknowledgments

Mijn UGent-hoofdstuk zou niet hetzelfde geweest zijn zonder mijn “LCT-chicks”, Florence, Laura en Lies. Florence en Lies, wij hebben een heel parcours samen afgelegd: van medestudenten, bestuursleden van MaChT en samen aan een doctoraat beginnen, tot het moment dat ik jullie familie mag noemen! Laura, Firenze was echt de start van onze vriendschap, je was zo in je element! Je hebt me zaken leren relativeren (en de juiste pasta kiezen bij de juiste saus...); ik heb je op tijd leren komen (of toch vaker...). Girls, bedankt voor alle steun het voorbije jaar en alle onvergetelijke momenten – ik ben overtuigd dat er nog vele zullen komen!

Bedankt aan mijn vrienden die altijd hebben geluisterd naar mijn LCT-verhalen. Evy, sinds de introductiedag maak je deel uit van mijn UGent-avontuur (incl. doctoraat), dus kan je zeker niet ontbreken in mijn dankwoord. Bedankt voor de herinneringen en alle steun tijdens de studies en het doctoraat. Lieve, Marlies en Saskia, bedankt voor alle niet-ingenieur gerelateerde geek talk, de koffietjes en taartjes en de tip-en-tricks bij mijn naaiprojecten. Hoewel verschillende van jullie hierboven zijn vermeld, ook een woordje van dank aan de “ski-bende”, voor de nodige time-out van tijd tot tijd. Florence & Kenny, Elke & Niels, Audrey & Steffen en Jasper, bedankt voor de ontelbare barbecues en avonturen op en naast de latten.

Tot slot wens ik mijn (schoon)familie te bedanken. Я хочу от всей души поблагодарить свою маму. Спасибо за каждую данную возможность и за то что ты всегда позволяешь мне идти своим путем. Maar ook Yvan, Rita, Didier, Omie, Severine, Thomas, Celine en Mathias, bedankt om mij te steunen maar vooral voor de gezellige familiemomenten. Jules, Amélie, Renée en Lou, bedankt voor jullie kinderlijke vreugde en enthousiasme!

Mijn allergrootste dank gaat uit naar mijn echtgenoot Jean-Luc. Schat, jij bent mijn rots in de branding. Bedankt om te luisteren naar de vele HTK-problemen, voor jouw geduld in mijn stress momenten en voor de motivatie tijdens het schrijven van mijn thesis. Ik kan niet verwoorden hoe dankbaar ik je hiervoor ben. Bedankt om voor ons Aurélietje te zorgen, zodat ik dit werk tot een goed einde kan brengen. We hebben al een hele weg afgelegd, maar gaan nog een prachtige toekomst tegemoet!

Lief, klein spookje Aurélie, ook jouw zou ik willen bedanken. Sommige nachten was je een echte kapoen, maar je bent zo een ongelooflijke flinke dochter en wij zijn zó trots op jou! Ook jij hebt geen gemakkelijk jaar achter de rug, maar bedankt om toch altijd zo vrolijk te zijn en een lach op ons gezicht te toveren. Ik ben overtuigd dat we vele onvergetelijke avonturen samen gaan beleven!

Het is tijd om dit hoofdstuk in mijn leven af te sluiten. Bedankt aan iedereen die heeft bijgedragen aan deze fantastische periode.

Juni 2021

Alexandra

TABLE OF CONTENTS

Table of contents	I
List of abbreviations, acronyms and symbols	IX
Abbreviation.....	XI
Acronyms	XI
Roman symbols.....	XIII
Greek symbols.....	XVII
Glossary	XIX
Summary	XXV
Samenvatting	XXXV
Chapter 1. Upgrading of byproducts in the processing of vegetable oils and fats	1
1.1 The rise of renewable resources	3
1.2 Vegetable oils as biomass resource	5
1.2.1 Valorization of a side stream in the biodiesel production	5
1.2.2 Waste stream in the production of edible oils as resource for minors.....	7
1.3 Glycerol and its conversion into valuable chemicals	7
1.3.1 Glycerol production.....	7
1.3.2 Glycerol as a platform chemical.....	9
1.4 Reaction mechanism of glycerol hydrogenolysis.....	12
1.4.1 Dehydration-hydrogenation mechanism.....	13
1.4.2 Dehydrogenation-dehydration-hydrogenation route	15
1.5 Development of effective catalysts for glycerol hydrogenolysis	15
1.5.1 Noble metal-based catalysts	15
1.5.2 First row transition metal-based catalysts	17
1.5.3 Copper-based catalysts	19
1.5.3.1 <i>Recent progress in Cu-based catalyst for glycerol hydrogenolysis</i>	19
1.5.3.2 <i>Strategies to improve the stability of Cu-based catalysts</i>	21
1.5.3.3 <i>Evolution of Cu species and their interplay</i>	23
1.6 Oil deodorizer distillates as resource for minor components	24
1.6.1 Squalene	26

Table of contents

1.6.2	Sterols	27
1.6.3	Tocopherols	28
1.7	Separation of the minor components	28
1.7.1	Isolation of minor components	29
1.7.1.1	<i>Crystallization and precipitation</i>	29
1.7.1.2	<i>Molecular distillation</i>	29
1.7.1.3	<i>Enzymatic or chemical modification</i>	30
1.7.1.4	<i>Supercritical extraction</i>	30
1.7.2	Pretreatment of the ODD	31
1.7.2.1	<i>Classical esterification</i>	31
1.7.2.2	<i>Supercritical esterification</i>	32
1.7.3	Integrated solution of esterification and extraction	32
1.8	Scope of this thesis	33
1.9	References	34
Chapter 2. Materials and methods		41
2.1	Design of supported Cu catalysts for glycerol hydrogenolysis	43
2.1.1	Material synthesis	43
2.1.2	Catalyst characterization	44
2.1.2.1	<i>Elemental analysis</i>	44
2.1.2.2	<i>Nitrogen sorption</i>	45
2.1.2.3	<i>Temperature-programmed techniques</i>	45
2.1.2.4	<i>(in situ) X-ray diffraction</i>	50
2.1.2.5	<i>Electron microscopy</i>	51
2.1.2.6	<i>X-ray photoelectron spectroscopy</i>	52
2.1.2.7	<i>Thermogravimetric Analysis</i>	54
2.1.3	Catalytic testing	54
2.1.3.1	<i>High-Throughput Kinetic setup for Mechanic Investigation</i>	54
2.1.3.2	<i>Intrinsic kinetics in a trickle bed regime</i>	63
2.2	Design of a process for the valorization of oil deodorizer distillates	64

2.2.1	Kinetic modelling	64
2.2.2	Process simulation methodology	67
2.2.2.1	<i>Model components</i>	67
2.2.2.2	<i>Thermodynamic models</i>	69
2.2.3	Economic analysis	70
2.2.4	Data analysis	72
2.3	References	73
Chapter 3. Co-metal induced stabilization of Al₂O₃ supported Cu for glycerol hydrogenolysis		77
3.1	Introduction	79
3.2	Results and discussion	79
3.2.1	Calcined catalyst characterization	79
3.2.2	Reduced catalyst characterization	83
3.2.3	Catalyst performance	86
3.2.4	Spent catalyst characterization	88
3.2.5	The role of Cu ⁰ particle size	90
3.3	Conclusions	90
3.4	References	92
	Supporting information	94
Chapter 4. Effect of La promotion on Al₂O₃ supported Cu species for glycerol hydrogenolysis		99
4.1	Introduction	101
4.2	Results and discussion	102
4.2.1	Calcined catalyst characterization	102
4.2.2	Reduced catalyst characterization	107
4.2.3	Catalyst performance evaluation and interpretation	117
4.2.4	Proposed reaction mechanism over La-Cu/ γ -Al ₂ O ₃ catalysts	120
4.2.5	Spent catalyst characterization	121
4.3	Conclusions	126
4.4	References	127
	Supporting information	130

Chapter 5. Assessment of the support on Cu and La-Cu catalysts for glycerol hydrogenolysis ..	141
.....	
5.1 Introduction	143
5.2 Results and discussion	144
5.2.1 Calcined catalyst characterization	144
5.2.2 Reduced catalyst characterization	148
5.2.3 Catalyst performance	154
5.3 Conclusions	156
5.4 References	158
Supporting information	160
Chapter 6. Techno-economic evaluation of squalene recovery from oil deodorizer distillates	167
.....	
6.1 Introduction	169
6.2 Results and discussion	171
6.2.1 Thermodynamic and kinetic modelling	171
6.2.2 Process simulations	177
6.2.3 Comparison between different ODDs	184
6.2.4 Economic analysis	187
6.3 Conclusions	191
6.4 References	192
Supporting information	195
Chapter 7. Conclusions and Perspectives	205
7.1 Understanding the factors controlling the catalyst performance for glycerol hydrogenolysis ..	207
.....	
7.1.1 Catalyst characterization	207
7.1.2 The role of Cu ⁰ and Cu ⁺	209
7.1.3 Factors controlling the selectivity	211
7.1.4 Perspectives	211
7.2 Valorization of oil deodorizer distillates	212
7.3 Generic conclusions on valorization of natural oil and fats derived side streams	214

7.4	References	216
Appendix A.	Assessment of transport limitations.....	219
Appendix B.	Experimental dataset for esterification of sunflower ODD with supercritical EtOH	
	231
Appendix C.	Parameter estimation in the esterification of sunflower ODD with supercritical	
	EtOH.....	237
Appendix D.	List of publications	241

LIST OF
ABBREVIATIONS, ACRONYMS
AND SYMBOLS

Abbreviation

ca.	circa, meaning “approximately”
c.f.	confer, meaning “compare”
e.g.	exempli gratia, meaning “for example”
i.e.	id est, meaning “that is”
rpm	rotations per minute

Acronyms

1,2-PD	1,2-propanediol
AVS	Athena Visual Studio
BE	Binding Energy
BET	Brunauer, Emmet and Teller
BJH	Barret, Joyner and Halenda
BP	By-Product cost (side product and waste streams) cost
CAPEX	Capital Expenditures or capital costs
CCD	Charge-Coupled Device
CMR	Contribution Margin Ratio
CONS	Consumables
DG	Diglyceride
EDX	Energy Dispersive X-ray spectroscopy
EOS	Equation Of State
FAEE	Fatty Acid Ethyl Ester
FAME	Fatty Acid Methyl Ester
FFA	Free Fatty Acid
FID	Flame Ionization Detector
FTIR	Fourier-Transform Infrared Spectroscopy
FWHW	Full Width at Half Maximum
G	Glycerol

List of abbreviations, acronyms and symbols

GC	Gas Chromatography
GM	Gross Margin
GMR	Gross Margin Ratio
GTBE	Glycerol tertiary-butyl ether
HTK-MI	High-Throughput Kinetic setup for Mechanic Investigation
ICP	Inductive Coupled Plasma
IUPAC	International Union of Pure and Applied Chemistry
JCPDS	Joint Committee on Powder Diffraction Standards
KE	Kinetic Energy
MG	Monoglyceride
MTBE	Methyl tert-butyl ether
NIST	National Institute of Standards and Technology
ODD	Oil Deodorizer Distillate
OES	Optical Emission Spectroscopy
OPEX	Operational Expenditures or operational costs
PR	Peng-Robinson equation of state
REV	Revenue of key products
RK	Redlich Kwong
RM	Raw Material cost
SF	Stoichiometric Factor
SP	Side Products revenue
S(T)EM	Scanning (Transmission) Electron Microscopy
SRK	Soave-Redlich-Kwong equation of state
TG	Triglyceride
TGA	Thermogravimetric Analysis
TOE	Tons of Oil Equivalent
TOF	Turn Over Frequency

TOS	Time On Stream
TPD	Temperature Programmed Desorption
TPR	Temperature Programmed Reduction
UNIQ	Uniquac equation of state
UTS	Utilities
VCM	Variable Contribution Margin
VCOP	Variable Cost of Production
VLE	Vapor-Liquid Equilibrium
WHSV	Weight Hourly Space Velocity
XPS	X-ray Photoelectron Spectroscopy
XRD	X-Ray Diffraction

Roman symbols

\varnothing	Average diameter of Cu agglomerates	nm
A_j	surface of the peak for component j	area
A	pre-exponential factor	reaction dependent
a_{tj}	number of t atoms in component j	-
a_{GL}	gas-liquid interfacial area	$m^2 m^{-3}_{\text{reactor}}$
a_{LS}	liquid-solid interfacial area	$m^2_L m^{-3}_{\text{cat-bed}}$
\bar{b}	vector of least squares estimators	-
b	instrumental width	rad
b	dilution degree of the catalyst bed	$m_{\text{inert}}^3 m_{\text{inert+cat}}^{-3}$
b_i	estimated model parameter	-
Ca_F	fluidum Carberry number	-
$c_{A(j)}$	concentration of reactant A in phase j	$\text{mol } m_j^{-3}$
$c_{A,i(j)}$	concentration of reactant A in the phase j at the gas-liquid interface	$\text{mol } m_{\text{gas}}^{-3}$

List of abbreviations, acronyms and symbols

$c_{A,i(s)}$	the concentration of reactant A in the liquid phase at the external pellet surface	mol mL^{-3}
C_j	concentration of component j	$\text{mol m}_{\text{fluid}}^{-3}$
CF_j	calibration factor for component j	mol\% area^{-1}
c_M	average number of Cu atoms per area	$\text{atoms}_{\text{Cu}} \text{m}^{-2}$
c_p	isobaric specific heat capacity	$\text{J kg}^{-1} \text{K}^{-1}$
d.f.	degree of freedom	-
$D_{A(\text{eff})}$	(effective) diffusion coefficient of component A	$\text{m}_{\text{fluid}}^3 \text{m}_{\text{reactor}}^{-1} \text{s}^{-1}$
$D_{a,\text{eff}}$	axial effective diffusion coefficient	$\text{m}_{\text{fluid}}^3 \text{m}_{\text{reactor}}^{-1} \text{s}^{-1}$
D_{Cu}	Dispersion of Cu^0	%
$D_{r,\text{eff}}$	radial effective diffusion coefficient	$\text{m}_{\text{fluid}}^3 \text{m}_{\text{reactor}}^{-1} \text{s}^{-1}$
d_h	hydraulic diameter	m
d_p	(inert) particle diameter	m
d_{pe}	equivalent pellet diameter	m
d_t	reactor diameter	m
$E_{a,i}$	activation energy for reaction i	J mol^{-1}
f_e	wetting efficiency	-
f_m	modified friction factor	-
F_A	molar flow rate of component A	mol s^{-1}
F_a	test statistic for lack-of-fit test	-
$F_{A,0}$	molar feed flow rate of component A	mol s^{-1}
$F_{i,j}$	molar outlet flow rate of response i at experiment j	mol s^{-1}
F_s	F value for the significance of a regression	-
h_{bed}	height of the catalyst bed	m
ΔH_r	reaction enthalpy	J mol^{-1}
K	shape factor	-
$k_{(\text{avg})}$	reaction rate coefficient (at average temperature)	reaction dependent
$k_{a,ij}$	binary interaction coefficient between i and j	-

List of abbreviations, acronyms and symbols

$k_{b,ij}$	binary interaction coefficient between i and j	-
k_G	mass transfer coefficient between the gas bulk and the gas-liquid interface	$m^3_G m^{-2} s^{-1}$
k_L	mass transfer coefficient for transfer from gas-liquid interface into bulk liquid	$m^3_L m^{-2} s^{-1}$
k_{LS}	mass transfer coefficient for transfer from bulk liquid to liquid-solid interface	$m^3_L m^{-2} s^{-1}$
k_v	volumetric rate coefficient	reaction dependent
m_j	mass of component j	g or kg
\dot{m}	mass outlet flow rate	$g s^{-1}$
MM_j	molar mass of component j	$kg mol^{-1}$
MSA_{Cu^0}	Metal surface area of Cu^0	$m^2 g^{-1}_{Cu}$
n	reaction order	-
n	number of reactants	-
N	number of reactions	-
N_A	Avogadro's constant	mol^{-1}
n_{exp}	number of experiments	-
$n_{parameters}$	number of parameters	-
n_{resp}	number of responses	-
n_{H_2}	consumed moles of H_2	$\mu mol g^{-1}$
Nu	Nusselt number ($= \alpha_p d_p \lambda^{-1}$), ratio of convective to conductive heat transfer	-
P	pressure	Pa
p_A	partial pressure of component A	Pa
P_{tot}	feed pressure	Pa
ΔP	pressure drop	Pa
Pe	Péclet number	-
$Pe_{p,F}^?$	Péclet number for radial effective diffusion based on the pellet diameter, ($=u d_p D_{r,eff}^{-1}$)	-

List of abbreviations, acronyms and symbols

Pr	Prandtl number ($= c_p \mu_g \lambda^{-1}$), the ratio of momentum diffusivity to thermal diffusivity	-
R	universal gas constant,	8.314472 J mol ⁻¹ K ⁻¹ 8.205736 10 ⁻⁵ m ³ atm mol ⁻¹ K ⁻¹
Re	Reynolds number ($= \rho_F d_{pe} u_s \mu_F^{-1}$), ratio of inertial forces to viscous forces	-
r_v	volumetric reaction rate	mol m ⁻³ s ⁻¹
$R_{v,j}$	volumetric production rate of component j	mol m ⁻³ s ⁻¹
r_w	specific reaction rate	mol kg _{cat} ⁻¹ s ⁻¹
$R_{w,j}$	specific production rate of component j	mol kg _{cat} ⁻¹ s ⁻¹
$S_{B,A}$	selectivity of reactant A towards product B	mol%
Sc	Schmidt number ($= \mu_g \rho_g^{-1} D_A^{-1}$), ratio of momentum diffusivity to mass diffusivity	-
Sh_{LS}	Sherwood number ($= k_{LS} d_p D_A^{-1}$), ratio of convective to diffusive transport	-
SK	Shape factor	-
SS	sum of squares	-
T	Temperature	K
t	test statistic	-
ΔT_{int}	internal temperature difference between the external surface and the average in the particle	K
$\Delta T_{boundary\ layer}$	temperature difference over the film surrounding the catalyst particle	K
ΔT_{rad}	radial temperature difference	K
u_F	fluidum velocity	m s ⁻¹
u_s	superficial velocity	m ³ m _{reactor} ⁻² s ⁻¹
V	volume	m ³
V_m	molar volume	cm ³ mol ⁻¹
W	catalyst mass	kg _{cat}

X_A	conversion of component A	mol%
x_A	molar fraction of the component A	-
$Y_{B,A}$	yield of reactant A towards product B	mol%

Greek symbols

α_{LS}	convection coefficient between solid (catalyst particle) and the liquid phase	$W \text{ m}_{\text{cat}}^{-2} \text{ K}^{-1}$
$\bar{\beta}$	vector of model parameters	-
Γ	Full Peak Width at Half-maximum	rad
ϵ_b	bed porosity	$\text{m}_{\text{void}}^3 \text{ m}_{\text{reactor}}^{-3}$
ϵ_{cat}	volume fraction of the catalyst in the bed	$\text{m}_{\text{cat}}^3 \text{ m}_{\text{reactor}}^{-3}$
η	effectiveness factor	-
θ	diffraction angle	rad
λ	wavelength	nm
$\lambda_{r,c}$	effective radial heat conduction coefficient	$W \text{ m}^{-1} \text{ K}^{-1}$
μ_F	fluidium viscosity	$\text{kg m}^{-1} \text{ s}^{-1}$
ν	kinematic viscosity	$\text{m}^2 \text{ s}^{-1}$
ν_j	stoichiometric coefficient of j	-
ρ	density	kg m^{-3}
ρ_p	density of a catalyst pellet	kg m^{-3}
τ	space time for a reactor without catalyst	s
τ''	space time for a reactor with a catalyst bed	$\text{kg}_{\text{cat}} \text{ s mol}_{\text{glycerol}}^{-1}$
ϕ	Thiele modulus ($= a_v^{-1} k_v^{1/2} D_A^{1/2}$), ratio of chemical reaction rate to diffusive mass transfer rate	-
Φ	Weisz modulus ($= \eta\phi^2$)	-

GLOSSARY

activation energy	For an elementary step, the difference in internal energy between transition state and reactants. A measure for the temperature dependence of the rate coefficient.
active site	The region on the catalyst surface which is responsible for adsorption of a species and a subsequent reaction.
Arrhenius relation	Expresses the dependence of a rate coefficient, k , corresponding with a chemical reaction on the temperature, T , and activation energy, E_a : $k = Ae^{-\frac{E_a}{RT}}$, with R the universal gas constant and A the pre-exponential factor
as prepared	The catalyst before calcination.
Brønsted acid	A chemical species that is a proton donor.
catalyst	Substance or material, which through repeated cycles of elementary steps, accelerates the conversion of reagents into products. Catalysts are classified into homogeneous, which are in the same phase with the reagents (<i>e.g.</i> acids and bases, metal complexes, ..), and heterogeneous, which are separated from the reactants by an interface (<i>e.g.</i> metals, metal oxides, ...). Here, reduced, active material.
coking	Build-up of carbon depositions during reaction.
conversion	Measure for the amount of a reactant that has been transformed into products as a result of a chemical reaction.
deactivation	The decrease in conversion in a catalytic reaction with time on stream under reaction conditions.
dehydration	A chemical reaction that involves the removal of water from an organic molecule.
dispersion	The level in which active sites are distributed over the catalyst surface.
dissociative chemisorption	Adsorption of a molecule with dissociation into two or more fragments, both or all of which are bound to the surface of adsorbent.
hydrogenation	A chemical reaction that involves the addition of hydrogen to an organic molecule.
hydrogenolysis	A chemical reaction that involves the cleavage of a C-C or a C-heteroatom bond by hydrogen.
<i>in situ</i>	Latin phrase meaning “on site”. <i>In situ</i> characterization means that the material is not physically moved from one apparatus to another between treatment and characterization.
Lewis acid	A chemical species that contains an empty orbital which is capable of accepting an electron pair.
mesopores	Pores of intermediate size, <i>i.e.</i> between 2 nm and 50 nm.

packed bed	A bed of solid catalyst particles loaded in a reactor.
parity diagram	A 2-dimensional scatter plot in which the model calculated values of the responses are displayed against the experimentally observed values.
poisoning	Refers to the partial or total deactivation of a catalyst caused by exposure to a range of chemical compounds, which can be reactants, products or impurities.
pre-exponential factor	The temperature-independent factor of a rate coefficient, also called the frequency factor.
promotor	Substance added to a catalyst in order to improve its performance, such as activity, selectivity or stability, in a chemical reaction. By itself the promotor has little or no catalytic effect. It can interact with the active component of the catalyst and thereby alter its properties.
residence time	The residence time, \bar{t} , of an infinitesimal element of a fluid is the total time that this element has spent inside a control volume V . It is defined as $dt = \frac{dV}{Q}$ or $\bar{t} = \int_0^{\bar{t}} dt = \int_0^V \frac{dV}{Q}$, in which Q is the volumetric flow rate of the fluid. However, the volumetric flow can vary inside the reactor, especially for a gas phase reactions as the number of moles in the reaction mixture can change (expansion or contraction), thus $Q(V)$. Therefore, one should take this volume change into consideration in the integration. To have a measure of the time available for reaction, the space time τ is defined.
residual plot	Plot showing the difference between model calculated and experimentally observed values as function of an operating condition, such as temperature, pressure, concentration, ...
selectivity	Measure for the amount in which a product is formed from the reactants as a result of a chemical reaction.
sintering	Coalescence of separate metal particles to become one bigger particle.
space time	The space time is the time needed to pass an element of the reaction mixture through the reactor, <i>i.e.</i> without any reaction taking place. It is thus defined as the ratio of the total volume of the reactor, V , over the inlet volumetric flow rate Q_0 : $\tau = \frac{V}{Q_0}$. In this sense, the space time differs from the actual residence time which will be impacted by contraction or expansion due to reaction. For a packed bed reactor, this element needs to pass through the catalyst bed with mass W and, hence, the space time can then be defined as: $\tau' = \frac{W}{Q_0}$. For a liquid feed, the changes in density due to the reaction are in most cases negligible, and thus the space time can be calculated as the ratio of the catalyst mass over the reactant molar flow rate F_0 : $\tau'' = \frac{W}{F_0} = \frac{MM_0}{\rho_0} \tau'$.
spent catalyst	The recovered catalyst after an activity or stability test.
structure sensitive	The relationship between the Cu agglomerates size and the turnover frequency.

surface coverage	Ratio of the amount of absorbed substance to the monolayer capacity.
support	Material, usually of high surface area, onto which the active catalytic material, present as the minor component, is dispersed. The support may be catalytically inert, but it may contribute to the overall catalytic activity.
trickle bed reactor	Is a chemical reactor that uses the downward movement of a liquid and a co-current (downward) or counter-current (upward) movement of a gas over a packed bed of catalyst particles.
turnover frequency	The number of molecules reacting per active site per unit time.
wet incipient impregnation	A commonly used technique for the synthesis of heterogeneous catalysts. Typically, the active metal precursor is dissolved in an aqueous or organic solution. Then the metal containing solution is added to a catalyst support, which is also dissolved.

SUMMARY

For several decades the interest into renewable resources, such as biomass, for chemicals and energy has increased due to dwindling fossil oil reserves and the impact of greenhouse gas emissions on the climate change. Bio-based counterparts are available or can be developed for practically any chemical and hence, the chemical industry plays a crucial role in the shift from a petroleum-based society to a green and environmental friendly one. The use of (waste) biomass not only brings environmental but also economic benefits. It helps to decrease the dependence on – depleting – fossil oil resources by utilization of widely available renewable resources. Since several years, a shift towards the valorization of waste or side streams of vegetable oils, characterized with low economic value, has occurred which can play an important role in achieving a green and sustainable economy.

On the one hand, the increased global demand for biodiesel, as an alternative fuel, simultaneously leads to an enhanced availability of the major side-product glycerol, adding up to 10 vol.% of the biodiesel production. Due to its C3 structure hosting three hydroxyl groups, glycerol has emerged as a key platform molecule. The economic viability of the biodiesel industry can be enhanced by converting glycerol into high value-added chemicals, such as 1,2-propanediol, which finds applications in polyester resins, de-icing fluids, food, drugs and cosmetic industry. More importantly, the catalytic hydrogenolysis of glycerol constitutes a green and, hence, more sustainable route towards 1,2-propanediol compared to the conventional one *via* petroleum derived propylene oxide.

To achieve high quality, a complex sequence of process steps is required to achieve the desired combination of taste, smell and color, leading to side streams such as the so-called Oil Deodorizer Distillate (ODD). Although this stream contains a certain fraction of valuable components, such as squalene, tocopherols and sterols, for the food, cosmetic and pharmaceutical industry, it has little economic value and is often considered as waste. The recuperation of these components would offer a more sustainable production route for them as the main source of squalene is the liver of deep-sea sharks, while sterols and tocopherols are mainly obtained *via* chemical synthesis from petroleum products.

It is foreseen that the global production of vegetable oils and biodiesel will rise continuously in the coming decades and, hence, it is interesting to investigate those as biomass resources. To this end, this PhD focusses on the valorization of side streams in vegetable oil processing on different scales. In the first part, the potential recovery of squalene from ODD was assessed via detailed process simulations. In the second part, a more systematic approach for investigating the impact of the Cu catalyst properties on the glycerol hydrogenolysis to 1,2-propanediol has been adopted, with the aim of retrieving strategic insights for the design of novel, high performing catalysts.

Factors controlling the catalyst performance for glycerol hydrogenolysis

Supported Cu based catalysts are commonly industrially used for glycerol hydrogenolysis due to their lower price compared to noble metals and their higher selectivity for C-O bond cleavage compared to other transition metals, resulting in a high selectivity to 1,2-propanediol. Irrespective of the support used, bare Cu catalysts are prone to deactivation phenomena, mostly due to sintering. By adding dopants, the catalytic performance, mainly the catalyst stability, is aimed at being enhanced. Various authors investigated (combinations of) dopants to improve the catalyst performance. However, no systematic investigation has been performed on commercially relevant Cu-based glycerol hydrogenolysis catalysts.

Therefore, Cu/ γ -Al₂O₃ catalysts doped with Ba, Ce, Cs and La were investigated for liquid-phase pure glycerol hydrogenolysis under industrially relevant conditions. The catalysts were prepared by sequential impregnation. First, the dopant was impregnated on the support, followed by an intermediate calcination step. Second, the Cu was impregnated onto the modified support, again followed by calcination. The Cu-catalyst exhibited pronounced deactivation after 68 h, while the Ba-, Ce- and La-doped catalysts remained almost stable in terms of glycerol conversion over time, see Figure 3.5. This catalyst deactivation could be assigned to sintering, as it was found that dopants stabilized the Cu⁰ particle size during reaction, and not by coke formation. Where the particle size, as determined by dissociative N₂O adsorption, of the spent Cu catalyst increased up to a factor 100 compared to the reduced one (*i.e.* from 1.8 nm to > 120 nm), a maximum increase of one order of magnitude was observed for the doped catalysts (*i.e.* from 1.7 nm to 15 nm). La-doping resulted in the most pronounced stabilization of the Cu⁰ particle size, which was also evidenced by the best stability in terms of glycerol conversion over time on stream.

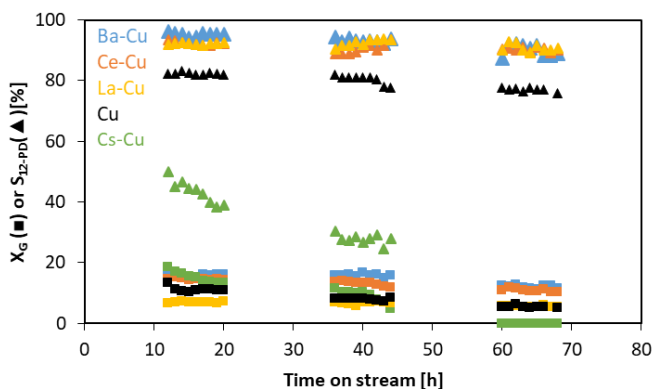


Figure 3.5. Glycerol conversion (■) and 1,2-propanediol selectivity (▲) at 473 K, 7.5 MPa, 135 kg_{cat} s mol⁻¹_{glycerol} and 7 mol_{H₂} mol⁻¹_{glycerol} for the Cu (black), Ba-Cu (blue), Ce-Cu (orange), Cs-Cu (green) and La-Cu (yellow) catalysts supported on γ -Al₂O₃

Moreover, the Ba, Ce and La-doped catalysts increased the selectivity towards 1,2-propanediol from 82 % to 96 %, 93 % and 92 %, respectively. The dehydration of glycerol leads to the formation of acetol which is consecutively hydrogenated to 1,2-propanediol, while 1,2-ethanediol is formed by C-C cleavage of glycerol, see Figure 3.6. For the Ba- and Ce-doped catalyst, the increased selectivity was attributed to an increase in total acidity of the catalyst. In the case of the Ce-doped and Ba-doped catalyst, the slight decrease in selectivity over time occurred mainly at the expense of an increase in 1,2-ethanediol, *i.e.* C-C rather than C-O bond cleavage occurred. For the La-doped catalyst, the 1,2-propanediol selectivity remained almost constant over the investigated timeframe.

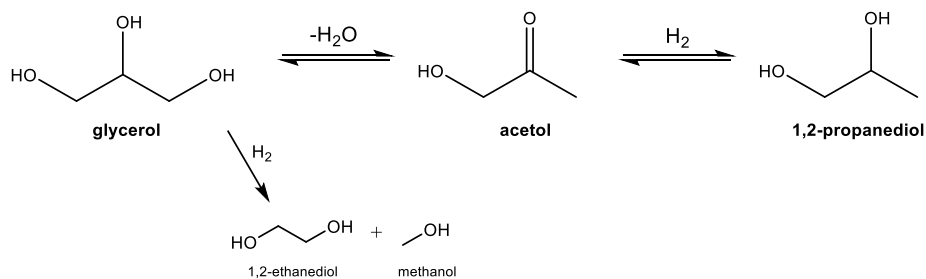


Figure 3.6. Reaction scheme of glycerol hydrogenolysis towards 1,2-propanediol.

As the La-doped catalyst was most promising in terms of catalytic stability, it was investigated further. In literature, there is no consensus on the active site in the hydrogenolysis reaction and the origin of the acidity. It is commonly accepted that γ -Al₂O₃ has intrinsic acidity and Cu^{δ+} sites contribute as Lewis acid sites because of their high electron affinity. To comprehensively elucidate the role of the different Cu species, controllable preparation of catalysts with various Cu⁺ or Cu⁰ amounts is necessary. Therefore, a series of 12 La-Cu/ γ -Al₂O₃ with different La/Cu mass ratios were prepared as La is able to modify the ratio between Cu⁺ and Cu⁰. Both La and Cu were homogeneously dispersed on the support after calcination and reduction. The La/Cu ratio had no significant impact on the physicochemical properties, *e.g.* surface area, average pore size and pore volume, of the calcined catalysts. After calcination, most of the Cu species on the catalyst surface were in the Cu²⁺ oxidation state. As a result of the La-Cu interaction, the number of Cu⁺ species increased up to 20 %. After reduction of the catalysts, there was a co-existence of both Cu⁺ and Cu⁰. At higher La/Cu ratios, the fraction of Cu⁺ was higher, as the Cu particle was smaller. The Cu-loading, rather than the promotion ratio, affected the size of the Cu⁰ particles (1.3 – 5.5 nm). It was found that with increasing La/Cu ratio, the amount of weak and moderate acid sites increased, associated with Lewis acid sites, while that of the strong acid sites decreased.

Due to an increased amount of moderately acid sites, introduced by Cu⁺, glycerol dehydration to acetol is enhanced, resulting in an increased selectivity to 1,2-propanediol, exceeding 82 %. The maximum 1,2-propanediol selectivity at these conditions was found to be 94 %, with 1,2-ethanediol as major side

product, for a La/Cu mass ratio of 0.088. It was found that glycerol hydrogenolysis to 1,2-ethanediol also requires a synergy between metal and acid sites. It can be concluded that glycerol dehydration to acetol proceeds mostly *via* the acid sites of the Cu species, where it further hydrogenates over the metallic Cu⁰ sites, see Figure 4.22. The undesired products require stronger acid sites, mostly provided by the support.

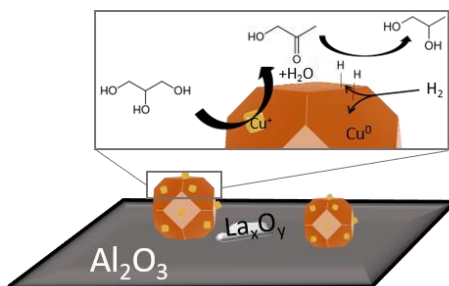


Figure 4.22. Schematic representation of proposed role of La-Cu/ γ -Al₂O₃ in glycerol hydrogenolysis. La-Cu/ γ -Al₂O₃ surface and the interaction between Cu⁺ and Cu⁰ in 1,2-propanediol formation.

A more pronounced variation of the acidic properties of the catalysts and their performance is expected to be achieved by the introduction of SiO₂ into the Al₂O₃ support. The considered Al₂O₃-SiO₂ supports are pure γ -Al₂O₃ (indicated as Al₂O₃), 99 wt.% γ -Al₂O₃ – 1 wt.% SiO₂ (indicated as 99Al₂O₃), 60 wt.% γ -Al₂O₃ – 40 wt.% SiO₂ (indicated as 60Al₂O₃) and pure SiO₂ (indicated as SiO₂). The total acidity decreased in the order of 60Al₂O₃ \geq 99Al₂O₃ > Al₂O₃ > SiO₂. The total acidity for the mixed phases was more pronounced than for their pure constituents. This trend was related to the creation of strong acid sites, most probably Brønsted acid sites, when SiO₂ is introduced in the Al₂O₃ framework. It was found that with increasing SiO₂-content, the Cu-support interaction decreased resulting in larger Cu⁰ particles (up to 10 nm) and a higher Cu⁺ surface fraction (up to 75 %). It was not possible to determine the dominant effect. However, it was clear that both the particle size of Cu⁰ and the acidity affected by the Cu⁺ fraction, enhanced the catalytic activity.

Overall, it was revealed that Cu supported catalysts exhibited a structure sensitivity, *i.e.* a relationship between the Cu⁰ particle size and the TOF, for the glycerol hydrogenolysis, see Figure 7.1. As two different slopes were identified, other factors, such as the coordination number of the Cu species, should play a role in the catalytic activity. On the one hand, the coordination number for defects, such as kink sites or step sites, is different (*i.e.* three and four, respectively). On the other hand, the different facets in a Cu particle, such as (110), (100) or (111), result in different coordination numbers of the surface layer atoms, *i.e.* seven, eight and nine respectively. It was assumed that the catalysts following relationship (A) in Figure 7.1 exhibit Cu⁰ species with a higher coordination number and, hence, a higher activity, compared to the catalysts following relationship (B).

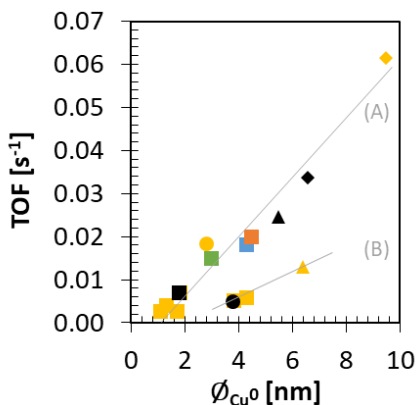


Figure 7.1 TOF at 12 h TOS, $125 \text{ kg}_{\text{cat}} \text{ s mol}^{-1}_{\text{glycerol}}$, 473 K, a total H_2 pressure of 7.5 MPa and a molar H_2 to glycerol ratio of 7 as function of the average diameter of the Cu^0 particle, ϕ_{Cu^0} , for pure glycerol hydrogenolysis for the Cu (black), Ba-Cu (blue), Ce-Cu (orange), Cs-Cu (green) and La-Cu (yellow) catalysts supported on Al_2O_3 (■), $99\text{Al}_2\text{O}_3$ (●), $60\text{Al}_2\text{O}_3$ (▲) and SiO_2 (◆).

To conclude, Ba, Ce and La are suitable as dopants, in this case, promoters for Cu-based catalysts for glycerol hydrogenolysis under industrial-like conditions. The metals act both as structural (inhibiting the sintering) and textural (increasing the selectivity) promoters. For the La-Cu catalysts, it was found that the La promotion inhibited the sintering of the Cu^0 particles as a result of the stronger La-Cu interaction. The presence of Cu^+ , which is considered to be weak-moderate Lewis acid, increased the total acidity of the catalysts and, hence, resulted in an increased 1,2-propanediol (> 86 %) selectivity compared to the Cu catalyst (82 %).

Oil deodorizer distillates as resource for squalene

Due to the increased awareness about marine life, which, among others, constitutes the main source of squalene via shark liver, the interest into a vegetable squalene source has increased, especially in the cosmetic industry. In most cases, the squalene concentration in vegetable oil is too low (1500-2100 ppm) for direct separation to be economically viable. However, ODD represent a promising opportunity for squalene recovery as its concentration is 150 times higher compared to that in the original vegetable oil. Therefore, process simulations were performed to compare olive, sunflower and soybean ODD as a vegetal source for squalene. This production route, as an alternative to extraction from deep-sea shark liver oil, is assessed in terms of squalene extraction yield, recovery and purity as well as techno-economics.

The ODD is a complex mixture of free fatty acids (FFA), fatty acid methyl esters (FAME), triglycerides (TG), diglycerides (DG), monoglycerides (MG), phytosterols and their esters, tocopherols, some aldehydes or ketones and hydrocarbons, such as squalene. The composition of the ODD depends on the type of refining and vegetable oil used. Chemically refined ODD comprises on average out of

20-30 wt.% of the minor components, *i.e.* tocopherols, sterols and squalene. The extraction of these components from ODD by supercritical CO_2 (sc- CO_2), which is considered a green solvent, is not straightforward because of the comparable solubility of the FFAs and the squalene in sc- CO_2 . By transforming the former *via* esterification with ethanol, the squalene recovery efficiency can be enhanced as the formed fatty acid ethyl esters (FAEE) have a lower solubility than squalene in sc- CO_2 . Simultaneously, the glycerides present in the oil also react with the ethanol (*i.e.* a transesterification). When the esterification is performed with a supercritical alcohol, no catalyst is required, which leads to the great advantage that no specific separation must be performed after reaction and that the product is not polluted by additional impurities. A purification is still required to achieve high purity of squalene. A vacuum distillation is performed to separate squalene from FAME. An additional distillation was included to separate FAEE from the sterols and tocopherols, increasing the economic viability even more. This three-step process, *i.e.* a supercritical esterification followed by a sc- CO_2 extraction and purification, is schematically presented in Figure 6.4.

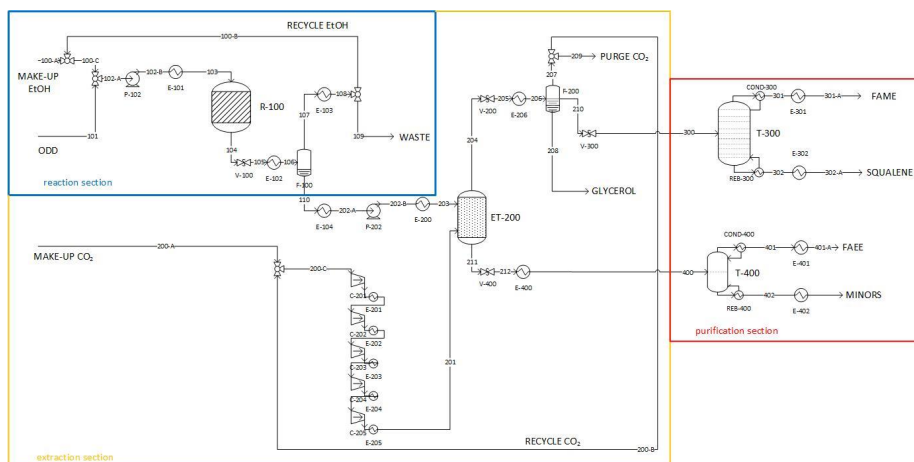


Figure 6.4. Process flow diagram for the supercritical esterification (blue section) and supercritical CO_2 -extraction (yellow section) for squalene purification (red section) for the olive, sunflower and soybean ODD.

The reaction kinetics of the FFA esterification and the transesterification reactions with supercritical ethanol were determined for sunflower ODD with ethanol at 15 MPa and varying space times (0 – 60 min), temperatures (523 K - 573 K) and ethanol to ODD ratios (0.3 - 1.5 $\text{g}_{\text{EtOH}} \text{g}^{-1}_{\text{ODD}}$). The reactions considered are the esterification of the FFA and the transesterification of the glycerides, which comprises three consecutive steps. The kinetic model is simplified by assuming the reactions to be irreversible and considering the chemical similarity, if not equivalence, of the consecutive transesterification reactions, leading to a kinetic model with only four kinetic parameters. The regression resulted in a globally significant model with statistically significant and physically meaningful values.

The activation energies for the esterification and transesterification reaction amount to $101 \pm 36 \text{ kJ mol}^{-1}$ and $27 \pm 8 \text{ kJ mol}^{-1}$, respectively.

In order to perform simulations, a proper selection of the models for the calculation of the thermodynamic properties, such as density, enthalpy, entropy, heat capacity, *etc.*, of each pure component and their mixtures has to be established. For the reaction section, an ideal property method was selected as it is assumed that non-idealities are accounted for via the estimated kinetic parameters. For the extraction section, the Redlich-Kwong-Aspen EOS was selected as it has been found to perform well at supercritical conditions with light gases as CO_2 . For the purification section, which is a low pressure section, the activity coefficient model UNIQUAC-Redlich-Kwong was used. Next, the complexity of the ODDs was assessed by the introduction of eight component families for which a model component was selected, *i.e.* for FFA (oleic acid), TG (tri-olein), DG (di-olein), MG (mono-olein), FAEE (ethyl oleate), phytosterols (β -sitosterol), tocopherols (α -tocopherol) and squalene. Additionally, interactions between the components may not be underestimated. Errors in the properties or interactions can lead to major issues in the determination of the process configuration, sizing and evaluation. Due to the absence of well determined phase equilibria for supercritical extraction for the components in this mixture in the software's database, it is difficult to obtain meaningful predictions. Therefore, binary interactions coefficients between sc- CO_2 and each model component of ODD were regressed to literature reported experimental data. Additionally, the binary interaction between TG and FFA, TG and sterols, FAME and squalene and ethanol and water were regressed as well to literature reported experimental data. It was found based on the parity diagrams that the thermodynamic model Redlich-Kwong-Aspen OES, with the estimated binary coefficients, was capable to predict vapor-liquid equilibria in an adequate way, resulting in reliable simulations.

During the process design, a versatile process configuration was aimed at, which is capable of processing different ODD feedstocks. Therefore a sensitivity analysis was performed to determine the optimal combination of operating conditions taking into account the determined reaction kinetics and suitable thermodynamic models. According to the simulation results, a final squalene product with purity $> 98 \text{ wt.}\%$ and $> 95 \%$ squalene recovery can be obtained upon the combination of a supercritical esterification of olive ODD, at 573 K, 15 MPa and an ethanol to ODD mass inlet ratio of 1, followed by a sc- CO_2 extraction at 333 K, 12 MPa and a solvent to feed mass ratio of 11. Both sunflower and soybean ODD can also be a good alternative source of pure squalene. After supercritical esterification of sunflower ODD, followed by extraction at 333 K, 12 MPa with a solvent to feed mass ratio of 15, a 98wt.% squalene product can be achieved with full recovery. A squalene recovery of 96 % was achieved with soybean ODD, resulting in a 98 wt.% squalene product. The reactor, extraction and distillation towers can be designed as such, that the same units can be used for different ODDs.

The soybean ODD yielded the highest yearly revenue of 15.6 M€, followed by the olive ODD (3.1 M€) and the sunflower ODD (2.2 M€) for a capacity of 1 kton_{ODD} per year. The soybean ODD yields a significantly higher revenue due to the higher amount of the minor-products, which have also a higher purity compared to olive and sunflower ODD. Nevertheless, its margin was the lowest due the high raw material price of the ODD itself. It was found that sunflower ODD is the most versatile feedstock, see Figure 6.8, due its lower sensitivity to price variations of a single product, *e.g.* squalene (major revenue for olive ODD) or the minors (major revenue for soybean ODD). For a high squalene demand, one should select olive ODD. In case of a drop in demand, one could easily switch to sunflower ODD as the corresponding revenue not only comes from squalene but also from FAEE in comparison with soybean ODD. Depending on the feedstock price, a switch to another ODD could easily be made owing to the flexibility of the process.

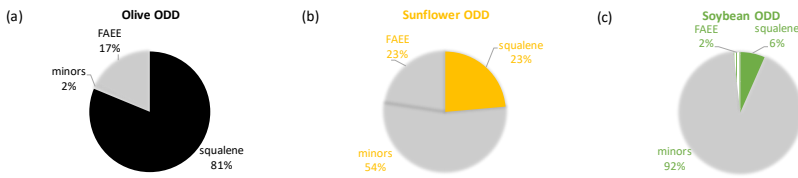


Figure 6.8. Percentage of the revenues from the key products, *i.e.* squalene (full) and minors (horizontal lines), and the side products, *i.e.* FAEE (vertical lines), for olive (black), sunflower (yellow) and soybean (green) ODD.

To conclude, it is clear that the feedstock that can be labeled as the most ‘profitable’ one depends on the market price of the feedstock and the products. Nonetheless, this flexible process configuration can contribute to the recovery of vegetable squalene in an economically viable way.

SAMENVATTING

Sinds enkele decennia is de interesse in hernieuwbare grondstoffen, zoals biomassa, voor chemicaliën en energie toegenomen als gevolg van afnemende fossiele oliereserves en door de uitstoot van broeikasgassen en het gevolg op de klimaatverandering. Biogebaseerde tegenhangers zijn beschikbaar of kunnen ontwikkeld worden voor vrijwel elke chemische stof en daarom speelt de chemische industrie een cruciale rol in de verschuiving van een op aardolie gebaseerde samenleving naar een groene en milieuvriendelijke samenleving. Het gebruik van (afval)biomassa levert niet alleen ecologische maar ook economische voordelen op. Het helpt de afhankelijkheid van – uitputtende – fossiele oliebronnen te verminderen door gebruik te maken van algemeen beschikbare hernieuwbare bronnen. Sinds enkele jaren vindt er een verschuiving plaats naar de valorisatie van afval- of nevenstromen van plantaardige oliën, gekenmerkt met een lage economische waarde, die een belangrijke rol kunnen spelen in het realiseren van een groene en duurzame economie.

Eenzijds leidt de toegenomen wereldwijde vraag naar biodiesel als alternatieve brandstof tegelijkertijd tot een verhoogde productie van het belangrijkste nevenproduct glycerol, goed voor 10vol.% van het biodieselproductieproces. Vanwege de C3-structuur die drie hydroxylgroepen herbergt, wordt glycerol aanzien als een belangrijke platformmolecule. De economische haalbaarheid van de biodieselindustrie kan worden verbeterd door glycerol om te zetten in chemicaliën met een hoge toegevoegde waarde, zoals 1,2-propaandiol, dat toepassingen vindt in polyesterharsen, ontdooivloeistoffen, voedsel, medicijnen en cosmetische industrie, enz. Daarenboven is de katalytische hydrogenolyse van glycerol tot 1,2-propaandiol groen en duurzaam, in vergelijking met de conventionele productie uit het petrochemische propyleenoxide.

Anderzijds heeft de snelle bevolkingsgroei de productie van hoogwaardige eetbare oliën gestimuleerd. Om oliën van hoge kwaliteit te verkrijgen, d.i. met de gewenste smaak, geur en kleur, moet een complexe opeenvolging van processtappen worden uitgevoerd. Bij dit proces worden zijstromen geproduceerd, waaronder, het zogenaamde ontgeuringsdestillaat (ODD). Hoewel deze zijstroom waardevolle componenten, zoals squaleen, tocoferolen en sterolen, voor de voedings-, cosmetische en farmaceutische industrie bevat, heeft het weinig economische waarde en wordt het vaak als afval beschouwd. De recuperatie van deze componenten zou voor een meer duurzame productie ervan kunnen zorgen, aangezien de belangrijkste bron van squaleen de lever van diepzeehaaien is, terwijl sterolen en tocoferolen voornamelijk worden verkregen via chemische synthese uit aardolieproducten.

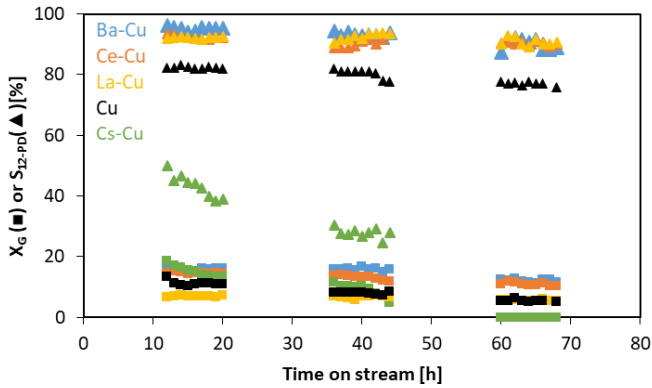
Men verwacht dat de wereldproductie van plantaardige oliën en biodiesel de komende decennia voortdurend zal stijgen, en daarom is het interessant om deze als biogebaseerde grondstoffen te onderzoeken. Dit doctoraat richt zich op de valorisatie van nevenstromen van plantaardige oliën op verschillende niveaus. In het eerste deel wordt de mogelijke winning van squaleen uit ODD onderzocht en beoordeeld via een gedetailleerde processimulatie. In het tweede deel wordt de impact van de Cu-katalysatoreigenschappen op de glycerol hydrogenolyse tot 1,2-propaandiol systematisch onderzocht,

met als doel het verkrijgen van strategische inzichten voor het ontwerp van nieuwe, goed performante katalysatoren.

Bepalende factoren voor de katalysatorprestaties in glycerolhydrogenolyse

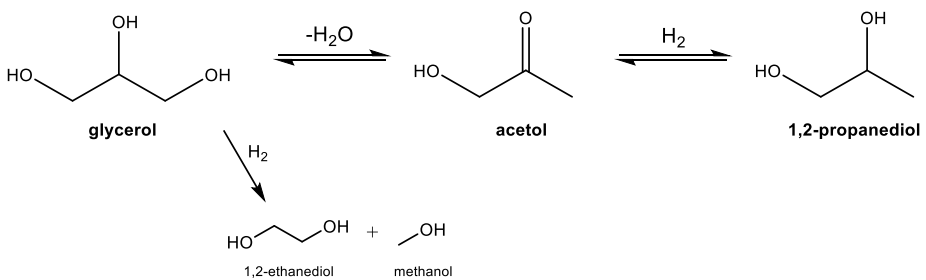
Cu-gebaseerde katalysatoren worden industrieel vaak gebruikt voor glycerolhydrogenolyse vanwege hun lagere prijs in vergelijking met edelmetalen en hun hogere selectiviteit voor C-O-splitsing in vergelijking met andere overgangsmetalen, wat resulteert in een hoge selectiviteit voor 1,2-propaandiol. Ongeacht de gebruikte drager zijn Cu-katalysatoren gevoelig voor deactivering, meestal door sintering. Door het toevoegen van doteermiddelen wordt beoogd de katalytische prestatie, voornamelijk de stabiliteit van de katalysator, te verbeteren. Verschillende auteurs hebben (combinaties van) doteermiddelen onderzocht om de prestaties van de katalysator te verbeteren, maar er is geen systematisch onderzoek gedaan naar commercieel relevante Cu-gebaseerde katalysatoren voor glycerolhydrogenolyse.

Daarom worden Cu/ γ -Al₂O₃ katalysatoren gedoteerd met Ba, Ce, Cs en La onderzocht voor hydrogenolyse van zuivere glycerol in de vloeibare fase onder industrieel relevante omstandigheden. De katalysatoren zijn bereid door sequentiële impregnatie. Eerst, werd het doteringsmiddel op de drager geïmpregneerd, gevolgd door een calcinatie. Vervolgens werd Cu op de gemodificeerde drager geïmpregneerd en werd deze opnieuw gecalcineerd. De Cu-katalysator vertoonde een uitgesproken deactivering na 68 uur, terwijl de Ba-, Ce- en La-gedoteerde katalysatoren qua glycerolconversie in de tijd vrijwel stabiel bleven, zie Figuur 3.5. Deze deactivering kon worden toegeschreven aan het sinteren en niet aan cokesvorming. Er werd gevonden dat doteermiddelen de Cu⁰-deeltjesgrootte tijdens de reactie stabiliseerden, en dus de sintering in bedwang hielden. Waar de deeltjesgrootte van de Cu-katalysator, zoals bepaald door dissociatieve N₂O-adsorptie, toenam tot een factor 100 vergeleken na de reactie (d.w.z. van 1,8 nm naar > 120 nm), werd een maximale toename van ongeveer één grootteorde waargenomen voor de gedoteerde katalysatoren (d.w.z. van 1,7 nm tot 15 nm). De La-dotering resulteerde in de meest uitgesproken stabilisatie van de Cu⁰-deeltjesgrootte, wat ook werd bewezen door de hoogste stabiliteit in termen van glycerolomzetting als functie van de reactietijd.



Figuur 3.5. Glycerolconversie (■) en 1,2-propanediolselectiviteit (▲) op 473 K, 7,5 MPa, $135 \text{ kg}_{\text{cat}} \text{ s mol}^{-1} \text{ glycerol}$ en $7 \text{ molH}_2 \text{ mol}^{-1} \text{ glycerol}$ voor de Cu (zwart), Ba-Cu (blauw), Ce-Cu (oranje), Cs-Cu (groen) en La-Cu (geel) katalysator gedragen op $\gamma\text{-Al}_2\text{O}_3$

Bovendien verhoogde de dotering met Ba, Ce en La de selectiviteit naar 1,2-propanediol van 82% naar respectievelijk 96%, 93% en 92%. De dehydratatie van glycerol leidt tot de vorming van acetol dat vervolgens wordt gehydrogeneerd tot 1,2-propanediol, terwijl 1,2-ethandioliol wordt gevormd door een C-C-splitsing van glycerol, zie Figuur 3.6. Voor de Ba- en Ce-gedoteerde katalysator werd de verhoogde selectiviteit toegeschreven aan een toename van de totale zuurtegraad van de katalysator. Bij de Ce- en Ba-gedoteerde katalysator trad een lichte afname in selectiviteit op met de tijd, voornamelijk als gevolg van een toename in 1,2-ethandioliol, d.w.z. C-C in plaats van C-O-splitsing. Voor de La-gedoteerde katalysator bleef de 1,2-propanediolselectiviteit vrijwel constant gedurende de onderzochte reactietijd.

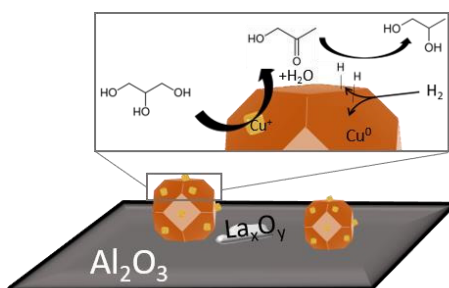


Figuur 3.6. Reactieschema van glycerolhydrogenolyse naar 1,2-propanediol.

Omdat de La-gedoteerde katalysator het meest veelbelovend was in termen van katalytische stabiliteit, werd deze gebruikt voor verder onderzoek. In de literatuur bestaat er geen consensus over de actieve site in de hydrogenolyse en de oorsprong van de zure sites. Het is algemeen aanvaard dat $\gamma\text{-Al}_2\text{O}_3$ een intrinsieke zuurtegraad heeft en $\text{Cu}^{\delta+}$ -sites bijdragen als Lewis-zure sites vanwege hun hoge

elektronenaffiniteit. Om de rol van de verschillende Cu-sites verder in kaart te brengen, is een controleerbare bereiding van katalysatoren met verschillende Cu^+ - of Cu^0 -hoeveelheden noodzakelijk. Daarom werd een reeks van twaalf La-Cu/ γ - Al_2O_3 -katalysatoren met verschillende La/Cu-massaverhoudingen gemaakt, aangezien La de verhouding tussen Cu^+ en Cu^0 kan wijzigen. Zowel La als Cu waren homogeen gedispergeerd op de drager, zowel na de calcinatie als na de reductie. De La/Cu-verhouding had geen significante impact op de fysisch-chemische eigenschappen, zoals specifiek oppervlak, gemiddelde poriegrootte en porievolume van de gecalcineerde katalysatoren. Na de calcinatie bevonden de meeste Cu-deeltjes op het katalysatoroppervlak zich in de Cu^{2+} -oxidatietoestand. Als gevolg van de La-Cu-interactie nam de hoeveelheid Cu^+ toe tot 20%. Na reductie van de katalysatoren was er een co-existentie van zowel Cu^+ als Cu^0 . Bij hogere La/Cu-verhoudingen was de fractie Cu^+ hoger, omdat het Cu-deeltje kleiner was. Meer dan de La/Cu-verhouding, beïnvloedde de Cu-lading de grootte van de Cu^0 -deeltjes (1,3 - 5,5 nm). Er werd gevonden dat met toenemende La/Cu-verhouding de hoeveelheid zwakke en matige zure sites, geassocieerd met Lewis zure sites, toenam terwijl die van de sterk zure sites afnam.

Door een verhoogde hoeveelheid matig zure sites, geïntroduceerd door Cu^+ , wordt de dehydratatie van glycerol tot acetol versterkt, wat resulteert in een verhoogde selectiviteit voor 1,2-propaandiol (>> 82 %). De maximale 1,2-propaandiolselectiviteit bij deze omstandigheden bleek 94% te zijn, met 1,2-ethaandiol als belangrijkste bijproduct, voor een La/Cu-verhouding van 0,088. Er werd gevonden dat de hydrogenolyse van glycerol tot 1,2-ethaandiol ook een synergie vereist tussen metaal en zure sites. Er kan worden geconcludeerd dat de dehydratatie van glycerol tot acetol voornamelijk verloopt via de zure sites van de Cu-deeltjes, waar het verder hydrogeneert over de metallische Cu^0 -sites, zie Figuur 4.22. De ongewenste producten worden gevormd op sterkere zure sites, meestal veroorzaakt door de drager.

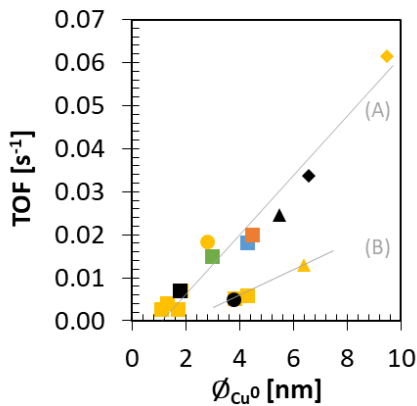


Figuur 4.22. Schematische weergave van het La-Cu/ γ - Al_2O_3 oppervlak en de synergie tussen Cu^+ en Cu^0 in de glycerol hydrogenolyse, met LAS = Lewis zure sites en BAS = Brønsted zure sites.

Een grotere variatie van de zure eigenschappen van de katalysatoren, is gerealiseerd door de introductie van SiO_2 in de Al_2O_3 -drager. De Al_2O_3 - SiO_2 -dragers zijn zuivere γ - Al_2O_3 (aangeduid als Al_2O_3), 99 gew.% γ - Al_2O_3 – 1 gew.% SiO_2 (aangeduid als 99 Al_2O_3), 60gew.% γ - Al_2O_3 – 40 gew.% SiO_2

(aangeduid als $60\text{Al}_2\text{O}_3$) en zuivere SiO_2 (aangeduid als SiO_2). De totale zuurtegraad nam af volgens: $60\text{Al}_2\text{O}_3 \geq 99\text{Al}_2\text{O}_3 > \text{Al}_2\text{O}_3 > \text{SiO}_2$. De totale zuurtegraad voor de gemengde fasen was hoger dan voor de zuivere dragers onderling. Deze trend hield verband met de introductie van sterk zure sites, hoogstwaarschijnlijk Brønsted-zure sites, wanneer SiO_2 wordt geïntroduceerd in het Al_2O_3 -structuur. Het bleek dat bij een toenemend SiO_2 -gehalte de Cu-drager interactie afnam, wat resulteerde in grotere Cu^0 deeltjes (tot 10 nm) en een hogere Cu^+ fractie (tot 75%). Het was niet mogelijk om het dominante effect te bepalen, maar het is duidelijk dat zowel de Cu^0 -deeltjesgrootte als de zuurtegraad, beïnvloed door de Cu^+ -fractie, de katalytische activiteit verhoogden.

Er werd onthuld dat de gedragen Cu-katalysatoren een structuurgevoeligheid vertoonden, d.w.z. een verband tussen de Cu^0 -deeltjesgrootte en de omzettingfrequentie (TOF), voor glycerolhydrogenolyse (Figuur 7.1). Aangezien er twee verschillende hellingen werden geïdentificeerd, is de structuurgevoeligheid niet alleen gerelateerd aan de ϕ_{Cu^0} . Daarom moeten andere factoren, zoals het coördinatiegetal van het Cu-deeltje, een rol spelen bij de katalytische activiteit. Enerzijds is het coördinatiegetal voor defecten, zoals knikken of stapplaatsen, verschillend (d.w.z. respectievelijk drie en vier). Anderzijds resulteren de verschillende kristalvlakken in een Cu-deeltje, zoals (110), (100) of (111), in verschillende coördinatiegetallen, respectievelijk zeven, acht en negen. Er werd aangenomen dat de katalysatoren volgens relatie (A) in Figuur 7.1 Cu^0 -deeltjes bevatten met een hoger coördinatiegetal en dus een hogere activiteit in vergelijking met de katalysatoren volgens relatie (B).



Figuur 7.1. Omzettingfrequentie (TOF) na een reactietijd van 12 h, op $125 \text{ kg}_{\text{cat}} \text{ s}^{-1} \text{ mol}^{-1}$ glycerol, 473 K, een totale H_2 druk van 7.5 MPa en een molaire H_2 tot glycerol verhouding van 7 als functie van de gemiddelde diameter van een Cu^0 deeltje, ϕ_{Cu^0} , voor pure glycerol hydrogenolyse over een Cu (zwart), Ba-Cu (blauw), Ce-Cu (oranje), Cs-Cu (groen) en La-Cu (geel) katalysator gedragen op Al_2O_3 (■), $99\text{Al}_2\text{O}_3$ (●), $60\text{Al}_2\text{O}_3$ (▲) en SiO_2 (◆).

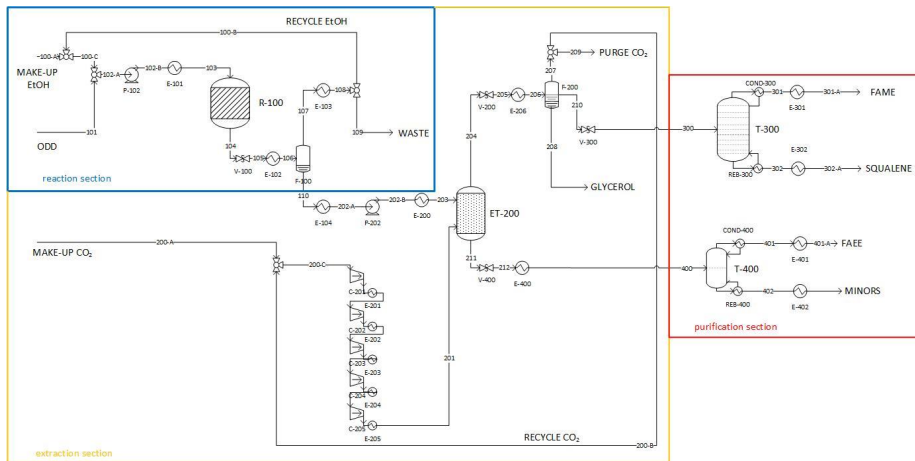
Samenvattend, Ba, Ce en La zijn geschikt als promotoren voor gedragen Cu-katalysatoren voor glycerolhydrogenolyse onder industriële omstandigheden. De metalen werken zowel als structurele (*i.e.* het remmen van het sinteren) en texturele (*i.e.* het verhogen van de selectiviteit) promotoren. Voor de

La-Cu-katalysatoren werd gevonden dat de La-promotie het sinteren van de Cu^0 -deeltjes remde als gevolg van de sterkere La-Cu-interactie. De aanwezigheid van Cu^+ , dat als zwak-matig Lewis zuur wordt beschouwd, verhoogde de totale zuurtegraad van de katalysatoren en resulteerde dus in een verhoogde 1,2-propaandiol (> 86 %) selectiviteit in vergelijking met de Cu-katalysator (82 %).

Ontgeuringsdestillaten als grondstof voor squaleen

Door het toegenomen bewustzijn over het zeeleven, dat, onder meer, de belangrijkste bron van squaleen uitmaakt via haaienlever, is de belangstelling voor een alternatieve plantaardige bron gegroeid, vooral in de cosmetische industrie. In de meeste gevallen is de squaleenconcentratie in plantaardige olie te laag (1500-2100 ppm) om de directe scheiding economisch haalbaar te maken. ODD vertegenwoordigt echter een veelbelovende mogelijkheid voor het winnen van squaleen, aangezien de concentratie ervan tot 150 keer hoger is in vergelijking met die in de oorspronkelijke, plantaardige olie. Daarom werden processimulaties uitgevoerd om olijf, zonnebloem en sojabonen ODD te vergelijken als een plantaardige bron voor squaleen. Deze productieroute, als alternatief voor extractie uit diepzeehaaienleverolie, wordt beoordeeld in termen van opbrengst, winning en zuiverheid van squaleenextractie en technisch-economische aspecten.

Het ODD is een complex mengsel van vrije vetzuren (FFA), vetzuurmethylesters (FAME), triglyceriden (TG), diglyceriden (DG), monoglyceriden (MG), fytoosterolen en hun esters, tocoferolen, aldehyden of ketonen en andere koolwaterstoffen, zoals squaleen. De samenstelling van de ODD hangt af van het type raffinage en de gebruikte plantaardige olie. Chemisch geraffineerde ODD omvat gemiddeld 20-30 gew.% van de minoren, dit zijn tocoferolen, sterolen en squaleen. De extractie van de minoren uit ODD met superkritisch CO_2 (sc- CO_2), dat als een duurzaam oplosmiddel wordt beschouwd, is niet eenvoudig vanwege de vergelijkbare oplosbaarheid van FFA's en squaleen in sc- CO_2 . Door de FFA's om te vormen via een verestering met ethanol, kan de squaleenrecuperatie worden verbeterd, aangezien de gevormde vetzuurethylesters (FAEE) een lagere oplosbaarheid hebben dan squaleen in sc- CO_2 . Tegelijkertijd reageren de in de olie aanwezige glyceriden ook met de ethanol (d.w.z. een omestering). Wanneer de verestering wordt uitgevoerd met een superkritisch ethanol, is geen katalysator nodig wat als groot voordeel heeft dat er na de reactie geen extra scheiding hoeft uitgevoerd te worden en dat het product niet wordt verontreinigd met de katalysator. Vervolgens is er nog steeds een scheiding nodig om een hoge zuiverheid van squaleen te bereiken. Er wordt een vacuümdestillatie uitgevoerd om squaleen van FAME te scheiden. Er is een extra destillatie nodig om FAEE te scheiden van de sterolen en tocoferolen, waardoor de economische haalbaarheid van het voorgestelde procedé nog meer wordt vergroot. Het volledige proces bestaat dus uit drie stappen, d.w.z. een superkritische verestering gevolgd door een sc- CO_2 -extractie en opzuivering, en wordt schematisch weergegeven in Figuur 6.4.



Figuur 6.4. Processchema voor de superkritische verestering (blauwe sectie) en superkritische CO₂-extractie (gele sectie) voor squalenopzuivering (rode sectie) voor het olijf, zonnebloem en soja ODD.

De reactiekinetiek van de FFA-verestering en de omsteringsreacties met superkritisch ethanol werden bepaald voor zonnebloem ODD bij 15 MPa en variërende ruimtetijden (0 – 60 min), temperaturen (523 K - 573 K) en ethanol tot ODD verhoudingen (0,3 - 1,5 g_{EtOH} g⁻¹_{ODD}). De beschouwde reacties zijn de verestering van de FFA en de omstering van de glyceriden, die uit drie opeenvolgende stappen bestaat. Het kinetisch model werd vereenvoudigd door aan te nemen dat de reacties onomkeerbaar zijn en dat er een chemische equivalentie van de opeenvolgende omsteringsreacties is, wat leidde tot een kinetisch model met vier kinetische parameters. De regressie resulteerde in een globaal significant model met statistisch significante en fysisch zinvolle waarden. De activeringsenergieën voor de veresterings- en omsteringsreactie zijn respectievelijk $101 \pm 36 \text{ kJ mol}^{-1}$ en $27 \pm 8 \text{ kJ mol}^{-1}$.

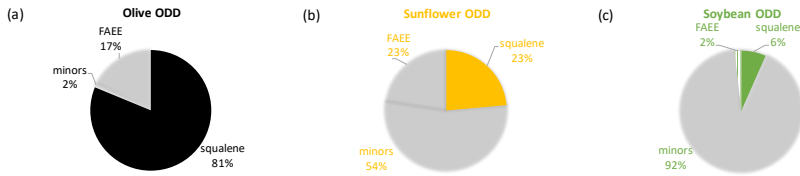
Om simulaties uit te voeren, moet een goede selectie worden gemaakt van de thermodynamische modellen die de dichtheid, de enthalpie, de entropie, de warmtecapaciteit, enz., berekenen voor zowel elke zuivere component als het mengsel. Voor de reactiesectie werd een ideaaltoestandsvergelijking gekozen omdat werd aangenomen dat niet-idealiteiten worden verklaard via de bepaalde kinetische parameters. Voor het extractiegedeelte werd de Redlich-Kwong-Aspen toestandsvergelijking gekozen, omdat deze goed blijkt te presteren onder superkritische omstandigheden met lichte gasen zoals CO₂. Voor de opzuiveringssectie, die een lagedruksectie is, werd het activiteitscoëfficiëntmodel UNIQUAC-Redlich-Kwong gebruikt. Vervolgens werd de complexiteit van de ODD's vereenvoudigd door introductie van acht componentfamilies waarvoor telkens een modelcomponent werd geselecteerd, namelijk voor FFA (oliezuur), TG (tri-oleïne), DG (di-oleïne), MG (mono-oleïne), FAEE (ethyl oleaat), fytosterolen (β -sitosterol), tocoferolen (α -tocoferol) en squaleen. Bovendien mogen interacties tussen de componenten niet worden onderschat. Fouten in de eigenschappen of interacties kunnen leiden tot grote problemen bij de procesconfiguratie, dimensionering en evaluatie. Wegens het ontbreken van goed

bepaalde geschatte fase-evenwichten bij de superkritische extractieomstandigheden van de componenten in dit mengsel in de database van de gebruikte software, is het moeilijk om zinvolle voorspellingen te verkrijgen. Daarom werd voor de binaire interactiecoëfficiënten tussen sc-CO₂ en elke ODD-modelcomponent een regressie met experimentele literatuurdata uitgevoerd. Daarnaast werd dit ook voor de binaire interactie tussen TG en FFA, TG en sterolen, FAME en squaleen en ethanol en water gedaan. Op basis van de pariteitsdiagrammen werd gevonden dat het thermodynamische model Redlich-Kwong-Aspen OES, met de geschatte binaire coëfficiënten, in staat was om damp-vloeistofevenwichten op een adequate manier te voorspellen, wat resulteerde in betrouwbare simulaties.

De verkregen reactiekinetiek en de gevalideerde thermodynamische modellen werden gebruikt om het volledig proces te ontwerpen waarbij gestreefd was naar een veelzijdige procesconfiguratie die in staat is om de verschillende ODD-grondstoffen te verwerken. De reactor, extractie- en destillatiekolommen zijn zo worden ontworpen dat dezelfde eenheden voor verschillende ODD's kunnen worden gebruikt. Daarom werd een sensitiviteitsanalyse uitgevoerd om de optimale combinatie van werkcondities te bepalen, rekening houdend met de bepaalde reactiekinetiek en geschikte thermodynamische modellen. Het optimale ontwerp geeft een squaleen eindproductontwerp gaf een eindproduct met een zuiverheid van > 98 gew.% en een recuperatie > 95% door de combinatie van een superkritische verestering van olijfolie-ODD, bij 573 K, 15 MPa en een ethanol tot ODD massa-inlaatverhouding van 1, gevolgd door een sc-CO₂-extractie bij 333 K, 12 MPa en een solvent tot veresterde ODD massaverhouding van 11. Bovendien blijkt uit het ontwerp dat zowel zonnebloemolie- als sojaolie-ODD een goede alternatieve bron kunnen zijn voor puur squaleen. Na superkritische verestering van zonnebloem ODD, gevolgd door een extractie bij 333 K, 12 MPa en een massaverhouding van solventsolvent tot voeding van 15, kan een product met 98 gew.% squaleen worden bereikt met volledige terugwinning. Een squaleenrecuperatie van 96% werd bereikt met sojaolie-ODD, resulterend in een 98 gew.% squaleenproduct.

De techno-economische analyse toont de hoogste jaaromzet (15,6 M€) voor sojaolie-ODD, gevolgd door olijfolie-ODD (3,1 M€) en zonnebloemolie- ODD (2,2 M€) voor een capaciteit van 1 kton_{ODD} per jaar. Het sojaolie-ODD heeft een aanzienlijk hogere opbrengst vanwege de grotere hoeveelheid van de secundaire producten, die ook een hogere zuiverheid hebben in vergelijking met olijfolie- en zonnebloemolie-ODD. Desalniettemin was de marge het laagst, vanwege de hoge grondstofprijzen van het ODD zelf. Verder bleek dat zonnebloemolie-ODD de meest veelzijdige grondstof is, zie Figuur 6.8, vanwege de lagere gevoeligheid voor prijschommelingen van één enkel product, vb. squaleen (belangrijkste inkomsten voor olijfolie-ODD) of de tocoferolen en sterolen (belangrijkste inkomsten voor sojaolie-ODD). Bij een hoge vraag naar squaleen moet men olijfolie-ODD verwerken. In het geval van een dalende vraag, zou men gemakkelijk kunnen overstappen op zonnebloemolie-ODD, aangezien deze niet alleen inkomsten verkrijgt uit squaleen, maar ook uit FAEE in vergelijking met sojaolie-ODD.

Afhankelijk van de grondstofprijs kan door de flexibiliteit van het proces, eenvoudig worden overgeschakeld naar een andere ODD.



Figuur 6.8. Percentage van de inkomsten van de belangrijkste producten, d.w.z. squaleen (volledig gevuld) en minors, d.w.z. de tocoferolen en sterolen, (horizontale lijnen), en de bijproducten, d.w.z. FAEE (verticale lijnen), voor olijfolie- (zwart), zonnebloemolie- (geel) en sojaolie-ODD (groen).

Het is duidelijk dat de grondstof die als de meest ‘winstgevend’ kan worden bestempeld, afhangt van de marktprijs van de grondstof en de producten. Desalniettemin kan deze flexibele procesconfiguratie bijdragen tot het winnen van plantaardig squaleen op een economisch haalbare manier.

CHAPTER 1.
UPGRADING OF BYPRODUCTS
IN THE PROCESSING OF
VEGETABLE OILS AND FATS

1.1 The rise of renewable resources

After the industrial revolution in the mid-18th century, the world’s population has grown from 1.2 billion to a present number amounting to 7.8 billion people.¹ It is projected that the population will reach 9.2 billion people by 2040 with significant increase in the prime working-age population in Africa and India (Figure 1.1A). Further, it is estimated that by 2030 the middle class will almost double from 3 to 5.5 billion people.² This rise will coincide with a significant increase in energy demand (Figure 1.1B). In 2017, the world’s total energy supply increased to an all-time high of 14 171 Million Tonnes of Oil Equivalent (MTOE, 1 TOE ~ 42 GJ) and it is expected that it will have increased by 20 % in 2040.² Oil, coal and natural gas are the main contributors accounting for 32 %, 27 % and 23 %, respectively, of the 2018 energy consumption. Biofuels and waste only contributed for 9 %.^{2,3}

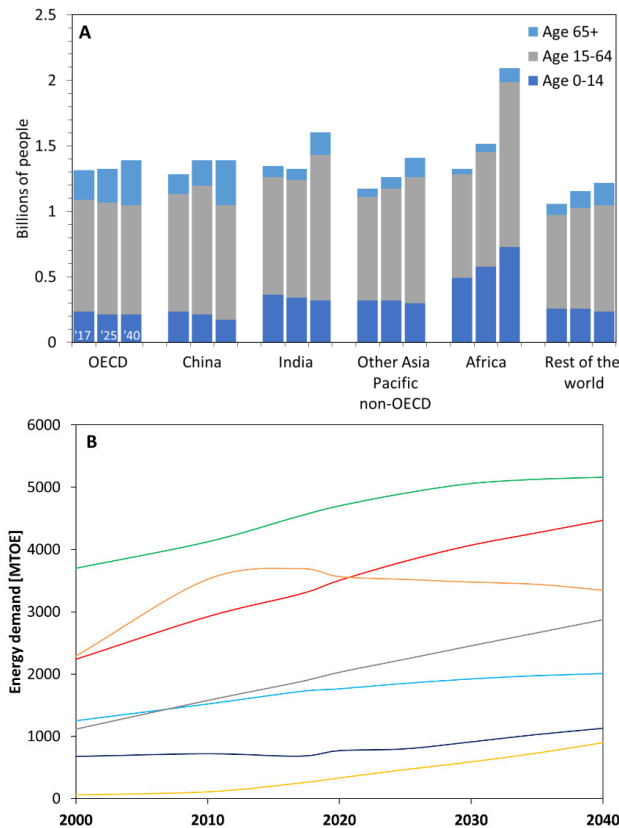


Figure 1.1. A: World demographics for 2017 (left column), forecast for 2025 (middle column) and 2040 (right column) for the youth population (dark blue), prime working-age (grey) and elderly (light blue).
OECD: Organization for Economic Co-operation and Development, with 38 member countries.
B: Global energy demand from 2010 to 2040 (forecast) of oil (green), coal (orange), natural gas (red), electricity (dotted grey), nuclear (dark blue), biomass (light blue), wind and solar (yellow).²

It is clear that fossil oil still is and will remain the main source for not only for energy, as indicated in Figure 1.1B, but also for the production of chemicals and derived products. In 2020, the production of chemical and polymers is estimated at 330 Mton/year, which accounts for 16 % of the use of fossil oil.⁴ By using fossil oil, the balance between CO₂ released to the environment, and the CO₂ that can be absorbed by plants, is entirely disrupted (Figure 1.2). This imbalance in the carbon cycle has already resulted in an increased CO₂ concentration in the atmosphere, inducing climate change, but is also responsible for an increased acidity of the oceans, altering marine life.

As the world's demand for energy, chemicals and derivatives is increasing every year², new alternatives must be developed to satisfy not only the energy need, but also the production of chemicals in a sustainable way and restore the balance to the global ecosphere. Internationally, measures have been decided and agreed upon to combat climate change and its impacts, see, *e.g.*, the Paris Climate Agreement⁵ and Sustainable Development Goal 13⁶.

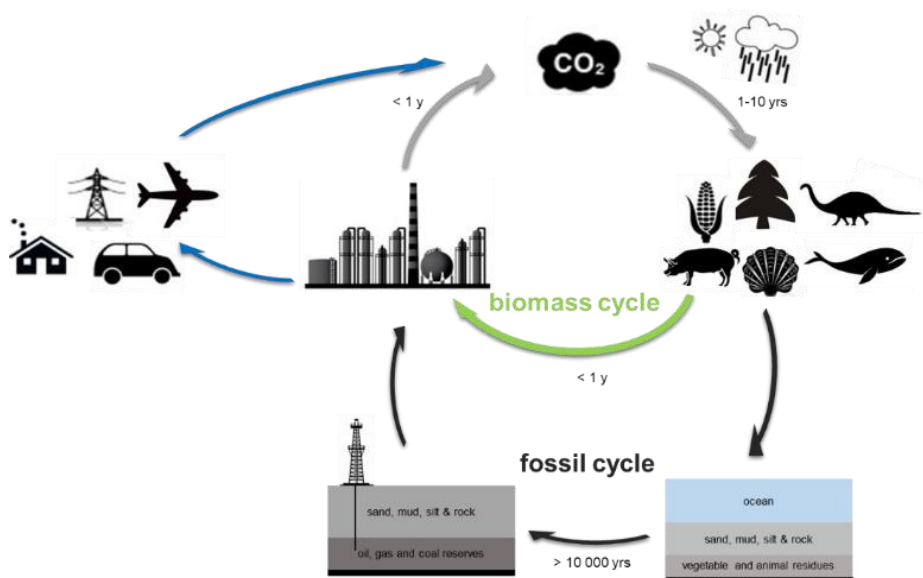


Figure 1.2. Simplified carbon cycle. Adapted from Thybaut *et al.*⁷.

Plants are capable of storing sunlight as chemical energy while consuming CO₂. In this process, carbon is captured from the air under the form of a stable organic compound. By eating plants, the carbon becomes part of fats and proteins in an animal. This makes biomass a renewable resource, maintaining a closed carbon cycle. Thus, the use of biomass and other renewable resources, as replacement for fossil oil, is essential for the sustainable development of our society. The public concerns on environmental issues and global climate change as well as the foreseen depletion of fossil fuel have increased the interest in bio-based chemicals. In 2020 the global bio-based chemical and polymer production was

estimated to be around 90 Mton/year⁴, of which 4.7 Mton/year was produced by the EU⁸, and it is anticipated that the world wide bio-based product market will yearly grow by *ca.* 10-15 % till 2025⁹⁻¹¹. From a technical point of view, almost all chemicals can be substituted by a bio-based counterpart and hence, the chemical industry plays an important role in the shift from a petroleum-based society to a green¹² and environmental friendly society. Currently, the cost for bio-based production exceeds in many cases the traditional route and there are many other challenges to overcome before one can consider biomass as part of the sustainable resource in the future. At all time, one should avoid the competition with the food production. Also, the overall life cycle assessment, including the use of land, processing costs, integration into the supply chain and the social-economic benefits, should be carefully addressed. Biomass mostly comprises of wood wastes, agricultural crops and their wastes, animal wastes or residues originating from food industries.

Using biomass or their waste streams brings not only considerable environmental, but also economic benefits. It helps to decrease the utilization of the depleting fossil oil by providing widely available renewable resources. The development of innovative and optimization of existing technologies could contribute to co-efficient outputs for energy production and value-added products from biomass.¹³

1.2 Vegetable oils as biomass resource

As stated before, biomass is a vegetable or animal derived material used as a feedstock in the chemical industry. It can be classified based on its chemical structure. Lignocellulosic biomass represents the most abundant biomass resource. The second type are lipids, such as vegetable oils and animal fats.¹⁴

In a typical vegetable oil processing plant, the oil is extracted from the seeds or beans by a sequence of mechanical and chemical extraction. To create a more stable oil for subsequent processing, a physical or chemical refining is carried out.¹⁵ The obtained refined, vegetable oil can be used for food applications (in the case of edible oils) or can be further processed (in the case of edible and non-edible oils). Due to the variety of fatty acids, glycerides, sterols, tocopherols, pigments, present in vegetable oils, it can be used for various applications such as solvents, lubricants, soaps, cosmetics, biofuels.

In 2019, the production of edible and non-edible vegetable oils exceeded 200 million metric tons.¹⁶ The main driving forces for this are the increased world population – and thus the need for edible oil – and the ever increasing demand for alternative fuels. It is foreseen that the world's production of edible oils and biodiesel will rise continuously in the decades to come, and, hence low value streams in these processes are interesting resources to investigate.

1.2.1 Valorization of a side stream in the biodiesel production

The increased global demand for biodiesel as an alternative fuel simultaneously led to an enhanced availability of the major side-product glycerol. This stream cannot be neglected as glycerol accounts for

10 vol.% of the resulting mixture from a transesterification process. Therefore, it is crucial to valorize this glycerol to increase the economic viability of the biodiesel industry.

Glycerol has emerged as a biomass-based feedstock in the chemical, solvent and fuel industry.^{17, 18} It is one of the key platform chemicals in these industries due to its unique chemical versatility thanks to its pronounced functionalization of the C3-backbone with three hydroxyl groups. The abundance of those hydroxyl functions is typical for biomass resources, which does not occur to a major extent in fossil resources. The effective H/C ratio, which is calculated as the ratio between hydrogen and carbon atoms in the molecule adjusted for the heteroatoms, of fossil and biomass resources is shown in Figure 1.3. The H/C ratio of transportation fuels (purple box) is close to the fossil oil ratio. As a result of the variety of oxygen containing groups in biomass, a much wider effective H/C ratio is obtained. The effective H/C ratio does not only cover the transportation fuels, but also that of chemicals (blue box), making biomass more versatile as a feedstock. When used for the production of chemicals instead of transportations fuels, as functional groups are already present, the number of processing steps can potentially be kept limited.

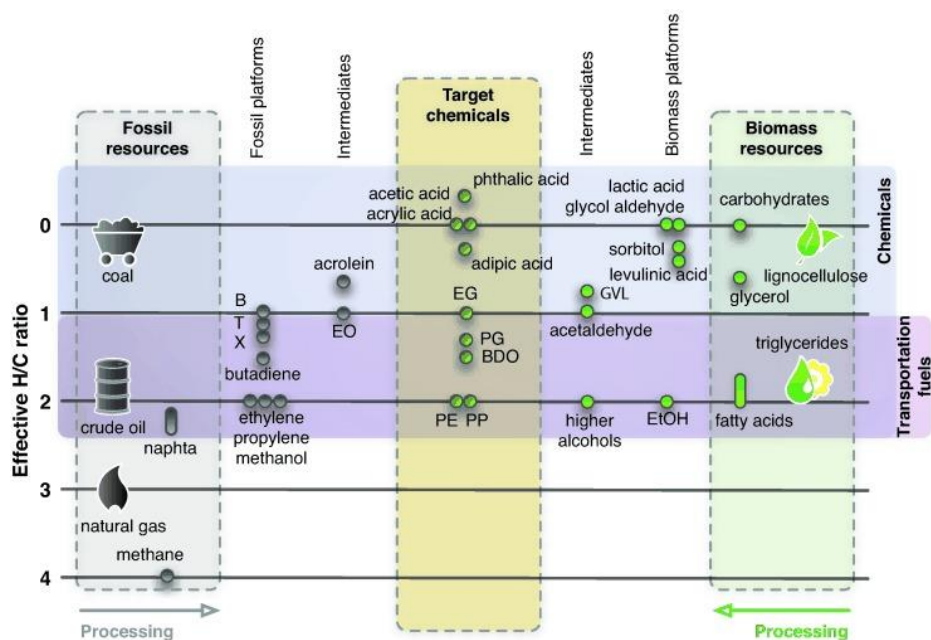


Figure 1.3. Effective H/C ratio, calculated as $[n(H)-2n(O)]/n(C)$, for fossil and biomass resources and their chemicals.

Used with permission from Vennestrøm et al.¹⁹, © (2011) John Wiley and Sons.

B = benzene, BDO = 1,4-butanediol, EG = ethylene glycol (1,2-ethanediol), EO = ethylene oxide, GVL = γ -valerolactone, PE = polyethylene, PG = propylene glycol (1,2-propanediol), PP = polypropylene, T = toluene, X = xylenes.

The valorization of the low value stream, glycerol, would not only increase the economic viability of the biodiesel industry but simultaneously contribute to the development of sustainable production routes

for currently petroleum-based products. Section 1.3 discusses the possible valorization of glycerol in more detail.

1.2.2 Waste stream in the production of edible oils as resource for minors

To produce edible oils such as olive, sunflower, palm, soybean or castor oil, a complex sequence of process steps has to be performed. First, the “crude” oil is produced *via* a sequence of crushing, milling, (screw) pressing and extraction. Secondly, a refining process consisting of degumming, pre-dewaxing, bleaching and deodorization is needed for the formation of oils with the desired properties (taste, smell and color). During the last step, a side stream, denoted as oil deodorizer distillate (ODD), is obtained.²⁰ Nowadays, this stream has little economic value and is often considered as waste. However, it contains some valuable “minor” components such as squalene (later converted into the more stable squalane), sterols and tocopherols, which are interesting and of great value for the food, cosmetic and pharmaceutical industry.

The increasing demand for these “minor” components justifies the aim to industrialize a valorizing process for the ODD. Moreover, at present the main source of squalene is the liver of deep-sea sharks, while sterols and tocopherols are mainly obtained *via* chemical synthesis out of petroleum products.²¹ Recuperation of these minor components from ODD would offer a sustainable alternative.

1.3 Glycerol and its conversion into valuable chemicals

Glycerol, commercially denoted as glycerin, was discovered in 1779 by the Swedish chemist Carl Wilhelm Scheele while making soap from oils and fats. It was only in 1811 that the French chemist Michel Eugene Chevreul proposed the name glycerin after the Greek word γλυκύς, which means sweet. In 1836 the French chemist Théophile-Jules Pelouze derived the empirical formula, $C_3H_8O_3$. One of his students, the Italian chemist Ascanio Sobrero synthesized nitroglycerin out of glycerol in 1847. The first industrial glycerol use dates from 1886, when the Swedish Alfred Bernhard Noble, also a student of Pelouze, patented a mixture with nitroglycerin and an absorbent inert as “dynamite”. This invention had an impact on the need of glycerol and resulted in a growth of vegetable oils and fats processing for its production.²²

1.3.1 Glycerol production

Today, glycerol is available on the market in two forms, *i.e.* synthetic and natural glycerol. The synthetic variant is produced by chemical conversion of propylene and constitutes about 10 % of the total glycerol market. From the 90% of glycerol obtained naturally, the majority is obtained as co-product in the oleochemical industry, mainly from biodiesel production (60-70 %). The market share of glycerol produced from saponification and the hydrolysis of triglycerides amounts to 12 % and 10 %, respectively.^{23, 24} Recent research showed that a small amount of glycerol can also be achieved from ODD.²⁵

The main glycerol market is situated in Europe, with a volume share of 29 % in 2019, followed by Asia and USA (each less than 25%). Some of the prominent players in the glycerol market are Cargill, Oleon, BASF, Kao Corporation and KLK Oleo.²⁶ Crude glycerol can be produced from fats and oils by three different processes: saponification, hydrolysis and transesterification. The general reaction scheme for glycerol is shown in Figure 1.4.

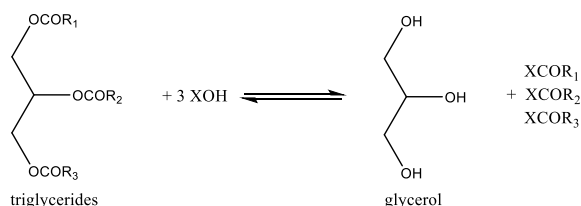


Figure 1.4. Glycerol production by saponification ($X = \text{Na}$ or K), hydrolysis ($X = \text{H}$) or transesterification ($X = \text{CH}_3$ or C_2H_5).

The saponification of triglycerides, present in fats and oils, with an alkali ($X = \text{Na}$ or K in Figure 1.4) yields glycerol and soap. The reaction of triglycerides with water ($X = \text{H}$ in Figure 1.4), hydrolysis, yields glycerol and fatty acids. When the triglycerides react with an alcohol (*e.g.* $X = \text{CH}_3$ or C_2H_5 in Figure 1.4), the transesterification results in glycerol and a fatty acid methyl ester (FAME, when methanol is used) or fatty acid ethyl ester (FAEE, in the case of ethanol).

The obtained glycerol is “crude” as it contains impurities due to the presence of unreacted reactants, salts or soap. The crude glycerol, with a purity in the range 20-60 %, could be purified by a number of steps to produce technical grade glycerol (≥ 98 % pure), which can be used in various applications. The market price of crude glycerol has crashed with the global increase of biodiesel production (Figure 1.5), due to the saturation of the glycerol market. However, in the spring of 2020, the European price of glycerol has tripled due to the coronavirus (COVID-19) outbreak. Crude glycerol prices increased from 19 cent l^{-1} to 40 cent l^{-1} , and for refined glycerol, the prices had shot up to above 1 euro l^{-1} . On the one hand, the travel restrictions have led some biodiesel producers, which are the major suppliers of glycerol, to cut or stop production. On the other hand, the demand of glycerol remained or even rose, for the use in sanitizer applications, resulting in an increased price.²⁷

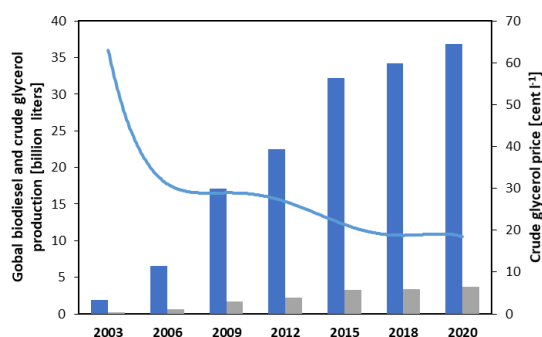


Figure 1.5. Overview of the global biodiesel (dark blue), crude glycerol (grey) production and crude glycerol price (line) just before the COVID-19 outbreak. Reproduced from Nomanbhay et al.²⁸, under the Creative Common Attribution 4.0 International License.

Glycerol production is expected to continue and even grow. To increase the sustainability of the biodiesel industry, the excess glycerol needs to be converted into high-value chemicals as it cannot be used directly as transportation fuel due to the higher effective H/C ratio (as shown in Figure 1.3). Its unique structure makes it very suitable as bio-renewable platform chemical.

1.3.2 Glycerol as a platform chemical

Glycerol is a non-toxic, colorless and odorless liquid. A comparison between the physicochemical properties of crude and pure glycerol is shown in Table 1.1.

Table 1.1. Overview of most important properties of pure and crude glycerol²⁹ and 1,2-propanediol³⁰.

	Pure glycerol	Crude glycerol	1,2-propanediol
Glycerol content [wt.%]	≥ 98	60 – 80	n.a.
Density [g cm ⁻³]	1.26	1.01 – 1.20	1.04
Boiling point [K]	563	382 – 394	460
Freezing point [K]	291	232 – 239	213
Vapor pressure at 343 K [mmHg]	0.017	80 – 175	0.05
Viscosity at 293 K [Pa s]	1.412	0.11 – 0.6	0.06

One of the most distinctive characteristics of pure glycerol is its high viscosity. This renders it suitable for use in hydraulic fluids, lubricants, as a thickening or bodying agent for liquid preparations, such as gels and syrups. Due to its low vapor pressure, it is effective as a humectant. Its hygroscopicity makes it ideal to act as a plasticizer. Glycerol has also anti-freezing properties, which makes it a useful admixture for cooling fluids. Further, it is also one of the major raw materials for the manufacturing of polyols for foams. In personal care and pharmaceutical applications, glycerol mainly acts as a lubricator or humectant. It is found in allergen immunotherapies, cough syrups, toothpaste, skin care products, etc. for its sweet taste. From a polymerization reaction with dicarboxylic acid, alkyd resins can be formed

which are used in some paints or coatings. By converting it into triacetin, it can be used as food additive, plasticizer. Other small applications include tobacco, detergents, cellophane and explosives. A distribution of the volume and industrial uses of glycerol is shown in Figure 1.6.

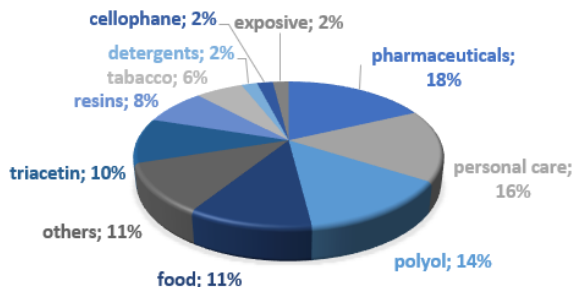


Figure 1.6. Overview of the industries and market share for glycerol. Reproduced from Pagliaro and Rossi²⁴ with permission from the Royal Society of Chemistry.

As mentioned earlier, the combination of a substantial increase in crude glycerol supply, the increased environmental awareness and its functionality, turns glycerol into an important platform molecule. To improve the economic viability of biodiesel production, it is necessary to convert the by-product glycerol into high value-added chemicals, which is possible thanks to the presence of three hydrophilic hydroxyl groups. An overview of the uses of glycerol as a platform molecule is depicted in Figure 1.7 and briefly further discussed below. More detailed information can be found in the work of Pagliaro and Rossi¹⁷ and Zhou *et al.*^{31, 32}.

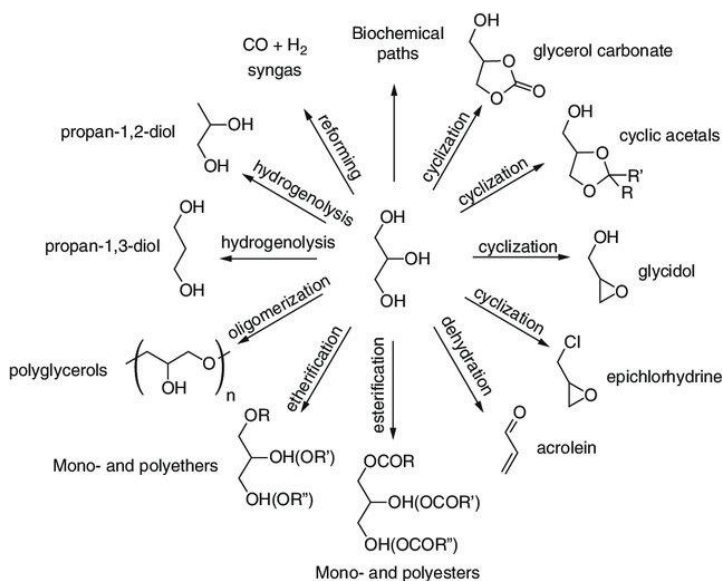


Figure 1.7. Glycerol as a platform molecule. Reprinted from Cecilia *et al.*³³ with permission from Springer.

Due to the excellent performance in burning and fuel cell applications, the demand for hydrogen as a fuel has increased. Glycerol can be converted into hydrogen or syngas *via* steam reforming, autothermal reforming, aqueous-phase reforming or supercritical water reforming.³¹ *Via* the water gas shift reaction the amount of hydrogen in the syngas can be further enhanced. Syngas can also be used for methanol synthesis or the production of diesel fuels *via* the Fisher-Tropsch process.

The carboxylation of glycerol with CO₂, which is a cyclization reaction, results in glycerol carbonate. This is mainly used as a solvent, *e.g.*, for glues or varnish, a lubricant for metallic surfaces or as a monomer for the synthesis of polycarbonates or polyurethanes.³⁴ The condensation reaction of glycerol with an aldehyde yields cyclic acetals, producing renewable and ash-free fuel additives. Acetals with a low molecular weight and flash point can be used as surfactants, flavors and disinfectants. The decomposition of glycerol carbonate yields glycidol. When the latter is polymerized, polyglycerol is obtained. This can be used for a variety of applications from cosmetics to controlled drug release. Epichlorohydrin, a building block for epoxy resins or other polymers, can be produced *via* a two-step reaction mechanism from glycerol.³⁴

Three dehydration products are typically produced from glycerol: when one water molecule is removed acetol or 3-hydroxypropionaldehyde can be obtained, while acrolein is the result of the removal of two water molecules. The dehydration is usually carried out over acidic catalysts.³⁴ Acrolein is mainly used for the production of super-absorber polymers, detergents or herbicide, while acetol or 3-hydroxypropionaldehyde are intermediates in the production of propanediols.

The esterification of glycerol with acids yields mono- and polyesters. Typically, base catalysts such as MgO, CeO₂, La₂O₃ or ZnO are reported for these esterification reactions. The mono-esters are widely used in food, pharmaceuticals and cosmetic industries.³²

The oligomerization of two or three glycerol molecules over basic catalysts results in diglycerol and triglycerol, respectively. These glycerol ethers have applications in various fields such as food-additive, cosmetics, fuel additive (*e.g.* GTBE or MTBE) or lubricants. Higher ether-linkages form polyglycerol, which can be used as a solvent to solubilize hydrophobic drugs.^{31, 32}

In the hydrogenolysis reaction, the cleavage of a C-O or C-C bond occurs simultaneously with hydrogen addition.³² The cleavage of a primary C-O bond results in 1,2-propanediol (*i.e.* propylene glycol), while that of the secondary C-O yields 1,3-propanediol. Excessive hydrogenolysis results in n-propanol or 2-propanol, ethanol, methanol. When a C-C bond is selectively broken, 1,2-ethanediol (*i.e.* ethylene glycol) and methanol are formed. The reaction mechanism will be discussed more in detail in section 1.4. The products, which are shown in Figure 1.9, have different applications. Ethylene glycol is used as a raw material for polyethylene terephthalate. The mono-alcohols are mainly used as solvents. 1,3-propanediol is used in resins, engine coolants, inks or for the production of polypropylene terephthalate for the use of carpet and textiles, *e.g.* Sonora™ or Corterra™ fibers.^{32, 35} The main concerns are the high

production cost due to expensive biological catalysts, *i.e.* algae, or low selectivity in case of heterogenous catalysts.³⁶ The other propanediol, 1,2-propanediol, has a wider range of applications depending on its purity, including food, pharmaceuticals, cosmetics, as a monomer for resins, aircraft deicing fluids, automotive coolants, paints and coatings, liquid detergents, inks, varnishes, tobacco humectants,... as shown in Figure 1.8. Some of its properties are shown in Table 1.1 in comparison to glycerol. It is a colorless, non-toxic, non-corrosive, hygroscopic liquid which has no taste, is less viscous in comparison to glycerol and has low volatility, but higher than that of glycerol.

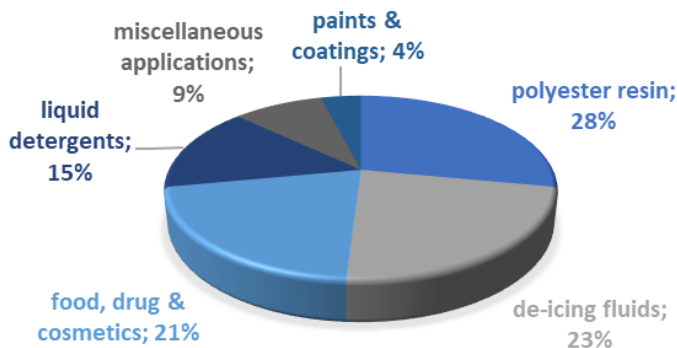


Figure 1.8. Overview of the industries and market share for 1,2-propanediol. Reproduced from Nanda *et al.*³⁷ with permission of Taylor & Francis.

At present, over 80 % of the market share of 1,2-propanediol is produced *via* the selective oxidation of propylene, in the presence of an acid catalyst. The USA is the main global supplier of 1,2-propanediol, accounting for 30 % of the supply, followed by China (22 %) and Germany (17 %).³⁷ The key market players for bio-based 1,2-propanediol are Dow, LyondellBassell Industries, Oleon (in collaboration with BASF), Cargill, Archer Daniels Midland and Huntsmann.³⁷⁻³⁹

Glycerol hydrogenolysis constitutes a promising ‘green’ and, hence, more sustainable route towards 1,2-propanediol, as it can replace the currently fossil-based raw material with a bio-derived one.

1.4 Reaction mechanism of glycerol hydrogenolysis

As stated in the previous section, one of the valorization routes for glycerol is the hydrogenolysis reaction which involves the breakage of a C-O or C-C bond in a molecule with a subsequent addition of a hydrogen atom, resulting in a wide range of products (Figure 1.9). The C-O hydrogenolysis reaction reduces the oxygen content in a molecule, making it suitable to convert biomass into transportation fuels and chemicals (see Figure 1.3).

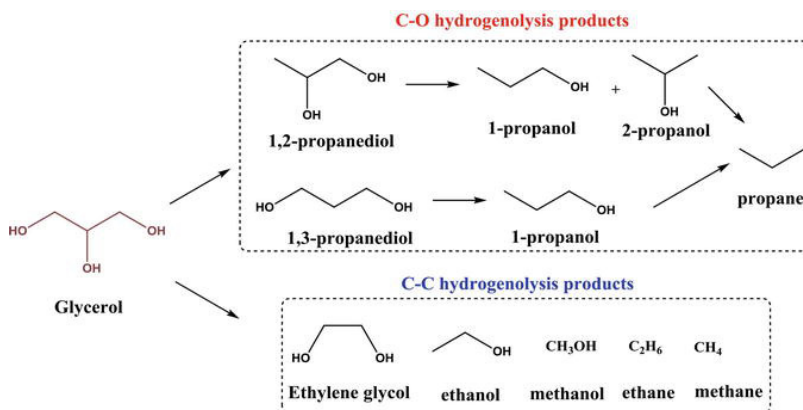


Figure 1.9. Glycerol hydrogenolysis production. Reproduced from Samudrala⁴⁰, under the Creative Common Attribution 4.0 International License.

To convert glycerol into 1,2-propanediol, one oxygen atom is removed in the form of H_2O from glycerol and hydrogen is added. According to literature^{41, 42}, there two main mechanisms for the production of 1,2-propanediol: the dehydration-hydrogenation mechanism under acid or neutral conditions (see 1.4.1) or the dehydrogenation-dehydration-hydrogenation mechanism under alkaline conditions (see 1.4.2).

1.4.1 Dehydration-hydrogenation mechanism

Figure 1.10 shows the dehydration-hydrogenation mechanism, relevant in case of neutral or acid catalysis. The dehydration step occurs on an acid site, while the hydrogenation step is catalyzed by a metal. The dehydration of a primary hydroxyl group, results in acetol *via* the keto-enol tautomerism of 2,3-dihydroxy-1-propene. Subsequent hydrogenation gives 1,2-propanediol. The dehydration of the secondary hydroxyl group yields 1,3-dihydroxy-1-propene, which is a tautomer of 3-hydroxypropionaldehyde. The hydrogenation then results in 1,3-propanediol.⁴³

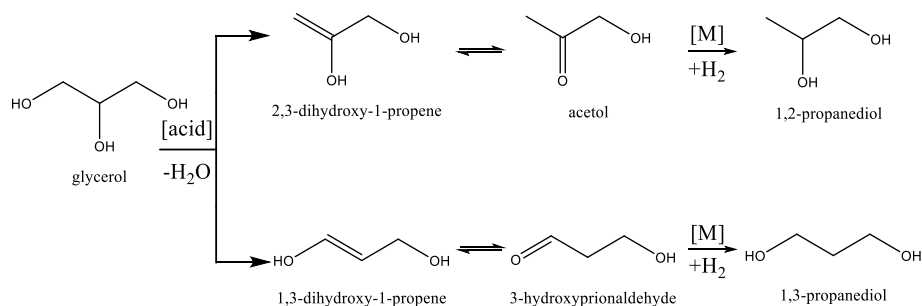


Figure 1.10. Dehydration-hydrogenation mechanism for glycerol hydrogenolysis to 1,2-propanediol and 1,3-propanediol. Reproduced based on Nakagawa and Tomishige⁴⁴, with permission from The Royal Society of Chemistry.

In the open literature there is still some controversy on whether Lewis or Brønsted acid sites perform the glycerol dehydration to acetol.^{40, 45} Lewis acid sites possess an empty orbital to accommodate a lone electron pair. A complex is formed by the interaction of the metal empty orbital on the catalyst surface with one of the hydroxyl groups of glycerol. Due to steric hindrance, such a complex is preferentially formed with a primary hydroxyl group rather than with a secondary one. Therefore, the thermodynamically more stable 2,3-dihydroxy-1-propene is formed which is first subject to keto-enol tautomerism and the obtained acetol is further hydrogenated to produce 1,2-propanediol. This proposed reaction mechanism of glycerol dehydration over Lewis acid sites is shown in Figure 1.11.

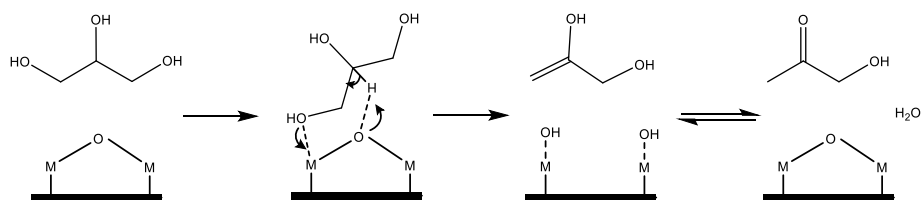


Figure 1.11. Reaction mechanism of glycerol dehydration into acetol over a Lewis acid site. Reproduced from Alhanash et al.⁴⁵ with permission of Elsevier.

In case of Brønsted acid sites, the proton can attack both the primary and secondary hydroxyl groups without any steric hindrance.^{45, 46} Yet, the protonation of a secondary hydroxyl group is kinetically favored as it generates a secondary carbocation (Figure 1.12), which is more stable compared to the primary carbocation from the protonation of a primary hydroxyl group (Figure 1.13). As 3-hydroxypropionaldehyde is thermodynamically unstable, this intermediate will be rapidly hydrogenated to form 1,3-propanediol. Nevertheless, Brønsted acid sites are also proposed to catalyze the dehydration of glycerol to acetol, even if an unstable primary carbocation is formed. The formation of 1,3-propanediol is thus favored over 1,2-propanediol in case of Brønsted acid sites.

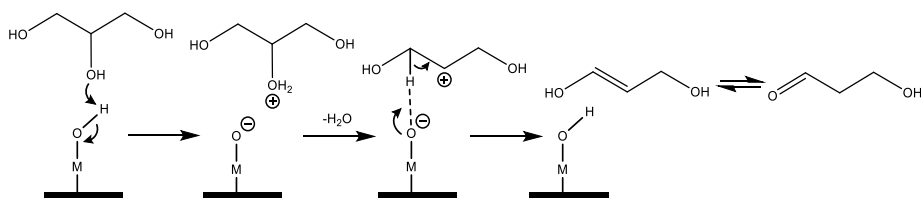


Figure 1.12. Reaction mechanism of glycerol dehydration into 3-hydroxypropionaldehyde over a Brønsted acid site. Reproduced from Alhanash et al.⁴⁵ with permission of Elsevier.

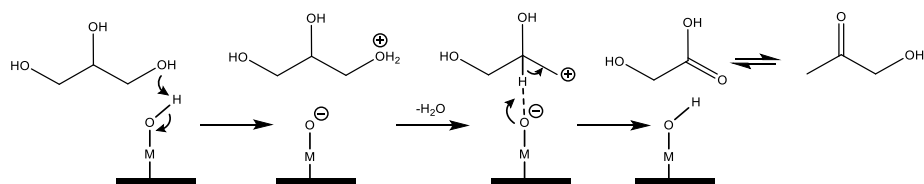


Figure 1.13. Reaction mechanism of glycerol dehydration into acetol over a Brønsted acid site. Reproduced based on Vila *et al.*⁴⁷ with permission of Elsevier.

1.4.2 Dehydrogenation-dehydration-hydrogenation route

When glycerol hydrogenolysis reaction is performed in alkaline conditions, a sequence of dehydrogenation, dehydration and hydrogenation steps occurs to produce 1,2-propanediol as shown in Figure 1.14. It is suggested by Montassier *et al.*⁴⁸ that glycerol first dehydrogenates on a metal site, followed by a dehydration of the glyceraldehyde intermediate on the base site of the catalyst. The formed 2-hydroxyacrolein undergoes a keto-enol tautomerism to pyruvaldehyde, which is consecutively hydrogenated on the metal sites of the catalyst, first to acetol and subsequently to 1,2-propanediol.

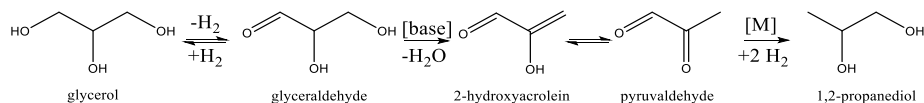


Figure 1.14. The dehydrogenation-dehydration-hydrogenation mechanism for glycerol hydrogenolysis to 1,2-propanediol. Reproduced based on Montassier *et al.*⁴⁸ with permission of Elsevier.

The metal sites on the catalysts serve thus both for the dehydrogenation and hydrogenation function. The dehydrogenation step is thermodynamically unfavorable as the hydrogenolysis of glycerol takes mostly place under mild to high hydrogen pressures. Therefore, the following dehydration step has to be much faster than de dehydrogenation step, *e.g.* by the addition of a base catalysator (LiOH or NaOH).

1.5 Development of effective catalysts for glycerol hydrogenolysis

Various metal catalysts are reported for glycerol hydrogenolysis to 1,2-propanediol. Noble metal-based catalysts, which are discussed in section 1.5.1, were explored in literature based on their known hydrogenation activity. Their stability did not outweigh the advantages of the transition metal-based catalyst, *i.e.* higher selectivity and lower cost, as discussed in section 1.5.2. For the completeness of the understanding, an overview of the noble metal-based catalysts was given.

1.5.1 Noble metal-based catalysts

Noble metals are well known for the capacity to activate hydrogen and, hence, are widely used as hydrogenation catalysts. For the stabilization of the noble metal atoms, they are anchored on a support, leading to a metal-support interaction. Thus, both the metal and the supports play an important role in the catalytic performance.⁴⁹

Dasari *et al.*⁴³ investigated commercial hydrogenation catalysts for the hydrogenolysis of an 80 wt.% glycerol solution at 4 MPa H₂ pressure and 473 K for 24 h. The highest conversions were achieved by the Ru/C (44 %) and Pt/C (35 %) catalysts, which was also observed by Miyazawa *et al.*⁵⁰. The Pt/C catalysts had a higher selectivity to 1,2-propanediol (83 %) compared to Ru/C (40 %). The higher selectivity over a Pt/C than Ru/C catalyst was also reported by Maris and Davis⁵¹ and by Kusunoki *et al.*⁵². Furikado *et al.*⁵³ compared noble metal (Rh, Ru, Pt and Pd) catalysts on various supports (C, SiO₂ and Al₂O₃) at 393 K and 8 MPa H₂ pressure in the 20 wt.% glycerol solution for 10 h. In these mild conditions, the Pd and Pt catalysts, regardless of the support, exhibited low conversion (< 1 %). In case of Ru, the carbon (3.5% conversion) proved to be a better support as compared to Al₂O₃ or SiO₂ (< 1 % conversion). In comparison to Pt and Rh, Ru is reported to be more selective towards C-C cleavage, resulting in a lower 1,2-propanediol selectivity.^{43, 48, 53} At these low temperatures, the Rh/SiO₂ catalysts exhibited the highest conversion (7.2 %). Vasiliadou *et al.*⁵⁴ investigated the hydrogenolysis of pure glycerol over a Ru/Al₂O₃ catalyst at 513 K and 8 MPa H₂ for 5 h and achieved up to 69 % conversion. The catalysts showed only a 38% selectivity towards 1,2-propanediol, with 1-propanol and 2-propanol as main products. Montassier *et al.*⁴⁸ showed that the formation of 1,2-ethanediol is always observed over the Ru/C catalysts, with a maximum 1,2-propanediol selectivity of 70 %. Gandarias *et al.*⁵⁵ achieved a conversion of 90 % of a 20 wt.% glycerol solution at 513 K and 4.5 MPa H₂ over a Pt/SiO₂-Al₂O₃ catalyst after 24 h. Pt catalyzed also C-C cleavage.⁵⁵ Overall, the low selectivity to 1,2-propanediol over Carbon supported noble metals is mainly obtained due to further hydrogenolysis products, such as 1-propanol and 2-propanol, especially at higher temperatures.^{54, 55}

To improve the selectivity towards a specific product, additives such as an acid can be employed. The cation-exchange resin Amberlyst 15 was one of the most effective co-catalysts to increase the 1,2-propanediol selectivity. From the comparative study of Miyazawa *et al.*⁵⁰, it was found that the formation of 1,2-propanediol was enhanced remarkably by the presence of the Amberlyst, while no impact was observed on the 1,3-propanediol formation under mild reaction conditions (393 K and 8 MPa H₂). This result can be explained by the mechanism in which a Lewis acid function is required for the dehydration, while the metal catalyzes the hydrogenation reaction (as discussed in section 1.4.1). A weak point is the thermal stability of Amberlyst 15. Balaraju *et al.*⁵⁶ investigated Ru/C catalysts with different inorganic solid acids, as those are thermally more stable compared to ion-exchange resins. Using Nb₂O₅ as a solid acid, a conversion of 63 % of a 20 wt.% glycerol solution and 66 % 1,2-propanediol selectivity was achieved at 453 K and 6 MPa H₂ pressure after 8 h. The C-C cleavage product, 1,2-ethanediol, was the main side product. At 423 K and only 0.5 MPa H₂, the use of Rh-incorporated Cs_{2.5}H_{0.5}PW₁₂O₄₀ catalyst resulted in excellent 1,2-propanediol selectivity (96 %) for a 20 wt.% glycerol solution (21 % conversion). At higher temperatures, the C-C cleavage to 1,2-ethanediol became more significant.⁵⁷

The addition of different bases such as MgO, NaOH, CaO, LiOH has been reported in literature for the hydrogenolysis of glycerol. The addition of NaOH to Pt/MgO or Pt/hydrotalcite catalysts showed higher glycerol conversion (50 % and 92 %, respectively) and 1,2-propanediol selectivity (82 % and 93 %, respectively) at 493 K and 3 MPa H₂ than a NaOH+Pt/C catalyst (conversion of 7 % with 82 % selectivity) for the hydrogenolysis of 20 wt.% glycerol solution.⁵⁸ Maris and Davis^{51, 59} found that the presence of NaOH or CaO helped the abstraction of H from the terminal hydroxyl in glycerol, as discussed in section 1.4.2, resulting in an enhanced glycerol hydrogenolysis of a 1 wt.% glycerol solution over a Ru/C or Pt/C catalyst at 4 MPa H₂ and 473 K. The addition of LiOH and NaOH, to a Ru/TiO₂ catalyst was investigated by Feng *et al.* at mild reaction conditions (443 K, 3 MPa H₂).⁶⁰ The addition of the aforementioned bases significantly decreased the selectivity to 1,2-ethanediol. The highest selectivity (87 %) and conversion (90 %) were observed using LiOH.

It can be summarized that almost all noble metals are good activators for hydrogen and thus effective catalysts for glycerol hydrogenolysis.⁴⁴ However, they show a high activity for C-C cleavage, which leads to more undesired products such as 1,2-ethanediol.^{43, 48, 53} As stated above, the use of an acid or base as a co-catalyst leads to 1,2-propanediol as the main product.

1.5.2 First row transition metal-based catalysts

Apart from noble metals, Cu, Ni and Co are also known for their capability to activate hydrogen and, hence, could also be used as hydrogenation catalysts. Although their hydrogenation activity is lower than that of noble catalysts, the much lower prices and global availability renders transition metal-based catalysts industrially important.⁴⁹

From the early 1940s, Cu-Cr were used for the production of lower polyols, such as 1,2-propanediol.⁶¹ Dasari *et al.*⁴³ investigated glycerol hydrogenolysis with Cu-Cr catalyst batch wise. It was found that a reduction procedure at 573 K, 1.4 MPa for 4 h, resulted in the highest 1,2-propanediol yield (58 %). The selectivity towards 1,2-propanediol increased until a reaction temperature of 473 K, higher temperatures led to excessive hydrogenolysis converting the propanediols into lower alcohols. These results show that Cu-Cr catalysts are effective for glycerol hydrogenolysis, with a high stability. Nevertheless, the toxic chromium limits its wide application.¹² Another Cu-based catalyst often used for glycerol hydrogenolysis is the industrially used Cu/ZnO, which is often applied for methanol synthesis^{62, 63}, water-gas shift reaction^{64, 65} or methanol steam reforming^{66, 67}. The ZnO is responsible for the dehydration step to form acetol, which is further hydrogenated on the Cu sites to 1,2-propanediol (corresponding to the dehydration-hydrogenation mechanism discussed in section 1.4.1). Bienholtz *et al.*⁶⁸ performed glycerol hydrogenolysis over a Cu/ZnO catalyst at temperatures between 463 K and 498 K at 5 MPa H₂ pressure and reported 46 % glycerol conversion with 90 % 1,2-propanediol selectivity. Balaraju *et al.*⁶⁹ achieved a maximum 1,2-propanediol selectivity of 92 % with a weight ratio of 50/50 Cu/ZnO at 37 % conversion. A high 1,2-propanediol selectivity (84 %) was achieved at 22 % conversion

at 473 K and 4.2 MPa on a Cu/ZnO catalyst (atomic ratio of 1.0) with Cu particle sizes around 20-30 nm.⁷⁰ It was found that the glycerol conversion decreased due to the aggregation of Cu and ZnO crystallites.⁶⁹⁻⁷¹ Although, these Cu/ZnO catalysts eliminated the use of Cr, the longer reaction time made it industrially less practical. Over the years, more Cu-based catalysts were developed for glycerol hydrogenolysis, which will be assessed in section 1.5.3.1.

Several researchers investigated Ni-based catalyst for glycerol hydrogenolysis. Although the main product is 1,2-propanediol, C-C-cleavage products are usually co-produced to a minor extent. Perosa and Tundo⁷² reached a 1,2-propanediol selectivity of 71 % at 97 % conversion for pure glycerol hydrogenolysis at 1 MPa H₂ and 463 K after 44 h over a Raney[®] Ni catalyst. In order to reduce process costs, Dasari *et al.*⁴³ investigated Raney[®] Ni and Raney[®] Cu catalysts for glycerol hydrogenolysis at 4 MPa and 473 K. Both catalysts reached almost 50 % conversion, but higher 1,2-propanediol selectivity was achieved using the Raney[®] Cu catalyst (69 % vs. 53 %). Zhao *et al.*⁷³ investigated a series of supported (various zeolites, SiO₂ and Al₂O₃) Ni catalysts. The accessibility of the acid sites, both Lewis and Brønsted, in the channels of the zeolite support played an important role in 1,2-propanediol production, which is attributed to the dehydration function of the acid sites in the zeolites. The best results in terms of glycerol (25 wt.% solution) conversion and 1,2-propanediol yields were achieved over a Ni/NaX catalyst.⁷³ The acidity was tuned further by ion-exchanging with NaNO₃ several times resulting in a maximum glycerol conversion of 87 % with 95 % selectivity for 1,2-propanediol at 473 K and 6 MPa H₂ pressure, after 10 h. Gandarias *et al.*⁷⁴ found that bimetallic Ni-Cu/Al₂O₃ catalysts showed better performances compared to pure Ni or Cu Al₂O₃ supported catalysts, due to the synergy between Cu and Ni.

Cobalt has not been studied extensively for glycerol hydrogenolysis. Guo *et al.*^{75, 76} tested several Co/ZnAlO, Co/MgO and CoNi catalysts for the hydrogenolysis of 10 wt.% glycerol to 1,2-propanediol. A maximum glycerol conversion of 71 % was obtained with a 1,2-propanediol selectivity amounting to 58 % at 473 K and 2.0 MPa H₂. It was found that not only the particle size and the amount of Co affected the conversion and selectivity, but also the exposed plane. Results showed that the (10-10) plane in hcp rods exhibited a two times higher activity and up to ten times higher 1,2-propanediol selectivity. Various Co-nests, Co-nanoflowers and Co-nanowires were investigated by Liu *et al.*⁷⁷ Independent of the type of nanomaterial, only a moderate selectivity towards 1,2-propanediol (57-72 %), as main product, was achieved at 493 K.

It is clear that the selectivity towards 1,2-propanediol over Co- or Ni-catalysts is often lower than that over Cu-based catalysts. Therefore, Cu-based catalysts are the most promising^{37, 42} for glycerol hydrogenolysis and the next section is assigned to recent development and understanding of Cu-based catalysts.

1.5.3 Copper-based catalysts

The red metal copper has been known and used since the early days of human race. It is a useful material with a wide range of applications because of the combination of its physical, chemical, electrical and thermal properties. In the last decades, Cu catalysts are receiving increased attention in the field of catalysis, as shown in Figure 1.15, due to its abundance and excellent catalytic performance in a variety of reactions.

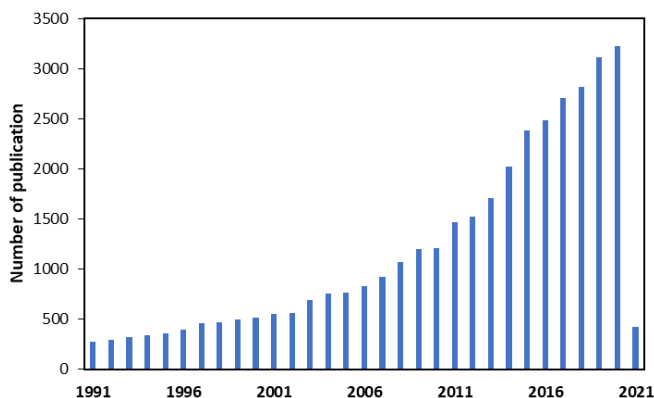


Figure 1.15. Number of publications related to Cu-based catalysis in the last 30 years. Data from Web of Science.

In what follows, an overview of the development in the Cu-based catalysts for glycerol hydrogenolysis is presented. In section 1.5.3.2, strategies are discussed to improve the catalyst stability, which is, indeed, the weak point of Cu based catalysts. An insight is given into the evolution of copper species and their interplay in section 1.5.3.3.

1.5.3.1 Recent progress in Cu-based catalyst for glycerol hydrogenolysis

Cu-based catalysts are often applied in industry due to their price compared to noble metals and their ability for C-O bond activation and/or cleavage. As stated in section 1.5.2, typical industrially employed catalysts, such as Cu-Cr, Cu-ZnO, were initially investigated for glycerol hydrogenolysis.⁷⁸ Later, other Cu-based catalysts supported on MgO, SiO₂ or Al₂O₃ were also reported by several research groups.⁴¹

One of the solid base supports used in glycerol hydrogenolysis, is MgO. As with ZnO, characterizations indicated that Cu/MgO with smaller sized Cu and MgO particles were more active for the hydrogenolysis reaction.⁷⁹⁻⁸¹ Yuan *et al.*⁸¹ achieved comparable 1,2-propanediol selectivity (96 %) and conversion (94 %) as for some noble metal-based catalysts, such as Ru/C^{50, 51, 59} or Rh/SiO₂⁵³ catalysts. The conversion of glycerol is assumed to follow the dehydration-hydrogenation route (section 1.4.1).

The effect of particle sized and dispersion was also studied on SiO₂ supported (commercial silica gel and SBA-15) Cu catalysts by Vasiliadou *et al.*⁸² The glycerol hydrogenolysis reaction was investigated at 513 K, 8 MPa H₂, 40 vol.% glycerol solution in n-butanol, for 5 h in a batch reactor. Their results show that different crystallite sizes (7.5 nm to 96 nm) resulted in different activities (20-50 % conversion), while all the catalysts gave 1,2-propanediol selectivities above 92 %. Smaller Cu particle sizes resulted in higher glycerol conversion. The strong loss in activity (78 %) in the second run was attributed to the sintering of Cu particles. Up to a decrease of 50 % activity and significant sintering of the Cu⁰ particles was observed by Huang *et al.*⁸³, in the second run of the Cu/SiO₂ catalyst. Wu *et al.*⁸⁴ prepared highly dispersed Cu clusters (*ca.* 1 nm) over SiO₂. The glycerol hydrogenolysis reaction was carried out at 473 K, 4.0 MPa H₂ with a 80 wt.% glycerol solution in a batch reactor. Similar to other literature, a conversion of 52 % was achieved. Zhu *et al.*⁸⁵ investigated a series of Cu/SiO₂ catalysts in a continuous fixed bed reactor at 473 K, 5.0 MPa H₂ using water as a solvent (10 wt.% glycerol) at a WHSV, *i.e.* the weight of feed per unit of weight of catalyst per hour, of 0.075 h⁻¹. A glycerol conversion of 89 % with a 98 % 1,2-propanediol selectivity was achieved with acetol as main by-product. Over 80 h time on stream, the glycerol dropped to 25 % because of the serious sintering, as evidenced by TEM.

Cu-Al spinel has been proposed for glycerol hydrogenolysis, resulting in a glycerol conversion and selectivity towards 1,2-propanediol above 90 %.⁸⁶ As the preparation of spinels requires high calcination temperatures, this causes difficulties in scaling up the catalyst synthesis. Therefore, impregnation or co-precipitation methods are frequently used for Cu on alumina catalysts. Cu/Zn/Al hydrotalcites were prepared *via* co-precipitation. Meher *et al.*⁸⁷ optimized the hydrotalcite and reaction conditions to obtain a maximum glycerol conversion of 52 % at 473 K and 1.4 MPa H₂ for a reaction time of 24 h with a 94 % selectivity to 1,2-propanediol. After regeneration, a decrease in the glycerol conversion was observed even though the 1,2-propanediol selectivity remained similar. The loss in activity was attributed to pore blockage. Huang *et al.*⁸⁸ achieved a selectivity of 81 % at 20 % conversion for glycerol hydrogenolysis at 473 K and 5 MPa H₂ over Cu/Zn/Al hydrotalcite. Higher conversions were achieved over impregnated catalysts. Wu *et al.*⁸⁴ prepared highly dispersed Cu clusters (*ca.* 1 nm) over boehmite (γ -AlO(OH)). The boehmite supported catalyst showed higher conversion (77 %) and 1,2-propanediol selectivity (93 %) compared to the SiO₂ supported (52 % conversion and 89 % selectivity). These results are assigned to the Lewis acid sites present in boehmite. Vila *et al.*⁴⁶ pointed out that the activation procedure of the catalyst has a significant effect on its performance due to the difference in copper surface species generated during this process. Longer calcination times (0.5 h vs. 2h) resulted in higher glycerol conversion (10 % - 30 %). Irrespective of the calcination time, the reduced catalysts give higher 1,2-propanediol selectivity (25 % - 70 %). Mane *et al.*⁸⁹ performed time on stream experiments of 400 h and achieved an average glycerol conversion of 90 % and 1,2-propanediol selectivity of 65 %.

Cu has a low C-C bond cleavage compared to noble catalysts. Even at mild temperatures, a 1,2-propanediol selectivity above 80 % is achieved. A high hydrogen pressure is often used to shift the equilibrium from acetol to 1,2-propanediol. Only several researches reported the characterization of the used catalyst, which showed severe deactivation by sintering. From the insights of the deactivation phenomena, upon which strategies can be developed to improve the catalysts stability.

1.5.3.2 Strategies to improve the stability of Cu-based catalysts

A wide range of catalytic performances for various reactions and glycerol hydrogenolysis in particular has been reported over Cu-based catalysts (Figure 1.16), the exact results depending on the operating conditions, catalyst and reactor type and operation mode. Most research has been performed batch wise with aqueous glycerol (up to 80 wt.%_{water}), despite continuous operation with pure glycerol being preferred in industry, resulting in a gap between the academic research and the industrial reality. Among others, the observation of deactivation phenomena is significantly more challenging when operating in batch mode.

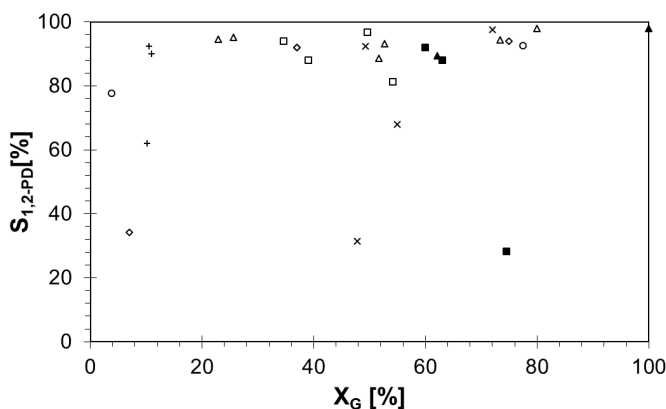


Figure 1.16. Overview of glycerol conversion (X_G) and corresponding 1,2-propanediol selectivity (S_{PG}) for selected examples of Cu-based catalysts supported on Al_2O_3 -support (\square)^{89,92}, MgO-support (\times)^{79, 80}, SiO_2 -support (\triangle)^{84, 93-95}, zeolites (\circ)^{84, 92}, ZnO-support (\diamond)^{69, 96} or ZrO_2 -support ($+$)⁹⁷ for aqueous glycerol hydrogenolysis operating in batch (open symbol) or continuous operation (closed symbol) at different operation conditions.

To improve the catalyst's stability, it is crucial to understand why Cu-based catalysts deactivate during the reaction. Based on characterization studies, four main causes^{98, 99} lead to the inactivation of Cu-based catalysts (shown in Figure 1.17).

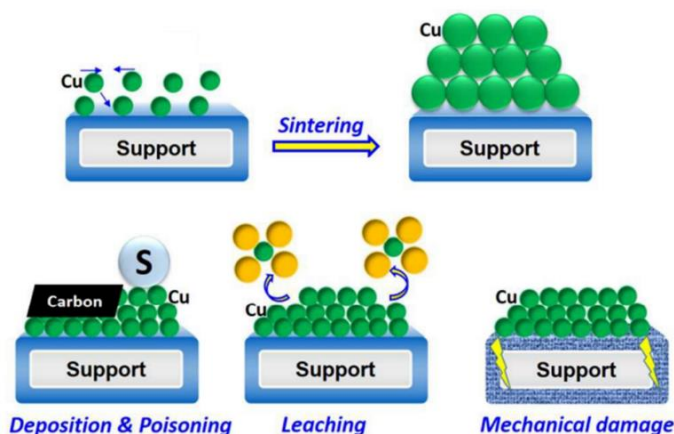


Figure 1.17. Schematic representation of deactivation mechanisms of Cu-based catalysts. Adapted from Ye *et al.*⁹⁹ with permission from the Royal Society of Chemistry.

Irrespective of the support used, bare Cu catalysts are prone to deactivation, mostly due to sintering.¹⁰⁰ The loss in copper metal surface area affects the catalyst activity and stability, resulting in a shorter operating lifetime.⁹⁸ As sintering is an irreversible deactivation process, regeneration will not prolong the catalyst life time. In the case of industrial Cu-based catalysts, mainly the catalyst stability, *i.e.* constant reactant conversion over time, is aimed at being enhanced. This can be achieved by the addition of a co-metal.^{101, 102} In the case this co-metal element has a positive effect on catalyst performance, it can also be denoted as a ‘promotor’.⁴⁹ This effect can be structural (*i.e.* increasing the selectivity by favoring a reaction path, by *e.g.* increasing the concentration of specific active sites), textural (*i.e.* modifying the catalyst such that sintering is inhibited, and thus preventing loss of active surface), or electronic (*i.e.* influencing the chemical binding of the adsorbate to the catalyst).⁴⁹ In practice, it is not always possible to perfectly distinguish these effects. Mane *et al.* screened various promoters (Al, Zn and Ba) in Cu-Cr catalysts for glycerol hydrogenolysis to 1,2-propanediol in batch. The Ba-promoted catalyst not only exhibited the highest stability in terms of conversion over time, but also the highest conversion of 34 % with a 84 % 1,2-propanediol selectivity at 493 K, 5.2 MPa H₂ and a 20 wt.% glycerol solution.¹⁰³ This was attributed to the enhanced acidity of the catalyst, catalyzing the dehydration of glycerol to acetol. The addition of metal oxides (Mn, Mg, Zr, Ce, Ba, Cr and W) was investigated on Cu/ZnO/Al₂O₄ catalysts. It was found that Ce was the most effective in improving the stability.¹⁰⁴ Zhu *et al.*⁹⁵ disclosed that the copper surface area decreased due to the agglomeration of the active Cu phase. In the work of Mane *et al.*^{89, 103}, the addition of Ba stabilized the crystallite size of Cu⁰, inhibiting sintering. A similar effect was observed for Ce and La-promotion.^{105, 106} Cs was found to prevent the over-oxidation to the formation inert CuO.¹⁰⁷

A second reason for deactivation is carbon deposition or catalyst poisoning in the presence of impurities. Cokes, *i.e.* carbon deposition by unwanted polymerization or condensation of organic

molecules, mostly blocks access of reactants to the metal surface sites. It can be removed from the catalysts surface by regeneration. However, cokes is usually not a major problem for Cu catalysts.⁹⁸ Rajkhowa *et al.*¹⁰⁸ investigated the long term stability of a commercial Cu-based catalyst for crude glycerol hydrogenolysis in an isothermal trickle-bed reactor at 473 K to 503 K in the presence of impurities. It was found that S is a strong poison for Cu-based catalysts.^{98, 108} Above a certain threshold, also deactivation by chlorides is observed, as a consequence of the sintering of formed CuCl_2 which has a lower melting point.

Leaching is the loss of active species, from the solid catalyst to a liquid medium, causing a irreversible deactivation of the catalyst. Durán-Martín *et al.*¹⁰⁹ found that not carbon deposition nor sintering was the most relevant deactivation cause for glycerol hydrogenolysis over Cu-Zn catalyst, but leaching of the Zn species. Huang *et al.*¹¹⁰ found that the incorporation of Y and La to Cu/SiO_2 inhibited the leaching of the Cu and could inhibit the sintering of copper.

During the loading of catalyst into the reactor, some mechanical degradation can occur due to crushing. Thermal treatments during the heating and reaction can add thermal stress leading to material degradation. A spherically shaped catalyst is favored for the mechanical strength.¹¹¹ Mechanical damage is rarely a significant cause of deactivation for Cu catalysts.⁹⁸

Despite the different phenomena that cause the deactivation of Cu-based catalysts, improvements can be integrated to meet the desired catalytic stability.

1.5.3.3 Evolution of Cu species and their interplay

Cu-based catalysts have been investigated in many reactions involving H_2 . Significant efforts have been made in preparing effective and stable catalysts in the last two decades. Undoubtedly, the Cu-dispersion and/or interaction between Cu species and the support and a promotor are the main factors in determining the catalytic activity, selectivity and stability. However, no consensus has been reached on the precise nature of the active species in catalytic reactions. It is generally accepted that a variety of copper species are present in calcined catalysts, depending on the preparation method and conditions, the use of additive agents and the calcination temperature. Such copper species include well dispersed CuO and bulk CuO, also often Cu_2O and immobilized Cu-ions, as such or as copper phyllosilicates or spinels.^{62, 93, 112-114}

CuO can change oxidation state from CuO *via* Cu_4O_3 and Cu_2O to metallic Cu. However, the general literature reports very little information on this mechanism. This could be due to the preparation of the CuO samples or different reduction conditions, which have kinetic effects for the formation of oxides. Furthermore, it is very difficult to investigate the reduced Cu species, because the *ex situ* experimental investigations may not correspond to the state of Cu under the reaction conditions. Various groups¹¹⁵⁻¹¹⁷ investigated the reduction mechanism for CuO and Cu_2O by H_2 . It was found that at 473 K, a

5% H_2 -95% He mixture with a flow rate above $15 \text{ cm}^3 \text{ min}^{-1}$, reduces the CuO directly to metallic Cu, without the formation of the suboxides Cu_4O_3 or Cu_2O .¹¹⁵ The reduction of CuO to Cu is easier compared to the reduction of Cu_2O to Cu, with apparent activation energies of 61 kJ/mol and 103 kJ/mol, respectively.¹¹⁵ To form Cu_2O , the H_2 supply needs to be limited, slowing down the reduction rate. Generally, CuO starts to reduce around 400 K and all Cu species are completely reduced around 525 K. In between, both Cu^0 and Cu^+ species coexist.

Several works^{118, 119} hypothesized in ester hydrogenation that Cu^+ enhances the catalytic activity by polarization of the C=O bond, while Cu^0 sites are responsible for dissociative hydrogen adsorption. In other research^{120, 121}, it was also concluded that Cu^+ functioned as acid site, weakening the electron density of C-O bond to accelerate its cleavage.

Zhu *et al.*⁸⁵ revealed that Cu^0 is responsible for the glycerol hydrogenolysis. Nevertheless, the role of Cu^+ cannot be ruled out. Where Cu^0 is responsible for the activation of the H_2 , Cu^+ sites play a role as Lewis acid sites to polarize the C-O bond of glycerol *via* the free electron pair in oxygen.^{85, 122} A maximum TOF was observed with a fraction of 40 % Cu^+ on the surface. Shan *et al.*¹²³ identified Cu-O-Si-O (Lewis acid sites) as dominant dehydration sites for glycerol dehydration to acetol, and this intermediate adsorbed to adjacent Cu^0 sites for subsequent hydrogenation. It was pointed out that Cu^+ species improves the glycerol conversion, while the atomic Cu^0/Cu^+ ratio is responsible for the observed 1,2-propanediol selectivity.⁴⁶ The role of Cu^+ in glycerol hydrogenolysis was also recognized by Mane *et al.*¹²⁴ The presence of Cu^+ helped the stabilization of Cu^0 , inhibiting sintering.

The research group of Liang found that the surface area of the Cu-Cr catalyst, the interaction of Cu and CuCr_2O_4 ¹²⁵ and the reduced state of synergetic effect of $\text{Cu}^0/\text{Cu}^{+126}$ were crucial for explaining the observed performances. It was found that Cu^0 was mainly responsible for hydrogen activation, while Cu^+ , as it may act as a Lewis acid site, was deemed responsible for the dehydration. The presence of CuCr_2O_4 enhanced the activity, serving as an “hydrogen delivery bridge”. A conversion of 52 % and 1,2-propanediol selectivity above 88 % were achieved at 483 K and 4.15 MPa H_2 , when a 60 wt.% glycerol solution was used in a batch reactor. In continuous operation, the same catalyst exhibited higher conversion (65 %) and selectivity (> 90 %). The better performance was attributed to the lower contact time, limiting the further hydrogenation to lower alcohols.^{89, 127}

1.6 Oil deodorizer distillates as resource for minor components

As stated before in section 1.2.1, ODDs are a side stream in the production of vegetable oils, which are a potential source for minor components such as sterols, tocopherols and squalene. As consumers are often willing to pay more for natural and bio-based products in cosmetics and personal care products, *i.e.* the main application markets of the minors, the higher production costs of the valorization of ODD is economically justified.

Table 1.2 represents the chemical composition of some crude vegetable oils. It is clear, that the concentration of squalene, tocopherols and sterols is in most of the cases too low to be economically effective for direct separation.

Table 1.2. Chemical composition of some crude oils. ¹²⁸⁻¹³⁰

Type oil	Fatty acid composition [wt.%]				Unsaponifiable	Sterols	Tocopherols	Squalene
	C16:0	C18:0	C18:1	C18:2	[wt.%]	[ppm]	[ppm]	[ppm]
Soybean	8-13.5	2-5.4	17-30	48-59	0.6	1820	2000	10-100
Olive	7.5-20	0.5-5	55-83	3-21	0.7	650	9000	1500-6000
Sunflower	5-7.6	2.7-6.5	14-39	48-74	0.6	1700-5200	440-1500	2100

There are two refining processes for the production of edible oils: physical and chemical refining. The difference are situated in how acids and gums are eliminated (Figure 1.18). As a result, the obtained byproducts, more particularly, the oil deodorizer distillate composition, will be different. During the refining process, the minor components are concentrated in the ODD (as shown in Table 1.3), rendering this distillate a potentially economically viable route for their valorization. For a detailed description of the processes, the reader is referred to Hamm *et al.*¹³¹ and The Lipid Library.¹³²

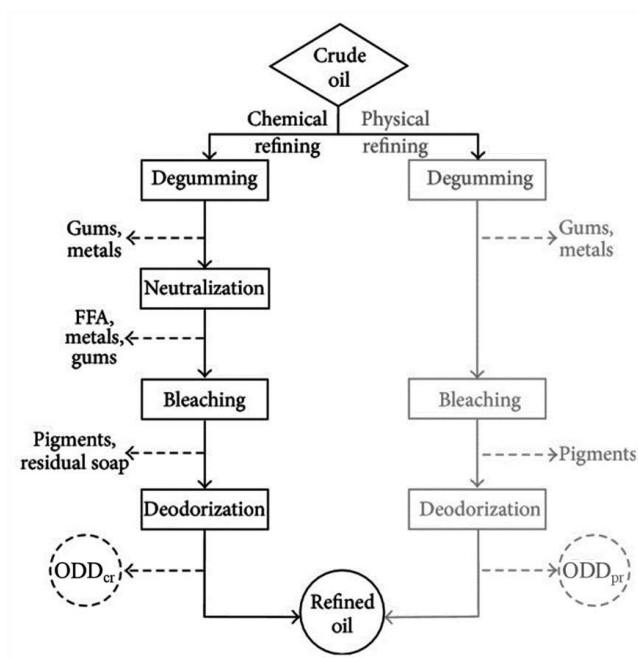


Figure 1.18. General overview of chemical and physical refining. Reproduced from Popa *et al.*¹²⁸.

The ODD from chemical refining can be employed as a raw material for recovering the minor components. The ODD originating from physical refining is less attractive, due to the comparatively higher free fatty acid (FFA) content.^{131, 133}

Table 1.3. Chemical composition of some ODDs obtained by chemical refining.¹²⁸⁻¹³⁰

Type ODD	FFAs [wt.%]	Others* [wt.%]	Total sterols [wt.%]	Total tocopherols [wt.%]	Squalene [wt.%]
Soybean	30-60	10-40	10-35	10	1-2
Olive	34.2	33.2	4.6	-	28
Sunflower	40	35	14	6.5	4.5

* Glycerides, fatty esters and other hydrocarbons.

Valorization of the ODD aims at recuperating three minor components present in this side stream, *i.e.*, sterols, tocopherols and most importantly squalene. In this section the physical and chemical properties of these three components are discussed. Furthermore, per component its commercial applications are listed and elaborated.

1.6.1 Squalene

Squalene is a multiple unsaturated hydrocarbon that belongs to the class of triterpenes. Its molecular formula is $C_{30}H_{50}$ and the structural formula is given in Figure 1.19. This organic compound finds its application in cosmetic, food and pharmaceutical industries. In the cosmetic industry, it is used in creams as moisturizer and skin emollient. In the food industry, squalene is interesting as a supplement due to its rejuvenating and vitalizing effect. It also lowers the cholesterol and triglyceride levels in animals. In pharmaceuticals, squalene can be used in combination with a surfactant as an immunologic adjuvant. It is added to vaccines to enforce the immune system and to increase response to the vaccine. Furthermore, it is used in different therapies during cancer treatment.¹³⁴

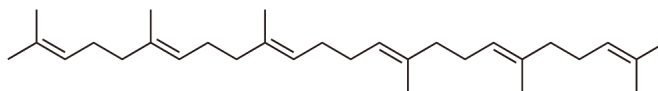


Figure 1.19. Structure formula of squalene

While squalene only occurs in relatively low percentages in plants and animals, it can be found in much higher amounts in the bodies of cartilaginous fish such as deep-sea sharks. The highest squalene concentration is found in the liver of deep sea sharks from the family *Squalidae*.¹²⁸ The liver of the deep-sea shark consists for 40-80% out of squalene. Due to this elevated percentage, this organ is the most important source of squalene at present.¹³⁵ Evidently, the recovery of squalene from sharks is highly controversial. Animal protecting and environmental organizations are actively putting this on the agenda and some cosmetic companies have already banned squalene acquired from shark livers from their products. Alternative sourcing processes for this valuable compound are of great interest and

extensively investigated. Options are extraction from oils, nuts, grains, seeds or valorization from ODD. Direct extraction from seeds, nuts or oil is not economically effective.¹²⁸ However, the olive and soybean oil deodorizer distillate, as stated in Table 1.3, constitute important natural resources for squalene.

Akgün *et al.*¹³⁵ used supercritical fluids for the extraction of squalene from olive oil ODD. The highest amount of squalene, 75 wt.% of the raffinate, was achieved at 325 K, 10.5 MPa and extraction time of 180 min. Bondioli *et al.*¹³⁶ recovered squalene from olive ODD with purity and yields above 90 % by supercritical countercurrent CO₂ extraction at 313 K and 15 MPa. Gunawan *et al.*¹³⁷ achieved 96 wt.% pure squalene from soybean ODD, by combining soxhlet extraction with additional purification.

1.6.2 Sterols

In this thesis, the focus will be on the phytosterols (from Greek φυτό, plant) because this type of sterols is present in the ODD. The three most important phytosterols are β -sitosterol, campesterol and stigmasterol for which the structure formulas are given in Figure 1.20. Their structures are characterized by four aromatic rings. Phytosterols are used as food additives because they are able to reduce the level of plasma cholesterol.¹³⁸ When the sterol is produced by animals, they are indicated as zoosterols (from the Greek word ζώο, animal). Cholesterol is the most famous zoosterol.

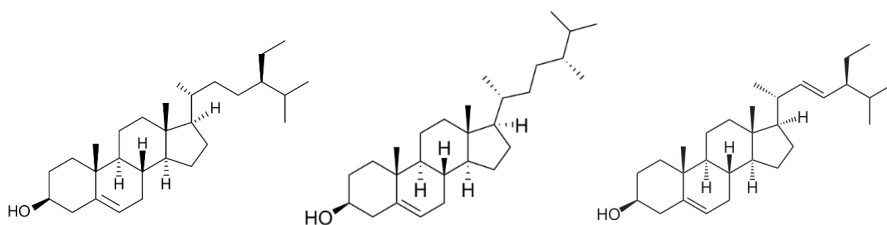


Figure 1.20. From left to right: β -sitosterol, campesterol, stigmasterol

Sterols are mostly produced *via* chemical synthesis.¹³⁹ This, however, requires a non-straightforward sequence of reactions. The complexity of this process stimulates the search to alternative sterol production routes such as extraction from natural sources. Isolation from vegetable oil is, *e.g.*, already investigated, but requires further optimization to be economically feasible.¹⁴⁰ Isolation from ODD is another possibility and seems more promising.¹³⁴

The isolation of sterols from sunflower ODD by hydrolysis, esterification and distillation resulted in a recovery of 42 % with a purity of 36 wt.%. The obtained stream was also enriched in tocopherols (30 wt.%).¹⁴¹ The separation of sterols from soybean ODD by crystallization, using a mixture of acetone and methanol as a solvent, resulted in 80 % of sterols in the solid phase.¹⁴²

1.6.3 Tocopherols

Tocopherols are organic molecules that appear in four isomers: α -tocopherol, β -tocopherol, γ -tocopherol and δ -tocopherol. The structure formulas are given in Figure 1.21. The position of the methyl-group on the chromanol ring determines which of the isomers is concerned.

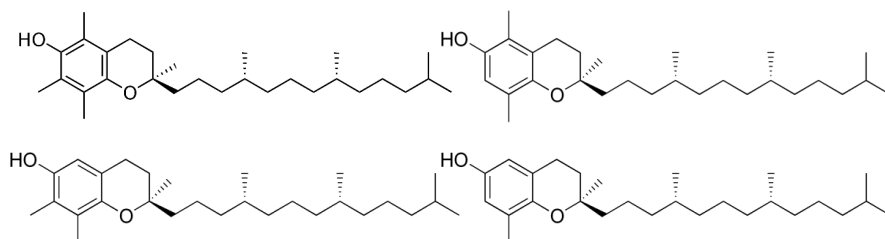


Figure 1.21. Top from left to right: α -tocopherol, β -tocopherol; bottom from left to right γ -tocopherol, δ -tocopherol

All these isomers exhibit vitamin E activity.¹⁴³ Tocopherols are naturally present in vegetable oils as well as in fruit and vegetables. In the food industry, they are used as additives because, they contribute to the conservation of ingredients, thanks to their strong antioxidant activity. They are recognized by their E-numbers E-306, E-307, E-308 and E-309. It is claimed that they have anti-carcinogenic properties and protect people against cardiovascular diseases.¹⁴⁴ Tocopherols are used in cosmetic industry as anti-oxidant, to increase the preservability of the product.¹⁴⁰

Similar to sterols, tocopherols are mostly chemically synthesized. Due to the increasing demand of tocopherols and scientific research that suggests that natural tocopherols are better for human health than synthetic variants, routes to acquire tocopherols from natural resources are intensively investigated.¹⁴⁵ Options are the extraction of tocopherols from vegetable oils or from ODD.¹⁴³

Supercritical CO₂ has been already used to increase the tocopherol concentration in soybean ODD. Concentrations of at least 40 wt.% could be technically and economically achieved.¹⁴⁶ The combination of CO₂ distillation-extraction allowed to recover 84 % of the tocopherols contained in soybean ODD with a purity of 17 wt.%.¹⁴⁷

1.7 Separation of the minor components

The different minor components are of industrial relevance. In this section different processes for the isolation of minor components are compared and evaluated. Firstly, there is focused on the isolation of the minor components themselves (section 1.7.1). Secondly, esterification and transesterification reactions as pretreatment of the ODD are suggested in section 1.7.2. And finally the optimal, integrated technique (a two-step process) is discussed in section 1.7.3.

1.7.1 Isolation of minor components

Using conventional methods such as vacuum and molecular distillation for separation of the minor components from the ODD stream, is difficult for three main reasons. Firstly, the volatilities of sterols and tocopherols and the molecular weights of the three minor components are very similar which results in difficult separation using these conventional techniques.^{148, 149} Secondly, temperatures required to perform a conventional separation method may cause thermal degradation of the minor components. Conversion of the free fatty acids (FFA) present in the ODD, into unwanted trans isomeric forms may occur as well.^{149, 150} And thirdly the conventional processes are very expensive.¹⁵⁰ With these constraints in mind, alternative options to directly isolate the minor components from the ODD stream are considered in this section. There are four categories which are discussed below: crystallization and precipitation, molecular distillation, chemical and enzymatic modification and extraction with supercritical CO₂.¹⁴⁹

1.7.1.1 *Crystallization and precipitation*

Crystallization followed by precipitation is a classical separation method which can be used to isolate the minor components from the ODD. By adding a solvent like acetone to the ODD, sterols or tocopherols, depending on the conditions, crystallize after which the precipitate can be removed from the supernate. Mostly, other separation methods are performed preceding or following this crystallization and precipitation step to remove other components of interest. The advantage of this method is that no thermal degradation occurs since this method can be performed at low temperatures. The great disadvantage is the necessity of a solvent which renders the method expensive, unattractive and environmentally unfriendly. Moreover, it has been observed that the proportion of solvent over treated stream needs to be very large to guarantee a good separation which further increases the costs. A last disadvantage is the fact that proper recycling of the solvent is not always straightforward. This may lead to traces of solvent present in the final product which often greatly affects the applicability.¹⁴⁹

1.7.1.2 *Molecular distillation*

To tackle the problem of thermal degradation of the components present in the ODD, molecular distillation (short-path distillation) instead of conventional distillation may be used. This distillation technique is performed at pressures lower than 1.3 Pa (vacuum). Over a path of 2 to 5 cm evaporating liquid is distilled while moving to the cooled surface of a condenser. The very short distillation gap results in limited residence time and relatively reduced temperatures are sufficient for the operations due to the vacuum. So, almost no thermal degradation can take place. Another advantage of this separation technique is that no solvents are required which makes this a more ecological friendly process than for example crystallization and precipitation. A great disadvantage, however, is the cost of this technique because vacuum atmosphere has to be maintained.¹⁴⁹

1.7.1.3 *Enzymatic or chemical modification*

The components present in the ODD stream may be enzymatically or chemically selectively transformed. This leads to a mixture with alternated components. Such a modification may be interesting when the transformation leads to a compounds pool where the affinity between the different components or component groups is reduced. These alternations then result in easier separation using other techniques. So chemical or enzymatic modification does not immediately lead to the separation of the minor components from the ODD. This technique requires an additional separation step so it is called a pretreatment step.

An example of enzymatic modification is the modification of sterols into sterol esters. The physical and chemical properties of these esters differ enough to more easily separate them from the tocopherols. However, this enzymatic modification requires the use of organic solvents, water and molecular sieves or other drying agents which makes it a complex, expensive and environmentally unfriendly.^{149, 151}

An important example of chemical modification is the esterification of the FFA's and glycerides present in the ODD. The chemical and physical properties of the FFA's are very similar to those of the minor components which makes separation difficult. However, when they are chemically converted, by reaction with an alcohol, esters are formed. The properties of these esters differ greatly from these of the minor components which leads to an easier separation.¹⁴⁹ Because FFA's and triglycerides are the main components in ODD, chemical modification is of great interest when considering valorization of ODD. It will be discussed in more detail in section 1.7.2.

1.7.1.4 *Supercritical extraction*

The final separation technique for separation of minor components from ODD is extraction with supercritical CO₂. During this process, supercritical CO₂ flows countercurrent with the ODD stream. The components showing high affinity with the supercritical CO₂ will be entrained to form the extract. The other components are collected as raffinate. This process has several advantages. Firstly, the low viscosity, high diffusivity and low surface tension of the supercritical CO₂ leads to a selective extraction.¹⁴⁹ Secondly, the use of CO₂ is interesting due to its inertness and nontoxicity which guarantees that further use of the final products is safe for cosmetic, food and pharmaceutical applications. A third advantage is the absence of solvent after separation which simplifies the further separation of the components (sequenced depressurization suffices). Furthermore, the fact that CO₂ becomes critical at 304.25 K means there are no risks for thermal degradation of the components. Lastly, the low cost of CO₂ makes the technique economically interesting.

All these advantages show that this technique is very promising for valorization applications of ODD. However, it is important to examine which components present in the ODD will be entrained with the supercritical CO₂. An exemplary composition ODD streams is given in Table 1.3. Mainly FFA's and glycerides are present. These components, having a high molecular weight and low volatility, all have

low solubility in supercritical CO₂ which means they will not be entrained to form the extract.¹⁴⁸ The minor components, squalene, tocopherols and sterols, have similar characteristics.^{149, 150} Consequently, no efficient separation will take place

To guarantee efficient separation of the minor components from the other components within the ODD stream, a pretreatment reaction must be performed. Choosing for an esterification as chemical modification preceding the extraction with supercritical CO₂ seems to be an interesting option because the chemical and physical properties of the formed esters differ pronouncedly from these of the minor components¹⁵².

1.7.2 Pretreatment of the ODD

As discussed in subsection 1.7.1, the minor components are more efficiently isolated from the ODD when a chemical modification precedes the extraction step. The reaction of an alcohol with FFAs (esterification) and the reaction of an alcohol with glycerides (transesterification) leads to the formation of fatty alkyl esters (FAEs). These have a higher solubility in supercritical CO₂ than the FFAs and glycerides, resulting in a better separation from the minor components during the consequent separation step (extraction with supercritical CO₂). Esterification can be performed under classical conditions or with a supercritical alcohol. Both options are briefly described in the following subsections. Furthermore, different alcohols can be used as esterification agent.

1.7.2.1 Classical esterification

During esterification, the FFAs and glycerides present in the ODD are converted into FAEs. This reaction can be chemically catalyzed (using an alkali or an acid), enzymatically catalyzed or heterogeneously catalyzed¹⁵³.

An example of a chemically (alkali) catalyzed esterification is called classical saponification and requires a strong base (for example NaOH).¹⁵² Afterwards, the base is replaced by an alcohol such as methanol or ethanol. Post-treatment steps are mandatory to obtain a clean ester mixture. The fatty acid salt which is formed simultaneously is known as soap.¹⁵³ H₂SO₄ is frequently used as strong acid during chemically (acid) catalyzed esterification.

Enzymatic esterification can be performed as well, but is less favorable than chemically catalyzed processes due to higher reaction times and costs.¹⁵⁴

Heterogeneously catalyzed esterification is another option. While both chemically and enzymatically catalyzed esterification require additional separation steps to remove the solvents used, heterogeneous catalyzed esterification does not have this disadvantage. An easy separation between product and catalyst is guaranteed and moreover, the catalyst can be reused.¹⁵³ A disadvantage is of course the cost of the selective catalyst.

1.7.2.2 Supercritical esterification

The most obvious disadvantage of classical esterification reactions is the need for solvents during reaction. These are expensive, not environmentally friendly and lead to difficult separation to recover the product afterwards. An alternative for classical esterification is esterification with a supercritical alcohol. Under these conditions no solvents are required which leads to the great advantage that no separation must be performed at the end and that the obtained product is not polluted by impurities. In the supercritical state, namely, the dielectric constant of the alcohol decreases because ions are formed from the alcohol.^{155, 156} Consequently, a single phase oil-alcohol mixture is formed instead of the two phase nature which is typical for an oil-alcohol mixture at ambient conditions. The existence of this single phase mixture accelerates the reaction.^{157, 158}

Note that supercritical esterification means that the alcohol used for esterification is at supercritical conditions; the reaction mixture eventually formed, is not supercritical.¹⁵²

1.7.3 Integrated solution of esterification and extraction

In subsection 1.7.1.4, it was indicated that extraction with supercritical CO₂ is the preferred technique to valorize the minor components from ODD. A pretreatment step is however highly recommended to guarantee an efficient separation of minor components and other compounds present in the ODD. As a pretreatment step, esterification (chemical modification) was suggested in section 1.7.2 during which the FFAs and glycerides are converted into FAEs. The chemical and physical properties of these esters differ more pronouncedly from these of the minor components which leads to more efficient separation. Studies^{134, 135} indeed show that preceding the extraction step with an esterification step, is promising for the aimed purpose. The research group of G. Reglero¹³⁴ compared the efficiency of extraction of sterols and tocopherols from sunflower ODD for ODD without and ODD with an esterification reaction as pretreatment. The esterification performed in this study was a classical, chemically catalyzed esterification (using H₂SO₄) with ethanol. It was clear that for the esterified ODD the fraction of minor components in the raffinate is much higher. For example at 18 MPa, the enrichment factor of the minor components in the raffinate for esterified ODD compared to the original ODD is 3.7 and 83% of sterols and tocopherols are recovered. Later, it was found that the same trends applied for the recuperation of squalen from squalene rich olive ODD.¹⁵⁹

To summarize, the minor components can be extracted from the FFAs and glycerides by extraction with supercritical CO₂. However, due to similar affinity of these components and the minor components with the CO₂, efficient separation is excluded. The solution is to precede the extraction process with an esterification with supercritical alcohol. This pretreatment transforms the FFAs and glycerides into esters which do show different affinity with the CO₂ than the minor components. In the meantime, an ester mixture is produced which can be of economic value as well.

1.8 Scope of this thesis

Biomass is a renewable, clean and abundant resource. During the last decades the interest into renewable resources for chemicals and energy has increased due to dwindling fossil oil reserves and the environmental impact of greenhouse gas emissions on climate change. On the other hand, the rapid population growth has driven the demand for high-quality edible oils. Therefore, oils and fats have a future as biomass resources. In particular, the valorization of waste, side streams, characterized with low economic value, can play an important role in achieving a green and sustainable economy. This thesis focusses on the valorization of side streams at various scales. **Chapter 2** describes the material synthesis and its characterization, the experimental and modelling procedures used in this work.

At the scale of the reaction in Chapters 3, 4 and 5, a systematic approach for investigating the impact of the Cu catalyst properties on the glycerol hydrogenolysis reaction is adopted, with the aim of retrieving strategic insights for the design of a novel, high performing catalyst generation. In **Chapter 3**, it is investigated how the co-metals Ba, Ce, Cs and La affect the performance of a Cu/ γ -Al₂O₃ catalyst. The effect of these co-metals on the physical, surface and bulk properties is determined. The catalysts are evaluated on their stability, catalytic activity and 1,2-propanediol selectivity. The La-doped catalysts exhibited the best improvement as compared to Cu in terms of stability as a function of time on stream. Therefore, **Chapter 4** explores the La promotion in more depth, i.e., by assessing how La promotion affects the catalyst's morphology, physical properties, distribution of surface Cu species, surface and bulk properties, as a function of the La/Cu ratio. The effect of the La/Cu ratio as compared to a Cu catalyst was assessed in terms of catalyst stability, by comparing the Cu⁰ particle size in the fresh and spent catalyst, activity and 1,2-propanediol selectivity. As the role of acidity – induced by Cu⁺ – proved to be important, **Chapter 5** assesses the effect of the support of Cu and La-Cu catalysts, by varying the fraction of SiO₂ (0, 40, 60 and 100 wt.%) in the Al₂O₃ support aiming at varying not only the acidity of the support but also the formation of Cu⁺ species. The physical, surface and bulk properties are determined to compare the supported Cu catalysts to a La doped one, to screen both the effect of the support, and its acidity, and the La-promotion. The catalysts are compared in terms of catalytic activity and 1,2-propanediol selectivity.

At the process scale, the potential recovery of squalene from oil deodorizer distillates is assessed *via* detailed process simulations in **Chapter 6**. A flexible process configuration is designed which is suitable for different ODD feedstocks, which are olive, sunflower and soybean ODD. These are compared to each other in terms of squalene yield, recovery and purity. Apart from squalene, two more value-added products were produced, *i.e.*, high purity ethyl esters and a mixture of tocopherols and sterols, which contribute to the economic viability of the process. Both the most profitable and the most flexible feedstock are identified.

The general conclusions of this work are given in **Chapter 7**.

1.9 References

- 1 Worldometer, Current World Population, 2021.
- 2 ExxonMobil Corporation, The 2019 Outlook for Energy: A Perspective to 2040, 2019.
- 3 International Energy Agency, Key World Energy Statistics 2020, 2020.
- 4 E. de Jong, H. Stichnothe, G. Bell, H. Jørgensen, Bio-Based Chemicals - a 2020 Update, IEA Bioenergy, 2020.
- 5 United Nations Climate Change, The Paris Agreement, Paris, 2015.
- 6 The Global Goals for Sustainable Development, Climate Action, 2015.
- 7 J.W. Thybaut, The Fossil Carbon Cycle Vs. The Biomass Carbon Cycle, 2014.
- 8 J. Spekrijse, T. Lammens, C. Parisi, T. Ronzon, M. Vis, Insights into the European Market for Bio-Based Chemicals, Publications Office of the European Union, 2019.
- 9 Grand View Research, Bio-Based Platform Chemicals Market Size, Share & Trends Analysis Report, 2019.
- 10 Businesswire, Global Bio-Based Platform Chemicals Market 2020-2024, (2020).
- 11 Market Research Future, Bio-Based Chemicals Market: Information by Type, (2019).
- 12 P.T. Anastas, J.C. Warner, Green Chemistry: Theory and Practice, Oxford University Press 2000.
- 13 J. Mou, C. Li, X. Yang, G. Kaur, C. Sze Ki Lin, Overview of Waste Valorisation Concepts from a Circular Economy Perspective, Waste Valorisation 2020, pp. 1-11.
- 14 K. Van Geem, I. Amghizar, F. Vermeire, D.B. Ruben, Production of Bio-Oil, Biofuels Production and Processing Technology, CRC Press 2017.
- 15 O'Brien, D. Richard, Introduction to Fats and Oils Technology, 2000.
- 16 Statista, Production of Vegetable Oils World Wide since 2000, 2020.
- 17 A. Behr, The Future of Glycerol. New Usages for a Versatile Raw Material. By Mario Pagliaro and Michele Rossi, ChemSusChem, 1 (2008) 653-653.
- 18 F. Bauer, C. Hultberg, Is There a Future in Glycerol as a Feedstock in the Production of Biofuels and Biochemicals?, Biofuels, Bioproducts and Biorefining, 7 (2013) 43-51.
- 19 P.N.R. Vennestrøm, C.M. Osmundsen, C.H. Christensen, E. Taarning, Beyond Petrochemicals: The Renewable Chemicals Industry, Angewandte Chemie International Edition, 50 (2011) 10502-10509.
- 20 A.M. Gavin, Edible Oil Deodorization, Journal of the American Oil Chemists' Society, 55 (1978) 783-791.
- 21 N.A. Akgün, G. Gece, E. Tekneci, Strategies to Obtain Tocopherols, Phytosterols and Squalene from Deodorizer Distillates and Acid Oils Using Supercritical Fluids, Recent Research Developments in Lipids, 9 (2013) 67-84.
- 22 R. Christoph, B. Schmidt, U. Steinberner, W. Dilla, R. Karinen, Glycerol, Ullmann's Encyclopedia of Industrial Chemistry.
- 23 R. Ciriminna, C.D. Pina, M. Rossi, M. Pagliaro, Understanding the Glycerol Market, European Journal of Lipid Science and Technology, 116 (2014) 1432-1439.
- 24 M. Pagliaro, M. Rossi, Glycerol: Properties and Production, The Future of Glycerol, Society of Chemistry 2010.
- 25 A. Bouriakova, P.S. Mendes, K. Elst, J. De Clercq, J.W. Thybaut, Techno-Economic Evaluation of Squalene Recovery from Oil Deodorizer Distillates, Chemical Engineering Research and Design, 154 (2020) 122-134.
- 26 Grand View Research, Global Glycerol Market Size, Share, Industry Report, 2020-2027, 2020.
- 27 S. Wright, Insight: Europe Glycerine Spot Prices Post Triple-Digit Rises on Fears of Further Biodiesel Output Cuts, Independent Commodity Intelligence Services, 2020.
- 28 S. Nomanbhay, R. Hussein, M.Y. Ong, Sustainability of Biodiesel Production in Malaysia by Production of Bio-Oil from Crude Glycerol Using Microwave Pyrolysis: A Review, Green Chemistry Letters and Reviews, 11 (2018) 135-157.
- 29 S. Gregory, Physical Properties of Glycerine, Marcel Dekker: New York 1991.
- 30 M. Sara, T. Rouissi, S.K. Brar, J.F. Blais, Chapter 5 - Propylene Glycol: An Industrially Important C3 Platform Chemical, in: S. Kaur Brar, S. Jyoti Sarma, K. Pakshirajan (Eds.) Platform Chemical Biorefinery, Elsevier, Amsterdam, 2016, pp. 77-100.

- 31 C.H. Zhou, H. Zhao, D.S. Tong, L.M. Wu, W.H. Yu, Recent Advances in Catalytic Conversion of Glycerol, *Catalysis Reviews*, 55 (2013) 369-453.
- 32 C.-H.C. Zhou, J.N. Beltrami, Y.-X. Fan, G.M. Lu, Chemoselective Catalytic Conversion of Glycerol as a Biorenewable Source to Valuable Commodity Chemicals, *Chemical Society Reviews*, 37 (2008) 527-549.
- 33 J.A. Cecilia, C. García-Sancho, P.J. Maireles-Torres, R. Luque, Industrial Food Waste Valorization: A General Overview, in: J.-R. Bastidas-Oyanedel, J.E. Schmidt (Eds.) *Biorefinery: Integrated Sustainable Processes for Biomass Conversion to Biomaterials, Biofuels, and Fertilizers*, Springer International Publishing, Cham, 2019, pp. 253-277.
- 34 Y. Zheng, X. Chen, Y. Shen, Commodity Chemicals Derived from Glycerol, an Important Biorefinery Feedstock, *Chemical Reviews*, (2008).
- 35 B.R. Sereshki, S.J. Balan, G.S. Patience, J.L. Dubois, Reactive Vaporization of Crude Glycerol in a Fluidized Bed Reactor, *Industrial & Engineering Chemistry Research*, 49 (2010) 1050-1056.
- 36 P. Gallezot, Chapter 1 - Metal Catalysts for the Conversion of Biomass to Chemicals, in: S.L. Suib (Ed.) *New and Future Developments in Catalysis*, Elsevier, Amsterdam, 2013, pp. 1-27.
- 37 M.R. Nanda, Z. Yuan, W. Qin, C. Xu, Recent Advancements in Catalytic Conversion of Glycerol into Propylene Glycol: A Review, *Catalysis Reviews*, 58 (2016) 309-336.
- 38 Market Intellica, *World Propylene Glycol Market by Product Type, Market, Players and Regions - Forecast to 2024*, 2019.
- 39 *Markets and Markets, Propylene Glycol Market by Source (Petroleum-Based, Bio-Based), Grade (Industrial, Pharmaceutical), End-Use Industry (Transportation, Building & Construction, Food & Beverage, Pharmaceuticals, Cosmetics & Personal Care), Region - Global Forecast to 2024*, 2018.
- 40 S.P. Samudrala, Glycerol Transformation to Value-Added 1, 3-Propanediol Production: A Paradigm for a Sustainable Biorefinery Process, *Glycerine Production and Transformation-an Innovative Platform for Sustainable Biorefinery and Energy*, IntechOpen2019.
- 41 H. Zhao, L. Zheng, X. Li, P. Chen, Z. Hou, Hydrogenolysis of Glycerol to 1, 2-Propanediol over Cu-Based Catalysts: A Short Review, *Catalysis Today*, (2019).
- 42 Y. Wang, J. Zhou, X. Guo, Catalytic Hydrogenolysis of Glycerol to Propanediols: A Review, *RSC Advances*, 5 (2015) 74611-74628.
- 43 M.A. Dasari, P.-P. Kiatsimkul, W.R. Sutterlin, G.J. Suppes, Low-Pressure Hydrogenolysis of Glycerol to Propylene Glycol, *Applied Catalysis A: General*, 281 (2005) 225-231.
- 44 Y. Nakagawa, K. Tomishige, Heterogeneous Catalysis of the Glycerol Hydrogenolysis, *Catalysis Science & Technology*, 1 (2011) 179-190.
- 45 A. Alhanash, E.F. Kozhevnikova, I.V. Kozhevnikov, Gas-Phase Dehydration of Glycerol to Acrolein Catalysed by Caesium Heteropoly Salt, *Applied Catalysis A: General*, 378 (2010) 11-18.
- 46 F. Vila, M. López Granados, M. Ojeda, J.L.G. Fierro, R. Mariscal, Glycerol Hydrogenolysis to 1,2-Propanediol with Cu/F-Al₂O₃: Effect of the Activation Process, *Catalysis Today*, 187 (2012) 122-128.
- 47 F. Vila, M. López Granados, R. Mariscal, Significance of Isomeric Reaction Intermediates in the Hydrogenolysis of Glycerol to 1,2-Propanediol with Cu-Based Catalysts, *Catalysis Science & Technology*, 7 (2017) 3119-3127.
- 48 C. Montassier, J. Ménéz, L. Hoang, C. Renaud, J. Barbier, Aqueous Polyol Conversions on Ruthenium and on Sulfur-Modified Ruthenium, *Journal of molecular catalysis*, 70 (1991) 99-110.
- 49 J. Hagen, *Industrial Catalysis*, 2005.
- 50 T. Miyazawa, Y. Kusunoki, K. Kunimori, K. Tomishige, Glycerol Conversion in the Aqueous Solution under Hydrogen over Ru/C+ an Ion-Exchange Resin and Its Reaction Mechanism, *Journal of Catalysis*, 240 (2006) 213-221.
- 51 E.P. Maris, R.J. Davis, Hydrogenolysis of Glycerol over Carbon-Supported Ru and Pt Catalysts, *Journal of Catalysis*, 249 (2007) 328-337.
- 52 Y. Kusunoki, T. Miyazawa, K. Kunimori, K. Tomishige, Highly Active Metal-Acid Bifunctional Catalyst System for Hydrogenolysis of Glycerol under Mild Reaction Conditions, *Catalysis Communications*, 6 (2005) 645-649.
- 53 I. Furikado, T. Miyazawa, S. Koso, A. Shimao, K. Kunimori, K. Tomishige, Catalytic Performance of Rh/SiO₂ in Glycerol Reaction under Hydrogen, *Green Chemistry*, 9 (2007) 582-588.

- 54 E. Vasiliadou, E. Heracleous, I. Vasalos, A. Lemonidou, Ru-Based Catalysts for Glycerol Hydrogenolysis—Effect of Support and Metal Precursor, *Applied Catalysis B: Environmental*, 92 (2009) 90-99.
- 55 I. Gandarias, P.L. Arias, J. Requies, M.B. Güemez, J.L.G. Fierro, Hydrogenolysis of Glycerol to Propanediols over a Pt/Asa Catalyst: The Role of Acid and Metal Sites on Product Selectivity and the Reaction Mechanism, *Applied Catalysis B: Environmental*, 97 (2010) 248-256.
- 56 M. Balaraju, V. Rekha, P.S.S. Prasad, B.L.A.P. Devi, R.B.N. Prasad, N. Lingaiah, Influence of Solid Acids as Co-Catalysts on Glycerol Hydrogenolysis to Propylene Glycol over Ru/C Catalysts, *Applied Catalysis A: General*, 354 (2009) 82-87.
- 57 A. Alhanash, E.F. Kozhevnikova, I.V. Kozhevnikov, Hydrogenolysis of Glycerol to Propanediol over Ru: Polyoxometalate Bifunctional Catalyst, *Catalysis Letters*, 120 (2008) 307-311.
- 58 Z. Yuan, P. Wu, J. Gao, X. Lu, Z. Hou, X. Zheng, Pt/Solid-Base: A Predominant Catalyst for Glycerol Hydrogenolysis in a Base-Free Aqueous Solution, *Catalysis Letters*, 130 (2009) 261-265.
- 59 E.P. Maris, W.C. Ketchie, M. Murayama, R.J. Davis, Glycerol Hydrogenolysis on Carbon-Supported PtRu and AuRu Bimetallic Catalysts, *Journal of Catalysis*, 251 (2007) 281-294.
- 60 J. Feng, J. Wang, Y. Zhou, H. Fu, H. Chen, X. Li, Effect of Base Additives on the Selective Hydrogenolysis of Glycerol over Ru/TiO₂ Catalyst, *Chemistry letters*, 36 (2007) 1274-1275.
- 61 H. Dreyfus, *Manufacture of Polyhydric Alcohols*, United States, 1941.
- 62 M. Behrens, S. Zander, P. Kurr, N. Jacobsen, J.r. Senker, G. Koch, T. Ressler, R.W. Fischer, R. Schlögl, Performance Improvement of Nanocatalysts by Promoter-Induced Defects in the Support Material: Methanol Synthesis over Cu/Zno: Al, *Journal of the American Chemical Society*, 135 (2013) 6061-6068.
- 63 J.M. Campos-Martín, J.L.G. Fierro, A. Guerrero-Ruiz, R.G. Herman, K. Klier, Promoter Effect of Cesium on C–C Bond Formation During Alcohol Synthesis from Co/H₂ over Cu/Zno/Cr₂O₃ catalysts, *Journal of Catalysis*, 163 (1996) 418-428.
- 64 A.M. Beale, E.K. Gibson, M.G. O'Brien, S.D.M. Jacques, R.J. Cernik, M.D. Michiel, P.D. Cobden, Ö. Pirgon-Galin, L.v.d. Water, M.J. Watson, B.M. Weckhuysen, Chemical Imaging of the Sulfur-Induced Deactivation of Cu/Zno Catalyst Bodies, *Journal of Catalysis*, 314 (2014) 94-100.
- 65 A. Budiman, M. Ridwan, S.M. Kim, J.-W. Choi, C.W. Yoon, J.-M. Ha, D.J. Suh, Y.-W. Suh, Design and Preparation of High-Surface-Area Cu/Zno/Al₂O₃ Catalysts Using a Modified Co-Precipitation Method for the Water-Gas Shift Reaction, *Applied Catalysis A: General*, 462 (2013) 220-226.
- 66 M.A. Díaz-Pérez, J. Moya, J.C. Serrano-Ruiz, J. Faria, Interplay of Support Chemistry and Reaction Conditions on Copper Catalyzed Methanol Steam Reforming, *Industrial & Engineering Chemistry Research*, 57 (2018) 15268-15279.
- 67 X. Xu, K. Shuai, B. Xu, Review on Copper and Palladium Based Catalysts for Methanol Steam Reforming to Produce Hydrogen, *Catalysts*, 7 (2017) 183.
- 68 A. Bienholz, F. Schwab, P. Claus, Hydrogenolysis of Glycerol over a Highly Active CuO/Zno Catalyst Prepared by an Oxalate Gel Method: Influence of Solvent and Reaction Temperature on Catalyst Deactivation, *Green Chemistry*, 12 (2010) 290-295.
- 69 M. Balaraju, V. Rekha, P.S. Sai Prasad, R.B.N. Prasad, N. Lingaiah, Selective Hydrogenolysis of Glycerol to 1, 2 Propanediol over Cu–Zno Catalysts, *Catalysis Letters*, 126 (2008) 119-124.
- 70 S. Wang, H. Liu, Selective Hydrogenolysis of Glycerol to Propylene Glycol on Cu–Zno Catalysts, *Catalysis Letters*, 117 (2007) 62-67.
- 71 Y. Du, C. Wang, H. Jiang, C. Chen, R. Chen, Insights into Deactivation Mechanism of Cu–Zno Catalyst in Hydrogenolysis of Glycerol to 1,2-Propanediol, *Journal of Industrial and Engineering Chemistry*, 35 (2016) 262-267.
- 72 A. Perosa, P. Tundo, Selective Hydrogenolysis of Glycerol with Raney Nickel, *Industrial & Engineering Chemistry Research*, 44 (2005) 8535-8537.
- 73 J. Zhao, W. Yu, C. Chen, H. Miao, H. Ma, J. Xu, Ni/Nax: A Bifunctional Efficient Catalyst for Selective Hydrogenolysis of Glycerol, *Catalysis Letters*, 134 (2010) 184-189.
- 74 I. Gandarias, P. Arias, J. Requies, M. El Doukkali, M. Güemez, Liquid-Phase Glycerol Hydrogenolysis to 1, 2-Propanediol under Nitrogen Pressure Using 2-Propanol as Hydrogen Source, *Journal of Catalysis*, 282 (2011) 237-247.

- 75 X. Guo, Y. Li, R. Shi, Q. Liu, E. Zhan, W. Shen, Co/Mgo Catalysts for Hydrogenolysis of Glycerol to 1, 2-Propanediol, *Applied Catalysis A: General*, 371 (2009) 108-113.
- 76 X. Guo, Y. Li, W. Song, W. Shen, Glycerol Hydrogenolysis over Co Catalysts Derived from a Layered Double Hydroxide Precursor, *Catalysis Letters*, 141 (2011) 1458.
- 77 Q. Liu, X. Cao, T. Wang, C. Wang, Q. Zhang, L. Ma, Synthesis of Shape-Controllable Cobalt Nanoparticles and Their Shape-Dependent Performance in Glycerol Hydrogenolysis, *RSC Advances*, 5 (2015) 4861-4871.
- 78 A. Marinouiu, G. Ionita, C.-L. Gáspár, C. Cobzaru, D. Marinescu, C. Teodorescu, S. Oprea, Selective Hydrogenolysis of Glycerol to Propylene Glycol Using Heterogeneous Catalysts, *Reaction Kinetics, Mechanisms and Catalysis*, 99 (2010) 111-118.
- 79 M. Balaraju, K. Jagadeeswaraiiah, P.S.S. Prasad, N. Lingaiah, Catalytic Hydrogenolysis of Biodiesel Derived Glycerol to 1,2-Propanediol over Cu-Mgo Catalysts, *Catalysis Science & Technology*, 2 (2012) 1967-1976.
- 80 Z. Yuan, J. Wang, L. Wang, W. Xie, P. Chen, Z. Hou, X. Zheng, Biodiesel Derived Glycerol Hydrogenolysis to 1, 2-Propanediol on Cu/Mgo Catalysts, *Bioresource technology*, 101 (2010) 7088-7092.
- 81 Z. Yuan, L. Wang, J. Wang, S. Xia, P. Chen, Z. Hou, X. Zheng, Hydrogenolysis of Glycerol over Homogenously Dispersed Copper on Solid Base Catalysts, *Applied Catalysis B: Environmental*, 101 (2011) 431-440.
- 82 E.S. Vasiliadou, T.M. Eggenhuisen, P. Munnik, P.E. de Jongh, K.P. de Jong, A.A. Lemonidou, Synthesis and Performance of Highly Dispersed Cu/Sio₂ Catalysts for the Hydrogenolysis of Glycerol, *Applied Catalysis B: Environmental*, 145 (2014) 108-119.
- 83 Z. Huang, F. Cui, J. Xue, J. Zuo, J. Chen, C. Xia, Cu/Sio₂ Catalysts Prepared by Hom- and Heterogeneous Deposition–Precipitation Methods: Texture, Structure, and Catalytic Performance in the Hydrogenolysis of Glycerol to 1,2-Propanediol, *Catalysis Today*, 183 (2012) 42-51.
- 84 Z. Wu, Y. Mao, M. Song, X. Yin, M. Zhang, Cu/Boehmite: A Highly Active Catalyst for Hydrogenolysis of Glycerol to 1,2-Propanediol, *Catalysis Communications*, 32 (2013) 52-57.
- 85 S. Zhu, X. Gao, Y. Zhu, W. Fan, J. Wang, Y. Li, A Highly Efficient and Robust Cu/Sio₂ Catalyst Prepared by the Ammonia Evaporation Hydrothermal Method for Glycerol Hydrogenolysis to 1,2-Propanediol, *Catalysis Science & Technology*, 5 (2015) 1169-1180.
- 86 B.K. Kwak, D.S. Park, Y.S. Yun, J. Yi, Preparation and Characterization of Nanocrystalline CuAl₂O₄ Spinel Catalysts by Sol–Gel Method for the Hydrogenolysis of Glycerol, *Catalysis Communications*, 24 (2012) 90-95.
- 87 L.C. Meher, R. Gopinath, S.N. Naik, A.K. Dalai, Catalytic Hydrogenolysis of Glycerol to Propylene Glycol over Mixed Oxides Derived from a Hydrotalcite-Type Precursor, *Industrial & Engineering Chemistry Research*, 48 (2009) 1840-1846.
- 88 L. Huang, Y.L. Zhu, H.Y. Zheng, Y.W. Li, Z.Y. Zeng, Continuous Production of 1, 2-Propanediol by the Selective Hydrogenolysis of Solvent-Free Glycerol under Mild Conditions, *Journal of Chemical Technology & Biotechnology: International Research in Process, Environmental & Clean Technology*, 83 (2008) 1670-1675.
- 89 R.B. Mane, C.V. Rode, Continuous Dehydration and Hydrogenolysis of Glycerol over Non-Chromium Copper Catalyst: Laboratory-Scale Process Studies, *Organic Process Research & Development*, 16 (2012) 1043-1052.
- 90 R. Mane, S. Kondawar, P. Niphadkar, P. Joshi, K. Patil, C. Rode, Effect of Preparation Parameters of Cu Catalysts on Their Physico-Chemical Properties and Activities for Glycerol Hydrogenolysis, *Catalysis Today*, 198 (2012) 321-329.
- 91 A. Wolosiak-Hnat, E. Milchert, B. Grzmil, Influence of Parameters on Glycerol Hydrogenolysis over a Cu/Al₂O₃ Catalyst, *Chemical Engineering & Technology*, 36 (2013) 411-418.
- 92 L. Guo, J. Zhou, J. Mao, X. Guo, S. Zhang, Supported Cu Catalysts for the Selective Hydrogenolysis of Glycerol to Propanediols, *Applied Catalysis A: General*, 367 (2009) 93-98.
- 93 Z. Huang, F. Cui, H. Kang, J. Chen, X. Zhang, C. Xia, Highly Dispersed Silica-Supported Copper Nanoparticles Prepared by Precipitation–Gel Method: A Simple but Efficient and Stable Catalyst for Glycerol Hydrogenolysis, *Chemistry of Materials*, 20 (2008) 5090-5099.

- 94 Z. Huang, H. Liu, F. Cui, J. Zuo, J. Chen, C. Xia, Effects of the Precipitation Agents and Rare Earth Additives on the Structure and Catalytic Performance in Glycerol Hydrogenolysis of Cu/SiO₂ Catalysts Prepared by Precipitation-Gel Method, *Catalysis Today*, 234 (2014) 223-232.
- 95 S. Zhu, X. Gao, Y. Zhu, Y. Zhu, H. Zheng, Y. Li, Promoting Effect of Boron Oxide on Cu/SiO₂ Catalyst for Glycerol Hydrogenolysis to 1, 2-Propanediol, *Journal of Catalysis*, 303 (2013) 70-79.
- 96 C.H. Zhou, K. Deng, M.D. Serio, S. Xiao, D.S. Tong, L. Li, C.X. Lin, J. Beltramini, H. Zhang, W.H. Yu, Cleaner Hydrothermal Hydrogenolysis of Glycerol to 1,2-Propanediol over Cu/Oxide Catalysts without Addition of External Hydrogen, *Molecular Catalysis*, 432 (2017) 274-284.
- 97 D. Durán-Martín, M. Ojeda, M.L. Granados, J.L.G. Fierro, R. Mariscal, Stability and Regeneration of Cu-ZrO₂ Catalysts Used in Glycerol Hydrogenolysis to 1,2-Propanediol, *Catalysis Today*, 210 (2013) 98-105.
- 98 M.V. Twigg, M.S. Spencer, Deactivation of Supported Copper Metal Catalysts for Hydrogenation Reactions, *Applied Catalysis A: General*, 212 (2001) 161-174.
- 99 R.-P. Ye, L. Lin, Q. Li, Z. Zhou, T. Wang, C.K. Russell, H. Adidharma, Z. Xu, Y.-G. Yao, M. Fan, Recent Progress in Improving the Stability of Copper-Based Catalysts for Hydrogenation of Carbon-Oxygen Bonds, *Catalysis Science & Technology*, 8 (2018) 3428-3449.
- 100 M.D. Argyle, C.H. Bartholomew, Heterogeneous Catalyst Deactivation and Regeneration: A Review, *Catalysts*, 5 (2015) 145-269.
- 101 A.B. Miller, M. Raghunath, V. Sokolovskii, C.G. Lugmair, J. Anthony F. Volpe, W. Shen, W. Turbeville, Catalyst for Polyol Hydrogenolysis, US20140249334A1, 2014.
- 102 L. Zhiguo, G. Zhenmei, L. Pei, Z. Weiwei, Method for Preparing Propylene Glycol by Glycerin Hydrogenolysis, CN201210419541.9A, 2012.
- 103 R. Mane, A. Ghalwadkar, A. Hengne, Y. Suryawanshi, C. Rode, Role of Promoters in Copper Chromite Catalysts for Hydrogenolysis of Glycerol, *Catalysis Today*, 164 (2011) 447-450.
- 104 F. Meshkini, M. Taghizadeh, M. Bahmani, Investigating the Effect of Metal Oxide Additives on the Properties of Cu/ZnO/Al₂O₃ Catalysts in Methanol Synthesis from Syngas Using Factorial Experimental Design, *Fuel*, 89 (2010) 170-175.
- 105 A. Iriondo, V.L. Barrio, J.F. Cambra, P.L. Arias, M.B. Güemez, R.M. Navarro, M.C. Sánchez-Sánchez, J.L.G. Fierro, Hydrogen Production from Glycerol over Nickel Catalysts Supported on Al₂O₃ Modified by Mg, Zr, Ce or La, *Topics in Catalysis*, 49 (2008) 46.
- 106 J.S. Moura, J.d.S.L. Fonseca, N. Bion, F. Epron, T.d.F. Silva, C.G. Maciel, J.M. Assaf, M.d.C. Rangel, Effect of Lanthanum on the Properties of Copper, Cerium and Zirconium Catalysts for Preferential Oxidation of Carbon Monoxide, *Catalysis Today*, 228 (2014) 40-50.
- 107 A.K. Santra, J.J. Cowell, R.M. Lambert, Ultra-Selective Epoxidation of Styrene on Pure Cu{111} and the Effects of Cs Promotion, *Catalysis Letters*, 67 (2000) 87-91.
- 108 T. Rajkhowa, J.W. Thybaut, G.B. Marin, Assessment of the Dominant Factors in Cu Catalyst Deactivation in Glycerol Hydrogenolysis, *American Institute of Chemical Engineers Annual Meeting* Salt Lake city, 2015.
- 109 D. Durán-Martín, M.L. Granados, J.L.G. Fierro, C. Pinel, R. Mariscal, Deactivation of Cu₂N Catalysts Used in Glycerol Hydrogenolysis to Obtain 1,2-Propanediol, *Topics in Catalysis*, 60 (2017) 1062-1071.
- 110 Z. Huang, F. Cui, J. Xue, J. Zuo, J. Chen, C. Xia, Cu/SiO₂ Catalysts Prepared by Hom- and Heterogeneous Deposition-Precipitation Methods: Texture, Structure, and Catalytic Performance in the Hydrogenolysis of Glycerol to 1, 2-Propanediol, *Catalysis Today*, 183 (2012) 42-51.
- 111 J.A. Moulijn, A. Van Diepen, F. Kapteijn, Catalyst Deactivation: Is It Predictable?: What to Do?, *Applied Catalysis A: General*, 212 (2001) 3-16.
- 112 P. Carniti, A. Gervasini, V.H. Modica, N. Ravasio, Catalytic Selective Reduction of NO with Ethylene over a Series of Copper Catalysts on Amorphous Silicas, *Applied Catalysis B: Environmental*, 28 (2000) 175-185.
- 113 L. Chen, T. Horiuchi, T. Osaki, T. Mori, Catalytic Selective Reduction of NO with Propylene over Cu-Al₂O₃ Catalysts: Influence of Catalyst Preparation Method, *Applied Catalysis B: Environmental*, 23 (1999) 259-269.
- 114 M.L. Dieuzeide, R. de Uriiaga, M. Jobbagy, N. Amadeo, Vapor Phase Hydrogenolysis of Glycerol to 1,2-Propanediol at Atmospheric Pressure over Copper Catalysts Supported on Mesoporous Alumina, *Catalysis Today*, 296 (2017) 19-25.

- 115 J.Y. Kim, J.A. Rodriguez, J.C. Hanson, A.I. Frenkel, P.L. Lee, Reduction of Cu₂O and Cu₂O with H₂: H Embedding and Kinetic Effects in the Formation of Suboxides, *Journal of the American Chemical Society*, 125 (2003) 10684-10692.
- 116 J.A. Rodriguez, J.Y. Kim, J.C. Hanson, M. Pérez, A.I. Frenkel, Reduction of Cu₂O in H₂: In Situ Time-Resolved Xrd Studies, *Catalysis Letters*, 85 (2003) 247-254.
- 117 M.K. Neylon, C.L. Marshall, A.J. Kropf, In Situ Exafs Analysis of the Temperature-Programmed Reduction of Cu-Zsm-5, *Journal of the American Chemical Society*, 124 (2002) 5457-5465.
- 118 R. Beerthuis, J.W. de Rijk, J.M.S. Deeley, G.J. Sunley, K.P. de Jong, P.E. de Jongh, Particle Size Effects in Copper-Catalyzed Hydrogenation of Ethyl Acetate, *Journal of Catalysis*, 388 (2020) 30-37.
- 119 Z. He, H. Lin, P. He, Y. Yuan, Effect of Boric Oxide Doping on the Stability and Activity of a Cu–SiO₂ Catalyst for Vapor-Phase Hydrogenation of Dimethyl Oxalate to Ethylene Glycol, *Journal of Catalysis*, 277 (2011) 54-63.
- 120 J. Gong, H. Yue, Y. Zhao, S. Zhao, L. Zhao, J. Lv, S. Wang, X. Ma, Synthesis of Ethanol Via Syngas on Cu/SiO₂ Catalysts with Balanced Cu⁰–Cu⁺ Sites, *Journal of the American Chemical Society*, 134 (2012) 13922-13925.
- 121 Q. Wang, Z. Yu, J. Feng, P. Fornasiero, Y. He, D. Li, Insight into the Effect of Dual Active Cu⁰/Cu⁺ Sites in a Cu/Zn–Al₂O₃ Catalyst on 5-Hydroxymethylfurfural Hydrodeoxygenation, *ACS Sustainable Chemistry & Engineering*, 8 (2020) 15288-15298.
- 122 H. Yue, X. Ma, J. Gong, An Alternative Synthetic Approach for Efficient Catalytic Conversion of Syngas to Ethanol, *Accounts of Chemical Research*, 47 (2014) 1483-1492.
- 123 J. Shan, H. Liu, K. Lu, S. Zhu, J. Li, J. Wang, W. Fan, Identification of the Dehydration Active Sites in Glycerol Hydrogenolysis to 1,2-Propanediol over Cu/SiO₂ Catalysts, *Journal of Catalysis*, 383 (2020) 13-23.
- 124 R.B. Mane, A.M. Hengne, A.A. Ghalwadkar, S. Vijayanand, P.H. Mohite, H.S. Potdar, C.V. Rode, Cu: Al Nano Catalyst for Selective Hydrogenolysis of Glycerol to 1, 2-Propanediol, *Catalysis Letters*, 135 (2010) 141-147.
- 125 Z. Ma, Z. Xiao, J.A. van Bokhoven, C. Liang, A Non-Alkoxide Sol–Gel Route to Highly Active and Selective Cu–Cr Catalysts for Glycerol Conversion, *Journal of Materials Chemistry*, 20 (2010) 755-760.
- 126 Z. Xiao, X. Wang, J. Xiu, Y. Wang, C.T. Williams, C. Liang, Synergetic Effect between Cu⁰ and Cu⁺ in the Cu–Cr Catalysts for Hydrogenolysis of Glycerol, *Catalysis Today*, 234 (2014) 200-207.
- 127 C. Rode, A. Ghalwadkar, R. Mane, A. Hengne, S. Jadhkar, N. Biradar, Selective Hydrogenolysis of Glycerol to 1, 2-Propanediol: Comparison of Batch and Continuous Process Operations, *Organic Process Research & Development*, 14 (2010) 1385-1392.
- 128 O. Popa, N.E. Băbeanu, I. Popa, S. Niță, C.E. Dinu-Pârnu, Methods for Obtaining and Determination of Squalene from Natural Sources, *BioMed Research International*, 2015 (2015) 16.
- 129 D.P. Schwartz, Improved Method for Quantitating and Obtaining the Unsaponifiable Matter of Fats and Oils, *Journal of the American Oil Chemists Society*, 65 (1988) 246-251.
- 130 Food and Agriculture Organization of the United Nations, Codex Standards for Fats and Oils from Vegetable Sources, 2001.
- 131 W. Hamm, R.J. Hamilton, G. Calliauw, *Edible Oil Processing*, Wiley 2013.
- 132 The American Oil Chemists' Society, *Edible Oil Processing*, 2020.
- 133 R. Verhé, T. Verleyen, V. Van Hoed, W. De Greyt, Influence of Refining of Vegetable Oils on Minor Components, *Journal of oil palm research*, 18 (2006) 168-179.
- 134 T. Fornari, L. Vázquez, C.F. Torres, E. Ibáñez, F.J. Señoráns, G. Reglero, Countercurrent Supercritical Fluid Extraction of Different Lipid-Type Materials: Experimental and Thermodynamic Modeling, *The Journal of Supercritical Fluids*, 45 (2008) 206-212.
- 135 N.A. Akgün, Separation of Squalene from Olive Oil Deodorizer Distillate Using Supercritical Fluids, *European Journal of Lipid Science and Technology*, 113 (2011) 1558-1565.
- 136 P. Bondioli, C. Mariani, A. Lanzani, E. Fedeli, A. Muller, Squalene Recovery from Olive Oil Deodorizer Distillates, *Journal of the American Oil Chemists' Society*, 70 (1993) 763-766.
- 137 S. Gunawan, N.S. Kasim, Y.-H. Ju, Separation and Purification of Squalene from Soybean Oil Deodorizer Distillate, *Separation and Purification Technology*, 60 (2008) 128-135.

- 138 M.-P. St-Onge, P.J.H. Jones, Phytosterols and Human Lipid Metabolism: Efficacy, Safety, and Novel Foods, *Lipids*, 38 (2003) 367-375.
- 139 N.V. Kovganko, S.K. Ananich, The Chemical Synthesis of Sterols: Latest Advances, *Chemistry of Natural Compounds*, 35 (1999) 229-259.
- 140 D.P. Cappoen L., De Ras K., De Saegher D., Verminnen A., Bio-Olie: Een Milieuvriendelijke Basis Voor Cosmetica, (2017).
- 141 S. Ghosh, D.K. Bhattacharyya, Isolation of Tocopherol and Sterol Concentrate from Sunflower Oil Deodorizer Distillate, *Journal of the American Oil Chemists' Society*, 73 (1996) 1271-1274.
- 142 K.-M. LIN, S.S. KOSEOGLU, Separation of Sterols from Deodorizer Distillate by Crystallization, *Journal of Food Lipids*, 10 (2003) 107-127.
- 143 K. Gast, M. Jungfer, C. Saure, G. Brunner, Purification of Tocochromanols from Edible Oil, *The Journal of Supercritical Fluids*, 34 (2005) 17-25.
- 144 G. Block, L. Langseth, *Antioxidant Vitamins and Disease Prevention*, 1994.
- 145 C.D. Beck M., De Mulder E., De Vuyst C., Van Wettere B., Van Bio-Olie Tot Cosmetica, (2016).
- 146 M. Mendes, F. Pessoa, A. Uller, An Economic Evaluation Based on an Experimental Study of the Vitamin E Concentration Present in Deodorizer Distillate of Soybean Oil Using Supercritical Co₂, *The Journal of Supercritical Fluids*, 23 (2002) 257-265.
- 147 C.J. Chang, Y.-F. Chang, H.-z. Lee, J.-q. Lin, P.-W. Yang, Supercritical Carbon Dioxide Extraction of High-Value Substances from Soybean Oil Deodorizer Distillate, *Industrial & Engineering Chemistry Research*, 39 (2000) 4521-4525.
- 148 G.K. Nagesha, B. Manohar, K. Udaya Sankar, Enrichment of Tocopherols in Modified Soy Deodorizer Distillate Using Supercritical Carbon Dioxide Extraction, *European Food Research and Technology*, 217 (2003) 427-433.
- 149 C. Torres, G. Torrelo, G. Reglero, Extraction and Enzymatic Modification of Functional Lipids from Soybean Oil Deodorizer Distillate, 2011.
- 150 T. Fang, M. Goto, X. Wang, X. Ding, J. Geng, M. Sasaki, T. Hirose, Separation of Natural Tocopherols from Soybean Oil Byproduct with Supercritical Carbon Dioxide, *The Journal of Supercritical Fluids*, 40 (2007) 50-58.
- 151 C.F. Torres, T. Fornari, G. Torrelo, F.J. Señoráns, G. Reglero, Production of Phytosterol Esters from Soybean Oil Deodorizer Distillates, *European Journal of Lipid Science and Technology*, 111 (2009) 459-463.
- 152 S.K. De Schepper S., Gonry P., De Weirdt W., Benats H., Elst K., Servaes K., Tevernier S., Geuens J., Thybaut J., De Clercq J., Success - Supercritical Solutions for Side-Stream Valorisation, *Fisch-Icon Projectenbudget 2015*, (2015).
- 153 A. Santana, J. Maçaira, M.A. Larrayoz, Continuous Production of Biodiesel Using Supercritical Fluids: A Comparative Study between Methanol and Ethanol, *Fuel Processing Technology*, 102 (2012) 110-115.
- 154 Y. Xu, W. Du, D. Liu, J. Zeng, A Novel Enzymatic Route for Biodiesel Production from Renewable Oils in a Solvent-Free Medium, *Biotechnology Letters*, 25 (2003) 1239-1241.
- 155 T. Pinnarat, P.E. Savage, Assessment of Noncatalytic Biodiesel Synthesis Using Supercritical Reaction Conditions, *Industrial & Engineering Chemistry Research*, 47 (2008) 6801-6808.
- 156 R. Alenezi, G.A. Leeke, J.M. Winterbottom, R.C.D. Santos, A.R. Khan, Esterification Kinetics of Free Fatty Acids with Supercritical Methanol for Biodiesel Production, *Energy Conversion and Management*, 51 (2010) 1055-1059.
- 157 D. Kusdiana, S. Saka, Kinetics of Transesterification in Rapeseed Oil to Biodiesel Fuel as Treated in Supercritical Methanol, *Fuel*, 80 (2001) 693-698.
- 158 N. Deslandes, V. Bellenger, F. Jaffiol, J. Verdu, Solubility Parameter of a Polyester Composite Material, *Journal of Applied Polymer Science*, 69 (1998) 2663-2671.
- 159 L. Vázquez, C.F. Torres, T. Fornari, F.J. Señoráns, G. Reglero, Recovery of Squalene from Vegetable Oil Sources Using Countercurrent Supercritical Carbon Dioxide Extraction, *The Journal of Supercritical Fluids*, 40 (2007) 59-66.

CHAPTER 2.
MATERIALS AND METHODS

2.1 Design of supported Cu catalysts for glycerol hydrogenolysis

This section includes all the methods and procedures used for the synthesis, the characterization, the catalytic testing under intrinsic kinetics conditions for the liquid hydrogenolysis of glycerol towards 1,2-propanediol.

2.1.1 Material synthesis

In this section, the synthesis procedure of the Cu-based catalysts is described. There is a variety of procedures for the preparations, typically consisting out (of the sequence) of the following three steps. First, the metal precursors, such as metal oxides or metal salts (nitrates, carbonates,...) are mixed under stirring as such or dissolved in a solvent. In a more advanced synthesis, one may consider the addition of complexing agents or surfactants to control the structure of the precursors in the solution. The choice of the metal precursors, complexing agents or surfactants and solvent will affect the structure of the metal. Then, the solvent is removed by *e.g.* evaporation or filtration. Bulk removal is typically followed by a mild drying process. The 'final' material structure prior to loading in the reactor is achieved by calcination, in principle performed under air. In this step, the residual solvent, anionic compounds such as nitrates are removed by decomposition or combustion.

All of the materials in this thesis are labelled as $xM-yCu/support$, in which x and y are the corresponding wt.%, and were synthesized using sequential wet impregnation. As the main goal of the co-metal was inhibiting the sintering of the Cu-particles, the co-metal was impregnated first on the support. Through this, the support is 'modified' by being (partly) covered by this co-metal and the growth of Cu-particles can be inhibited. The procedure consisted out of two main steps, each consisting out of the three typical procedures steps.

(1) Impregnation of the co-metal on the support

- i. The support was suspended in 10 ml of distilled water per gram support. At the same time, the desired metal precursor was dissolved in 6.6 ml of distilled water per wt.% of the desired metal. The support and metal solutions were mixed and stirred at 500 rpm at room temperature for 2 h.
- ii. The water was evaporated at 363 K, after which the sample is further dried in air at 393 K for 1.5 h
- iii. The calcination was performed at 673 K, using a heating rate of 2 K min^{-1} in static air for 2 h.

(2) Impregnation of the Cu

- i. The x wt.% $M/support$ powder was suspended in 150 mL of demineralized water, mixed and stirred at 500 rpm for 2 h with the desired amount of copper, which was dissolved in 75 mL of demineralized water.
- ii. The same water removal treatment as in the first step was used.

- iii. The same thermal treatment as in the first step was performed.

For comparison, a bare 10 wt.% Cu/support catalyst is also prepared. The list of chemicals used is presented in Table 2.1.

Table 2.1. List of chemical precursors and supports used for the synthesis of the materials used in this work.

Chemical	Purity	Provider
$BaCO_3$	≥ 99 %	Sigma-Aldrich
$Ce(NO_3)_3 \cdot 6H_2O$	≥ 99 %	Sigma-Aldrich
Cs_2CO_3	≥ 99 %	Sigma-Aldrich
$Cu(NO_3)_2 \cdot 5/2H_2O$	≥ 99 %	Sigma-Aldrich
$La(NO_3)_3 \cdot 6H_2O$	≥ 99 %	Sigma-Aldrich
$\gamma-Al_2O_3$, Puralox SCCa-150/200	98 %	Sasol
1 wt.% SiO_2 – 99 wt.% $\gamma-Al_2O_3$, Siral 1		Sasol
40 wt.% SiO_2 – 60 wt.% $\gamma-Al_2O_3$, Siral 40		Sasol
SiO_2	≥ 99.5 %	Sigma-Aldrich

2.1.1.2 Catalyst characterization

This section describes all the procedures used for characterization of the synthesized catalysts. This includes ICP (section 2.1.2.1), N_2 -sorption (section 2.1.2.2), H_2 -TPR (section 2.1.2.3.1), N_2O -s-TPR (section 2.1.2.3.2), NH_3 -TPD (section 2.1.2.3.3), (*in situ*) XRD (section 2.1.2.4), S(T)EM-EDX (section 2.1.2.5), XPS (section 2.1.2.6) and TGA (section 2.1.2.7).

2.1.2.1 Elemental analysis

Quantitative chemical analysis of a solid material can be achieved by Inductive Coupled Plasma Optical Emission Spectrometry (ICP-OES). A plasma is created in which a solution containing the material is brought, resulting in excitation of the atoms and, hence, in characteristic emission radiation from the material when the excited atoms return to their ground state. The emission radiation causes distinct spectral lines at specific wavelengths, allowing the identification of the elements present in the analyzed material. The measured intensity of the spectral lines can be related, after calibration, to the weight percentage of the respective element in the material. Almost all elements can be determined by ICP-OES, with the exception of hydrogen, oxygen and fluorine.

The elemental analysis was performed using a Agilent 720-ES ICP-OES with axially-viewed plasma configuration and simultaneous CCD detection. Before the elemental analysis, the sample was prepared by dissolving 10 mg of dried and ground sample in concentrated aqua regia solution ($HNO_3:HCl$) (1:3, v:v). The solution was heated up to 383 K during 2 h in the autodigestor Vulcan 42 (Questron) and diluted up to 20 ml with ultrapure water before being analyzed by ICP-OES. Measurements were performed at the Unité de Catalyse et Chimie du Solide at Lille University.

2.1.2.2 Nitrogen sorption

The determination of the specific surface area and the pore structure of a porous catalyst is achieved by the adsorption of gas molecules. Typically, N_2 is selected because it does not interact chemically with the catalyst surface.

Nitrogen adsorption-desorption isotherms are obtained at 77 K by cooling with liquid nitrogen and represent the equilibrated specific volume of adsorbed N_2 as function of the relative pressure (p/p^0), where p^0 is the vapor pressure of N_2 . The IUPAC classification of adsorption isotherms, containing both the adsorption and desorption branch, are shown in Figure 2.1. Note that in type IV and V isotherms, hysteresis is observed. This means that at a certain relative pressure, the specific volume of the adsorbate is higher during desorption than during adsorption. This behavior is typical for capillary condensation in mesoporous structures.

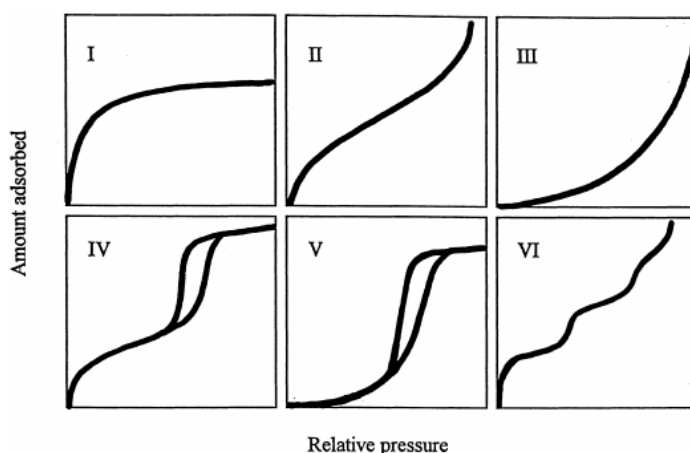


Figure 2.1. IUPAC classification of physisorption isotherms. Type I: microporous solids with small external surfaces. Type II: unrestricted monolayer-multilayer adsorption on a non-porous or macroporous material with strong adsorbate-adsorbent interactions. Type III: non-porous or macroporous material with weak adsorbate-adsorbent interaction behavior. Type IV: mesoporous material with strong adsorbate-adsorbent interactions and capillary condensation. Type V: multilayer adsorption on a mesoporous material with weak adsorbate-adsorbent interactions and capillary condensation. Type VI: multilayer adsorption on a uniform non-porous adsorbent

N_2 -adsorption/desorption experiments, at 77 K, were performed using a Tristar II 3020 Micrometrics apparatus for textural analysis. Each measurement was preceded by sample degassing at 473 K for 2 h to eliminate adsorbates such as H_2O and CO_2 . The specific surface area was determined using the Brunauer-Emmet-Teller method^{1,2} by the classical five-point method ($0.05 < p/p^0 < 0.35$). The Barrett-Joyner-Halenda method² was used to calculate the specific pore volume and mean pore size from the desorption isotherm.

2.1.2.3 Temperature-programmed techniques

Temperature-programmed techniques are often used in heterogeneous catalysis to assess the (chemical) interaction between a gas and a solid surface. After a pre-treatment, a gas mixture is sent over the sample

applying a linear temperature ramp under a specific atmosphere in near-ambient pressure. Temperature-Programmed Reduction (TPR) uses a reductive gas to examine the surface chemistry of the metals oxides. Temperature-Programmed Desorption (TPD) determines the total number of sites which respond to a particular probe molecule under certain conditions and thus provides information on the distribution of strengths of these sites.

The gas composition is monitored by means of a Thermal Conductivity Detector (TCD). The TCD monitors the difference in thermal conductivity between the feed and product flow. When the reduction of the metal oxides (in case of a TPR) or the adsorption of probe molecule (in case of a TPD) takes place, the gas composition of the product flow will change and a difference of the thermal conductivity between the feed and the product will be detected by the TCD. All temperature-programmed interactions were carried out in an Autochem II 2920, shown in Figure 2.2.

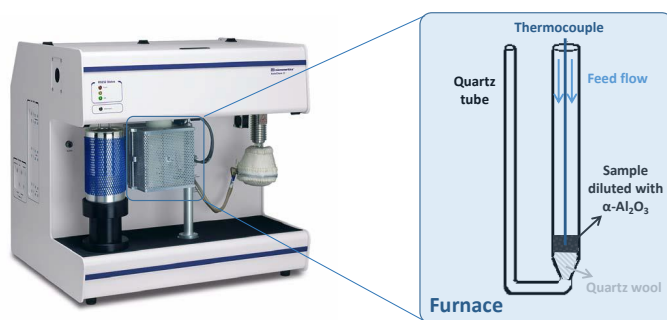


Figure 2.2. The temperature programmed reactions setup, Micromeritics Autochem II 2920, with a schematic representation of the reactor and furnace. Reproduced from Buekens⁵.

2.1.2.3.1 H_2 -TPR

Temperature-programmed reduction (TPR) is a technique to determine the most efficient reduction conditions. The calcined catalyst, in an oxidized form, is submitted to a temperature rise while a reducing mixture of H_2 -Ar is flowed over it. The U-tube reactor was filled with approximately 0.1 g of catalyst and diluted with 0.9 g inert material to ensure isothermicity. The procedure consisted out of three steps, as indicated in Figure 2.3:

- (1) During the pretreatment, $50 \text{ cm}^3 \text{ min}^{-1}$ He-gas was sent over the catalyst, while the temperature was increased to 473 K at a rate of 90 K min^{-1} to remove the physisorbed adsorbates from the catalyst. After 5 min at 473 K, the catalyst was cooled down to 383 K, at a rate of 90 K min^{-1} .
- (2) After waiting for 20 min at 383 K, the gas flow was switched to 10 vol.% H_2 -Ar (Air Liquide), followed by a 5 min stabilization time.
- (3) Next, $60 \text{ cm}^3 \text{ min}^{-1}$ of this reducing mixture was sent over the catalyst, while submitting it to a temperature increase to 723 K at 8 K min^{-1} . This temperature is maintained for 30 min. During the heating, the copper oxides present on the catalyst were reduced by H_2 and changes in the H_2

concentration in the gas result in a difference in its thermal conductivity. The temperature at which the reduction takes place is indicative for the species which is being reduced. After the procedure, the sample was cooled down to 298 K, at a rate of 90 K min⁻¹.

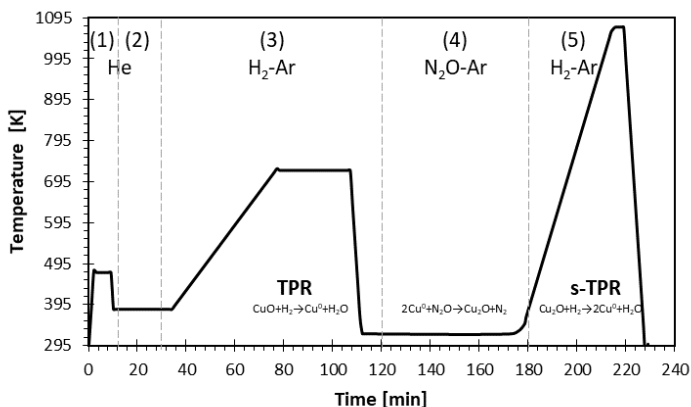


Figure 2.3. Temperature and gas profile for the H₂-TPR and N₂O-sTPR procedure applied on the catalysts.

Based on the TPR-profile, it is possible to calculate the percentage of the Cu oxides that are reduced, according to equation (2.1). The degree of reduction is defined as the ratio of the reduced amount of Cu to the total amount of Cu in the sample. The numerator was calculated from the amount of H₂ consumed in the TPR analysis, *i.e.* $n_{H_2\text{consumed}}$ [mol g⁻¹_{cat}], assuming the reduction of CuO to Cu⁰. The denominator was calculated taking the real Cu content, *wt.* %_{Cu} determined by ICP-OES [g_{cu} g_{cat}], into account in the sample with mass m_{sample} [g_{cat}].

$$\text{degree of reduction [\%]} = \frac{n_{H_2\text{ consumed in TPR}}}{m_{\text{sample}} \text{wt. \%}_{Cu} MM_{Cu}} 100\% \quad (2.1)$$

2.1.2.3.2 N₂O s-TPR

To be able to express the catalyst performance in terms of Turn Over Frequency (TOF, equation (2.15) in section 2.1.3.1.4), it is essential to have a reliable method for the determination of the Cu dispersion, D_{Cu} , and the related parameters such as specific Cu surface area, MSA_{Cu} , and the average diameter of the Cu aggregates, ϕ_{Cu} . Typically, H₂ or CO chemisorption experiments are performed to determine the dispersion of the catalyst.^{4, 5} However, the existence of weak reversible chemisorption and uncertain adsorption stoichiometry associated with these probe molecules, renders them unsuitable for Cu-based catalysts.

N₂O as a probe molecule has been used most frequently for investigating Cu-based catalysts.⁶⁻⁸ The procedure with N₂O is based on that reported by Gervasini et al.⁹ This method is used to determine the D_{Cu} , and MSA_{Cu} with qualitative and quantitative information by a successive analysis of H₂-TPR, a surface oxidation by N₂O and another H₂-TPR of the freshly oxidized Cu surface (defined as s-TPR).

Through the s-TPR, it is possible to distinguish between surface Cu species and bulk Cu. The first three steps are equal to that of a normal H₂-TPR procedure, as shown in Figure 2.3. Next, a constant flow of 1 % N₂O-Ar gas (Air Liquide) was sent over the catalyst at 323 K for 1 h, during which surface Cu⁰ species react with N₂O and form Cu⁺. In the last step, a 10 % H₂-Ar gas at a flow rate of 60 cm³ min⁻¹ was sent over the catalyst at 1073 K (ramp: 20 K min⁻¹) thereby reducing Cu⁺ species to Cu⁰. The TCD analysis was used to calculate the amount of consumed H₂.

The Cu dispersion, D_{Cu} , was defined as the ratio of the Cu exposed at the surface to the total amount of Cu in the sample. The numerator was calculated from the amount of H₂ consumed in the s-TPR analysis, assuming the reduction of Cu₂O to Cu⁰.

$$D_{Cu} = \frac{1}{2} \frac{n_{H_2 \text{ consumed in s-TPR}}}{m_{\text{sample wt. \%Cu}} MM_{Cu}} 100\% \quad (2.2)$$

The specific Cu surface area, MSA_{Cu} [m² g⁻¹_{Cu}], is a measure for the number of active sites on the catalyst. It is calculated based on (2.3), in which n_{H_2} is the experimentally consumed moles of H₂ [μmol g⁻¹_{cat}], SF is the assumed stoichiometric factor of the reduction reaction ratio (2 mol_{Cu} mol⁻¹_{H₂}), N_A is the Avogadro's number, C_M is the average number of Cu atoms per area, assuming equally exposed (100), (110) and (111) planes, *i.e.* 1.47 10¹⁹ atoms_{Cu} m⁻² and the Cu content (wt.%_{Cu}).

$$MSA_{Cu} = \frac{n_{H_2} N_A SF}{10^4 C_M \text{wt. \%Cu}} \quad (2.3)$$

The average diameter of the Cu aggregates, ϕ_{Cu} [nm], is correlated with the MSA and calculated *via* (2.4), where SK is a constant representing the available surface area of a particle (5) and ρ_{Cu} the density of Cu (8.92 g cm⁻³)

$$\phi_{Cu} = \frac{10^3 SK}{MSA_{Cu} \rho_{Cu}} \quad (2.4)$$

2.1.2.3.3 NH₃-TPD

For the determination of acidic sites, ammonia (NH₃) was used as a probe molecule during a TPD. For the measurement of the total number of acid sites, *ca.* 0.2 g of sample, diluted with 0.8 g of inert material, was analyzed. The TPD procedure is shown in Figure 2.4. First, the sample was heated in an inert atmosphere (Ar, 25 cm³ min⁻¹) up to 473 K at a heating rate of 90 K min⁻¹. After 5 min, the temperature was decreased to 383 K at a cooling rate of 90 K min⁻¹ and kept at that temperature for 20 min. In step 3, the catalyst was then reduced at 473 K (ramp: 8 K min⁻¹) for 15 min. After the reduction the temperature was decreased to 423 K (ramp: 90 K min⁻¹) and then the gas flow was switched to 4 vol.% NH₃-He with a flow rate of 15 cm³ min⁻¹ (step 4). After 30 min, the gas was switched to Ar (25 cm³ min⁻¹) to remove the physisorbed NH₃. Finally, the temperature was increased to 873 K at a heating rate of 10 K min⁻¹. The amount of desorbed NH₃ was detected by a TCD. The higher the

temperature at which ammonia desorbs, the stronger the acid site it was adsorbed to. Based on the integration of the TPD-profile, it was possible to calculate the total amount of acid sites.

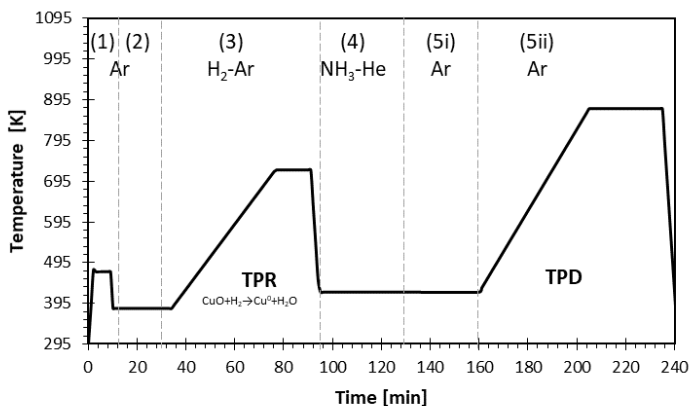


Figure 2.4. Temperature and gas profile for the NH_3 -TPD procedure applied on the catalysts.

For the uncalcined support (Figure 2.5A), two peaks can easily be distinguished, while the profile of the calcined support indicated the presence of three kinds of acid sites (Figure 2.5B). Therefore, it was chosen to use three peaks for the fitting of all profiles, corresponding to weak, moderate and strong acid sites. The first peak, α , around 500 K could be attributed to weak acid sites, while the γ peak (above 740 K) was associated with strong acid sites, which is a combination of both strong Lewis and strong Brønsted sites^{10, 11}. The support exhibited also moderate acid sites, situated as a β peak between 550 K and 660 K. The total acid site concentration, which is considered to correspond with the amount of desorbed NH_3 , decreased from $88 \mu\text{mol g}^{-1}$ to $50 \mu\text{mol g}^{-1}$ by calcination. The support consists of a combination of Al_2O_3 , with strong Al-O bonds, and hydrated Al_2O_3 , with surface O-H bonds. The weaker O-H bonds have a higher Brønsted acidity, as they have the ability to transfer their proton to other species/molecules.¹² During the calcination, the removal of some of these surface O-H resulted in a decreased amount of strong acid sites, simultaneously creating tetrahedral Al^{3+} lattice sites, which acted as weak-moderate Lewis acids.^{12, 13}

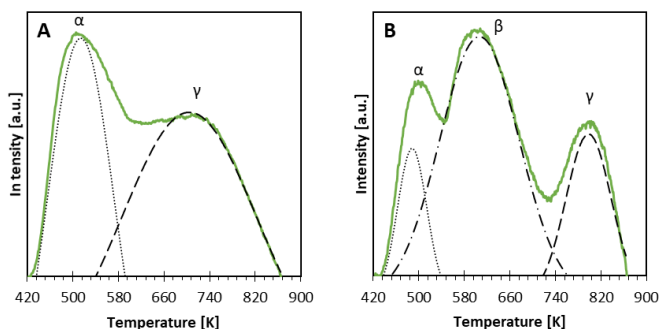


Figure 2.5. NH_3 -TPD profile (full line) of (A) the uncalcined and (B) the calcined $\gamma\text{-Al}_2\text{O}_3$ support with weak (dotted line), moderate (dashed-dot line) and strong acid sites (dashed line).

2.1.2.4 (in situ) X-ray diffraction

X-ray diffraction is a nondestructive technique for the characterization of the crystallographic properties of a material, such as structures, phases, crystal orientation, average grain crystal size. As crystals are formed by a periodic array of atoms, diffraction occurs as a result of the interaction of the photons with the electrons of the material, when an X-ray is sent through the material. The irradiation with X-rays causes a constructive and destructive interference, generating a unique diffraction pattern, referred to as Bragg diffraction peaks. The peak width of the material increases with decreasing crystallinity. An amorphous sample shows a broad diffraction peak (Figure 2.6A), while a crystallite reveals well-defined peaks at specific scattering angles (Figure 2.6B). A schematic illustration of Bragg's diffraction is shown in Figure 2.6C.

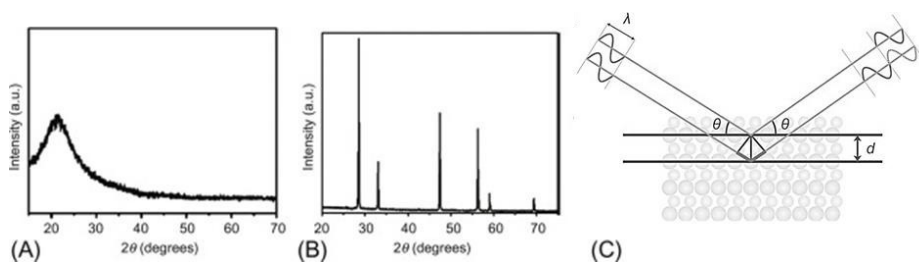


Figure 2.6. XRD patterns of an amorphous (A) and a crystalline (B) material and (C) schematic representation of reflections from adjacent planes within the crystal. Reproduced from Lamas et al.¹⁴ Copyright © 2017 William Andrew Publishing.

Scherrer postulated the dependence between the peak width and the crystallite size based on (2.5). In this relation, the average crystallite size d_{XRD} is related to an instrument constant K , the X-ray wavelength λ , the full peak width at half-maximum Γ , the instrumental width b and diffraction angle θ . The instrumental width of the apparatus was determined based on a reference measurement using LaB_6 crystals.

$$d_{XRD} = \frac{K\lambda}{(\Gamma - b)\cos(\theta)} \quad (2.5)$$

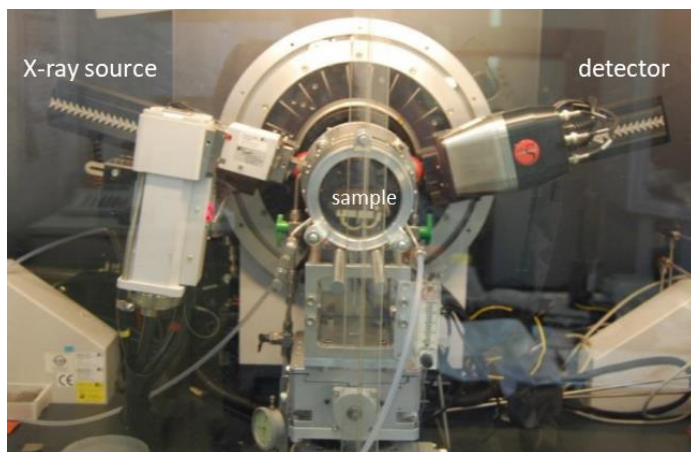


Figure 2.7. Overview of the *in situ* X-ray diffraction setup with the reactor chamber wall.

To identify the crystalline phases of the fresh and *in situ* reduced samples, powder X-ray diffraction was performed using a Siemens Diffractometer Kristalloflex D5000 (XRD) or a Bruker D8-AXS Discover setup (XRD) and a linear Vantec detector (*in situ* XRD), and a $\text{CuK}\alpha$ X-ray source ($\lambda = 0.154$ nm) under continuous scan mode. For the measurements, *ca.* 10 mg of the catalyst was evenly spread on a Si-wafer. For the reduced samples, the chamber was evacuated to 4 Pa and flushed with He. A temperature ramp of 10 K min^{-1} was applied to 723 K with 5 % H_2 - 95 % He at 1.1 NmL s^{-1} .

2.1.2.5 Electron microscopy

The surface is analyzed by Scanning Electron Microscopy (SEM) with Energy Dispersive X-ray spectroscopy (EDX). An electron beam is sent to a sample, resulting in various scattering processes (Figure 2.8).

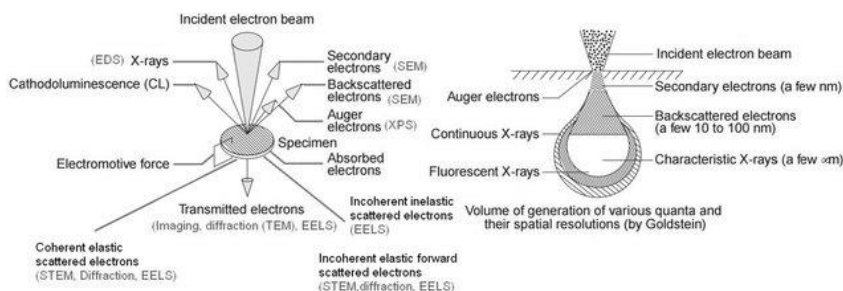


Figure 2.8. Overview of scattering processes occurring due to interaction between an electron beam and a specimen. Reprinted from Tozman.¹⁵

In (S)TEM, the transmitted electrons are measured. When the probe electrons are transmitted, a so-called bright-field (S)TEM image is formed. The backscattered and secondary electrons form the so-called dark-field (S)TEM image. Based on the (S)TEM images, nanoscale morphological information is obtained.

Energy dispersive X-ray spectrometry (EDX) is used for local chemical analysis. This technique relies on the interaction between the probe electron and the specimen. When an excited electron returns to its original shell, characteristic X-rays are emitted. These X-rays contain information on the elemental composition of the sample. The combination EDXS with S(T)EM, results in a localized composition of the sample.

A JEOL JEM-2200FS, Cs-corrected microscope operated at 200 kV, which was equipped with a Schottky-type field-emission gun (FEG) and EDX JEOL JED-2300D, was used. Specimen preparation consisted of immersing a lacey carbon film supported on a Ni grid into the sample powder.

2.1.2.6 X-ray photoelectron spectroscopy

X-ray photoelectron spectroscopy (XPS) is a technique for analyzing the surface chemistry of a material. XPS can measure elemental composition, chemical and electronic state of elements with a material. XPS spectra are obtained by irradiating a solid surface with a beam of X-rays while simultaneously measuring the kinetic energy of electrons that are emitted from the top 1-10 nm of the material being analyzed (Figure 2.8). A photoelectron spectrum is recorded by counting ejected electrons over a range of electron kinetic energies.

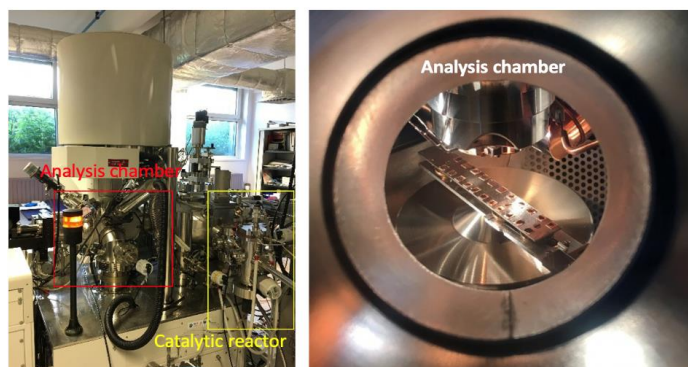


Figure 2.9. XPS equipment: analysis chamber which is coupled to the catalytic reactor where the samples can be treated with reactive gases up to 1173 K and then transferred under vacuum towards XPS for the analysis.

The composition and oxidation state of the elements present on the catalysts surface were determined using XPS. The XPS spectra were recorded at a residual pressure of 10^{-9} mbar on a Kratos Axis UltraDLD electron energy spectrometer operating with a monochromatic Al-K α (1486.6 eV), which is shown in Figure 2.9. The pass energy of the hemispherical analyzer was set at 160 eV for the wide scan

and 40 eV for narrow scans. In the latter conditions, the Full Width at Half Maximum (FWHM) of the Ag 3d_{5/2} peak of a standard silver sample was about 0.9 eV. Charge stabilization was achieved by using the Kratos Axis device. Peak deconvolution was performed using curves with a 70 % Gaussian type and a 30 % Lorentzian type and a Shirley nonlinear sigmoid-type baseline. The following peaks are used for the quantitative analysis: O 1s, C 1s, La 3d, Cu 2p, Cu LMM Auger peak, Al 2p, Si 2p. Molar fractions are calculated using peak areas normalized on the basis of acquisition parameters after a Shirley background subtraction and corrected with experimental sensitivity factors and transmission factors provided by the manufacturer. The Binding Energy (BE) scale was calibrated by measuring the C 1s peak (BE = 284.8 eV) from the surface contamination and the accuracy of the measurement was ± 0.1 eV. Differential surface charging of the samples is ruled out by checking the reproducibility of XPS spectra in repeated scans under different X-ray exposures. Software CasaXPS was used for the analysis of XPS spectra, separating elemental species in different oxidation states, and calculating relative concentrations of chemical elements. For the fitting of the data, the following peak positions were used (Table 2.2). For the fitting of the Cu-species, standard were used (Table 2.3).

Table 2.2. Peak positions for applied in the fitting

	BE [eV]
O 1s OH	531.7
O 1s OH	530.7
C 1s C-H	284.9
C 1s C-C	286.9
C 1s C=O	289.1
La 3d	835.6
La 3d	838.5
Al 2p Al-O	74.5
Al 2p Al-OH	76.8
Cu 2p Cu ₂ O+Cu ⁰	932.5
Cu 2p CuO	933.5
Cu 2p satellite	941.1
Cu 2p satellite	943.7
Si 2p	102.1

Table 2.3. Fitting parameters of the Cu standards.

	BE [eV]	FWHM [eV]	KE _{max} [eV]
CuO (2p _{3/2})	933.51	3.0	918.10
Cu ₂ O	932.49	0.9	916.54
Cu ⁰	932.67	0.9	918.64

2.1.2.7 Thermogravimetric Analysis

During a thermogravimetric analysis (TGA) a sample is continuously weighted while heating under a flowing gas. The measured weight loss provides information on changes in sample composition (desorption of components), thermal stability (breaking of chemical bonds) or kinetic parameters (when a reducing atmosphere is used).

The TGA was performed using a Netzsch Jupiter STA 449 F3 apparatus. Approximately 20 mg spent catalyst sample, without any washing or drying step, was loaded in an alumina crucible. The material was heated at 10 K min^{-1} in air (100 mL min^{-1}).

2.1.3 Catalytic testing

The stability and activity of the synthesized catalysts for glycerol hydrogenolysis were screened using a packed-bed reactor operating in a trickle-flow regime. The High-Throughput Kinetic setup for Mechanistic Investigation was used to obtain reliable data (see section 2.1.3.1). As it is intended to focus on the chemical reaction not altered by transport phenomena, the experiments were performed under intrinsic kinetics conditions, which are determined in section 2.1.3.1.5. It is important to know the intrinsic kinetics to avoid problems when scaling up from lab to industrial scale.

2.1.3.1 High-Throughput Kinetic setup for Mechanic Investigation

The glycerol hydrogenolysis experimentation is performed on the High-Throughput Kinetic setup for Mechanic Investigation (HTK-MI), shown in Figure 2.10, constructed by Zeton B.V., available within the Laboratory for Chemical Technology.



Figure 2.10. HTK-MI setup. (a) front view, (b) liquid pump section, (c) gas feed section, (d) reaction section and (e) liquid waste collection. Reproduced from van der Brogt et al.¹⁶, under the Creative Common Attribution 4.0 International License.

The setup comprises eight plug flow reactors, grouped pair-wise in separate furnaces. One can distinguish three main sections: the feed section, the reactor section and the effluent and analysis section. There are both manual and pneumatic valves present in the setup. The pneumatic valves are controlled with a LabVIEW control program. With this software it is possible to control the flow rates in the feed section, the temperature and pressure of the reactor. In the next paragraphs, these three most essential sections for experiments are discussed in detail: the feed section (see section 2.1.3.1.1), the reaction section (see section 2.1.3.1.1) and the analysis section (see section 2.1.3.1.3).

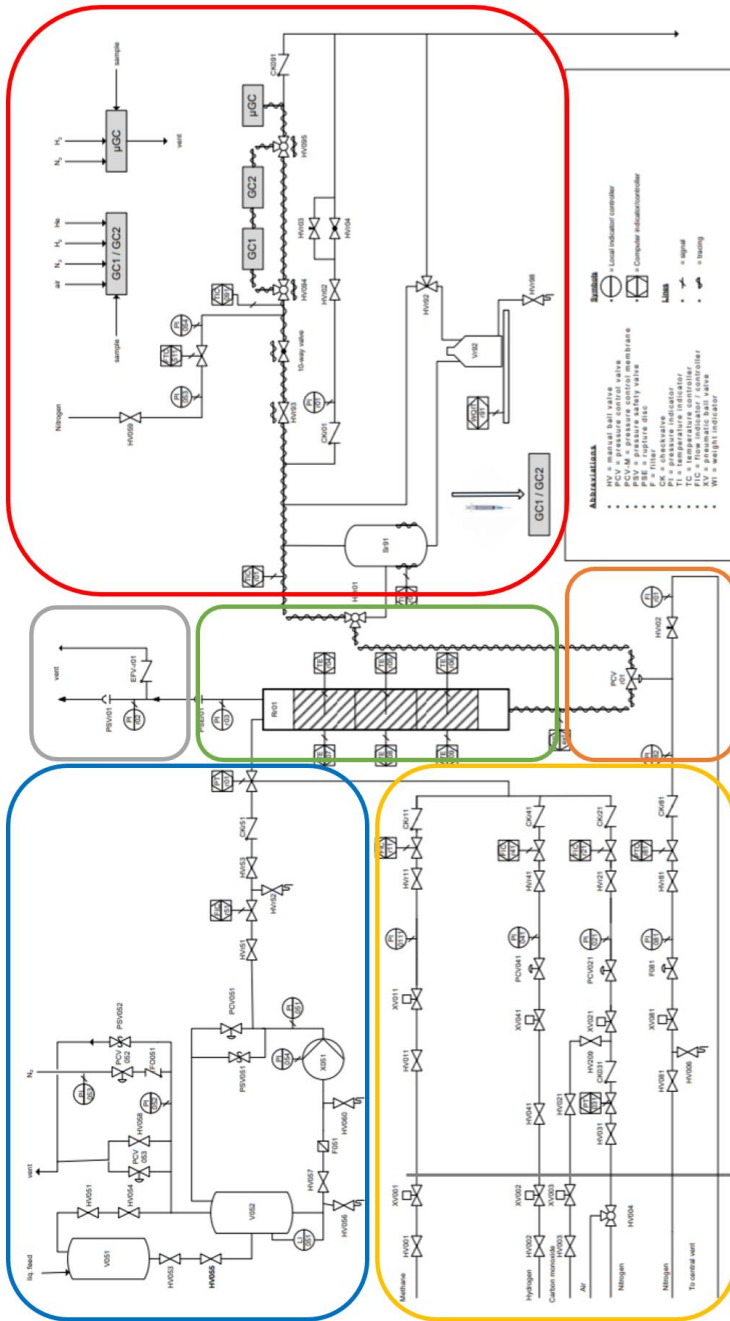


Figure 2.11. Flow diagram of one reactor in the HTK-MI: the liquid feed section (blue), the gas feed section (yellow), the reaction section (green), the reactor overpressure safety system (grey), the reactor back pressure section (orange) and an analysis section (red).

2.1.3.1.1 Feed section

The feed section contains a liquid feed and several gas feeds, which can be sent at different flow rates to the reactor. In the hydrogenolysis experiments, the liquid feed consists of the pure reactant (glycerol), while the gas feed consists of hydrogen and nitrogen. Pure glycerol was used as reactant as previous research¹⁷ showed severe deactivation of the catalyst by the impurities present in crude glycerol. The nitrogen was only used during the reduction of the catalyst and to reach the reaction pressure. During the reaction, pure hydrogen was used as gas feed. The experimental procedure is discussed in more detail in section 2.1.3.1.5.

The liquid feed is supplied from a glass vessel *via* a piston-pump. The gaseous feed is supplied from gas cylinders. The hydrogen cylinder is installed in a safety cabinet and equipped with its own safety device. For each of the gases, a pneumatic valve is present which closes in cases of emergency shutdown. After this valve, the gas flow is sent to the corresponding thermal mass flow controller (Bronkhorst®), the range of which is expressed in normal liters per hour (NI h⁻¹). The controllers are available in three different ranges: 0.2 – 10 NI h⁻¹ (type 1), 2 – 100 NI h⁻¹ (type 2), and 20 – 1000 NI h⁻¹ (type 3).

All of the controllers are calibrated for a reference component, *i.e.* N₂. When using a different gas than the reference one, a correction factor has to be taken into account due to the difference in heat capacity and molar mass, in order to define the setup value for the LabVIEW interface. The flow rate that has to be set to F_0^k , is determined *via* equation (2.6), with α the correction factor, F_0^{ref} the flow rate set in the LabVIEW interface, F_0^k the feed flow rate of the actual component fed to the reactor. The correction factor can be calculated with the web application Fluidat® or be determined experimentally.

$$F_0^k = \alpha F_0^{ref} \quad (2.6)$$

Before entering the reactor, the liquid feed is mixed with the gas feed after passing a check valve which prevents backflow from the reactor.

2.1.3.1.2 Reaction section

Each reactor in the HTK-MI is a tube made of AISI 316 cold worked steel with an inner diameter of 1.9 mm and a height of 89 cm, which allows pressures up to 20.5 MPa and temperatures up to 922 K. The reactor tube is paired with a second reactor and placed in a single reactor block. For each block, the temperature and pressure can be controlled. The gas and liquid flow rates of each reactor in a block can be controlled individually.

Per block, the temperature is controlled at three points along the reactor length with two N-type thermocouples (o.d. 3 mm). One thermocouple is placed at the outer wall of the tube, while the other is placed in the catalyst bed. The choice of control (inside the catalyst bed or at the wall) can be specified in the LabVIEW interface. For measuring intrinsic kinetics, it is more interesting to use the one inside

the catalyst bed. However, a better temperature control is obtained by the one at the reactor wall due to the reduction in response time in the control system.

The catalyst is a fine powder and, hence, it should be pelletized into particles of a larger diameter to prevent it from being blown out of the reactor by the gas flow. The diameter of the pellets is determined by correlations to avoid transport limitations (for more details see Supporting Information), and is in the range of 630 to 710 μm . The catalyst bed should be placed in the isothermal area of the reactor to ensure preheating and mixing of the feed. Inert material is used to place the catalyst at the desired position. The employed inert material is α -alumina which is available in different ranges: 0.5-1.5 mm, 1.5-2.5 mm and 2.5-3.5 mm. The largest particles, with diameters between 2.5 and 3.5 mm, are placed at the bottom of the reactor to prevent entrainment of the smaller inert particles by the feed, which is flowing co-currently from the top of the to the bottom of the reactor. The reactor is filled up to ca. 40% of the length by the middle-sized (1.5-2.5 mm) particles. On top of them, the small-size particles are used to place the catalyst in the middle of the reactor. Then, the catalyst bed itself is added. The catalyst bed consists of catalyst pellets with dilution material, as discussed in 2.1.3.1. The amount of dilution is determined to minimize the temperature gradient (Appendix A). On top of the catalyst bed, inert material, with particles between 1.5 and 2.5 mm, is placed to ensure a good mixing of the feed and a plug flow over the catalyst bed.

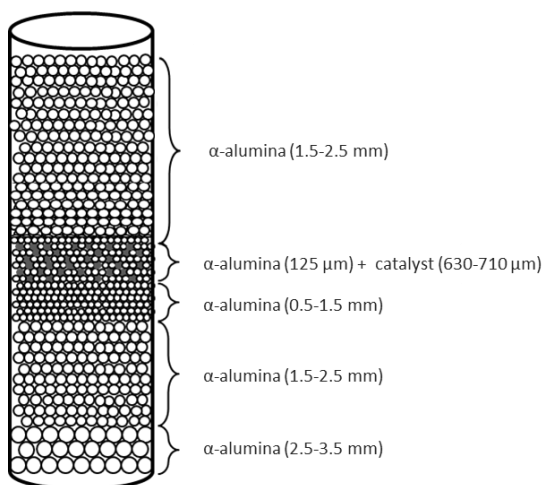


Figure 2.12. Schematic overview of the reactor filling

The pressure in the reactor is controlled by a back pressure regulator. The reactor effluent, consisting of gas and liquid, passes through one side of the pressure control valve, while nitrogen is sent to the other side of the membrane. When the pressure at the reactor side is slightly higher than the back pressure, the reactor effluent will flow towards the analysis section. When that is not the case, the membrane remains closed, causing the pressure to increase till it reaches the desired pressure. As a

result, the flow rate through such a back pressure regulator inherently exhibits fluctuations which are, however, practically negligible with the typical flow rates used in this work.

2.1.3.1.3 Analysis section

The reactor effluent is separated in a flash drum at temperatures of maximum 313 K and atmospheric pressure. The unreacted H₂ is sent to the vent. The liquid phase can be sampled for analysis and subsequently sent to the liquid storage tanks. The liquid samples are diluted with an internal standard, a mixture of 96 wt.% butanol and 4 wt.% 1,4-butanediol, before being introduced into the gas chromatograph (GC).

The analysis is performed with a FID-equipped GC (Agilent Technologies 6850 series II network GC system), loaded with a highly polar capillary column (Agilent CP-Wax 57 CB glycols column, 25 m x 0.25 mm i.d. x 0.2 µm poly-ethylene glycol). The Flame Ionization Detector (FID) detects the ions that are formed by combustion of these compounds in a hydrogen flame. The quantity of these ions is proportional to the concentration of the different compounds in the mixture. The used GC settings are listed in Table 2.4. Since the FID has different sensitivity dependent on the compound, a calibration factor has to be used to obtain quantitative results.

Table 2.4. Settings for the GC inlet, column and FID.

<i>Parameter</i>	<i>Set-point</i>
<i>Inlet</i>	
<i>Temperature [K]</i>	543
<i>Pressure [kPa]</i>	108
<i>He flow rate [mL min⁻¹]</i>	111.5
<i>Split ratio [-]</i>	60:1
<i>Column</i>	
<i>Pressure [kPa]</i>	108
<i>He flow rate [mL min⁻¹]</i>	1.8
<i>FID</i>	
<i>Temperature [K]</i>	573
<i>H₂ flow rate [mL min⁻¹]</i>	35
<i>Air flow rate [mL min⁻¹]</i>	350

In order to perfectly differentiate between the components in the reactor effluent *via* analysis of retention times, a specific temperature program is applied. The GC-oven is first heated from 313 K to 343 K at a rate of 5 K min⁻¹. After that, the heating rate is increased to 15 K min⁻¹ until 383 K is reached. This temperature is kept for 3 min. As a last step, the temperature is increased from 383 K to 453 K at a rate of 10 K min⁻¹. This temperature is again kept constant for 3 min. In Table 2.5 the retention times,

corresponding to the mentioned temperature program are listed for the products with their calibration factors.

Table 2.5. The retention time of the compounds for the applied GC procedure and its calibration factors

Compound	Retention time [min]	Molar calibration factor [-]
methanol	2.07	4.55
2-propanol	2.30	1.89
ethanol	2.34	2.17
1-propanol	2.39	1.67
butanol	5.41	1.52
acetol	7.52	2.49
propionic acid	11.20	2.50
1,2-propanediol	12.37	1.53
1,2-ethanediol	12.96	2.60
1,3-propanediol	15.40	1.60
1,4-butanediol	17.21	1.00
glycerol	21.04	1.68

2.1.3.1.4 Data treatment

Space time and weight hourly space velocity

Apart from the temperature and pressure, also the space time determines the observed performances. The space time τ'' represents the ratio between the catalyst mass W [kg_{cat}] and the molar inlet flow rate of the feed F_0 [$\text{mol}_{\text{feed}} \text{s}^{-1}$] and, hence, has as units $\text{kg}_{\text{cat}} \text{s mol}^{-1}_{\text{feed}}$. It quantifies the time that an average molecule has for reaction:

$$\tau'' = \frac{W}{F_0} \quad (2.7)$$

Industrially, the weight hourly space velocity (WHSV) is more frequently used. The *WHSV* is defined as the mass inlet flow rate of the feed F_0^{wt} [$\text{kg}_{\text{feed}} \text{s}^{-1}$] divided by the catalyst mass W [kg_{cat}] in the reactor.

$$\text{WHSV} = \frac{F_0^{\text{wt}}}{W} \quad (2.8)$$

Determination of the outlet composition

For glycerol hydrogenolysis experiments, an optimized GC method was developed which leads to a quantitative separation of the different components without being too time-consuming. To translate the chromatograms into mixture compositions, the calibration factors for different components must be known. The calibration factors were determined experimentally and are listed in Table 2.5. Using these calibration factors, CF_i , the relative molar composition of the reactor effluent can be calculated *via* equation (2.9), in which A_i is the area of peak i obtained from raw GC data.

$$x_i = \frac{A_i C F_i}{\sum_{j=1}^n A_j C F_j} \quad (2.9)$$

The composition of the liquid reactor effluent is determined using an external standard (ES), *i.e.* 1,4-butanediol. The reactor effluent was diluted with a solution of 4 wt.% 1,4-butanediol in a solvent, *i.e.* butanol. The molar flow rate of every component F_i [mol s⁻¹] can be calculated when the molar fraction of the component x_i and the total molar flow rate F_{tot} [mol s⁻¹] are known.

$$F_i = x_i F_{tot} = x_i \frac{F_{ES,0}}{x_{ES}} \quad (2.10)$$

The gaseous reactor effluent consisted mainly of hydrogen and had a negligible contribution to the carbon balance. The mass balance was verified *via* electronic weighing of the feed as well as the effluent recipient. During the experiments the total mass outlet flow rate is calculated based on a 90-95 % mass balance closure. The normalization method was applied to calculate the outlet flow rates, to be used for further data assessment.¹⁶

The mean molecular mass of the liquid can be calculated *via* equation (2.11), where MM_j is the molar mass of component j [g mol⁻¹].

$$MM_m = \sum_{j=1}^n x_j MM_j \quad (2.11)$$

Based on the total mass outlet flow rate of the liquid product \dot{m} , the normalized molar outlet flow rate of component i , $F_{i,norm}$, is determined *via* the mean molecular mass of the liquid, respectively MM_m .

$$F_{i,norm} = x_i \frac{\dot{m}}{MM_m} \quad (2.12)$$

Calculation of the catalytic performance parameters

To investigate and compare the catalytic performances, the conversion of glycerol, the selectivity of glycerol towards product i and the yield of a certain product i are calculated.

The conversion of glycerol, X_G , is calculated in (2.13) *via* the molar inlet flow rate $F_{G,0}$ [mol s⁻¹] and molar outlet flow rate F_G [mol s⁻¹].

$$X_G = \frac{F_{G,0} - F_G}{F_{G,0}} \quad (2.13)$$

The selectivity for a component i was carbon-based and determined according to equation (2.14), with $a_{c,G}$ the number of carbon atoms in glycerol, F_i the molar outlet flow rates of a component i (mol s⁻¹) respectively.

$$S_{i,G} = \frac{a_{C,i}F_i}{a_{C,G}(F_{G,0} - F_G)} \quad (2.14)$$

The yield of a product i , $Y_{i,G}$, is expressed as the conversion multiplied by the selectivity of that product.

The average Turn Over Frequency (TOF) is defined in (2.15) as the ratio of the molar rate of the converted glycerol to the number of active Cu sites, n_{Cu^0} , calculated from the N_2O -sorption (as discussed in 2.1.2.3.2).

$$TOF = \frac{(F_G^0 - F_G)}{n_{Cu^0}} \quad (2.15)$$

The activity is defined in (2.16) as the ratio of the mass flow rate in which glycerol is converted, $\dot{m}_{G,converted}$ ($kgG s^{-1}$), to the total amount of catalyst used, W_{cat} (kg_{cat}).

$$activity = \frac{\dot{m}_{G,converted}}{W_{cat}} \quad (2.16)$$

2.1.3.1.5 Experimental procedure

Prior to the reaction, the calcined catalyst was reduced to obtain Cu^0 , which is assumed to be the active phase (as discussed in Chapter 1 section 1.6.3). The reduction profile contained three steps, as shown in Figure 2.13:

- (1) The reactor was heated from room temperature to 473 K at 3 K min^{-1} in inert atmosphere, *i.e.* 45 $Nl h^{-1} N_2$ at 0.5 MPa, to remove the adsorbed molecules from the surface. The temperature was maintained for 5 h.
- (2) The reactor was heated to 623 K (at 3 K min^{-1}) and kept for 2 h in a reductive atmosphere, *i.e.* 45 $Nl h^{-1} N_2$ and 5 $Nl h^{-1} H_2$ at a total pressure of 0.5 MPa.
- (3) The catalyst was further reduced for 3 h at this temperature using 20 $Nl h^{-1} H_2$ at 0.5 MPa.

The reaction was carried out at 473 K, a pressure of 7.5 MPa, a spacetime of 125 $kg_{cat} s mol^{-1}$ and a molar H_2 to glycerol ratio of 7 as a reference, unless stated otherwise. At these conditions, the occurrence of intrinsic kinetics, which are discussed in section 2.1.3.2, has been assured. Thus after the reduction, the reactor was cooled to the reaction temperature (step 4). Finally, the pressure was increased to 7.5 MPa (step 5). Once the pressure was reached, the liquid and gas feed were switched on. At these conditions, it takes *ca.* three hours for the feed to reach the reactor and four hours for the reactor effluent to reach the sampling point. Therefore, to be sure of a stable composition, the first sample was always taken after 12 h TOS.

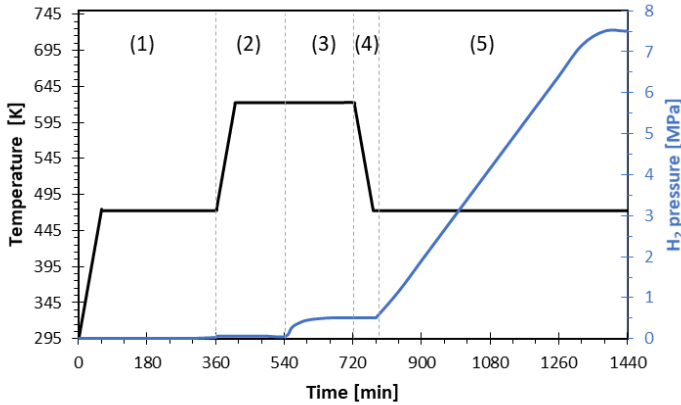


Figure 2.13. In situ catalyst pre-treatment prior to the reaction (black line = temperature, blue line = H₂ pressure).

2.1.3.2 Intrinsic kinetics in a trickle bed regime

The experimental conditions were determined such that the measurement of intrinsic kinetics, *i.e.* free from mass and heat transport effects, was allowed. A sensitivity analysis is performed for the following operating conditions: temperature, space time, molar hydrogen to glycerol ratio, pellet diameter and catalyst dilution. The experimental range for each of these conditions, for which the intrinsic kinetic regime is satisfied, is shown in Table 2.6.

Table 2.6. Summary of the operating conditions for intrinsic kinetics.

Operating condition	Experimental range
Pressure [MPa]	7.5
Temperature [K]	473-513
Space time [kg _{cat} s mol ⁻¹]	133-795
F _{H₂} / F _{glycerol} [mol mol ⁻¹]	4-7
Pellet diameter [μm]	630-710
Inert particles diameter [μm]	125
Dilution [%]	50

The assessment of the transport effects is based on various criteria, for which a more theoretical background is given in the Appendix A. A general criterion for intrinsic kinetics is given by equation (2.17), meaning that the difference in observed, R^{obs} , and intrinsic, R^{intr} , production rate due to any gradient, should be smaller than 5 %.

$$\left| \frac{R^{obs} - R^{intr}}{R^{intr}} \right| < 0.05 \quad (2.17)$$

The effect of axial and radial dispersion, as well as the pressure drop were negligible. Mass transport was assessed by calculating the corresponding Carberry numbers¹⁸, for external mass transport, or the Weisz parameter¹⁹, for internal mass transport, at the most severe operation conditions. As can be seen in Table 2.7, the Carberry number for H₂ at the liquid-solid interface exceeds the limiting value, such that the criterion is not fulfilled. This can indicate that some concentration gradients may not be negligible. However, as the correlations were not determined for our system, this was experimentally assessed in previous work under similar conditions. By varying the catalyst loading, while keeping the time to process a volume of the feed constant, the conversion remained constant. Therefore, it was concluded from the experimental assessment that no mass transport limitations occurred.²⁰

Table 2.7. Criteria for intrinsic kinetics evaluated at most severe conditions: 513 K, 7.5 MPa, 795 kg_{cat} s mol⁻¹, 7 mol_{H₂} mol⁻¹_{glycerol}, $d_p = 630 \mu\text{m}$ and $d_{\text{inert}} = 125 \mu\text{m}$. Values from previous research²⁰: $R_w^{\text{obs}} = 1.5 \cdot 10^{-3} \text{ mol kg}^{-1} \text{ s}^{-1}$, $E_a = 84 \text{ kJ mol}^{-1}$, $|\Delta H_r| = 89 \text{ kJ mol}^{-1}$

Phenomena	Criterion	Equation	Observed value
Pressure drop	$\Delta P/P$	(A.1)	$2 \cdot 10^{-3} < 0.02$
Mass transport	$Ca_{\text{H}_2, \text{gas-liquid}}$	(A.9)	$0.03 < 0.05$
	$Ca_{\text{H}_2, \text{liquid-solid}}$	(A.10)	$0.21 > 0.05$
	$Ca_{\text{glycerol, liquid-solid}}$		$0.04 < 0.05$
	Φ_{H_2}	(A.12)	$8.6 \cdot 10^{-8} < 0.14$
	Φ_{glycerol}		$1.3 \cdot 10^{-8} < 0.14$
Heat transfer	Radial, ΔT_{rad}	(A.15)	$1.1 \text{ K} < 1.4 \text{ K}$
	External, $\Delta T_{\text{boundary layer}}$	(A.17)	$0.7 \text{ K} < 1.4 \text{ K}$
	Internal, ΔT_{int}	(A.23)	$2 \cdot 10^{-2} \text{ K} < 1.4 \text{ K}$

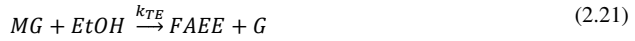
2.2 Design of a process for the valorization of oil deodorizer distillates

This section describes the procedures for the technical feasibility and economic viability of an oil deodorizer distillate valorization process. Via a three-step process, i.e. an esterification with supercritical ethanol, followed by an extraction with supercritical CO₂ and a purification step, squalene, sterols and tocopherols are recovered from the ODD. Kinetic parameters are determined by regression for the first process step using Athena Visual Studio® while the complete process is simulated in Aspen Plus®.

2.2.1 Kinetic modelling

The esterification experiments of sunflower ODD with ethanol were performed by VITO. For the kinetic modelling of the supercritical esterification of sunflower ODD, 30 experiments were considered at 15 MPa with space time τ (0 – 60 min), temperature (523 K - 573 K) and ethanol to ODD ratio (0.3 g_{EIOH} g⁻¹_{ODD} - 1.5 g_{EIOH} g⁻¹_{ODD}). The dataset can be found in Appendix B.

The esterification and transesterification reactions were assumed to be irreversible, as ethanol was in excess (molar excess ratio of 1.4 for mass ratio of 0.3 $\text{g}_{\text{EtOH}} \text{g}^{-1}_{\text{ODD}}$), shifting the reaction towards the product side. The transesterification reactions are consecutive and chemically analogous. Therefore, it was assumed that the same rate coefficient, k_{TE} , can be applied for each of the consecutive steps.



In equation (2.18) to (2.21) FFA stands for free fatty acid, EtOH for ethanol, TG, DG and MG for tri-, di- and monoglyceride, respectively, FAEE for fatty acid ethyl ester, G for glycerol and k_E and k_{TE} are the rate coefficient of the esterification and the transesterification reaction, respectively.

A pseudo-homogeneous, isothermal, plug flow reactor model was used to determine the outlet flow rates for all components. To calculate these outlet flow rates, a set of differential equations, (2.22), has to be solved. The initial conditions of the set of differential equations are $F_i = F_i^0$ at $V = 0$.

$$\frac{dF_i}{dV} = R_i \quad \text{with } i = 1, \dots, n_{resp} \quad (2.22)$$

Where V is the reactor volume [m^3], F_i^0 is the inlet molar flow rate [mol s^{-1}], F_i is the molar outlet flow rate [mol s^{-1}] and R_i the net production rate [$\text{mol m}^{-3} \text{s}^{-1}$] of component i . In total n_{resp} responses, *i.e.* eight (the number of components in reactions (2.18) to (2.21)), are taken into account. The net production rate, see equation (2.23), is obtained as the sum of the reaction rates, r_j [$\text{mol m}^{-3} \text{s}^{-1}$], of the elementary steps in which a component is produced ($v_{ij} > 0$) or consumed ($v_{ij} < 0$), where v_{ij} is the stoichiometric coefficient of component i in reaction j . The reaction rates, r_j , are given by equation (2.30) to (2.33).

$$R_i = \sum_j v_{ij} r_j \quad \text{with } i = 1, \dots, n_{resp} \quad (2.23)$$

The integration of the set of differential equations (2.22) yields the molar outlet flow rate of each component. As FAME, tocopherol, sterol and squalene, do not undergo reaction, their molar flow rates remain constant throughout the reactor. This implies that the corresponding R_i equals zero. Therefore, no separate differential equations were necessary for these components. Of course, their presence was accounted for in the calculation of the concentrations of the other components *via* the average molecular weight of the mixture, as described in the Appendix C.

The net rates of formation R_i are shown in equation (2.24) to (2.29), with r_1 the reaction rate for the esterification of FFA and r_2 to r_4 the reaction rates for respectively the transesterification of TG, DG and MG.

$$R_{FAEE} = -R_{EtOH} = \sum_{i=1}^4 r_i \quad (2.24)$$

$$R_{FFA} = -R_{H_2O} = -r_1 \quad (2.25)$$

$$R_{TG} = -r_2 \quad (2.26)$$

$$R_{DG} = r_2 - r_3 \quad (2.27)$$

$$R_{MG} = r_3 - r_4 \quad (2.28)$$

$$R_G = r_4 \quad (2.29)$$

The reaction rates r_i follow the law of mass action and are hence, expressed as function of the rate coefficient k_i and the concentration of the reactants, equations (2.30) to (2.33). It is assumed that the components behave as an ideal solution in the reactor.

$$r_1 = k_E[FFA][EtOH] \quad (2.30)$$

$$r_2 = k_{TE}[TG][EtOH] \quad (2.31)$$

$$r_3 = k_{TE}[DG][EtOH] \quad (2.32)$$

$$r_4 = k_{TE}[MG][EtOH] \quad (2.33)$$

The rate coefficient, k_i [$\text{m}^3 \text{mol}^{-1} \text{s}^{-1}$], is expressed by the Arrhenius relation in reparametrized form, see equation (2.34) and (2.35), where $A_{i,T_{avg}}$ is the pre-exponential factor at average temperature [$\text{m}^3 \text{mol}^{-1} \text{s}^{-1}$], $E_{a,i}$ the activation energy [J mol^{-1}], R the universal gas constant [$\text{J mol}^{-1} \text{K}^{-1}$], T the reactor temperature [K] and T_{avg} the average reactor temperature of the experiments [K], *i.e.* 550 K. This reparameterization avoids a too strong correlation between the pre-exponential factor and the activation energy during regression.²¹

$$k_E = A_{E,T_{avg}} e^{-\frac{E_{a,E}}{R} \left(\frac{1}{T} - \frac{1}{T_{avg}} \right)} \quad (2.34)$$

$$k_{TE} = A_{TE,T_{avg}} e^{-\frac{E_{a,TE}}{R} \left(\frac{1}{T} - \frac{1}{T_{avg}} \right)} \quad (2.35)$$

The kinetic parameters, *i.e.* $A_{i,T_{avg}}$ and $E_{a,i}$, of the rate equations were estimated by minimizing the residuals sum of squares (SS_{RES}), between the experimental molar outlet flow rates, F , and the model calculated ones, \hat{F} of FFA, FAEE, TG, DG, MG, glycerol and water. The minimization is done by adjusting the estimated kinetic model parameters \bar{b} , which are expected to approach the real parameters $\bar{\beta}$ when the optimum is reached.

$$SS_{RES} = \sum_{i=1}^{n_{resp}} \sum_{j=1}^{n_{exp}} (F_{i,j} - \hat{F}_{i,j})^2 \xrightarrow{\bar{b} \rightarrow \hat{\beta}} \min \quad (2.36)$$

Due to the non-linearity of the SS_{RES} , this function can potentially have more than a single minimum. Only one of these corresponds to the global minimum and, hence, to the best parameter estimates. Several methods exist to minimize the SS_{RES} , *e.g.* the method of the steepest descent, the Rosenbrock method, and the Levenberg-Marquardt method.²² The latter is implemented in Athena Visual Studio, a user-friendly platform for simulation and regression purposes.²³ To start the parameter estimation, initial values are needed. These initial values need to be as close as possible to the real values to ensure that the solution is the desired global minimum instead of a local minimum. Initial estimates were retrieved from reported literature or based on theoretical considerations.²⁴

The global significance of the model and the significance of all parameters was assessed by performing, the F-test and t-test respectively.²¹ Parity diagrams were employed for visualizing the model performance. The regression is considered to be significant when the calculated F value exceeds the tabulated one, *i.e.* 3.84. An estimated parameter is assumed to be significantly different from 0, when the calculated value exceeds the tabulated t-value at a 95% confidence interval, *i.e.* 1.98. For the statistical tests, the degrees of freedom are calculated as $n_{exp}(n_{resp} - n_{parameters})$.

2.2.2 Process simulation methodology

The simulations were performed using the Aspen Plus® V10 software. The procedure consists of defining representative components (see section 2.2.2.1), selecting the appropriate thermodynamic model (see section 2.2.2.2) and selecting the required equipment and operating conditions. For obtaining the mass and energy balances for each unit, the default convergence methods were used. The compressors were assumed to have an isentropic efficiency of 72 %, while the pumps were simulated at 80 % efficiency.^{25, 26} A stage efficiency of 100 % was assumed for the distillation towers, meaning that the number of stages equals the theoretical one. The separation in flash vessels was operated adiabatically. A stage pressure drop of 1 kPa was assumed in the distillation towers. The pressure drop in the other equipment was not considered. The following utilities were assumed to be available in the plant: low pressure steam at 0.6 MPa and a saturation temperature of 432 K, medium pressure steam at 2 MPa and a saturation temperature of 485 K, high pressure steam at 4 MPa and a saturation temperature of 523 K. For heating above 523 K, fuels were used. The cooling was achieved by cooling water at 313 K.

2.2.2.1 Model components

The complexity of the ODDs was simplified by a lumping approach for component families.²⁷ These are necessary to appropriately describe the behavior of the complex ODD stream during the reaction, extraction and separation steps of the process. In the current state-of-the-art, this complex mixture is often simulated as a simple mixture of three or four key components²⁸⁻³⁰, missing crucial information

for the design of the separation section/units. Typically, the ODD is represented by TG or/and FFA and one ‘minor’ component of interest. In this work, for each component family present in the ODD stream, a model component was selected. The physicochemical properties of these model components represent the properties of the whole component family, *i.e.* all of the various components within the component family.

Vegetable oils consist mainly of palmitic (16:0), oleic (18:1) and linoleic acids (18:2). Olive oil contains mostly oleic acids, while sunflower and soybean oils contain more linoleic acid.³¹ However, the corresponding glycerides of the latter fatty acid are not present in the Aspen Plus software database. This impedes the estimation of the physicochemical properties of the components and the mixture. Therefore, oleic acid (C₁₈H₃₄O₂) was selected as model component for the representation of the FFAs. The corresponding glycerides of the oleic acid, triolein (C₅₇H₁₀₄O₆), diolein (C₃₉H₇₂O₅) and monolein (C₂₁H₄₀O₄), were used as model compounds for the representation of respectively the TG, DG and MG. Fatty acid esters are also found in vegetable oils³¹ and the corresponding model component was assumed to be methyl oleate (FAME, C₁₉H₃₆O₂), as oleic acid was selected for the representation of the FFAs. The esterification of the FFA and transesterification reaction of the glycerides with ethanol results in the fatty acid ethyl esters (FAEEs), which were represented by ethyl oleate (C₂₀H₃₈O₂). Tocopherols occur in four different isomers. In olive and sunflower oil, α -tocopherol is the most abundant one, while γ -tocopherol is the most abundant one in soybean oil³¹. The total tocopherol fraction was represented by α -tocopherol as the experimental equilibrium data in literature³²⁻³⁴, which was needed for the thermodynamic model in section 2.2.2.2, were obtained with α -tocopherol. β -sitosterol is the most important sterol in vegetable oils and fats, with only traces of cholesterol, campesterol and stigmasterol being present.³¹ The total phytosterol content was, hence, lumped as β -sitosterol. The composition of the different ODDs is shown in Table 2.8.

Table 2.8. Mass fractions in the olive, sunflower and soybean ODDs, as determined by GC analysis³⁵

<i>component families</i>	<i>model component</i>	<i>olive ODD</i> [wt.%]	<i>sunflower ODD</i> [wt.%]	<i>soybean ODD</i> [wt.%]
<i>FFA</i>	oleic acid	62.2	24.3	20.5
<i>triglycerides</i>	triolein	13.6	56.7	2.14
<i>diglycerides</i>	diolein	2.75	1.89	7.20
<i>monoglycerides</i>	monolein	1.86	1.25	4.25
<i>FAME</i>	methyl oleate	7.02	2.88	2.07
<i>phytosterols</i>	β -sitosterol	2.49	8.00	33.9
<i>tocopherols</i>	α -tocopherol	0.11	2.79	26.7
<i>squalene</i>	squalene	9.97	2.20	3.28

2.2.2.2 Thermodynamic models

One of the most important steps in a simulation is the selection of a property method. The correct property method ensures that the thermodynamic and transport properties of the pure components and their mixtures are calculated accurately. For non-ideal liquid solutions at low pressures (< 1 MPa), activity coefficient models are used on a regular basis.³⁶ The low pressure sections in the simulated process schemes include the adiabatic separation, for recycling the ethanol excess from the reaction section and for the CO₂-recovery of the extraction section, and the distillation towers, for the purification of the ester stream as well as the squalene stream. For these operations, the UNIQUAC-Redlich-Kwong (UNIQUAC-RK) activity model was selected.

For the simulation of the reaction section, the IDEAL property method was selected as the used kinetic parameters were obtained by the law of mass action, see section 2.2.1.

For the calculation of thermodynamic properties at high pressures, typically the (p,V,T)-relation is simulated by an equation of state (EOS).³⁶ Mendes *et al.*²⁸ simulated the separation of tocopherols, stigmaterol and squalene in linoleic acid, as representative of soybean ODD, using the Peng-Robinson EOS at pressures between 9 to 35 MPa. Vázquez *et al.*³⁰ applied the Group Contribution EOS³⁷ in the simulation of the squalene recovery in the range of 15 to 23 MPa, directly from olive ODDs, represented by a mixture of ethyl oleate, methylmyristate and triolein. The same EOS was implemented by Fornari *et al.*²⁹ in the simulation of the sc-CO₂ extraction of tocopherols and phytosterols from olive ODDs.

In this work, the Redlich-Kwong-Aspen (RK-ASPEN) EOS was selected for the supercritical processes.³⁶ In comparison to the Peng-Robinson EOS, which is widely used, the RK-ASPEN EOS has been found to perform well at supercritical conditions³⁸⁻⁴¹ due to its applicability at high pressures and temperatures in presence of light gases, such as CO₂, for mixtures of small and large molecules. Equation (2.37) represents the cubic equation state for the RK-ASPEN EOS, where p is the pressure [atm], R is the universal gas constant, T is the temperature [K], V_m is the molar volume [cm³ mol⁻¹], and a [atm cm³ mol⁻¹] and b [cm³ mol⁻¹] are the quadratic mixing rule parameters.³⁶

$$p = \frac{RT}{V_m - b} - \frac{a}{V_m(V_m + b)} \quad (2.37)$$

For a pure component, the parameters a and b depend on the critical temperature and pressure.⁴² For a mixture, the calculation of these parameters becomes somewhat more complex making use of the one fluid theory, see equations (2.38) and (2.39), to account for the mixture composition, including interaction, on top of the pure component values. These parameters were retrieved from the pure 35 or the NIST-TRC database, available in Aspen Plus®. The vapor pressure calculation was improved by extrapolation at supercritical temperatures through a generalized temperature dependency for a .⁴²

$$a = \sum_i \sum_j x_i x_j \sqrt{a_i a_j} (1 - k_{a,ij}) \quad (2.38)$$

$$b = \sum_i \sum_j x_i x_j \frac{b_i + b_j}{2} (1 - k_{b,ij}) \quad (2.39)$$

The interactions between molecules i and j are calculated *via* binary interaction coefficients $k_{a,ij}$ [-] and $k_{b,ij}$ [-] for which a linear temperature dependence is proposed, see equations (2.40) and (2.41). It is assumed that $k_{ij} = k_{ji}$.

$$k_{a,ij} = k_{a,ij}^0 + k_{a,ij}^1 \frac{T}{1000} \quad (2.40)$$

$$k_{b,ij} = k_{b,ij}^0 + k_{b,ij}^1 \frac{T}{1000} \quad (2.41)$$

2.2.3 Economic analysis

To evaluate the process on a realistic scale, a capacity of 1 kton_{ODD} per year was assumed, corresponding to *ca.* 1% of the European produced ODDs.⁴³ The plant was assumed to operate 330 days per year.

The estimation of the Capital Costs (CAPEX) was performed using the Aspen Process Economic Analyzer (APEA). Capital costs are associated with the construction of a new plant or the modification of an existing one. The APEA uses data collected from engineering, procurement, and construction companies and equipment manufacturers to estimate the total installed equipment costs, which includes both the direct costs (*i.e.* the equipment and its installation, the associated instrumentation and controls, piping, electrical systems, land and yard improvements and buildings) and the indirect costs (*i.e.* engineering and supervision for the construction, legal expenses, construction expenses, contractor's fees and contingency).

The following assumptions were made for feedstock, product, consumables, waste and utilities costs. Costs are reported in current prices for October 2018 in Europe.

- The minimum selling price of 2nd generation bio-EtOH varied between € 0.28 kg⁻¹⁴⁴ to € 0.94 kg⁻¹⁴⁵ over the last two decades. Due to these fluctuations, the maximum price was set as the base case.
- The price of the ODD as raw material depends on the tocopherol content, with a minimum of € 0.56 kg⁻¹_{ODD} for 5 wt.% of tocopherol and € 0.13 kg⁻¹_{ODD} per additional percentage of tocopherol content⁴⁶. The prices of the olive and sunflower ODDs were € 0.56 kg⁻¹_{ODD}, while due to high tocopherol content of soybean ODD (Table 2.8), the price was set at € 3.4 kg⁻¹_{ODD}.
- In Europe, the squalene price was estimated at € 32 kg⁻¹.⁴⁷
- The FAEE price was assumed to be equal to the market price of FAME (biodiesel), *i.e.* € 0.73 kg⁻¹.⁴⁸

- Tocopherols and sterols are of great value for the pharmaceutical industry as natural source for vitamin E and drug synthesis respectively.⁴⁹ A similar price setting, as for the vegetable ODD price, was deduced for the minor mixture product.⁴⁶ This resulted in a price of € 1.7 kg⁻¹_{mixture} for the olive minor product (66 wt.% sterols and 3 wt.% tocopherols in the presence of FAEE, see Chapter 6), and € 13 kg⁻¹_{mixture} for the sunflower ODD minor product (68 wt.% sterols and 24 wt.% tocopherols in the presence of FAEE, see Chapter 6). The price of the tocopherol rich product recovered from the soybean ODD was € 24 kg⁻¹_{mixture} (56 wt.% sterols and 44 wt.% tocopherols, see Chapter 6). Regarding these values, one should keep in mind that in these price calculations only the tocopherol content was taken into account. This can result in an underestimation of the product price, since enrichment in sterols was neglected.
- No value was given to the stream enriched in FAME, as the content of the components is too low. However, further purification steps could result in an additional added-value for this product.
- Due to the oversupply of glycerol, as a result of the biodiesel production, no value was given to this stream.⁵⁰
- To address the greenhouse gas problematics, a CO₂-capturing process was selected as the CO₂ solvent source. The price of pure CO₂ obtained from a sucrose fermentation was € 0.01 kg⁻¹_{CO₂}.⁵¹
- The liquid disposal costed € 1.05 kg⁻¹⁵², while CO₂ emission costed € 18.3 ton⁻¹.⁵³
- The European gas and electricity price for non-household consumers were € 25 MWh⁻¹⁵⁴ and € 77 MWh⁻¹⁵⁵ respectively. Based on a boiler efficiency of 85 %, a thermal energy price of € 10 GJ⁻¹ was calculated. Cooling water at 313 K was provided for € 25 per 1000 m³.²⁵

A simple profitability analysis of the process was evaluated based on the gross margin and contribution margin ratio, according to the methodology of Towler and Sinnott.²⁵ The gross margin is known as the sum of the key product revenue (REV) and the difference between revenues of the side product and the waste streams cost (BP), minus the raw material costs (RM), as described in equation (2.42). The gross margin can also be expressed as a ratio, equation (2.43). The raw materials are the components consumed by the process; these do not include the consumables such as solvents.

$$\text{gross margin (GM)} = REV + BP - RM \quad (2.42)$$

$$\text{gross margin ratio (GMR)} = \frac{REV + BP - RM}{REV} \times 100\% \quad (2.43)$$

The variable cost of production (VCOP) is calculated in equation (2.44) as the sum of the raw material, consumable (CONS) and utilities (UTS) cost minus the revenues of the side products and the waste streams cost.

$$\text{variable cost of production (VCOP)} = RM + CONS + UTS - BP \quad (2.44)$$

An indication of the process profitability on a fixed-cost-free basis is achieved *via* the variable contribution margin (VCM), equation (2.45). The contribution margin ratio (CMR), which indicates how much of the revenues is not spent on the coverage of the fixed costs, is calculated as the ratio of the VCM over the REV, equation (2.46).

$$\text{variable contribution margin (VCM)} = REV - VCOP \quad (2.45)$$

$$\text{contribution margin ratio (CMR)} = \frac{REV - VCOP}{REV} \times 100\% \quad (2.46)$$

2.2.4 Data analysis

The conversion of a component i is defined in equation (2.47) by its (normalized) inlet and outlet molar flow rate.

$$X_i = \frac{F_{i,0} - F_i}{F_{i,0}} \quad (2.47)$$

To compare the different ODDs and the process efficiency, the squalene recovery and extraction yield are calculated. The overall squalene recovery [$\text{g}_{\text{squalene}} \text{kg}^{-1}_{\text{ODD}}$] of the process, which is discussed in detail in Chapter 6, was calculated as the ratio between the amount of squalene recovered in the process and the mass of ODD fed.

$$R_{\text{squalene}} = \frac{m_{\text{squalene}}}{m_{\text{ODD}}^0} \quad (2.48)$$

The extraction yield [$\text{g}_{\text{squalene}} \text{g}^{-1}_{\text{squalene}}$] was defined over the extraction tower, and calculated as the mass of squalene in the extract to mass of squalene fed to the extraction tower.

$$Y_{\text{extraction}} = \frac{m_{\text{squalene out ET-200}}}{m_{\text{squalene in ET-200}}} \quad (2.49)$$

2.3 References

- 1 M. Naderi, Chapter Fourteen - Surface Area: Brunauer–Emmett–Teller (Bet), in: S. Tarleton (Ed.) *Progress in Filtration and Separation*, Academic Press, Oxford, 2015, pp. 585-608.
- 2 R. Bardestani, G.S. Patience, S. Kaliaguine, *Experimental Methods in Chemical Engineering: Specific Surface Area and Pore Size Distribution Measurements—Bet, B_{jt}, and D_{ft}*, *The Canadian Journal of Chemical Engineering*, 97 (2019) 2781-2791.
- 3 L. Buelens, *Process Concept and Materials For Carbon Dioxide Capture and Conversion: Super-Dry Reforming of Methane*, Ghent University, 2019.
- 4 A. Dandekar, M. Vannice, Determination of the Dispersion and Surface Oxidation States of Supported Cu Catalysts, *Journal of Catalysis*, 178 (1998) 621-639.
- 5 M. Muhler, L.P. Nielsen, E. Törnqvist, B.S. Clausen, H. Topsøe, Temperature-Programmed Desorption of H₂ as a Tool to Determine Metal Surface Areas of Cu Catalysts, *Catalysis Letters*, 14 (1992) 241-249.
- 6 B. Dvořák, J. Pašek, Determination of the Specific Copper Surface Area by Chromatographic Technique, *Journal of Catalysis*, 18 (1970) 108-114.
- 7 E. Guerreiro, O. Gorriç, J. Rivarola, L. Arrúa, Characterization of Cu/SiO₂ Catalysts Prepared by Ion Exchange for Methanol Dehydrogenation, *Applied Catalysis A: General*, 165 (1997) 259-271.
- 8 J. Scholten, J. Konvalinka, Reaction of Nitrous Oxide with Copper Surfaces. Application to the Determination of Free-Copper Surface Areas, *Transactions of the Faraday Society*, 65 (1969) 2465-2473.
- 9 A. Gervasini, S. Bennici, Dispersion and Surface States of Copper Catalysts by Temperature-Programmed-Reduction of Oxidized Surfaces (S-Tpr), *Applied Catalysis A: General*, 281 (2005) 199-205.
- 10 S. Bhatia, J. Beltramini, D.D. Do, Temperature Programmed Analysis and Its Applications in Catalytic Systems, *Catalysis Today*, 7 (1990) 309-438.
- 11 M.A. Sanhoob, O. Muraza, M. Yoshioka, M. Qamaruddin, T. Yokoi, Lanthanum, Cerium, and Boron Incorporated Zsm-12 Zeolites for Catalytic Cracking of N-Hexane, *Journal of Analytical and Applied Pyrolysis*, 129 (2018) 231-240.
- 12 N. Katada, K. Suzuki, T. Noda, G. Sastre, M. Niwa, Correlation between Brønsted Acid Strength and Local Structure in Zeolites, *The Journal of Physical Chemistry C*, 113 (2009) 19208-19217.
- 13 S. Komhom, O. Mekasuwandumrong, P. Praserttham, J. Panpranot, Improvement of Pd/Al₂O₃ Catalyst Performance in Selective Acetylene Hydrogenation Using Mixed Phases Al₂O₃ Support, *Catalysis Communications*, 10 (2008) 86-91.
- 14 D.G. Lamas, M. de Oliveira Neto, G. Kellermann, A.F. Craievich, 5 - X-Ray Diffraction and Scattering by Nanomaterials, in: A.L. Da Róz, M. Ferreira, F. de Lima Leite, O.N. Oliveira (Eds.) *Nanocharacterization Techniques*, William Andrew Publishing 2017, pp. 111-182.
- 15 P. Tozma, Search for Magnets with Properties Intermediate between Nd-Fe-B and Ferrite, University of Dublin, 2016.
- 16 K. van der Borght, K. Toch, V. Galvita, J.W. Thybaut, G.B. Marin, Information-Driven Catalyst Design Based on High-Throughput Intrinsic Kinetics, *Catalysts*, 5 (2015) 1948.
- 17 T. Rajkhowa, J.W. Thybaut, G.B. Marin, Assessment of the Dominant Factors in Cu Catalyst Deactivation in Glycerol Hydrogenolysis, American Institute of Chemical Engineers Annual Meeting Salt Lake city, 2015.
- 18 J.J. Carberry, *Chemical Reaction Engineering - Inter-Lntraphase Diffusion and Chemical Reaction*, *Industrial & Engineering Chemistry*, 61 (1969) 51-53.
- 19 P. Weisz, C. Prater, Interpretation of Measurements in Experimental Catalysis, *Advances in Catalysis*, Elsevier 1954, pp. 143-196.
- 20 T. Rajkhowa, G.B. Marin, J.W. Thybaut, A Comprehensive Kinetic Model for Cu Catalyzed Liquid Phase Glycerol Hydrogenolysis, *Applied Catalysis B: Environmental*, 205 (2017) 469-480.
- 21 K. Toch, J.W. Thybaut, G.B. Marin, A Systematic Methodology for Kinetic Modeling of Chemical Reactions Applied to N-Hexane Hydroisomerization, *AIChE Journal*, 61 (2015) 880-892.
- 22 W.E. Stewart, M. Caracotsios, *Computer-Aided Modeling of Reactive Systems*, John Wiley & Sons 2008.
- 23 M. Caracotsios, Athenavizual Studio. Retrieved From.

- 24 J.A. Dumesic, *The Microkinetics of Heterogeneous Catalysis*, American Chemical Society 1993.
- 25 G. Towler, R. Sinnott, *Chemical Engineering Design*, Second Edition ed. 2013.
- 26 World Pumps, *Selection of Gas Compressors - Part 1*, 2011.
- 27 P. Nachtergaele, T. De Somer, B. Gelaude, J. Hogie, J.W. Thybaut, S. De Meester, D. Drijvers, J. Dewulf, *Mechanistic Modelling of a Fatty Acid Distillation Plant: Iterative Approach for Component Lumping and Industrial Validation*, Virtual AIChE Annual Meeting proceedings, (2020).
- 28 M. Mendes, F. Pessoa, G. Coelho, A. Uller, *Recovery of the High Aggregated Compounds Present in the Deodorizer Distillate of the Vegetable Oils Using Supercritical Fluids*, *The Journal of Supercritical Fluids*, 34 (2005) 157-162.
- 29 T. Fornari, L. Vázquez, C.F. Torres, E. Ibáñez, F.J. Señoráns, G. Reglero, *Countercurrent Supercritical Fluid Extraction of Different Lipid-Type Materials: Experimental and Thermodynamic Modeling*, *The Journal of Supercritical Fluids*, 45 (2008) 206-212.
- 30 L. Vázquez, C.F. Torres, T. Fornari, F.J. Señoráns, G. Reglero, *Recovery of Squalene from Vegetable Oil Sources Using Countercurrent Supercritical Carbon Dioxide Extraction*, *The Journal of Supercritical Fluids*, 40 (2007) 59-66.
- 31 A. Thomas, *Fats and Fatty Oils*, Ullmann's Encyclopedia of Industrial Chemistry, (2000).
- 32 P.J. Pereira, M. Goncalves, B. Coto, E.G. de Azevedo, M.N. da Ponte, *Phase Equilibria of Co₂ + DL- α -Tocopherol at Temperatures from 292 K to 333 K and Pressures up to 26 Mpa*, *Fluid Phase Equilibria*, 91 (1993) 133-143.
- 33 T. Fang, M. Goto, M. Sasaki, T. Hirose, *Phase Equilibria for the Ternary System Methyl Oleate+ Tocopherol+ Supercritical Co₂*, *Journal of Chemical & Engineering Data*, 50 (2005) 390-397.
- 34 T. Fang, M. Goto, Z. Yun, X.-l. Ding, T. Hirose, *Phase Equilibria for Binary Systems of Methyl Oleate-Supercritical Co₂ and α -Tocopherol-Supercritical Co₂*, *The Journal of Supercritical Fluids*, 30 (2004) 1-16.
- 35 S. De Schepper, K. Schatteman, P. Gonry, W. De Weirdt, H. Benats, K. Elst, E. D'hondt, J. Geuens, S. Tevernier, A. Bouriakova, J. De Clercq, J.W. Thybaut, *Efficient Supercritical (Trans-)Esterification of Vegetable Oil Deodorizer Destillates*, internal communication, SUCCESS-project.
- 36 Aspen Technology, *Aspen Physical Property System*, 2013. Retrieved from http://profsite.um.ac.ir/~fanaei/private/Property%20Methods%208_4.pdf.
- 37 S.I. Sandler, *Equations of State for Phase Equilibrium Computations*, in: E. Kiran, J.M.H.L. Sengers (Eds.) *Supercritical Fluids: Fundamentals for Application*, Springer Netherlands, Dordrecht, 1994, pp. 147-175.
- 38 S. Glišić, O. Montoya, A. Orlović, D. Skala, *Vapor-Liquid Equilibria of Triglycerides-Methanol Mixtures and Their Influence on the Biodiesel Synthesis under Supercritical Conditions of Methanol*, *Journal of the Serbian Chemical Society*, 72 (2007) 13-27.
- 39 I. Gracia, M. García, J. Rodríguez, M. Fernández, A. De Lucas, *Modelling of the Phase Behaviour for Vegetable Oils at Supercritical Conditions*, *The Journal of Supercritical Fluids*, 48 (2009) 189-194.
- 40 N. Machado, C. Campos Ferreira, E. Costa, M. Araújo, A. Mancio, *Simulation of Biofuels Deacidification by Multistage Gas Extraction Using Co₂ as Solvent with Aspen-Hysys*, 2017.
- 41 S. Glišić, D. Skala, *The Problems in Design and Detailed Analyses of Energy Consumption for Biodiesel Synthesis at Supercritical Conditions*, *The Journal of Supercritical Fluids*, 49 (2009) 293-301.
- 42 P.M. Mathias, *A Versatile Phase Equilibrium Equation of State*, *Industrial & Engineering Chemistry Process Design and Development*, 22 (1983) 385-391.
- 43 E. Scott, *Eu-28 Oilseeds and Products Annual*, 2017.
- 44 A. Aden, M. Ruth, K. Ibsen, J. Jechura, K. Neeves, J. Sheehan, B. Wallace, L. Montague, A. Slayton, J. Lukas, *Lignocellulosic Biomass to Ethanol Process Design and Economics Utilizing Co-Current Dilute Acid Prehydrolysis and Enzymatic Hydrolysis for Corn Stover* (Report No. NREL/TP-510-32438) National Renewable Energy Laboratory 2002.
- 45 F.K. Kazi, J.A. Fortman, R.P. Anex, D.D. Hsu, A. Aden, A. Dutta, G. Kothandaraman, *Techno-Economic Comparison of Process Technologies for Biochemical Ethanol Production from Corn Stover*, *Fuel*, 89 (2010) S20-S28.
- 46 D.S. Laoretani, O.A. Iribarren, *Procedure for the Selection among Technologies. Treatment of Deodorizer Distillate Oil*, *Industrial & Engineering Chemistry Research*, 53 (2014) 16803-16812.

- 47 R. Ciriminna, V. Pandarus, F. Béland, M. Pagliaro, Catalytic Hydrogenation of Squalene to Squalane, *Organic Process Research & Development*, 18 (2014) 1110-1115.
- 48 Neste, Biodiesel Prices. Retrieved on 15-10-2018 from <https://www.neste.com/corporate-info/investors/market-data/biodiesel-prices-sme-fame-0>.
- 49 S. Ramamurthi, A.R. McCurdy, Enzymatic Pretreatment of Deodorizer Distillate for Concentration of Sterols and Tocopherols, *Journal of the American Oil Chemists' Society*, 70 (1993) 287-295.
- 50 G.M. Lari, G. Pastore, M. Haus, Y. Ding, S. Papadokonstantakis, C. Mondelli, J. Pérez-Ramírez, Environmental and Economical Perspectives of a Glycerol Biorefinery, *Energy & Environmental Science*, 11 (2018) 1012-1029.
- 51 H. Naims, Economics of Carbon Dioxide Capture and Utilization—a Supply and Demand Perspective, *Environmental Science and Pollution Research*, 23 (2016) 22226-22241.
- 52 R. Turton, R.C. Bailie, W.B. Whiting, *Analysis, Synthesis, and Design of Chemical Processes*, Prentice Hall 2012.
- 53 M. Scott, Europe's Carbon Market Starts Doing Its Job of Cutting Emissions - a Decade Late, *Forbes*.
- 54 Eurostat, Gas Prices for Non-Household Consumers - Bi-Annual Data (from 2007 Onwards). Retrieved from http://appsso.eurostat.ec.europa.eu/nui/show.do?dataset=nrg_pc_203&lang=en, 2018.
- 55 Eurostat, Electricity Prices for Non-Household Consumers - Bi-Annual Data (from 2007 Onwards). Retrieved from http://appsso.eurostat.ec.europa.eu/nui/show.do?dataset=nrg_pc_205&lang=en, 2018.



CHAPTER 3. CO-METAL INDUCED STABILIZATION OF Al_2O_3 SUPPORTED CU FOR GLYCEROL HYDROGENOLYSIS

A modified version of this chapter was published as:

Alexandra Bouriakova, Pedro S.F. Mendes, Benjamin Katryniok, Jeriffa De Clercq, Joris W. Thybaut

Co-metal induced stabilization of alumina-supported copper: impact on the hydrogenolysis of glycerol to 1,2-propanediol

Catalysis Communications, 146 (2020), 106134

3.1 Introduction

As stated in Chapter 1, the catalytic hydrogenolysis of glycerol constitutes a promising ‘green’ and, hence, more sustainable route towards 1,2-propanediol production compared to the conventional one *via* petroleum derived propylene oxide. It has been widely accepted that supported Cu based catalysts are suitable for glycerol hydrogenolysis with high selectivity to 1,2-propanediol. As already mentioned in Chapter 1, irrespective of the support used, bare Cu catalysts are prone to deactivation phenomena (see section 1.5.3.2).

By doping, ‘impurities’ (such as an additional metal) are deliberately added to the catalyst or support aiming at performance enhancement. In the case of Cu catalysts, mainly the catalyst stability, *i.e.*, constant conversion over time, is aimed at being enhanced. Alkali (*e.g.* Cs), alkaline-earth (*e.g.* Ba) and rare earth metals (*e.g.* La or Ce) are widely studied as dopants in catalysis.¹ Various authors investigated (combinations of) dopants to improve the catalyst performance, as discussed in Chapter 1. Nevertheless, no systematic research has been performed on commercially relevant Cu-based glycerol hydrogenolysis catalysts. In this chapter, Cu/ γ -Al₂O₃ catalysts doped with Ba, Ce, Cs and La are investigated for liquid-phase pure glycerol hydrogenolysis under continuous operation. Those metals are expected to be representative of the most patented co-metals², belonging to their respective groups in the periodic table. The effect of the co-deposition metals on the reaction was clarified by comparing catalyst activity, TOF, glycerol conversion, 1,2-propanediol selectivity and stability by comparison of reduced, *i.e.* prior to the reaction, and spent, *i.e.* post reaction, catalyst.

3.2 Results and discussion

In section 3.2.1, characterization prior to reaction and reduction is discussed. The effect of doping on the reduction and type of Cu species is reported in section 3.2.2. In section 3.2.3, the effect of doping is compared in terms of catalyst activity, TOF, glycerol conversion and 1,2-propanediol selectivity and stability between the reduced and spent catalyst, the characterization of the latter being discussed in section 3.2.4. In section 3.2.5, the role of the dopants on the Cu⁰ particle size is addressed.

3.2.1 Calcined catalyst characterization

The doped catalysts, featuring nominal values of 1 wt.% co-metal (M) and 10 wt.% Cu, denoted as “M-Cu”, were prepared *via* a sequential wet impregnation according to the synthesis method described in Chapter 2 section 2.1.1. The metal loadings of the calcined catalysts, measured by ICP (see Chapter 2 section 2.1.2.1), are reported in Table 3.1. The actual metal loadings are lower than the nominal ones, *i.e.* 1 wt.% for the dopant and 10 wt.% for Cu, which is attributed to the hygroscopic nature of the precursors. The Cs content is less precise because of the high detection limit for this element in ICP analysis. At a nominal value of 1 wt.% of Cs, it is difficult to have accurate results.

Table 3.1. Physicochemical properties of the calcined support, bare Cu and doped Cu/ γ -Al₂O₃ catalysts.

	support	Cu	Ba-Cu	Ce-Cu	Cs-Cu	La-Cu
Cu loading [wt.%] ^a	n.a.	7.20	7.59	7.73	8.12	7.90
Co-metal loading [wt.%] ^a	n.a.	n.a.	0.62	0.72	0.12	0.92
S_{BET} [m ² g ⁻¹ _{support}] ^b	185	160	161	161	170	174
V_{meso} [cm ³ g ⁻¹ _{support}] ^c	0.39	0.40	0.40	0.39	0.41	0.41
d_{pore} [nm] ^c	6.9	6.8	6.2	6.6	7.1	6.5
d_{CuO} [nm] ^d	n.a.	33	25	29	35	30

^a calculated from the results obtained by ICP-OES

^b determined by BET-method

^c determined by BJH-desorption method

^d determined by XRD patterns using the Scherrer's equation

Figure 3.1 shows that for all catalysts a type IV N₂-sorption isotherm (Chapter 2 section 2.1.2.2) was observed, which is typical for mesoporous materials such as PURALOX® γ -Al₂O₃.³ No significant effect of the dopant and Cu impregnation on the BET surface area was found, which ranged between 160 - 170 m² g⁻¹_{support}. No significant effect was found on the specific pore volume and pore size either, amounting, to 0.39 - 0.41 cm³ g⁻¹_{support} and 6.2 - 6.9 nm, respectively (Table 3.1).

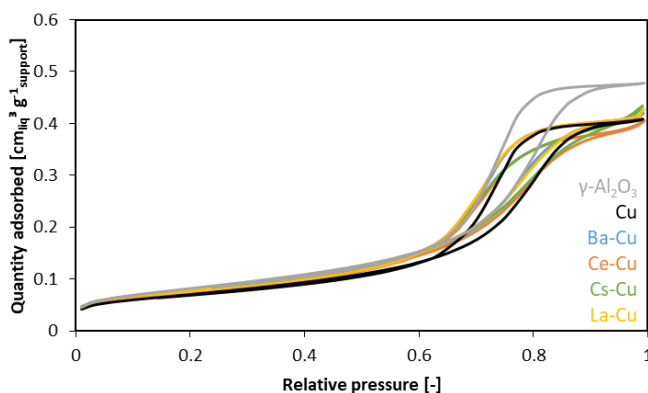


Figure 3.1. N₂-sorption isotherms and the differential pore size distribution of the support (grey), Cu (black), Ba-Cu (blue), Ce-Cu (orange), Cs-Cu (green) and La-Cu (yellow) catalysts supported on γ -Al₂O₃.

To identify the crystalline phases of the calcined catalysts XRD was applied, according to the procedure in Chapter 2 section 2.1.2.4. Broad diffraction peaks for γ -Al₂O₃ (JCPDS 00-050-0741) at 31.8° (Al₂O₃(220)), 37.5° (Al₂O₃(311)), 39.2° (Al₂O₃(222)), 45.7° (Al₂O₃(400)) were observed for all catalysts, as show in Figure 3.2. This indicates a limited crystallinity of the support material, as expected. The calcined catalysts exhibited main characteristic diffraction peaks of of CuO(002) at 35.4° and CuO(111) at 38.6°, and minor diffraction peaks at 32.5° (CuO(-110)), 48.7° (CuO(-202)), 51.4° (CuO(112)) and 53.5° (CuO(020)), according to JCPDS 00-045-0937. The most characteristic peak of Cu₂O at 36.4° (JCPDS 00-005-0667), is situated in the broad diffraction peak of the support and could therefore not be identified in the XRD patterns. Thus, it could be concluded that Cu₂O is highly dispersed, highly amorph

or not present. All calcined catalysts exhibited the delafossite CuAlO₂ phase, albeit less pronounced for the Ce-doped catalyst. Only for the Ba-doped Cu-catalysts a diffraction peak corresponding to the dopant was visible (at 25°), as the fraction of dopant was close to the XRD detection limit of 1 wt.%. From the Scherrer's equation, it was calculated that the CuO crystallites of the calcined catalysts are in the order of magnitude of 35 - 40 nm.

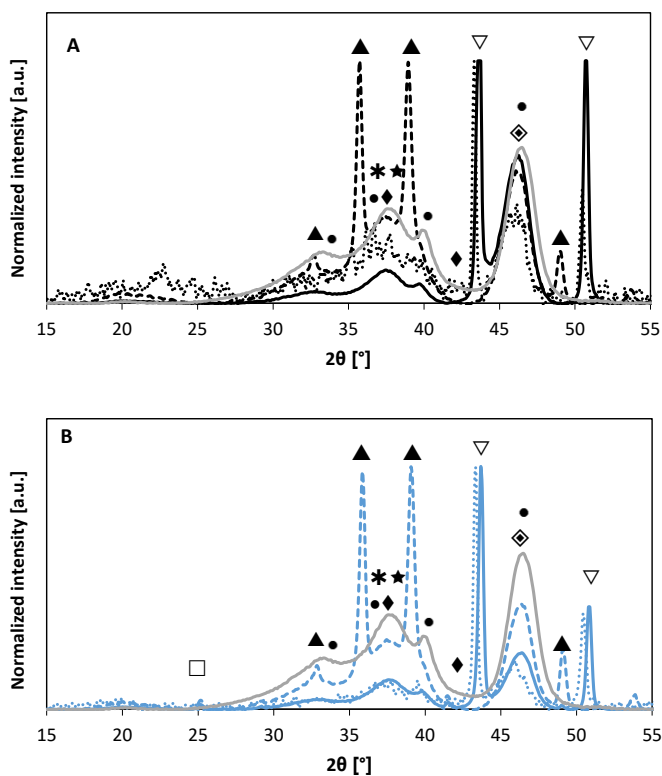


Figure 3.2 XRD patterns of the calcined (dashed lines), in-situ reduced (full lines) and spent (dotted lines) Cu (A, black), Ba-Cu (B, blue), Ce-Cu (C, orange), Cs-Cu (D, green) and La-Cu (E, yellow) catalysts supported on γ -Al₂O₃ (grey) with CuLaO₂ (◇), CuO (▲), Cu₂O (◆), Cu⁰ (▽), γ -Al₂O₃ (●), CuAl₂O₄ (★) and CuAlO₂ (*).

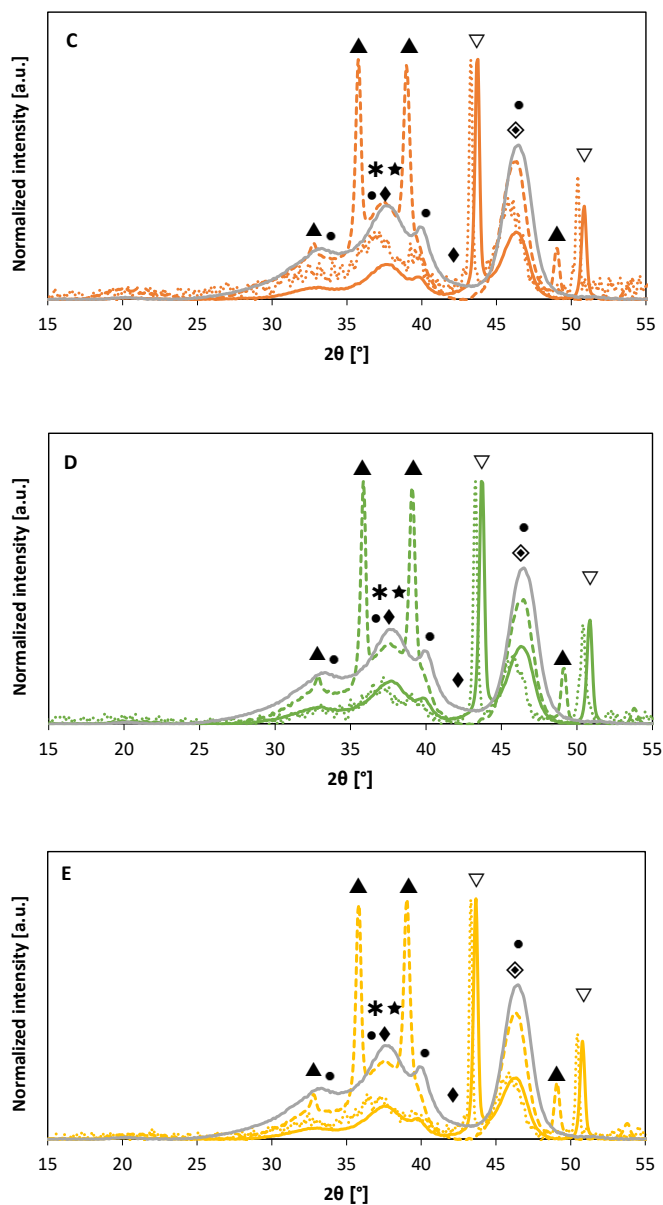


Figure 3.2 (continued). XRD patterns of the calcined (dashed lines), in-situ reduced (full lines) and spent (dotted lines) Cu (A, black), Ba-Cu (B, blue), Ce-Cu (C, orange), Cs-Cu (D, green) and La-Cu (E, yellow) catalysts supported on γ - Al_2O_3 (grey) with CuLaO_2 (\diamond), CuO (\blacktriangle), Cu_2O (\blackstar), Cu^0 (∇), γ - Al_2O_3 (\bullet), CuAl_2O_4 (\star) and CuAlO_2 (\times).

In summary, the impregnation of a co-metal and Cu has no significant effect on the textural properties of the calcined catalyst. The dopant metals are well dispersed as they were not detectable with XRD, while the Cu particles are mostly present as a CuO phase.

3.2.2 Reduced catalyst characterization

Various authors reported Cu⁰ to be the active phase for glycerol hydrogenolysis.⁴⁻⁸ Therefore, the catalysts in their reduced state were characterized, according to the procedures described in Chapter 2.

The crystalline structure of the bare Cu and doped Cu/ γ -Al₂O₃ catalysts was investigated by XRD. After *in-situ* reduction with H₂/He, all CuO peaks disappeared and, as could reasonably be expected, new peaks corresponding to Cu⁰ (JCPDS 00-004-0836) became visible, see Figure 3.2.^{7, 9} Various authors reported this to be the active phase for hydrogenolysis.⁴⁻⁸ Since the diffraction peaks of Cu₂O overlap with those of the support, it was again concluded that Cu₂O is either highly dispersed, highly amorphous or not present at all. Based on the Scherrer equation, the calculated Cu⁰ crystallite sizes ranged from 40 nm to 75 nm, suggesting a sintering of the Cu particles upon reduction.

N₂O adsorption revealed that the specific metallic area of Cu⁰ surface atoms, MSA_{Cu⁰}, see Chapter 2 section 2.1.2.3.2, decreased upon doping with Ba, Ce and Cs,¹⁰ while it increased by doping with La, see Table 3.2. For Ba-doping this differs from the results obtained on Ba-doped Ru-based catalysts, for which Ba-doping increased the concentration of active sites.¹¹⁻¹³ Calculated diameters of the Cu⁰ aggregates, ϕ_{Cu^0} , were below 2 nm for bare Cu and La-Cu catalysts. However, for the other doped catalysts, it amounted to 3.0 - 4.5 nm. This is a pronounced difference compared to the calculated Cu⁰ crystallites based on the Scherrer equation (40 - 75 nm), which effect can be attributed to the different characterization methods. The determination of the Cu aggregates size with N₂O adsorption takes all the surface Cu species, including the amorphous ones, into account, while XRD detects crystalline phases in the bulk. The presence of a few big bulk particles, which contain a relatively high amount of Cu compared to a lot of very small Cu particles, can give rise to the Cu⁰ particle sizes as detected by XRD. The diameter of the Cu⁰ aggregates, ϕ_{Cu^0} , is considered to be more relevant, as the population of the smaller particles will be larger. The Cu dispersion, D_{Cu} , was calculated from the amount of H₂ consumed in the s-TPR analysis, as described in Chapter 2 section 2.1.2.3.2. It defines the ratio of the total number of Cu surface atoms to the total number of Cu atoms. For the bare Cu catalyst, a dispersion around 11 % was obtained. Ba-, Ce- and Cs-doping decreased the dispersion in the range of 5 - 8 %, while La-doping slightly increased the dispersion up to 13 %. A lower dispersion can indicate that the Cu metal is more difficult to reduce, *e.g.* due to a strong interaction with the support.¹⁴

Table 3.2. Physical properties of the reduced, bare Cu and doped Cu/ γ -Al₂O₃ catalysts.

	Cu	Ba-Cu	Ce-Cu	Cs-Cu	La-Cu
d_{Cu^0} [nm] ^a	75	50	48	42	52
Degree of reduction [%] ^b	78	89	87	82	89
MSA_{Cu^0} [m ² g ⁻¹ cat] ^c	24	10	10	15	25
ϕ_{Cu^0} [nm] ^c	1.8	4.3	4.5	3.0	1.7
D_{Cu^0} [%] ^c	11	5.1	5	7.9	13
Total acid sites [μ mol g ⁻¹] ^d	60	61	61	40	55

^a determined by XRD patterns using the Scherrer's equation

^b determined from H₂-TPR

^c determined via dissociative N₂O adsorption

^d determined via NH₃-TPD

To elucidate the nature of the Cu species and the effect of the dopants on the reduction behavior in the catalysts, a TPR experiment was performed, according to the procedure found in Chapter 2 section 2.1.2.3.1, of which the profiles are shown in Figure 3.3. The presence of different peaks indicates that the reduction occurs in various consecutive steps. The first reduction peak, α , might be ascribed to highly dispersed CuO species¹⁵ and/or (Cu-O-Cu)²⁺ species¹⁶, the second reduction peak, β , to the reduction of CuO particles with weak support interactions^{6, 17} and the last reduction peak, γ , to bulk CuO^{6, 15, 17}. A small peak, β' , is ascribed to CuO particles with strong support interactions.^{6, 17} It can be seen that La brings the reduction temperature of the first reduction peak, α , down. This decrease in reduction temperature can be attributed to the increased dispersion of Cu species and the smaller ϕ_{Cu^0} , as observed in Table 3.2^{18, 19}. The Ce- and Cs-doped catalyst showed a shift in the CuO species with weak support interactions (β) and even no CuO species with strong support interactions (β') were present. Gamarra *et al.*²⁰ and Malleshham *et al.*²¹ found that Cu species that interact with Ce species are more easily reduced, which is in agreement with the TPR-profile. The Ba-doped catalyst has the highest amount of bulk CuO species and CuO particles with strong support interactions (β'). This could be the reason for the lower dispersion of the Ba-doped catalyst. From Table 3.2, it can be concluded that all doped catalysts showed an increased hydrogen uptake, resulting in higher degree of reduction in comparison to the bare Cu catalyst. Notwithstanding, the difference in the degree of reduction of the doped catalysts, is rather small.

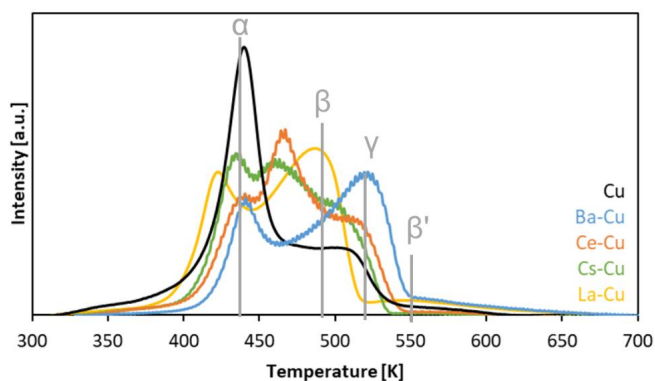


Figure 3.3. H₂-TPR profile of the Cu (black), Ba-Cu (blue), Ce-Cu (orange), Cs-Cu (green) and La-Cu catalyst (yellow).

The acidity of the bare support and the supported Cu-based catalysts was characterized by NH₃-TPD, see Chapter 2, section 2.1.2.3.3, and shown in Table 3.2. The γ -Al₂O₃ supported has an acidity of 50 $\mu\text{mol}_{\text{NH}_3} \text{g}^{-1}_{\text{cat}}$. The acid site distribution are overall similar for all catalysts, as can be observed in Figure 3.4. The catalysts exhibit three desorption peaks, corresponding to weak (*ca.* 500 K), moderate (between *ca.* 550 and 650 K), and strong (> 660 K) acid sites. The total number of acid sites decreased upon Cs-doping compared to the Cu catalyst. Ba and Ce significantly increased the strong acid sites, contrary to La, where the weak and moderate acid site increased. However, one should keep in mind that no conclusion can be made on the nature of the acid sites.

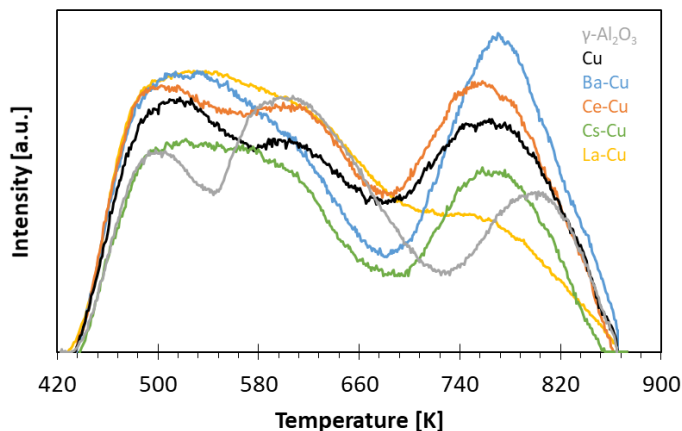


Figure 3.4. NH₃-TPD profile of the calcined γ -alumina support (grey), Cu (black), Ba-Cu (blue), Ce-Cu (orange), Cs-Cu (green) and La-Cu catalyst (yellow).

In summary for the reduced catalysts, most of the species are Cu⁰, as the degree of reduction exceeds 78 %. The average diameter of the Cu⁰ aggregates varied between 1.7 and 4.5 nm. The La-doped

catalysts exhibited the smallest Cu^0 aggregates with the highest dispersion. Ba-, Ce- and La-doping slightly increased the total number of acid sites, compared to the bare Cu catalyst.

3.2.3 Catalyst performance

Catalytic experiments were performed on HTK-MI setup, a detailed description of the setup can be found in section 2.1.3.1 (Chapter 2). The catalyst's activity was measured within the intrinsic kinetic regime, as defined in section 2.1.3.2 (Chapter 2). The fixed-bed reactor was operated in the trickle-bed regime at 473 K, 7.5 MPa, an inlet molar H_2 to glycerol ratio of 7 and a space time τ'' of 135 $\text{kg}_{\text{cat}} \text{s mol}^{-1}_{\text{glycerol}}$. Figure 3.5 shows the performance, calculated according to the procedures in Chapter 2 section 2.1.3.1.4, in terms of the glycerol conversion and 1,2-propanediol selectivity of the investigated catalysts over a period of 68 hours. Doping the Cu catalyst did not drastically modify the initial glycerol conversion (ca. 15 %), except for the La-doped catalyst (ca. 8 %). The slightly higher conversion for the Ba- and Ce-doped catalyst could be attributed to an increase in acid site concentration.²²⁻²⁴ The catalysts in this work, investigated under pure liquid phase glycerol, exhibited comparable space time yield as a commercial Cu catalyst investigated for liquid phase glycerol hydrogenolysis in continuous, fixed bed operation ($8 \cdot 10^{-4} \text{ mol}_{1,2\text{-PD}} \text{ s}^{-1} \text{ kg}_{\text{cat}}^{-1}$ - $1 \cdot 10^{-3} \text{ mol}_{1,2\text{-PD}} \text{ s}^{-1} \text{ kg}_{\text{cat}}^{-1}$ vs. $1 \cdot 10^{-3} \text{ mol}_{1,2\text{-PD}} \text{ s}^{-1} \text{ kg}_{\text{cat}}^{-1}$, respectively).²⁵

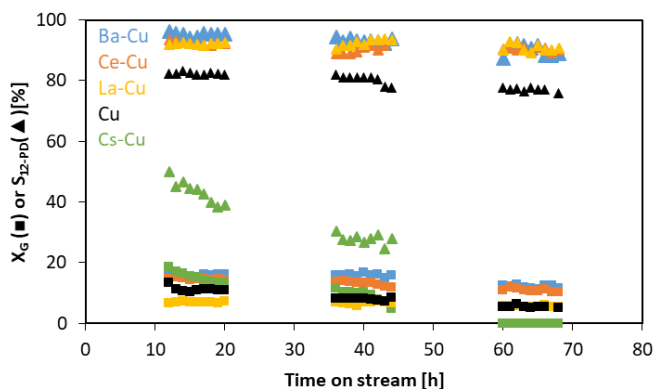


Figure 3.5. Glycerol conversion (■) and 1,2-propanediol selectivity (▲) at 473 K, 7.5 MPa, $135 \text{ kg}_{\text{cat}} \text{ s mol}^{-1}_{\text{glycerol}}$ and $7 \text{ mol}_{\text{H}_2} \text{ mol}^{-1}_{\text{glycerol}}$ for the Cu (black), Ba-Cu (blue), Ce-Cu (orange), Cs-Cu (green) and La-Cu (yellow) catalysts supported on $\gamma\text{-Al}_2\text{O}_3$.²⁶

Concerning the catalyst stability, see Figure 3.5, the bare Cu-catalyst exhibited a noticeable deactivation during 68 h on stream, as well as the Cs-doped catalyst, which deactivated even faster. Conversely, the Ba-, Ce- and La-doped catalysts were more stable than the bare Cu-catalyst, which was attributed to the stabilization of the Cu^0 particle size during the reaction (as discussed in section 3.2.4).

Doping the bare Cu-catalyst had no pronounced effect on the overall catalyst activity in terms of initial glycerol conversion. Ba, Ce and La doping increased the 1,2-propanediol selectivity compared to the bare Cu catalyst. Those dopants, hence, exhibit properties of a structural promotor (Chapter 1 section 1.5.3.2). Furthermore, the catalyst stability, in terms of glycerol conversion, 1,2-propanediol selectivity and Cu⁰ particle size, in terms of the average diameter of the Cu⁰ aggregates (which is discussed in section 3.2.4), was improved by incorporation of these dopants. Their effect on the catalyst and more specific on the Cu⁰ particle, is discussed in the next section.

3.2.4 Spent catalyst characterization

After testing the catalysts' performances for 68 h TOS at 473 K, 7.5 MPa, an inlet molar H₂ to glycerol ratio of 7 and a space time τ' of 135 kg_{cat} s mol⁻¹_{glycerol} in glycerol hydrogenolysis (see section 3.2.3), the catalysts are denoted as "spent".

The metal content of the spent catalysts is shown in Table 3.4. On all catalysts between 6 wt.% (La-doped) and 35 wt.% (Cs-doped) of Cu has been lost (Table 3.4 cf. Table 3.1). The La-containing catalyst also exhibits the lowest co-metal leaching. Even though there was leaching, the significant deactivation of Cs-doped catalyst, which is observed in section 3.2.3, could not be correlated to the loss of active phase. As the amount of leached metal did not correspond to the decrease in activity over the investigated time frame, additional leaching seems to be part of a run-in phase of the catalyst.

Table 3.4. Physical properties of the spent (i.e. after 68 h TOS), bare Cu and doped Cu/ γ -Al₂O₃ catalysts.

	Cu	Ba-Cu	Ce-Cu	Cs-Cu	La-Cu
Cu loading [wt.%] ^a	5.39	5.76	6.38	5.37	7.47
Co-metal loading [wt.%] ^a	n.a.	0.16	0.57	0.09	0.84
d_{Cu^0} [nm] ^b	135	91	102	200	66
MSA_{Cu^0} [m ² g ⁻¹ _{cat}] ^c	0.3	3	3	0.3	3
Φ_{Cu^0} [nm] ^c	127	10	13	116	14
D_{Cu^0} [%] ^c	0.2	2.1	1.7	0.2	5.4
Weight loss <625 K [%] ^d	27	23	8	10	4
Weight loss >625 K [%] ^d	1	3	1	2	1

^a calculated from the results obtained by ICP-OES

^b determined by XRD patterns using the Scherrer's equation

^c determined via dissociative N₂O adsorption

^d determined using TGA

The possible structural changes of the catalyst due to the exposure to reaction conditions were investigated by XRD (Figure 3.2). No significant changes in phases were identified. Based on the Scherrer equation, an increase in Cu⁰ crystallite size of the spent catalyst was observed (comparison between Table 3.4 and Table 3.2). The sintering of the Cu species was also evident from the average diameter of the aggregates, Φ_{Cu^0} , which increased up to two orders of magnitude (i.e. from 1.7 nm to 127 nm for the bare Cu-catalyst). As a result, one can clearly see that the spent Cu⁰ surface area, decreased compared to the reduced catalysts for all samples. It is noteworthy that Ba-, Ce- and

La-doping reduced the sintering of the Cu⁰, based on the average diameter of the aggregates, by one order of magnitude compared to the bare Cu-catalyst.

To quantify the carbonaceous species deposited on the spent catalyst, a TGA (see Chapter 2, section 2.1.2.7) was performed. The spent catalysts were not pretreated before the analysis. Figure 3.7 presents the TGA profiles of the catalysts after 68 h TOS. Based on literature, the carbon forms may be classified in terms of oxidation temperature as “light” coke (below 625 K), amorphous carbon (between 625 K and 825 K) or non-reactive graphitic carbon species (above 825 K).^{27,28} Weight losses for pure glycerol, propylene glycol and ethylene glycol have been reported respectively in the following temperature ranges: 473-523 K^{29,30}, 360-430 K³⁰ and 400-473 K³⁰. The weight gain as a result of Cu oxidation to CuO is situated at 723-903 K³¹. As can be seen from Figure 3.7, the most pronounced weight loss is situated around 573 K and most likely originates from remaining adsorbed components on the catalyst and “light coke”. Therefore, only the weight loss above 625 K was considered as coke, see Table 3.4. The weight loss of 1 wt.% to 3 wt.% suggests that coke formation is minimal. Correspondingly, it is concluded that sintering of the Cu species is the main reason for deactivation of the catalysts.

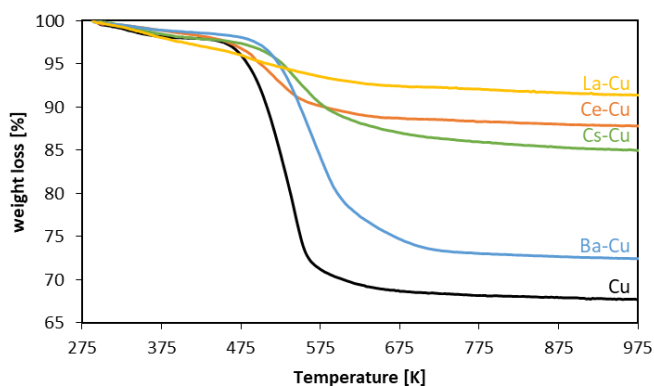


Figure 3.7. TGA-profiles of the spent Cu (black), Ba-Cu (blue), Ce-Cu (orange), Cs-Cu (green) and La-Cu (yellow) catalysts.

Exposure to reaction conditions has not caused significant changes in the crystalline phases. The extend of the Cu and co-metal leaching in all catalysts, was in the same order of magnitude, excluding leaching as mean deactivation mechanism. Further, the coke formation was around 1-3 wt.% for all catalysts, indicating that a minor amount of cokes was formed during the reaction on the catalysts. However, a significant change in Cu particle size was observed in the spent catalysts. The sintering of the Cu particles was slowed down by the presence of co-metals. Nonetheless, it can be concluded that the deactivation occurred due to sintering of the Cu particles.

3.2.5 The role of Cu⁰ particle size

Figure 3.8 depicts the combined results from catalytic performance and characterization of the catalysts. A clear relationship between the average diameter of the Cu⁰ aggregates, ϕ_{Cu^0} , (of both the reduced and the spent catalyst) and the TOF was established, showing that glycerol hydrogenolysis is a structure sensitive reaction³² for Cu-based catalysts supported on γ -alumina, which is in line with the conclusions made on SiO₂ supported catalysts.^{33,34}

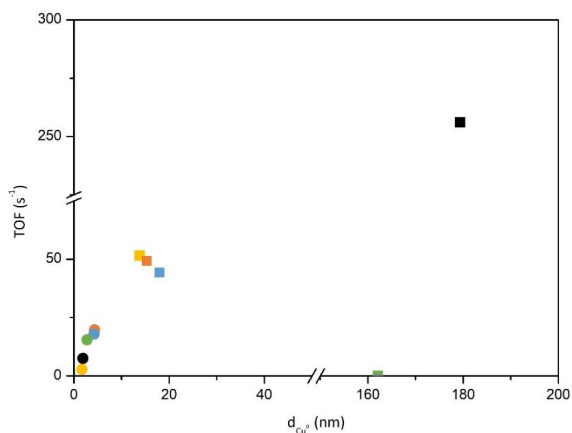


Figure 3.8. TOF as function of the average diameter of the Cu⁰ aggregates, ϕ_{Cu^0} , at 12 h (●) and 68 h (■) TOS for pure glycerol hydrogenolysis for the Cu (black), Ba-Cu (blue), Ce-Cu (orange), Cs-Cu (green) and La-Cu (yellow) catalysts supported on γ -Al₂O₃.

The only exception is the Cs-doped catalyst for which no glycerol conversion was observed, even though the particle size only increased by 50 while that of bare Cu grew 100-fold. Hence, modification of Cu properties, other than particle size, must have occurred. For all the other catalysts, it is worth noting that the Cu⁰ particle size increased only fourfold for the Ba- and Ce-doped ones, and eight times for the La-doped one. Thus, those dopants stabilize the Cu⁰ particle and act as textural promoters, as well as structural promoters (Chapter 1 section 1.5.3.2).

3.3 Conclusions

Ba-, Ce-, Cs- and La-doped Cu/ γ -Al₂O₃ catalysts were evaluated for liquid phase glycerol hydrogenolysis to 1,2-propanediol in comparison to the bare Cu/ γ -Al₂O₃ catalyst. Characterization revealed that the incorporation of the dopants on the Cu-catalyst did not significantly change the physicochemical properties of the calcined catalyst. The bare Cu-catalyst exhibited pronounced deactivation after 68 h, while the Ba-, Ce- and La-doped catalysts remained almost stable in terms of glycerol conversion over time. Conversely, the observed catalyst deactivation could be assigned to sintering and not by coke formation. It was found that dopants stabilized the Cu⁰ particle size during reaction, inhibiting sintering. Where the particle size, as determined by dissociative N₂O adsorption, of

the spent bare Cu catalyst increased up to a factor 100 compared to the freshly reduced one, a maximum increase of one order of magnitude was observed for the doped catalysts. Moreover, these doped catalysts revealed increased the selectivity towards 1,2-propanediol. Therefore, Ba, Ce and La act both as structural and textural promoters. The change in Cu⁰ particle size led to a linear increase of the TOF revealing that the Cu/ γ -Al₂O₃ catalysts can be considered as structure sensitive for the liquid glycerol hydrogenolysis reaction.

As the La-doped catalyst improved most the catalytic stability by inhibiting sintering of the Cu⁰ particle, which is the main deactivation reason of Cu catalyst, its promotion will be further investigated in Chapter 4.

3.4 References

- 1 H. Al-Megren, *Petrochemical Catalyst Materials, Processes, and Emerging Technologies*, IGI Global 2016.
- 2 A.B. Miller, M. Raghunath, V. Sokolovskii, C.G. Lugmair, J. Anthony F. Volpe, W. Shen, W. Turbeville, *Catalyst for Polyol Hydrogenolysis*, US20140249334A1, 2014.
- 3 M. Trueba, S.P. Trasatti, γ -Alumina as a Support for Catalysts: A Review of Fundamental Aspects, *European journal of inorganic chemistry*, 2005 (2005) 3393-3403.
- 4 E. Vasiliadou, A. Lemonidou, *Kinetic Study of Liquid-Phase Glycerol Hydrogenolysis over Cu/Sio 2 Catalyst*, *Chemical Engineering Journal*, 231 (2013) 103-112.
- 5 S. Sato, M. Akiyama, R. Takahashi, T. Hara, K. Inui, M. Yokota, *Vapor-Phase Reaction of Polyols over Copper Catalysts*, *Applied Catalysis A: General*, 347 (2008) 186-191.
- 6 Z. Huang, F. Cui, H. Kang, J. Chen, X. Zhang, C. Xia, *Highly Dispersed Silica-Supported Copper Nanoparticles Prepared by Precipitation– Gel Method: A Simple but Efficient and Stable Catalyst for Glycerol Hydrogenolysis*, *Chemistry of Materials*, 20 (2008) 5090-5099.
- 7 L. Guo, J. Zhou, J. Mao, X. Guo, S. Zhang, *Supported Cu Catalysts for the Selective Hydrogenolysis of Glycerol to Propanediols*, *Applied Catalysis A: General*, 367 (2009) 93-98.
- 8 E. Vasiliadou, A. Lemonidou, *Investigating the Performance and Deactivation Behaviour of Silica-Supported Copper Catalysts in Glycerol Hydrogenolysis*, *Applied Catalysis A: General*, 396 (2011) 177-185.
- 9 A. Wolosiak-Hnat, E. Milchert, B. Grzmil, *Influence of Parameters on Glycerol Hydrogenolysis over a Cu/Al₂O₃ Catalyst*, *Chemical Engineering & Technology*, 36 (2013) 411-418.
- 10 J.S. Moura, J.d.S.L. Fonseca, N. Bion, F. Epron, T.d.F. Silva, C.G. Maciel, J.M. Assaf, M.d.C. Rangel, *Effect of Lanthanum on the Properties of Copper, Cerium and Zirconium Catalysts for Preferential Oxidation of Carbon Monoxide*, *Catalysis Today*, 228 (2014) 40-50.
- 11 I. Rossetti, N. Pernicone, L. Forni, *Promoters Effect in Ru/C Ammonia Synthesis Catalyst*, *Applied Catalysis A: General*, 208 (2001) 271-278.
- 12 D. Szmigiel, H. Bielawa, M. Kurtz, O. Hinrichsen, M. Muhler, W. Raróg, S. Jodzis, Z. Kowalczyk, L. Znak, J. Zieliński, *The Kinetics of Ammonia Synthesis over Ruthenium-Based Catalysts: The Role of Barium and Cesium*, *Journal of Catalysis*, 205 (2002) 205-212.
- 13 S.E. Siporin, R.J. Davis, *Isotopic Transient Analysis of Ammonia Synthesis over Ru/Mgo Catalysts Promoted by Cesium, Barium, or Lanthanum*, *Journal of Catalysis*, 222 (2004) 315-322.
- 14 J.J.F. Scholten, *Metal Surface Area and Metal Dispersion in Catalysts*, in: B. Delmon, P. Grange, P. Jacobs, G. Poncelet (Eds.) *Studies in Surface Science and Catalysis*, Elsevier 1979, pp. 685-714.
- 15 M. Behrens, S. Zander, P. Kurr, N. Jacobsen, J.r. Senker, G. Koch, T. Ressler, R.W. Fischer, R. Schlögl, *Performance Improvement of Nanocatalysts by Promoter-Induced Defects in the Support Material: Methanol Synthesis over Cu/Zno: Al*, *Journal of the American Chemical Society*, 135 (2013) 6061-6068.
- 16 A. Yin, X. Guo, W.-L. Dai, K. Fan, *The Nature of Active Copper Species in Cu-Hms Catalyst for Hydrogenation of Dimethyl Oxalate to Ethylene Glycol: New Insights on the Synergetic Effect between Cu₀ and Cu⁺*, *The Journal of Physical Chemistry C*, 113 (2009) 11003-11013.
- 17 M.L. Dieuzeide, R. de Urriaga, M. Jobbagy, N. Amadeo, *Vapor Phase Hydrogenolysis of Glycerol to 1,2-Propanediol at Atmospheric Pressure over Copper Catalysts Supported on Mesoporous Alumina*, *Catalysis Today*, 296 (2017) 19-25.
- 18 K.W. Siew, H.C. Lee, J. Gimbin, C.K. Cheng, *Characterization of La-Promoted Ni/Al₂O₃ Catalysts for Hydrogen Production from Glycerol Dry Reforming*, *Journal of Energy Chemistry*, 23 (2014) 15-21.
- 19 A. Iriondo, V.L. Barrio, J.F. Cambra, P.L. Arias, M.B. Güemez, R.M. Navarro, M.C. Sánchez-Sánchez, J.L.G. Fierro, *Hydrogen Production from Glycerol over Nickel Catalysts Supported on Al₂O₃ Modified by Mg, Zr, Ce or La*, *Topics in Catalysis*, 49 (2008) 46.
- 20 D. Gamarra, C. Belver, M. Fernández-García, A. Martínez-Arias, *Selective Co Oxidation in Excess H₂ over Copper– Ceria Catalysts: Identification of Active Entities/Species*, *Journal of the American Chemical Society*, 129 (2007) 12064-12065.

- 21 B. Mallesham, P. Sudarsanam, B.V.S. Reddy, B.M. Reddy, Development of Cerium Promoted Copper–Magnesium Catalysts for Biomass Valorization: Selective Hydrogenolysis of Bioglycerol, *Applied Catalysis B: Environmental*, 181 (2016) 47-57.
- 22 R. Mane, A. Ghalwadkar, A. Hengne, Y. Suryawanshi, C. Rode, Role of Promoters in Copper Chromite Catalysts for Hydrogenolysis of Glycerol, *Catalysis Today*, 164 (2011) 447-450.
- 23 W. Yu, J. Zhao, H. Ma, H. Miao, Q. Song, J. Xu, Aqueous Hydrogenolysis of Glycerol over Ni–Ce/Ac Catalyst: Promoting Effect of Ce on Catalytic Performance, *Applied Catalysis A: General*, 383 (2010) 73-78.
- 24 I. Jiménez-Morales, F. Vila, R. Mariscal, A. Jiménez-López, Hydrogenolysis of Glycerol to Obtain 1,2-Propanediol on Ce-Promoted Ni/Sba-15 Catalysts, *Applied Catalysis B: Environmental*, 117-118 (2012) 253-259.
- 25 T. Rajkhowa, G.B. Marin, J.W. Thybaut, A Comprehensive Kinetic Model for Cu Catalyzed Liquid Phase Glycerol Hydrogenolysis, *Applied Catalysis B: Environmental*, 205 (2017) 469-480.
- 26 A. Bouriakova, P.S.F. Mendes, B. Katryniok, J. De Clercq, J.W. Thybaut, N₂-Sorption and Catalytic Results of Doped Cu-Catalysts for Glycerol Hydrogenolysis, 2020.
- 27 S.M.M. Nataj, S.M. Alavi, G. Mazloom, Modeling and Optimization of Methane Dry Reforming over Ni–Cu/Al₂O₃ Catalyst Using Box–Behnken Design, *Journal of Energy Chemistry*, 27 (2018) 1475-1488.
- 28 Y. Cao, P. Maitarad, M. Gao, T. Taketsugu, H. Li, T. Yan, L. Shi, D. Zhang, Defect-Induced Efficient Dry Reforming of Methane over Two-Dimensional Ni/H-Boron Nitride Nanosheet Catalysts, *Applied Catalysis B: Environmental*, 238 (2018) 51-60.
- 29 M. Almazrouei, S. Elagroudy, I. Janajreh, Transesterification of Waste Cooking Oil: Quality Assessment Via Thermogravimetric Analysis, *Energy Procedia*, 158 (2019) 2070-2076.
- 30 A. Toxqui-Terán, C. Leyva-Porras, M.Á. Ruíz-Cabrera, P. Cruz-Alcantar, M.Z. Saavedra-Leos, Thermal Study of Polyols for the Technological Application as Plasticizers in Food Industry, *Polymers*, 10 (2018) 467.
- 31 R. Valencia, J.A. Tirado, R. Sotelo, F. Trejo, L. Lartundo, Synthesis of 1,2-Propanediol through Glycerol Hydrogenolysis on Cu–Al Mixed Oxides, *Reaction Kinetics, Mechanisms and Catalysis*, 116 (2015) 205-222.
- 32 M.B. Taghavi, G.M. Pajonk, S.J. Teichner, On the Structure-Sensitive and Structure-Insensitive Catalytic Reactions and Their New Characteristics, Demonstrated with Copper-Supported Catalysts, *Journal of Colloid and Interface Science*, 71 (1979) 451-465.
- 33 Y. Wang, J. Zhou, X. Guo, Catalytic Hydrogenolysis of Glycerol to Propanediols: A Review, *RSC Advances*, 5 (2015) 74611-74628.
- 34 E.S. Vasiliadou, T.M. Eggenhuisen, P. Munnik, P.E. de Jongh, K.P. de Jong, A.A. Lemonidou, Synthesis and Performance of Highly Dispersed Cu/Sio₂ Catalysts for the Hydrogenolysis of Glycerol, *Applied Catalysis B: Environmental*, 145 (2014) 108-119.

Supporting information

Table 3.SI.1. Performance of the undoped Cu/ γ -Al₂O₃ catalyst at 473 K, 7.5 MPa, 135 kg_{cat} s mol⁻¹ glycerol and 7 mol_{H₂} mol⁻¹ glycerol as function of TOS.

TOS (h)	X _G (%)	S _{1,2-propanediol} (%)	S _{acetol} (%)	S _{1,2-ethanediol} (%)	S _{others} (%)
12	15	82	15	1	1
13	15	82	15	1	1
14	15	83	15	1	1
15	15	82	15	1	1
16	15	82	15	1	2
17	14	82	14	1	2
18	14	83	14	1	2
19	14	82	14	1	3
20	13	82	13	1	4
36	14	82	14	1	3
37	13	81	13	1	4
38	13	81	13	1	4
39	14	81	14	1	4
40	14	81	14	1	4
41	14	81	14	1	4
42	14	80	14	1	5
43	14	78	14	1	7
44	14	78	14	1	7
60	15	78	15	1	6
61	15	77	15	1	6
62	15	78	15	1	6
63	15	77	15	1	7
64	15	78	15	1	6
65	15	77	15	1	6
66	16	77	16	1	6
68	15	76	15	1	8

Table 3.SI.2. Performance of the Ba-Cu/ γ -Al₂O₃ catalyst at 473 K, 7.5 MPa, 135 kg_{cat} s mol⁻¹_{glycerol} and 7 mol_{H₂} mol⁻¹_{glycerol} as function of TOS.

TOS (h)	X _G (%)	S _{1,2-propanediol} (%)	S _{acetol} (%)	S _{1,2-ethanediol} (%)	S _{others} (%)
12	16	96	2	2	1
13	16	96	2	2	1
14	16	95	1	3	1
15	15	94	3	2	1
16	15	94	2	2	1
17	16	96	2	2	1
18	16	95	2	2	1
19	16	95	2	2	1
20	16	95	2	2	1
36	16	94	2	2	1
37	16	93	3	3	2
38	16	94	3	3	1
39	16	93	3	3	1
40	17	93	3	3	1
41	16	93	3	3	1
42	16	93	3	3	1
43	15	92	3	4	1
44	16	94	3	2	1
60	12	87	2	8	2
61	12	92	3	4	1
62	13	92	3	4	1
63	12	92	3	5	1
64	12	91	3	5	1
65	11	92	3	4	1
66	12	88	5	6	1
68	12	88	3	7	2

Table 3.SI.3. Performance of the Ce-Cu/ γ -Al₂O₃ catalyst at 473 K, 7.5 MPa, 135 kg_{cat} s mol⁻¹ glycerol and 7 mol_{H₂} mol⁻¹ glycerol as function of TOS.

TOS (h)	X _G (%)	S _{1,2-propanediol} (%)	S _{acetol} (%)	S _{1,2-ethanediol} (%)	S _{others} (%)
12	15	93	4	2	1
13	15	93	4	2	1
14	15	93	4	2	1
15	14	92	4	3	1
16	15	92	3	4	1
17	15	92	4	3	1
18	14	92	4	3	1
19	15	93	4	2	1
20	14	92	5	2	1
36	14	89	4	5	1
37	14	89	5	5	1
38	14	89	5	4	1
39	13	89	5	5	1
40	13	91	3	4	1
41	13	91	2	5	2
42	13	90	4	4	1
43	12	92	3	4	1
44	12	93	3	3	1
60	11	91	2	6	1
61	12	91	4	5	1
62	11	90	3	6	1
63	11	91	3	5	1
64	11	90	3	6	1
65	11	91	4	4	1
66	11	91	4	4	1
68	10	89	3	6	2

Table 3.SI.4. Performance of the Cs-Cu/ γ -Al₂O₃ catalyst at 473 K, 7.5 MPa, 135 kg_{cat} s mol⁻¹_{glycerol} and 7 mol_{H₂} mol⁻¹_{glycerol} as function of TOS.

TOS (h)	X _G (%)	S _{1,2-propanediol} (%)	S _{acetol} (%)	S _{1,2-ethanediol} (%)	S _{others} (%)
12	18	50	40	7	3
13	17	45	43	8	3
14	16	47	43	7	3
15	15	44	46	7	2
16	15	44	46	8	2
17	14	43	47	7	3
18	14	40	49	9	3
19	13	38	49	9	4
20	13	39	48	10	3
36	12	30	55	12	3
37	10	28	57	11	4
38	10	27	58	10	4
39	10	29	56	8	8
40	10	27	54	8	12
41	9	28	61	8	2
42	8	29	62	7	2
43	7	25	52	10	14
44	5	28	53	8	11
60	0	n.a.	n.a.	n.a.	n.a.
61	0	n.a.	n.a.	n.a.	n.a.
62	0	n.a.	n.a.	n.a.	n.a.
63	0	n.a.	n.a.	n.a.	n.a.
64	0	n.a.	n.a.	n.a.	n.a.
65	0	n.a.	n.a.	n.a.	n.a.
66	0	n.a.	n.a.	n.a.	n.a.
68	0	n.a.	n.a.	n.a.	n.a.

Table 3.SI.5. Performance of the La-Cu/ γ -Al₂O₃ catalyst at 473 K, 7.5 MPa, 135 kg_{cat} s mol⁻¹ glycerol and 7 mol_{H₂} mol⁻¹ glycerol as function of TOS.

TOS (h)	X _G (%)	S _{1,2-propanediol} (%)	S _{acetol} (%)	S _{1,2-ethanediol} (%)	S _{others} (%)
12	7	92	1	5	2
13	7	92	1	3	3
14	7	92	2	5	1
15	7	92	1	5	2
16	7	92	1	5	1
17	7	92	2	5	1
18	7	92	2	4	2
19	7	92	2	4	3
20	7	93	2	4	2
36	7	90	1	6	3
37	7	92	1	5	2
38	6	92	2	5	2
39	6	93	1	4	2
40	7	92	2	4	2
41	7	93	2	3	2
42	7	94	2	3	2
43	7	94	2	3	2
44	7	93	2	3	2
60	6	90	1	6	2
61	6	93	2	3	2
62	6	93	2	4	2
63	6	90	2	5	3
64	5	89	2	6	3
65	5	92	2	5	2
66	6	90	2	6	2
68	5	90	2	7	1

CHAPTER 4.
EFFECT OF LA PROMOTION ON Al_2O_3
SUPPORTED CU SPECIES FOR
GLYCEROL HYDROGENOLYSIS

4.1 Introduction

Currently, Cu-based catalysts are mainly used to perform selective glycerol hydrogenolysis to 1,2-propanediol. However, bare Cu is known to suffer from unsatisfactory activity and stability.¹ Promoters were reported to particularly increase the catalytic stability.² Modification of Cu/ γ -Al₂O₃ catalysts with La, resulted in an improved catalytic stability, as was discussed in Chapter 3.

To convert glycerol into 1,2-propanediol, one oxygen atom is removed in the form of H₂O from glycerol and one hydrogen atom is added. As stated in Chapter 1 section 1.4 there are two main mechanisms for the formation of 1,2-propanediol: the dehydration-hydrogenation mechanism (acidic medium)^{3, 4} or the dehydrogenation-dehydration-hydrogenation mechanism (alkaline medium)⁵. It is commonly accepted that γ -Al₂O₃ has intrinsic acidity.⁶ Cu^{δ+} sites are considered as Lewis acidic because of their high electron affinity.⁷⁻¹³ Therefore, it can be assumed that glycerol hydrogenolysis over a Cu/ γ -Al₂O₃ catalyst proceeds according to the dehydration-hydrogenation mechanism. In literature, there is no consensus on the active site in the hydrogenolysis reaction nor on the origin of the acidity. On the one hand, various researchers are convinced that Cu⁰ is the active site for both steps in the dehydration-hydrogenation mechanism.¹⁴⁻¹⁷ As discussed in section 1.5.3 (Chapter 1), other researchers believe in the synergetic effect between Cu⁺ and Cu⁰, or the role of Cu⁺ as active site.^{10, 12, 18-22} To elucidate the role of the different Cu species, controllable preparation of catalysts with various Cu⁺ or Cu⁰ amounts is necessary. La₂O₃ was found to modify the Cu⁺ and Cu⁰ sites in Cu/SiO₂ catalysts.^{23, 24} Nevertheless, no literature has been published regarding the effect of La promotion on Cu species in γ -Al₂O₃ supported catalysts for glycerol hydrogenolysis.

In this chapter, a series of La-Cu catalysts were prepared by sequential impregnation. By varying the La and Cu loading, 12 different promotion ratios were assessed to modify the Cu⁺ and Cu⁰ species. The catalysts were comprehensively characterized by various techniques including ICP, BET, (*in situ*) XRD, N₂O adsorption, H₂-TPR, NH₃-TPD, XPS and STEM-EDX. Liquid phase glycerol hydrogenolysis was performed in a fixed bed reactor operated in trickle flow regime to study the catalytic performance of five selected La-Cu catalysts in comparison to bare Cu. The La-Cu with respectively the highest and lowest MSA_{Cu^0} were selected. The two La-Cu catalysts that showed the same MSA_{Cu^0} as the bare Cu catalyst but different Cu particle sizes, were chosen as well. Finally, the effect of particle size of catalyst at equal promotor ratio was assessed. The effect of the La/Cu ratio was investigated by comparing the surface species, catalysts activity, TOF, glycerol conversion and 1,2-propanediol selectivity to a bare Cu catalyst and between the La/Cu catalysts themselves. The catalysts stability was investigated by comparing the Cu⁰ particle size *prior* and *post* reaction.

4.2 Results and discussion

4.2.1 Calcined catalyst characterization

Industrially, a high density of active sites on the employed catalysts, which is mostly achieved at high metal loadings, is desirable to maximize the volumetric activity. However, to prove relationships between catalyst structure and catalytic performance, more moderate metal loadings (< 20-25 wt.%) are advisable.^{25, 26} In Chapter 3, it was clear that even a small amount as 1.0 wt.% of La, increased the stability of the Cu catalyst. Therefore, a series of La-Cu/ γ -Al₂O₃ catalysts with nominal La and Cu values: x wt.% La – 10 wt.% Cu ($x = 0, 1.0, 1.5, 2.0$), x wt.% La – y wt.% Cu ($x = 1.5, 2.0, 2.5$ and $y = 15, 20, 25$) were prepared *via* a sequential wet impregnation according to the synthesis method described in section 2.1.1 (Chapter 2) and compared to a 10 wt.% Cu/ γ -Al₂O₃.

The La and Cu loading were determined by ICP-OES, see section 2.1.2.1 (Chapter 2), and are summarized in Table 4.1. The actual La and Cu loading are systematically lower than the nominal ones. This was attributed to the hygroscopic nature of the precursors, leading to an overestimation of the actually introduced amounts during the synthesis. No lanthanum was leached during the synthesis as the La loading in the intermediate La/ γ -Al₂O₃ materials was the same as for the La-Cu/ γ -Al₂O₃ catalyst. The catalysts are referred to as x La- y Cu/ γ -Al₂O₃, whereby x and y are the nominal loadings.

Table 4.1. Comparison of the bulk (determined by ICP) and surface (determined by XPS) metal loading and mass promotor ratio, the BET surface area, the average mesoporous volume, the average pore diameter and crystallite CuO size of the calcined x La- y Cu/ γ -Al₂O₃ catalysts.

	La [wt.%]		Cu [wt.%]		La/Cu		S_{BET}^a	V_{meso}^b	D_p^b	d_{CuO}^c
	ICP	XPS	ICP	XPS	ICP	XPS	[m ² g ⁻¹ _{support}]	[cm ³ g ⁻¹ _{support}]	[nm]	[nm]
Support	n.a.	n.a.	n.a.	n.a.	n.a.	n.a.	185	0.39	6.9	n.a.
10Cu	0.00	0.00	7.59	2.68	0.000	0.00	164	0.40	6.8	30
1.0La-10Cu	0.45	0.88	7.3	5.54	0.062	0.16	174	0.44	6.5	29
1.5La-10Cu	0.70	0.89	7.94	3.71	0.088	0.24	173	0.44	7.2	21
1.5La-15Cu	0.71	1.37	11.91	5.05	0.060	0.27	192	0.45	6.7	24
1.5La-20Cu	0.72	0.75	16.16	4.03	0.045	0.19	185	0.43	6.7	27
1.5La-25Cu	0.60	1.43	15.89	8.92	0.038	0.16	172	0.40	6.6	41
2.0La-10Cu	0.95	1.02	7.39	3.03	0.129	0.34	173	0.38	8.6	22
2.0La-15Cu	0.86	1.38	10.74	4.62	0.080	0.30	188	0.46	6.4	26
2.0La-20Cu	0.83	0.95	13.97	2.85	0.059	0.33	192	0.47	6.5	27
2.0La-25Cu	0.72	1.31	15.67	6.06	0.046	0.22	178	0.47	6.5	31
2.5La-15Cu	0.94	0.47	10.01	3.94	0.094	0.12	188	0.40	6.4	25
2.5La-20Cu	0.92	1.70	13.04	5.73	0.071	0.30	177	0.38	6.5	30
2.5La-25Cu	0.95	1.74	16.49	5.44	0.058	0.32	173	0.42	6.5	40

The support and the catalysts were characterized by N₂ sorption (section 2.1.2.2, Chapter 2). A type-IV N₂-adsorption isotherm was observed for all catalysts (see Figure 4.1 and Figure 4.SI.1), which is expected since the support (PURALOX® γ -Al₂O₃) is mesoporous.²⁷ The presence of the mesopores (2 – 50 nm) is confirmed by pore size distribution (Table 4.1). The hysteresis loops are classified as type H1, which is typical for materials with cylindrical pore channels.²⁸ The BET surface area exhibits a small decrease due to the La and Cu impregnation without a clear trend as function of metal loading or promoter ratio was observed, same for the average mesoporous volume and average pore volume. The first ranged between 164 and 192 m² g⁻¹_{support} (Table 4.1) and the mesoporous volume and mean pore size varied between 0.38 – 0.47 cm³ g⁻¹_{support} and 6.4 – 8.6 nm, respectively (Table 4.1). Therefore, it is concluded that the impregnation of La and Cu has no significant influence on the textural properties of the support.

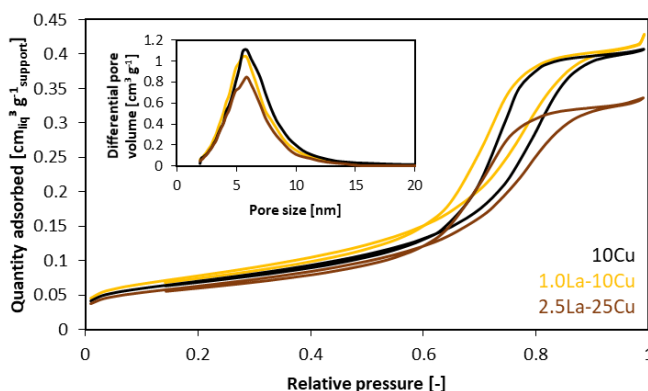


Figure 4.1. N₂-sorption isotherms and differential pore size distribution of the 10Cu catalyst (black), 1.0La-10Cu (yellow) catalyst and 2.5La-25Cu (brown), as representative for the La-Cu catalysts.

The crystalline phases of the catalysts and support were determined via XRD analysis, according to the method described in section 2.1.2.4 (Chapter 2), as shown in Figure 4.2 and Figure 4.SI.2. Broad diffraction peaks for γ -Al₂O₃ at 31.8°, 37.5°, 39.2°, 45.7° (JCPDS 00-050-0741), respectively corresponding to the Al₂O₃₍₂₂₀₎, Al₂O₃₍₃₁₁₎, Al₂O₃₍₂₂₂₎, Al₂O₃₍₄₀₀₎ facets, as present on the support, were detected for all catalysts, see Figure 4.2. This indicates a limited crystallinity of the support. The calcined La-Cu catalysts exhibited main characteristic diffraction peaks of CuO₍₀₀₂₎ at 35.4° and CuO₍₁₁₁₎ at 38.6°, and minor diffraction peaks at 32.5° (CuO₍₋₁₁₀₎), 48.7° (CuO₍₋₂₀₂₎), 51.4° (CuO₍₁₁₂₎) and 53.5° (CuO₍₀₂₀₎), according to JCPDS 00-045-0937. For none of the catalysts, the most characteristic peak of Cu₂O₍₁₁₁₎ at 36.4° (JCPDS 00-005-0667) could be detected. Therefore, it can be deduced that Cu₂O was either highly dispersed or highly amorphous, either present in a very little amount or not at all. Due to a La-loading below 8.5 $\mu\text{mol}_{\text{La}} \text{m}^{-2}$,²⁹ characteristic peaks for lanthanum oxides (La₂O₃, JCPDS 03-065-3185 and LaO, JCPDS 00-033-0716) were not observed. The main diffraction peaks of the mixed Cu-Al phase,

CuAl_2O_4 at 36.8° ($\text{CuAl}_2\text{O}_4(400)$, JCPDS 00-33-0448) and CuAlO_2 at 37.1° ($\text{CuAlO}_2(012)$, JCPDS 01-075-1792), overlapped with the broad diffraction peak for $\text{Al}_2\text{O}_3(311)$. Most likely, those phases were not present, since based on the $\text{CuO-Al}_2\text{O}_3$ phase diagram, they only formed above 773 K.^{30, 31} From the Scherrer equation, the CuO crystallite sizes were calculated in the range of 20 to 40 nm (Table 4.1).

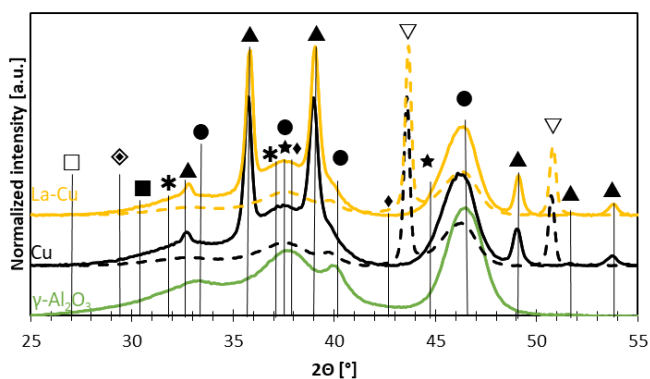


Figure 4.2. XRD pattern of the support (green) and the calcined (full line) and reduced (dashed lines) 10Cu catalyst (black) and 1.0La-10Cu (yellow) catalysts, as representative for the La-Cu catalysts. Phases: with LaO (■), La_2O_3 (□), CuLaO_2 (◇), CuO (▲), Cu_2O (●), Cu (▽), $\gamma\text{-Al}_2\text{O}_3$ (●), CuAl_2O_4 (★) and CuAlO_2 (✱)

The chemical surface composition and oxidation states in the calcined La-Cu catalysts were analyzed *via* XPS, according to the procedures in section 2.1.2.3 (Chapter 2). As XPS is a surface technique, the representativeness of the results to the whole catalyst should be verified by comparing the La/Al and Cu/Al mass ratios determined by XPS (surface composition) to those as determined by ICP (bulk composition), see Table 4.SI.1. Note that the La surface composition almost corresponds to that of the bulk, even though Cu is deposited after La (Figure 5.3A). For all catalysts, it is clear that quite some Cu is present as bulk Cu, rather than being exposed at the surface (Figure 5.3B).

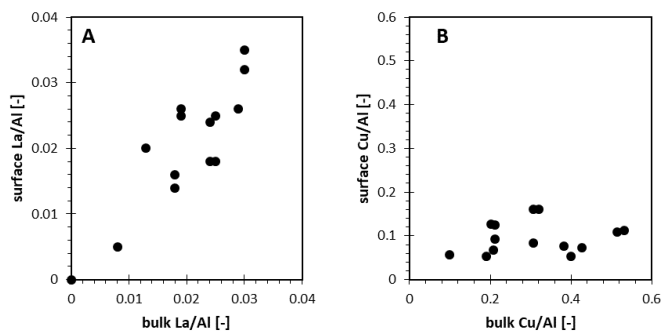


Figure 5.3. Comparison of bulk, determined by ICP-OES, and surface, determined by XPS, La/Cu (A) and Cu/Al (B) mass ratios in the calcined catalysts.

The photoelectron peaks at 932.6 eV were assigned to the binding energy (BE) of Cu 2p_{3/2}, as illustrated in Figure 4.4. The presence of a strong satellite peak between 942 eV and 948 eV is ascribed to a contribution by Cu²⁺. Due to the asymmetry of the Cu 2p_{3/2} peak, one could expect that the Cu²⁺ species are not only ascribed to CuO (933.5 eV), but also to CuAl₂O₄ (935 eV).³² However, no indication of CuAl₂O₄ was found in the O 1s and Al 2p spectra (Figure 4.SI.3) or the XRD diffraction pattern (Figure 4.2 and Figure 4.SI.2). Therefore, the asymmetry is ascribed to the interactions between La and Cu. This interaction is also observed in the La 3d spectra (Figure 4.SI.4A), where the spin-orbit splitting decreases from 4.6 eV to 2.6 eV with increasing La/Cu ratio.

When comparing the Cu 2p_{3/2} BE of the bare Cu catalysts to the La-Cu catalysts, a shift to lower BE was observed (Figure 4.5A, Table 4.SI.1). For a constant Cu loading (*i.e.* the same symbol), the BE decreases with increased La loading (*i.e.* different colors). This may indicate that, as La is added first, the Cu particles are preferentially located next to the La particles rather than covering them, as the bulk La/Al corresponded well with the surface La/Al ratio (Figure 5.3A). The overlap of the d-orbitals of La and Cu creates a strong La-Cu interaction (as also observed in Figure 4.SI.4A), resulting in a shift to lower BE for Cu 2p_{3/2}.³³ The latter can lead to the formation of Cu species with a lower oxidation state, such as Cu⁺, which is in agreement with the observations by *in situ* XRD (see further in Figure 4.9).

As such, the relative amount of Cu²⁺ decreases with the increasing percentage of surface La and varies between 100% and 80% (Figure 4.5B, Table 4.SI.1), in which the remaining Cu species are Cu⁺. The observed trends are an interplay between the La-Cu interactions and the CuO particle size (Table 4.1).

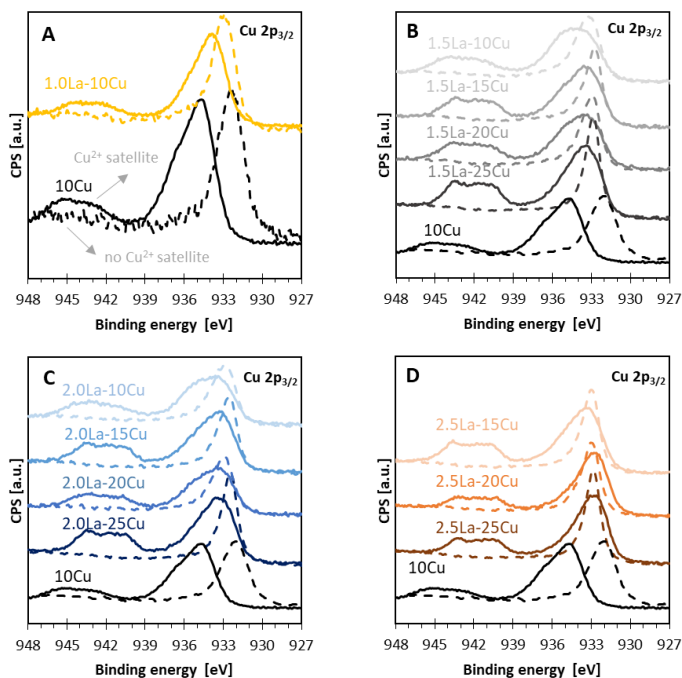


Figure 4.4. $\text{Cu } 2p_{3/2}$ spectra of calcined (full line) and reduced (dashed line) 10Cu catalyst (black) and (A): 1.0La-10Cu (yellow); (B): 1.5La-yCu; (C): 2.0La-yCu and (D): 2.5La-yCu.

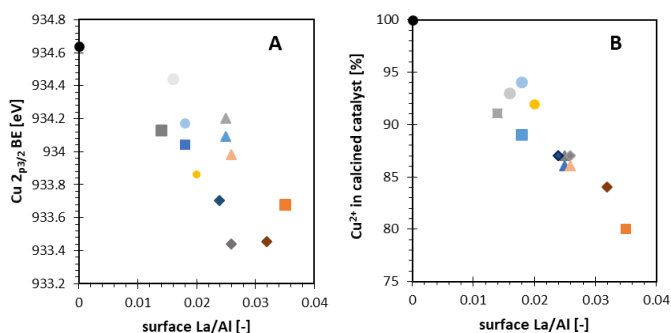


Figure 4.5. Effect of surface La on the $\text{Cu } 2p_{3/2}$ BE (A) and percentage of Cu^{2+} species (B) for the 10Cu catalyst (black), 1.0La-10Cu (yellow); 1.5La-yCu (grey) and 2.0La-yCu (blue) and 2.5La-yCu (orange), in which $y = 10$ (●), $y = 15$ (▲), $y = 20$ (■), $y = 25$ (◆).

The material morphology was studied by means of STEM (section 2.1.2.5, Chapter 2). Figure 4.6.A shows the dark-field STEM images of the calcined 10Cu and 1.0La-10Cu catalysts and illustrates well the characteristics of a mesoporous alumina support. The alumina support consists of very thin flakes, stacked in a disordered manner, resulting in the blurred image. As a result, it was not possible to measure the metal particles' size from the STEM pictures. In both samples the porous structure was visible^{34, 35}, while for the 1.0La-10Cu even the presence of the cylindrical channels, as evidenced by N_2 -sorption, was

evidenced. From the corresponding EDX elemental maps in Figure 4.6.E and Figure 4.6.F, it can be seen that both Cu and La are well dispersed over the γ -Al₂O₃ support.

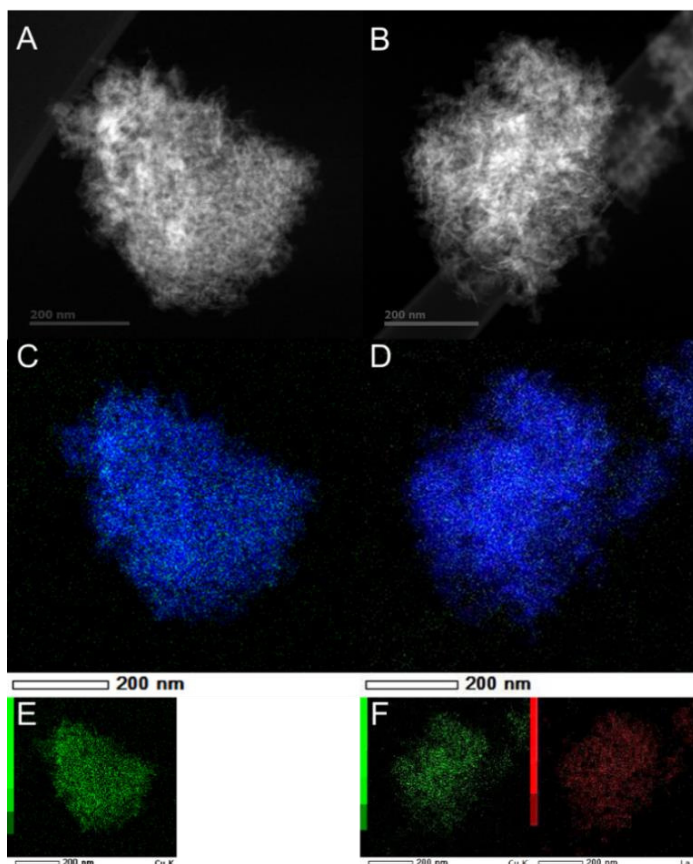


Figure 4.6. Dark-field STEM image of the calcined 10Cu (A) and 1.0La-10Cu (B). The corresponding EDX elemental map with the distribution of Al (blue), Cu (green) and La (red) is shown in C and D. The individual EDX maps of Cu and La are shown in E, corresponding to the dark-field image A, and in F, corresponding to the dark-field image B.

It can be summarized that the La promotion has no pronounced effect on the textural properties of the catalysts. The calcined catalysts have a homogenous distribution of dispersed La and Cu particles. The La-Cu interaction resulted in Cu species with a lower oxidation state, but the major part of the species remained in the Cu²⁺ oxidation state. The calcination of the support resulted in the decrease of strong acid sites, with the formation of moderate acid sites.

4.2.2 Reduced catalyst characterization

Prior to reaction, the catalysts were reduced to activate the Cu. The behavior of the different Cu species in the calcined catalysts was analyzed *via* H₂-TPR (according to the procedures in section 2.1.2.3.1, Chapter 2), phase changes being identified by *in situ* XRD (see section 2.1.2.4 in Chapter 2 for details).

The reduced catalyst was characterized by means of XRD for the identification of crystalline phase and crystallite size, dissociative N_2O adsorption for the determination of the metal surface area and dispersion (see section 2.1.2.3.2 in Chapter 2 for details), XPS for the identification of the oxidation state of the reduced catalysts (see section 2.1.2.6 in Chapter 2 for details) and the morphology was investigated by STEM (see section 2.1.2.5 in Chapter 2 for details).

As one can see from Figure 4.2, representative Cu^0 XRD peaks appeared at 43.3° for $Cu^0_{(111)}$ and at 50.5° for $Cu^0_{(200)}$ (JCPDS 00-004-0836) after reduction at 723 K. No characteristic peaks of CuO remained and, again, no characteristic peak of Cu_2O at 36.4° (JCPDS 00-005-0667) was identified, impeding any conclusion on Cu_2O . Based on the Scherrer equation, Cu^0 particle sizes were calculated in the range from 40 nm to 80 nm, see Table 4.SI.2, meaning that during the reduction, the Cu aggregates doubled in size compared to initial CuO (Table 4.1).

The specific surface area of the Cu aggregates, MSA_{Cu^0} , and the average diameter of the aggregates, ϕ_{Cu^0} are summarized in Table 4.SI.2. The MSA_{Cu^0} was found to be between 17 and $34 \text{ m}^2 \text{ g}^{-1}_{cat}$, which is higher compared to typical supported Cu-based catalysts in literature with similar Cu loading ($10\text{-}30 \text{ m}^2 \text{ g}^{-1}_{cat}$).³⁶⁻³⁸ The ϕ_{Cu^0} increases with the Cu loading (Figure 4.7A). This is expected, since a higher Cu loading enlarges the probability of agglomeration of the Cu particles during synthesis.³⁹ The catalysts exhibited a dispersion, D_{Cu^0} , between 4 % and 20 %. The dispersion decreases with increasing Cu loading (Figure 4.7B), as it is inversely related to the ϕ_{Cu^0} .

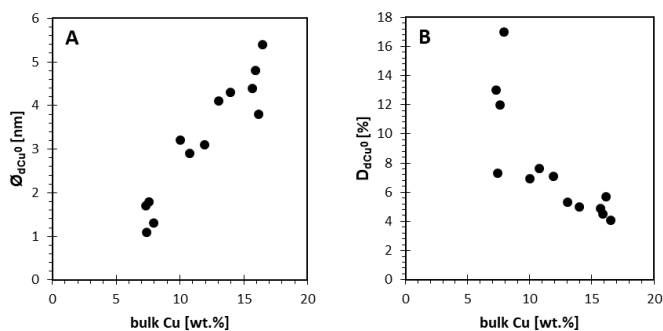


Figure 4.7. Effect of the bulk Cu loading in La-Cu catalysts on ϕ_{Cu^0} (A) and D_{Cu^0} (B).

The effect of promotion on the overall reduction behavior of the calcined catalysts has been investigated *via* H_2 -TPR. This analysis provides insights into the amount of the surface species and catalyst reducibility, assuming the reduction reaction stoichiometry. Figure 4.8 shows the reduction profile of all catalysts. It can be clearly seen that the addition of La to the 10Cu catalyst (Figure 4.8A) decreased the intensity of the α peak, while the latter increased for the β peak. The first reduction peak, α , might be ascribed to highly dispersed CuO species⁴⁰ and/or $(Cu-O-Cu)^{2+}$ species¹⁹, the second

reduction peak, β , to the reduction of CuO particles with weak support interactions^{41, 42}. The 1.0La10Cu catalyst did not show any bulk CuO, corresponding to the γ -peak⁴⁰⁻⁴², but had a higher number of CuO particles with strong support interactions^{41, 42}, corresponding to β' . For the other catalysts (Figure 4.8B to D), three main reduction peaks can be distinguished. At higher Cu-loadings, the reduction peaks shift to higher temperature. The reduction peak γ increases with higher Cu-loading, as result of larger Cu particles (Table 4.SI.2). For all catalysts, the hydrogen consumed during H₂-TPR was somewhat lower than the stoichiometric value needed for the complete reduction from CuO to Cu⁰, resulting in a degree of reduction between 76 % and 98 % (Table 4.SI.2). This means that on the calcined surface not all Cu species are fully oxidized, as no pretreatment was performed. Moreover, this amount is in agreement with the determined amount of Cu²⁺ on the calcined catalysts by XPS (Figure 4.5). Most likely, the remaining amount of Cu⁸⁺ species have a strong interaction with the support, whereby they could not be fully reduced to Cu⁰. Thus, it is plausible that in addition to Cu⁰ species, lower amount of Cu⁸⁺ species are present after reduction, as indicated by the *in situ* XRD in Figure 4.9.

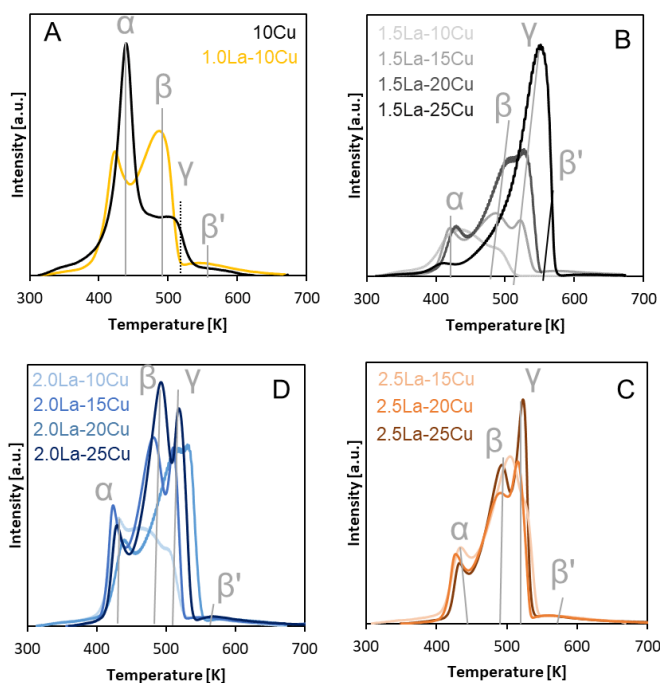


Figure 4.8. TPR profiles of the calcined catalysts with (A): 10Cu (black), 1.0La-10Cu (yellow); (B): 1.5La-yCu; (C): 2.0La-yCu and (D): 2.5La-yCu.

To study the evolution of the CuO phase during the reduction, the 1.0La10Cu catalyst was investigated by means of *in situ* XRD, see Figure 4.9. The characteristic peaks of CuO at 32.5°, 35.4°, 38.6° and 48.7° decrease between 500 and 520 K to form Cu⁰ with main peak at 43.3° and 50.5°. The broad

diffraction peaks for $\gamma\text{-Al}_2\text{O}_3$ at 39.2 and 45.7° kept their intensity during the reduction process. However, it is clear that the intensity between 34.5° and 38.6° changes during the reduction process. This area does not only correspond to diffraction $\gamma\text{-Al}_2\text{O}_3(311)$, but also to that of $\text{Cu}_2\text{O}_{(111)}$ and the mixed Cu-Al phases, (CuAlO_2 and CuAl_2O_4). In section 4.2.1, it was concluded based on XPS that no Cu-Al phases were present on the catalyst surface. Therefore, based on the change in intensity, it can be presumed that $\text{Cu}_2\text{O}_{(111)}$ species were present in the calcined catalyst, as evidenced by XPS (Figure 4.11), and transformed as a change in intensity around 42.3° , corresponding to $\text{Cu}_2\text{O}_{(200)}$, was observed. When a Cu_2O particle in the calcined catalyst consists mostly out of $\text{Cu}_2\text{O}_{(111)}$, but has a minor amount of $\text{Cu}_2\text{O}_{(100)}$, the surface energy can be reduced by transforming to the morphology with a higher fraction of $\text{Cu}_2\text{O}_{(100)}$,⁴³ as represented in Figure 4.10. The low intensity of the Cu_2O species is most likely due to the low amount of Cu_2O , as evidenced by XPS and the degree of reduction (Table 4.SI.1 and Table 4.SI.4).

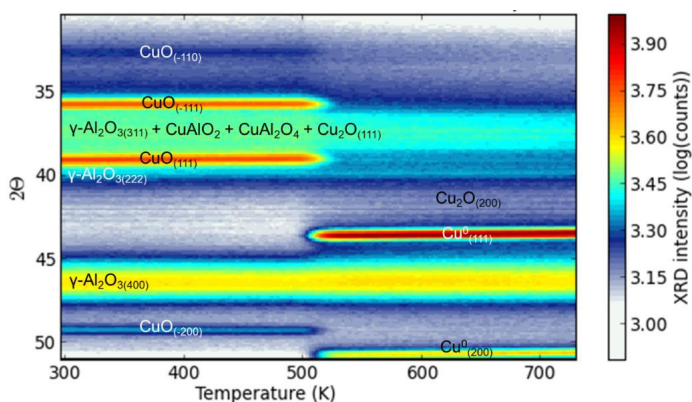


Figure 4.9. Contour plots as function of temperature of the diffraction peak evolution between 32° and 52° for phase identification during reduction with 1.1 NmL s^{-1} $5 \text{ vol.}\% \text{ H}_2\text{-He}$ of Cu oxides present in the $1.0\text{La-}10\text{Cu}$ catalyst.

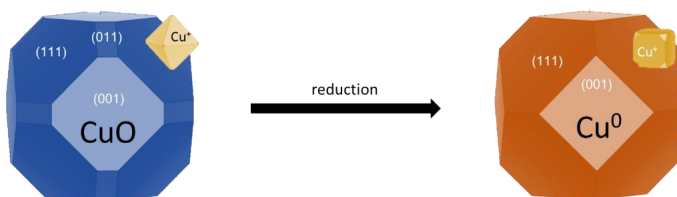


Figure 4.10. Representation of the phase transformation in the Cu particles during reduction

The oxidation states and the composition at the surface of the reduced La-Cu catalysts were also analyzed by XPS. For the reduced samples, the Cu/Al ratio decreased with approximately 50% compared to the calcined samples (Table 4.SI.1, cf. Table 4.1). As the reduction temperature is not high enough to allow diffusion of Cu into the Al_2O_3 structure^{44, 45}, this indicates a lower dispersion (and thus

sintering) of the Cu particles. This is in agreement with the change in Cu crystallite size observed by XRD (Table 4.1, *cf.* Table 4.SI.2). There was no satellite peak between 942 and 944 eV ascribed to Cu²⁺, implying reduction of Cu²⁺ to Cu⁺ and/or Cu⁰ (Figure 4.4). Comparing the calcined to the reduced catalysts, the largest shift to lower BE was observed for the unpromoted catalyst, from 934.6 eV (Cu²⁺) to 932.3 eV (Cu⁰), whereby one can presume that the latter is either due to the larger particle size or less Cu⁺ species. For the La-Cu catalysts, the BE of the reduced catalysts also shifted, however staying closer to its original value as compared to the BE shift of the bare Cu catalyst, indicating the presence of a strong interaction between La and Cu, which either hindered the sintering to larger particles. Due to the similar BE between Cu⁺ (932.2 ± 0.1 eV) and Cu⁰ (932.6 ± 0.3 eV), it is hard to discriminate between those Cu species.⁴⁶ Hence, Cu LMM Auger transition BE is employed to identify these Cu species, taking into account the standards discussed in 2.1.2.6 (Chapter 2). The Cu LMM spectrum shows larger differences between the kinetic energy (KE) of the Cu species compared to the BE, *i.e.* a difference of 1.8 eV between Cu⁺ and Cu⁰. As shown in Figure 4.11, the Cu LMM spectra of the reduced La-Cu catalysts present an asymmetrical broad peak, suggesting the coexistence of Cu⁺ and Cu⁰ on the catalysts surface.⁴⁶ Even if the intensity of the Auger peaks is low, the concentration of the individual species was determined. When looking carefully at the individual Cu⁰ and Cu⁺ species present on the surface of the reduced catalysts, the strong La-Cu interaction is again noticeable. The higher the La/Cu surface ratio, the higher the percentage of Cu⁺ species remained present after the reduction (shown in Figure 4.12). The values are summarized in Table 4.SI.4.

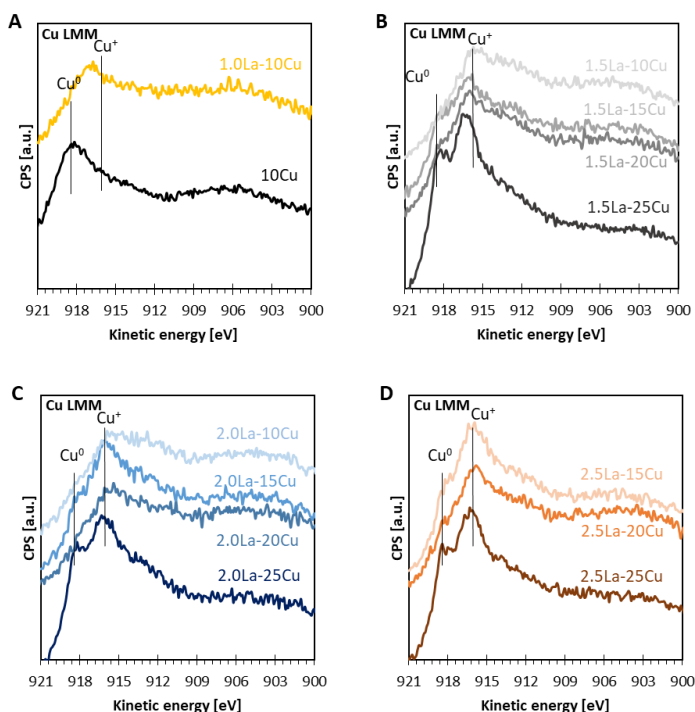


Figure 4.11. Cu LMM spectra of the catalysts after reduction at 623 K using 100 %H₂ at 0.33 NmL s⁻¹. (A): 10Cu (black), 1.0La-10Cu (yellow); (B): 1.5La-yCu; (C): 2.0La-yCu and (D): 2.5La-yCu.

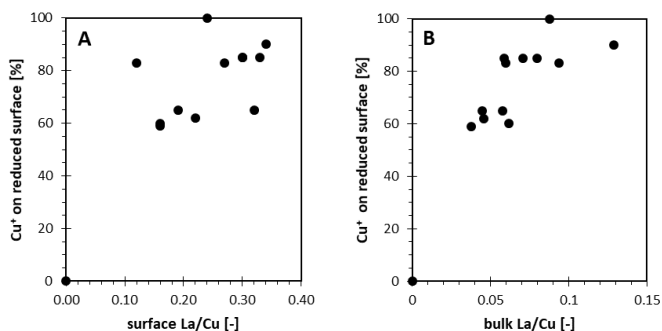


Figure 4.12. Effect of surface (A) and bulk (B) La/Cu mass ratio on the percentage of surface Cu⁺ after reduction at 623 K using 100 %H₂ at 20 cm³ min⁻¹ (sccm).

The modified Auger parameter could also be employed to obtain further information on the oxidation state of Cu *via* a Wagner plot. As can be deduced from Figure 4.13, most modified Auger parameters of the La-Cu catalysts are in the region of Cu₂O, indicating that the surface of the reduced catalysts is mostly covered with Cu⁺ than with Cu⁰.⁴⁶ Only the 10Cu catalyst showed more Cu⁰ than Cu⁺ on the surface.

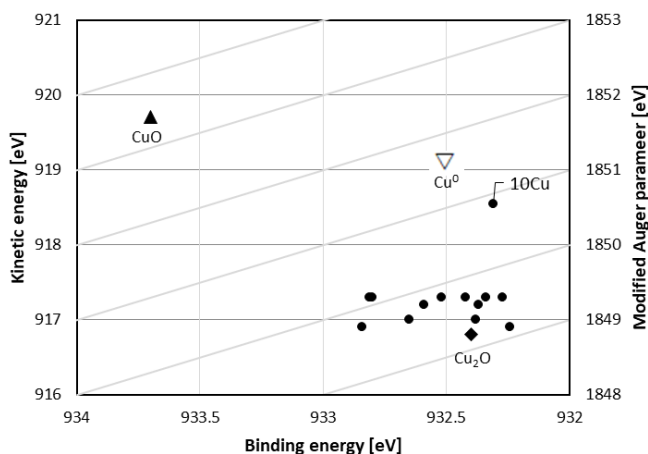


Figure 4.13. Wagner plot for Cu for the catalysts reduced at 623 K using 100 %H₂ at 0.33 NmL s⁻¹. Cu 2p_{3/2} BE and Cu LMM Auger KE for different Cu states: CuO (▲), Cu₂O (◆) and Cu⁰ (▽).⁴⁶

Figure 4.14 shows the dark-field STEM images of the reduced 10Cu and 1.0La-10Cu catalysts. For both catalysts, it is clear that La and Cu remain highly dispersed (Figure 4.14E and Figure 4.14F). Figure 4.15. shows the dark-field STEM images of the reduced 1.5La-10Cu, 2.0La-10Cu, 1.5La-20Cu and 2.0La-20Cu catalysts. For the 2.0La-10Cu catalyst, a catalyst grain with larger Cu particles was found, however, the number was too small to obtain a particle size distribution. In most images, no well-defined Cu-particles were identified, assuming that most of the Cu particles are highly dispersed nanoparticles. The presence of a few of the larger Cu particles is in agreement with the Cu⁰ crystallites detected by XRD (Table 4.SI.2).

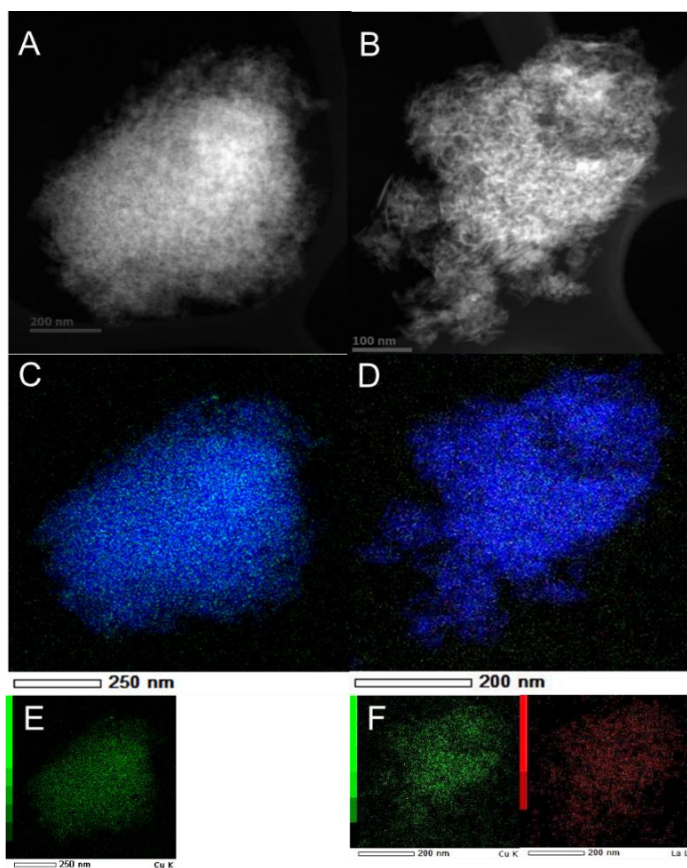


Figure 4.14. Dark-field STEM image of 10Cu (A) and 1.0La-10Cu (B) ex-situ reduced at 723 K using 10 vol.% H₂-Ar. The corresponding EDX elemental map with the distribution of Al (blue), Cu (green) and La (red) is shown in C and D. The individual EDX maps of Cu and La are shown in E, corresponding to the dark-field image A, and in F, corresponding to the dark-field image B.

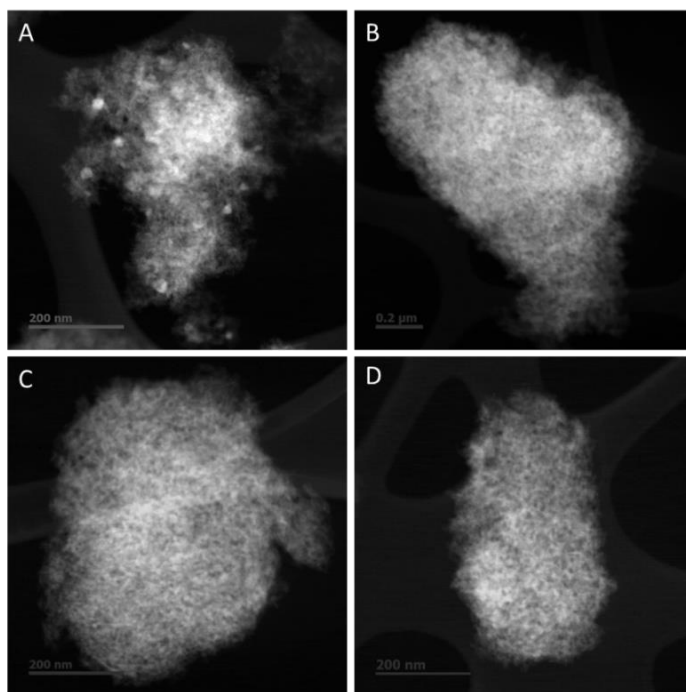


Figure 4.15. Dark-field STEM image of 2.0La-10Cu (A), 2.0La-20Cu (B), 1.5La-10Cu (C) and 1.5La-20Cu (D) catalysts *ex-situ* reduced at 723 K using 10 vol.% H₂-Ar.

The acidity of the reduced catalysts was characterized by NH₃-TPD and compared with the calcined bare support, see Figure 4.16. The addition of Cu resulted in a slight increase of the total acidity (Table 4.SI.2). Compared to the calcined support, the addition of Cu resulted in the formation of weak and strong acid sites (Figure 4.16A). Moreover, it is clear that the interaction between La and Cu resulted in a different NH₃-TPD profile compared to that obtained for the Cu-only catalyst. All La-promoted catalysts exhibited a significant increase in the signal in the weak-moderate acid site region, compared to the support, and a lower signal in the region of the strong acid sites (Table 4.SI.3).

The effect of the promoter ratio on the distribution of acid site types is shown Figure 4.17A. Promotion slightly increased the fraction of weak-moderate acid sites and decreased the number of strong acid sites (Figure 4.17B). Lee *et al.*⁴⁷ reported that a higher La content decreased the strong acidity in zeolites, due to the preferential interaction between La and strong acid hydroxyl groups on the surface. XPS (*vide infra*) showed an increased amount of surface Cu⁺, which correspond to Lewis acidity species because of the electron affinity⁷⁻¹³, upon La-promotion (Figure 4.12B).

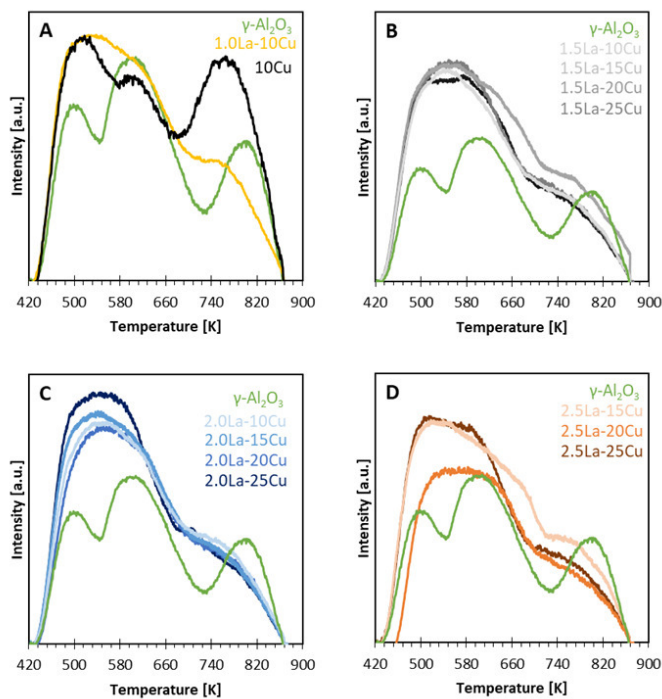


Figure 4.16. NH_3 -TPD profiles of the calcined support (green) and the reduced catalysts (A): 10Cu (black), 1.0La-10Cu (yellow); (B): 1.5La-yCu; (C): 2.0La-yCu and (D): 2.5La-yCu. Intensities were normalized per support mass, such that additional acidity generated by metal deposition can be visually identified.

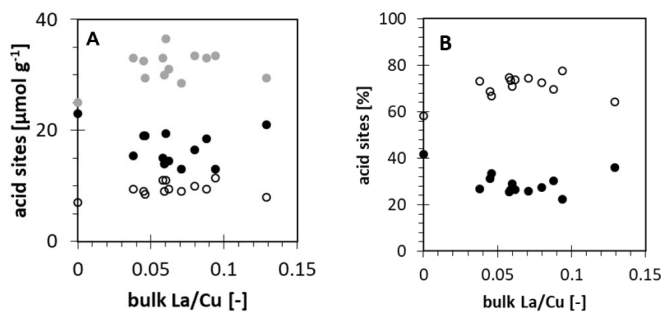


Figure 4.17. (A) Effect of the bulk La/Cu mass ratio on the total amount of weak (\circ), moderate (\odot) and strong (\bullet) acid sites, as determined by NH_3 -TPD. (B) Effect of the bulk La/Cu mass ratio on the fraction of amount of weak+moderate (\circ) and strong (\bullet) acid sites, as determined by NH_3 -TPD.

In summary, after reduction, the Cu agglomerates remain well dispersed ($\Phi_{\text{Cu}^0} = 1.3 - 5.5$ nm), whereby the dispersion of Cu^0 on the reduced catalysts increases with decreasing Cu loading. Most of the Cu^0 particles sizes are between 1-10 nm, as detected by dissociative N_2O chemisorption, while some

larger bulk Cu⁰ crystallites were measured with XRD. Due to the important La-Cu interaction a significant amount of non-reduced Cu⁺ species remains present after the reduction – most probably on top of the Cu⁰ particles – whereby, the acidity of the catalysts also slightly increases, as Cu⁺ species are considered as moderate Lewis acids.

4.2.3 Catalyst performance evaluation and interpretation

To investigate the effect of La/Cu mass ratio on the catalytic performance, *i.e.* the catalyst's stability, activity and selectivity, five La-Cu catalysts were selected and compared to the 10Cu catalyst. A La-Cu catalyst with the similar MSA_{Cu^0} as the 10Cu catalyst but different Cu particle sizes, *i.e.* 1.5La-20Cu was selected. The 1.0La-10Cu and 2.0La-20Cu catalysts were also selected as those exhibited the same promoter ratio, however, with different Cu particles. Finally, the La-Cu catalysts with respectively the highest and lowest MSA_{Cu^0} , *i.e.* 1.5La-10Cu and 2.0La-10Cu, were also selected. Catalytic experiments were performed on HTK-MI setup, a detailed description of the setup can be found in section 2.1.3.1 (Chapter 2). Liquid glycerol hydrogenolysis was performed in a fixed-bed reactor operated under trickle-bed regime. The experimental conditions were chosen within the intrinsic kinetics regime, as described in section 2.1.3.2 (Chapter 2).

Figure 4.18A shows the effect of the La/Cu mass ratio on the catalyst stability, expressed as the relative decrease in glycerol conversion over 68 h TOS (Table 4.SI.5 till Table 4.SI.10). It is clear that La-Cu catalyst exhibited a better catalyst stability compared to the Cu-only catalyst. The increased stability was attributed to a lower extent of sintering (*vide supra*, section 4.2.5).

Figure 4.18B shows the effect of the La/Cu ratio on the catalyst activity. As already discussed in Chapter 3, La-promotion did not increase the catalyst activity.⁴⁸ For a constant MSA_{Cu^0} (25 m² g⁻¹), the activity even rather decreases upon La 'promotion'. This indicates that a tradeoff will be needed between stability and activity. The Cu-only catalyst has a higher activity even though no acidic Cu⁺ is present on the surface (Table 4.SI.6). However, a small acid contribution of Cu was estimated (Table 4.SI.3), which could be the result of some Cu-Al₂O₃ interactions. Therefore, it seems that the active sites on the Cu-only and the La-Cu catalysts are different.

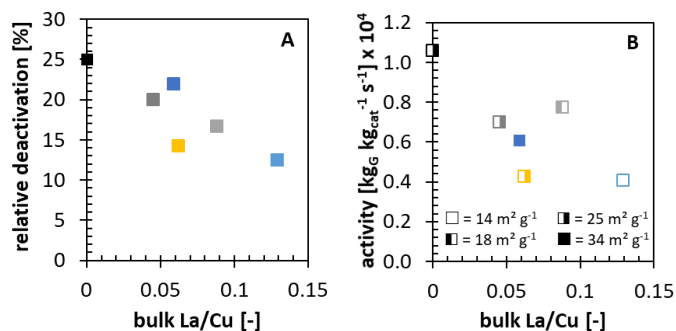


Figure 4.18. Effect of bulk La/Cu mass ratio on (A) the stability and (B) activity. Activity is determined after 12 h time on stream at $135 \text{ kg}_{\text{cat}} \text{ s mol}^{-1}_{\text{glycerol}}$, 473 K, a total H_2 pressure of 7.5 MPa and a molar H_2 to glycerol ratio of 7 for the 10Cu (black), 1.5La-20Cu (dark grey), 2.0La-20Cu (dark blue), 1.0La-10Cu (yellow), 1.5La-10Cu (light grey) and 2.0La-10Cu (light blue).

From Figure 4.19, the TOF increases with ϕ_{Cu^0} . Overall, it is clear that the Cu-based catalyst exhibits a structure sensitivity, which is in agreement with literature^{25, 49}. Interestingly, two different size-dependencies of the TOF were observed. The Cu surface of all catalysts consists mainly of $\text{CuO}_{(200)}$ and $\text{CuO}_{(111)}$ facets, as evident from XRD in Figure 4.2 and Figure 4.SI.2, but also exhibits different defect sites such as corners, steps and kink sites. It is generally assumed that sites with lower coordination numbers, *i.e.* the defects, have higher adsorption strengths and, hence, may have different chemical reactivities.^{25, 50} The obtained results indicate that other aspects than the La/Cu ratio (Figure 4.18) are the factors controlling the catalyst activity. It is clear that in addition to the ϕ_{Cu^0} , other factors such as the facets, control the catalyst activity for glycerol hydrogenolysis.

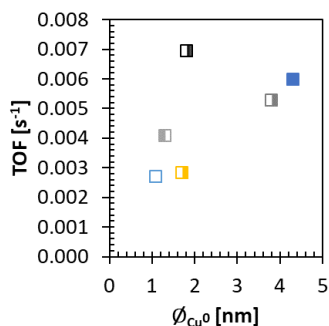


Figure 4.19. TOF as a function of ϕ_{Cu^0} , determined by N_2O sorption, for the 10Cu (black), 1.5La-20Cu (dark grey), 2.0La-20Cu (dark blue), 1.0La-10Cu (yellow), 1.5La-10Cu (light grey) and 2.0La-10Cu (light blue) catalyst calculated after 12 h time on stream at $135 \text{ kg}_{\text{cat}} \text{ s mol}^{-1}_{\text{glycerol}}$, 473 K, a total H_2 pressure of 7.5 MPa and a molar H_2 to glycerol ratio of 7.

The 1,2-propanediol selectivity seemed to increase up to a La/Cu mass ratio of 0.088 (*i.e.* the 1.5La-10Cu catalyst), see Figure 4.20A. The 2.0La-10Cu catalyst, which has the largest La/Cu mass ratio, showed a lower 1,2-propanediol selectivity. The latter has almost the same total acidity compared to the 1.5La-10Cu catalyst (Table 4.SI.2) but exhibited a different acid site distribution (Figure 4.17). To better understand this effect, Figure 4.20B shows the 1,2-propanediol selectivity as a function of the acid sites introduced by the Cu loading, *i.e.* the concentration of weak and moderate sites present in addition to those on the bare support (Table 4.SI.3). It is clear that an increasing concentration of weak-moderate Cu acid sites contributes to the increase in selectivity, which that is not the case for the support acid sites (Figure 4.SI.5A). It seems that the main difference between the Cu/Al₂O₃ and La-Cu/Al₂O₃ catalysts can be attributed to the Lewis acidity of Cu⁺, as a result of the La-Cu interactions. The weak-moderate Cu⁺ acid sites in La-Cu catalysts, enhanced glycerol conversion to acetol (Figure 4.SI.5B), which is the rate-determining step¹⁷, and consequently resulted in higher 1,2-propanediol selectivity.

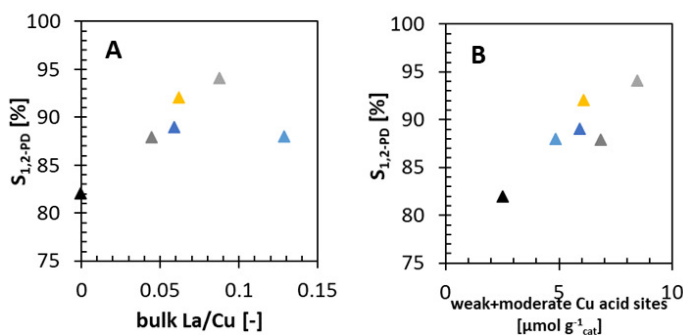


Figure 4.20. Effect of (A) bulk La/Cu mass ratio and the effect of the weak+moderate Cu acid sites (B) in the 10Cu (black), 1.5La-20Cu (dark grey), 2.0La-20Cu (dark blue), 1.0La-10Cu (yellow), 1.5La-10Cu (light grey) and 2.0La-10Cu (light blue) catalyst on the 1,2-propanediol selectivity, determined after 12 h time on stream at $135 \text{ kg}_{\text{cat}} \text{ s mol}^{-1}_{\text{glycerol}}$, 473 K, a total H₂ pressure of 7.5 MPa and a molar H₂ to glycerol ratio of 7. Error bars are determined as experimental error.

A minor amount of 1,3-propanediol or degradation products, such as 1-propanol and 2-propanol, were also observed over some catalysts (Table 4.SI.5 till Table 4.SI.10). For all catalysts, the undesired C-C cleavage, forming 1,2-ethanediol was observed. The selectivity of 1,2-ethanediol was not directly related to the number of strong acid sites (Figure 4.21A), which are generally assumed to promote C-C cleavage. This could be related to the low selectivity towards the product and a higher experimental error. However, the La-Cu catalysts exhibited an increase in 1,2-ethanediol selectivity with increasing total number of acid sites per Cu⁰ site (Figure 4.21B). This indicates that for the direct hydrogenolysis of glycerol to 1,2-ethanediol and methanol both an acid and a metal site are required, rather than only a metal site.

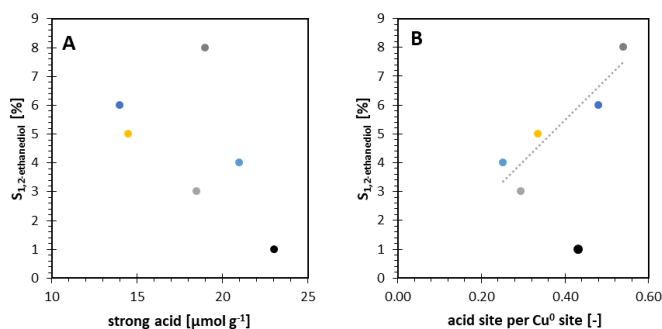


Figure 4.21. Effect of (A) strong acid sites, determined by NH_3 -TPD, and (B) strong acid sites per Cu^0 sites, determined by determined by N_2O sorption, for the 10Cu (black), 1.5La-20Cu (dark grey), 2.0La-20Cu (dark blue), 1.0La-10Cu (yellow), 1.5La-10Cu (light grey) and 2.0La-10Cu (light blue) catalyst on the 1,2-ethanediol selectivity determined after 12 h TOS at $135 \text{ kg}_{\text{cat}} \text{ s mol}^{-1}_{\text{glycerol}}$, 473 K, a total H_2 pressure of 7.5 MPa and a molar H_2 to glycerol ratio of 7. Error bars were not shown for the clarity of the figures.

In conclusion, the La-promoted catalysts exhibited structure sensitivity for glycerol hydrogenolysis, *i.e.* larger particles exhibit a higher TOF. With an increased La/Cu ratio, an increase in the stability of the catalyst was observed, due to the La-Cu interactions. It seemed that the activity rather decreased with promotor ratio, causing a tradeoff between the stability and activity. As a result of the increased amount of mostly weak+moderate acid sites, introduced by Cu^+ , the dehydration of glycerol to acetol is enhanced, resulting in an increased selectivity to 1,2-propanediol, exceeding 82 %. A maximum selectivity of 94 % was observed for La/Cu = 0.088.

4.2.4 Proposed reaction mechanism over La-Cu/ γ - Al_2O_3 catalysts

As mentioned before, the most accepted mechanism for the formation of 1,2-propanediol is the dehydration-hydrogenation route, see Chapter 1 section 1.4.1. In the first step, glycerol is dehydrated over on an acid site to acetol or 3-hydroxypropionaldehyde, while in the second step, these intermediates undergo a hydrogenation, which is catalyzed by a metal, to 1,2-propanediol or 1,3-propanediol, respectively. The analysis of the results of this chapter allowed to propose the following mechanism for glycerol hydrogenolysis over La-Cu/ γ - Al_2O_3 , see Figure 4.22. In this mechanism it is taking into account that Cu particles, rather than the support, are the active sites for the dehydration to acetol.

As evidenced by the STEM, both the La and Cu are well dispersed. After the reduction of the catalysts, Cu^+ and Cu^0 co-existed. At higher La/Cu ratios, more Cu^+ remained on the surface. The Cu-loading affected mostly the size of the Cu^0 particles (1.3 – 5.5 nm), however, some larger Cu clusters (40 – 75 nm) will be also presented.

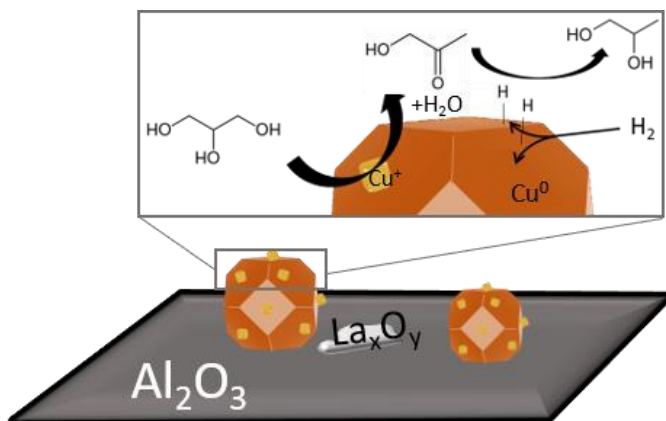


Figure 4.22. Schematic representation of proposed role of La-Cu/ γ -Al₂O₃ in glycerol hydrogenolysis. La-Cu/ γ -Al₂O₃ surface and the interaction between Cu⁺ and Cu⁰ in 1,2-propanediol formation.

As shown in Figure 4.22, H₂ adsorbs dissociative on the Cu⁰ surface with the formation of two hydrogen atoms. H₂ adsorbs dissociative on any Cu⁰ surface with the formation of two adsorbed hydrogen atoms. The adsorption of glycerol then occurs on Cu⁺, induced by the La-Cu interaction. It is assumed, inspired by the mechanism proposed by Alhanash *et al.*³, that a primary hydroxyl group of glycerol interacts with the Cu⁺, which has Lewis acidity, and an O atom of Cu₂O abstracts a proton on the adjacent carbon. Cu⁺ weakens the electron density of the C-O bond^{11, 51}, accelerating its cleavage; yielding acetol and water by regeneration of the active site (dehydration). Finally, acetol reacts with two of the hydrogen atoms on the Cu⁰ surface, leading to the formation of 1,2-propanediol. An acid site in the proximity of a Cu⁰ site contributed to side product formation.

4.2.5 Spent catalyst characterization

During the reaction, the catalyst can undergo changes in particle size, oxidation state and morphology. Therefore, the six investigated catalysts were also thoroughly characterized after reaction.

As discussed in Chapter 3, the Cu catalysts exhibit almost no leaching (Table 4.SI.11 *cf.* Table 4.1). From the XRD patterns of the spent catalysts, shown in Figure 4.23, one can see that the CuO signal reappeared, especially in the case of the 10Cu catalyst. This indicates that some amount of the Cu species reoxidized or some CuO sintered during the reaction. Further, it can be observed that the diffraction peaks of Cu⁰ are very sharp, indicating larger crystallite sizes.

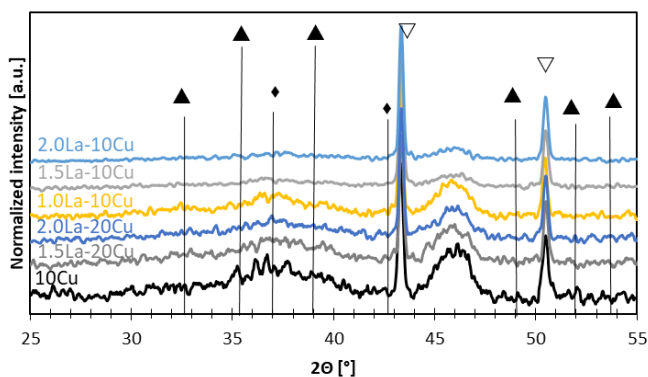


Figure 4.23. XRD pattern of the spent 10Cu (black), 1.5La-20Cu (dark grey), 2.0La-20Cu (dark blue), 1.0La-10Cu (yellow), 1.5La-10Cu (light grey) and 2.0La-10Cu (light blue) catalyst with CuO (▲), Cu₂O (◆) and Cu (▽).

Based on the Scherrer's equation, Cu⁰ crystallites in the range of 50 to 150 nm were obtained, see Figure 4.24, which decreased with increasing La/Cu mass ratio. This trend was also confirmed by dissociative N₂O adsorption on the spent catalysts.

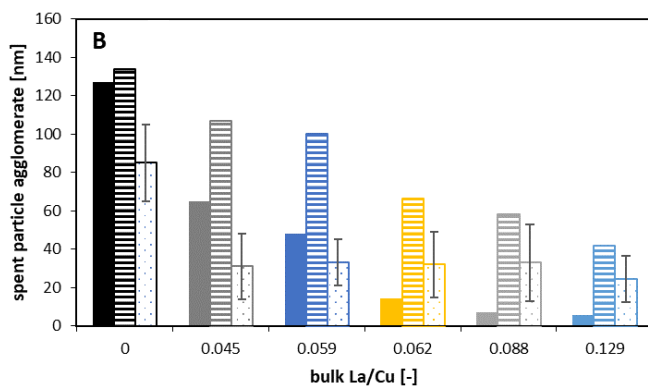


Figure 4.24. Effect of La/Cu on the spent Cu particle size, d_{Cu^0} , determined by dissociative N₂O adsorption (full bars), Scherrer equation (striped bars) and STEM (dotted bars) of 10Cu (black), 1.5La-20Cu (dark grey), 2.0La-20Cu (dark blue), 1.0La-10Cu (yellow), 1.5La-10Cu (light grey) and 2.0La-10Cu (light blue) catalyst.

To investigate the morphology of the spent catalysts, STEM images of the spent catalysts, without any pretreatment (Figure 4.25), were made and a particle size distribution was determined (see later in Figure 4.26). Figure 4.25 shows the dark-field STEM images of the spent 10Cu and spent 1.0La-10Cu catalyst. Whereas in the calcined and reduced catalysts, Cu was highly dispersed, there is a clear presence of large Cu particles after reaction. Notwithstanding, the population of highly dispersed Cu was still present, see Figure 5.16F. For the spent 1.5La-10Cu, 1.5La-20Cu, 2.0La-10Cu and 2.0La-20Cu catalysts the particle size distribution of the large particle population (> 10 nm) was determined based on almost 500 particles. For the 10Cu and 1.0La-10Cu catalyst, the particle size distribution was established with a lower number of particles, respectively 30 and 117. For the unpromoted catalyst, larger agglomerates

were observed, while for the La-Cu catalysts the majority of the Cu particles form agglomerates of *ca.* 20-30 nm, as shown in Figure 4.26. Based on dark-field STEM, the stabilizing effect of La was evident. The effect of the promotor ratio was less straightforward to interpret as compared to other characterization method (Figure 4.24). Thus, La-promotion inhibited sintering of not only Cu⁰, but of all Cu species in the catalyst as it is impossible to distinguish different oxidation states in STEM. As discussed in section 4.2.2, the La-Cu interactions also increased the amount of Cu⁺ species, reducing again the extent of Cu species sintering.

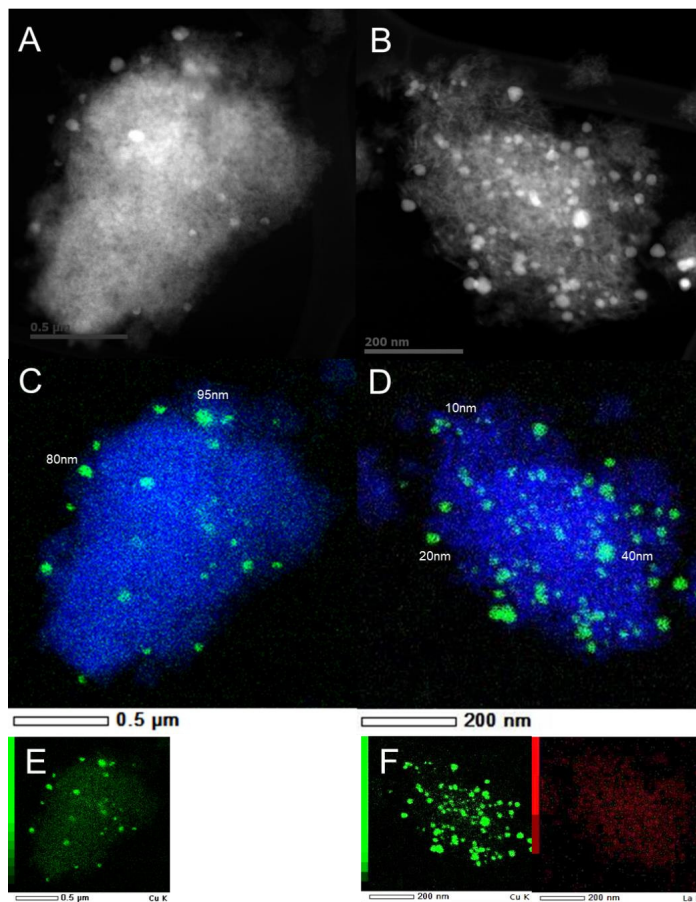


Figure 4.25. Dark-field STEM image of spent 10Cu (A) and 1.0La-10Cu (B) catalyst. The corresponding EDX elemental map with the distribution of Al (blue), Cu (green) and La (red) is shown in C and D. The individual EDX maps of Cu and La are shown in E, corresponding to the dark-field image A, and in F, corresponding to the dark-field image B.

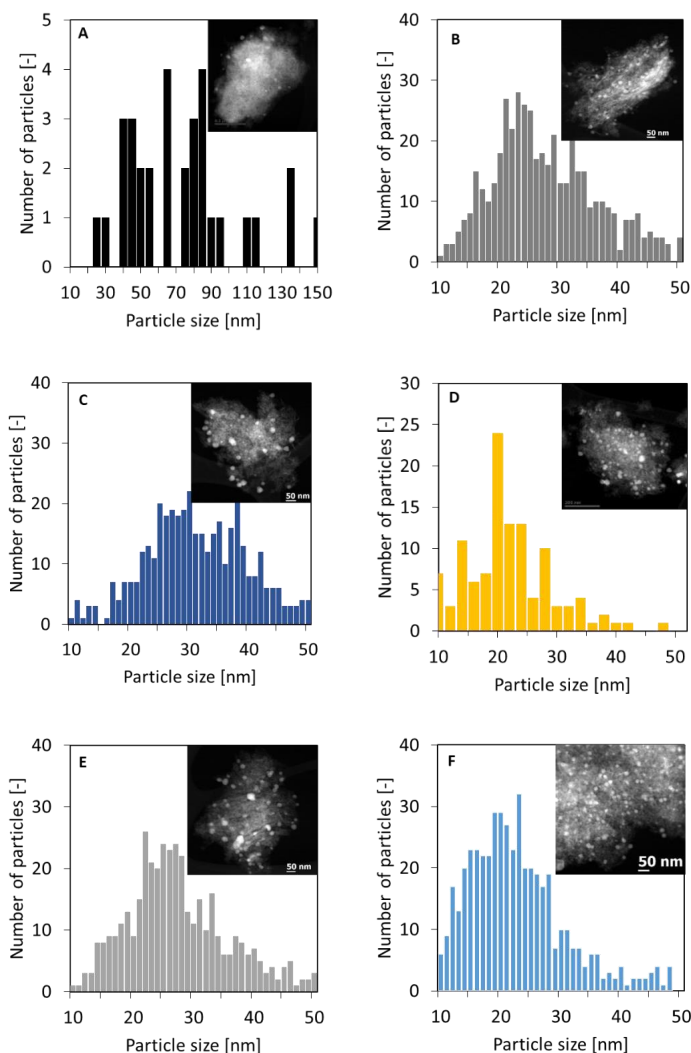


Figure 4.26. Particle size distribution of Cu based on dark-field STEM of spent 10Cu (A), 1.5La-20Cu (B), 2.0La-20Cu (C), 1.0La-10Cu (D), 1.5La-10Cu (E) and 2.0La-10Cu (F) catalysts.

The surface state of spent Cu and La-Cu catalysts was probed by XPS. A small satellite peak between 942 and 944 eV was detected and ascribed to Cu^{2+} , see Figure 4.27, implying some reoxidation compared to the reduced catalysts. It was chosen to calculate the sum of ($\text{Cu}^0 + \text{Cu}^+$), summarized in Table 4.SI.12, instead of determining the individual amount of the species Cu^+ and Cu^0 , due to the low intensity of the Cu LMM signal (Figure 4.SI.6). The percentage of ($\text{Cu}^0 + \text{Cu}^+$) present in the spent catalysts, see Figure 4.28, increased with the La/Cu ratio. Due to the strong La-Cu interactions, we again assume that more

Cu⁺ was present on the surface of the reduced catalysts, as discussed in section 4.2.2 (*cf.* Figure 4.12). Thus, less Cu⁺ will be present on the surface, when that particle sinters.

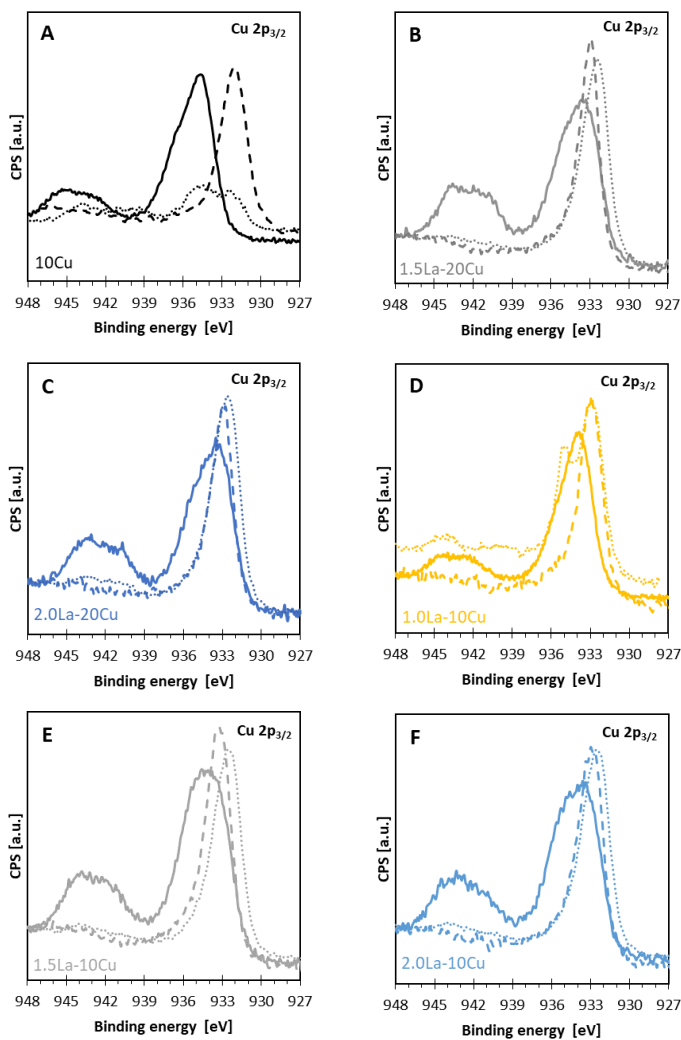


Figure 4.27. Effect of promotion on the Cu 2p_{3/2} spectra of the calcined (full line), reduced (dashed line) and spent (dotted line) 10Cu (A), 1.5La-20Cu (B), 2.0La-20Cu (C), 1.0La-10Cu (D), 1.5La-10Cu (E) and 2.0La-10Cu (F) catalysts

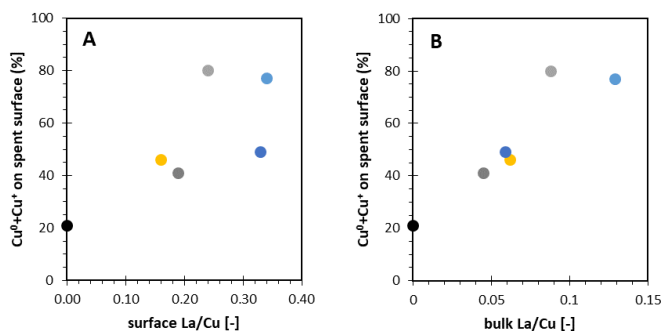


Figure 4.28. Effect of surface (A) and bulk (B) La/Cu mass ratio on the percentage of surface (Cu^0+Cu^+) species of the spent 10Cu (black), 1.5La-20Cu (dark grey), 2.0La-20Cu (dark blue), 1.0La-10Cu (yellow), 1.5La-10Cu (light grey) and 2.0La-10Cu (light blue) catalysts.

From the characterization of the spent catalysts, it can be concluded that sintering of the Cu particles occurred ($\phi_{\text{Cu}^t} = 10 - 100 \text{ nm}$), but was impeded by the presence of La. This is in agreement with Chapter 4. Furthermore, due to the strong La-Cu interaction, Cu^+ remained present on the surface. As a result, less Cu^+ will be present on the surface, when that particle sinters (at low La/Cu).

4.3 Conclusions

In this chapter, the effect of La-promotion on $\gamma\text{-Al}_2\text{O}_3$ supported Cu catalyst for glycerol hydrogenolysis towards 1,2-propanediol was assessed. Different promoter ratios were employed to tune the amounts of Cu^+ and Cu^0 species.

Both La and Cu were homogeneously dispersed on the support after calcination and reduction. The La/Cu ratio had no significant effect on the physicochemical properties (*e.g.* surface area, average pore size and pore volume) of the calcined catalysts. After the reduction of the catalysts, Cu^+ and Cu^0 co-existed. It was found that with increasing La/Cu ratio, the amount of weak and moderate acid sites increased, while that of the strong acid sites decreased.

The effect of the La/Cu ratio was assessed in terms of catalyst stability, activity and 1,2-propanediol selectivity as compared to a Cu catalyst. The activity seemingly decreased with promotion ratio, causing a tradeoff between stability and activity. Sintering of the Cu particles occurred, but its extent was reduced by the presence of La thanks to the La-Cu interaction. It was shown that product selectivity in glycerol hydrogenolysis on La-Cu/ Al_2O_3 catalysts depends on both acid and metal sites. The weak-moderate Cu^+ acid sites in La-Cu catalysts, rather than the support, enhanced the dehydration of acetol, and consequently to the 1,2-propanediol selectivity. The insights gained in this chapter provided a new view on the role of Cu^+ and therefore the complexity of glycerol hydrogenolysis. As the differences between the various La-Cu catalysts in terms of total acidity and catalytic performance is rather small, the influence of the support was assessed in Chapter 5.

4.4 References

- 1 S. Zhu, X. Gao, Y. Zhu, Y. Zhu, H. Zheng, Y. Li, Promoting Effect of Boron Oxide on Cu/SiO₂ Catalyst for Glycerol Hydrogenolysis to 1, 2-Propanediol, *Journal of Catalysis*, 303 (2013) 70-79.
- 2 J. Hagen, *Industrial Catalysis*, 2005.
- 3 A. Alhanash, E.F. Kozhevnikova, I.V. Kozhevnikov, Gas-Phase Dehydration of Glycerol to Acrolein Catalysed by Caesium Heteropoly Salt, *Applied Catalysis A: General*, 378 (2010) 11-18.
- 4 F. Vila, M. López Granados, R. Mariscal, Significance of Isomeric Reaction Intermediates in the Hydrogenolysis of Glycerol to 1,2-Propanediol with Cu-Based Catalysts, *Catalysis Science & Technology*, 7 (2017) 3119-3127.
- 5 C. Montassier, J. Ménézo, L. Hoang, C. Renaud, J. Barbier, Aqueous Polyol Conversions on Ruthenium and on Sulfur-Modified Ruthenium, *Journal of molecular catalysis*, 70 (1991) 99-110.
- 6 H. Pines, W.O. Haag, Alumina: Catalyst and Support. I. Alumina, Its Intrinsic Acidity and Catalytic Activity, *Journal of the American Chemical Society*, 82 (1960) 2471-2483.
- 7 Y. Zhu, X. Kong, B. Peng, L. Li, Z. Fang, Y. Zhu, Efficient Cu Catalyst for 5-Hydroxymethylfurfural Hydrogenolysis by Forming Cu–O–Si Bonds, *Catalysis Science & Technology*, 10 (2020) 7323-7330.
- 8 R.J. Chimentão, P. Hirunsit, C.S. Torres, M.B. Ordoño, A. Urakawa, J.L.G. Fierro, D. Ruiz, Selective Dehydration of Glycerol on Copper Based Catalysts, *Catalysis Today*, (2020).
- 9 R.-P. Ye, L. Lin, Q. Li, Z. Zhou, T. Wang, C.K. Russell, H. Adidharma, Z. Xu, Y.-G. Yao, M. Fan, Recent Progress in Improving the Stability of Copper-Based Catalysts for Hydrogenation of Carbon–Oxygen Bonds, *Catalysis Science & Technology*, 8 (2018) 3428-3449.
- 10 J. Shan, H. Liu, K. Lu, S. Zhu, J. Li, J. Wang, W. Fan, Identification of the Dehydration Active Sites in Glycerol Hydrogenolysis to 1,2-Propanediol over Cu/SiO₂ Catalysts, *Journal of Catalysis*, 383 (2020) 13-23.
- 11 Q. Wang, Z. Yu, J. Feng, P. Fornasiero, Y. He, D. Li, Insight into the Effect of Dual Active Cu⁰/Cu⁺ Sites in a Cu/ZnO–Al₂O₃ Catalyst on 5-Hydroxymethylfurfural Hydrodeoxygenation, *Acs Sustainable Chemistry & Engineering*, 8 (2020) 15288-15298.
- 12 S. Zhu, X. Gao, Y. Zhu, W. Fan, J. Wang, Y. Li, A Highly Efficient and Robust Cu/SiO₂ Catalyst Prepared by the Ammonia Evaporation Hydrothermal Method for Glycerol Hydrogenolysis to 1,2-Propanediol, *Catalysis Science & Technology*, 5 (2015) 1169-1180.
- 13 H. Yue, X. Ma, J. Gong, An Alternative Synthetic Approach for Efficient Catalytic Conversion of Syngas to Ethanol, *Accounts of Chemical Research*, 47 (2014) 1483-1492.
- 14 E. Vasiliadou, A. Lemonidou, Kinetic Study of Liquid-Phase Glycerol Hydrogenolysis over Cu/SiO₂ Catalyst, *Chemical Engineering Journal*, 231 (2013) 103-112.
- 15 E. Vasiliadou, A. Lemonidou, Investigating the Performance and Deactivation Behaviour of Silica-Supported Copper Catalysts in Glycerol Hydrogenolysis, *Applied Catalysis A: General*, 396 (2011) 177-185.
- 16 S. Sato, M. Akiyama, R. Takahashi, T. Hara, K. Inui, M. Yokota, Vapor-Phase Reaction of Polyols over Copper Catalysts, *Applied Catalysis A: General*, 347 (2008) 186-191.
- 17 T. Rajkhowa, G.B. Marin, J.W. Thybaut, A Comprehensive Kinetic Model for Cu Catalyzed Liquid Phase Glycerol Hydrogenolysis, *Applied Catalysis B: Environmental*, 205 (2017) 469-480.
- 18 Z. Xiao, X. Wang, J. Xiu, Y. Wang, C.T. Williams, C. Liang, Synergetic Effect between Cu⁰ and Cu⁺ in the Cu-Cr Catalysts for Hydrogenolysis of Glycerol, *Catalysis Today*, 234 (2014) 200-207.
- 19 A. Yin, X. Guo, W.-L. Dai, K. Fan, The Nature of Active Copper Species in Cu-Hms Catalyst for Hydrogenation of Dimethyl Oxalate to Ethylene Glycol: New Insights on the Synergetic Effect between Cu⁰ and Cu⁺, *The Journal of Physical Chemistry C*, 113 (2009) 11003-11013.
- 20 X. Li, M. Xiang, D. Wu, Hydrogenolysis of Glycerol over Bimetallic Cu₂ Catalysts Supported on Hierarchically Porous Sapo-11 Zeolite, *Catalysis Communications*, 119 (2019) 170-175.
- 21 K. Samson, M. Śliwa, R.P. Socha, K. Góra-Marek, D. Mucha, D. Rutkowska-Zbik, J.F. Paul, M. Ruggiero-Mikołajczyk, R. Grabowski, J. Słoczyński, Influence of ZrO₂ Structure and Copper Electronic State on Activity of Cu/ZrO₂ Catalysts in Methanol Synthesis from CO₂, *ACS Catalysis*, 4 (2014) 3730-3741.

- 22 R.B. Mane, A.M. Hengne, A.A. Ghalwadkar, S. Vijayanand, P.H. Mohite, H.S. Potdar, C.V. Rode, Cu: Al Nano Catalyst for Selective Hydrogenolysis of Glycerol to 1, 2-Propanediol, *Catalysis Letters*, 135 (2010) 141-147.
- 23 J. Huang, T. Ding, K. Ma, J. Cai, Z. Sun, Y. Tian, Z. Jiang, J. Zhang, L. Zheng, X. Li, Modification of Cu/SiO₂ Catalysts by La₂O₃ to Quantitatively Tune Cu⁺-Cu⁰ Dual Sites with Improved Catalytic Activities and Stabilities for Dimethyl Ether Steam Reforming, *ChemCatChem*, 10 (2018) 3862-3871.
- 24 X. Zheng, H. Lin, J. Zheng, X. Duan, Y. Yuan, Lanthanum Oxide-Modified Cu/SiO₂ as a High-Performance Catalyst for Chemoselective Hydrogenation of Dimethyl Oxalate to Ethylene Glycol, *ACS Catalysis*, 3 (2013) 2738-2749.
- 25 R. Beerthuis, J.W. de Rijk, J.M.S. Deeley, G.J. Sunley, K.P. de Jong, P.E. de Jongh, Particle Size Effects in Copper-Catalyzed Hydrogenation of Ethyl Acetate, *Journal of Catalysis*, 388 (2020) 30-37.
- 26 Krijn P. de Jong, *Synthesis of Solid Catalysts*, 2009.
- 27 K.S. Sing, D. Everett, R. Haul, L. Moscou, R. Pierotti, J. Rouquerol, T. Siemieniowska, Reporting Physisorption Data for Gas/Solid Systems with Special Reference to the Determination of Surface Area and Porosity (Recommendations 1984), *Pure appl. chem*, 57 (1985) 603-619.
- 28 K.S.W. Sing, R.T. Williams, Physisorption Hysteresis Loops and the Characterization of Nanoporous Materials, *Adsorption Science & Technology*, 22 (2004) 773-782.
- 29 M. Bettman, R. Chase, K. Otto, W. Weber, Dispersion Studies on the System La₂O₃-Al₂O₃, *Journal of Catalysis*, 117 (1989) 447-454.
- 30 T. Mimani, Instant Synthesis of Nanoscale Spinel Aluminates, *Journal of Alloys and Compounds*, 315 (2001) 123-128.
- 31 K.T. JACOB, C.B. ALCOCK, Thermodynamics of Cu₂O and Cu₂O₂ and Phase Equilibria in the System Cu₂O-CuO-Al₂O₃, *Journal of the American Ceramic Society*, 58 (1975) 192-195.
- 32 X. Li, Q. Zhang, H. Xie, X. Gao, Y. Wu, G. Yang, P. Wang, S. Tian, Y. Tan, Facile Preparation of Cu-Al Oxide Catalysts and Their Application in the Direct Synthesis of Ethanol from Syngas, *ChemistrySelect*, 2 (2017) 10365-10370.
- 33 M.G. Mason, Electronic Structure of Supported Small Metal Clusters, *Physical Review B*, 27 (1983) 748-762.
- 34 Y. Xie, D. Kocaefer, Y. Kocaefer, J. Cheng, W. Liu, The Effect of Novel Synthetic Methods and Parameters Control on Morphology of Nano-Alumina Particles, *Nanoscale research letters*, 11 (2016) 1-11.
- 35 L. Samain, A. Jaworski, M. Edén, D.M. Ladd, D.-K. Seo, F. Javier Garcia-Garcia, U. Häussermann, Structural Analysis of Highly Porous Γ -Al₂O₃, *Journal of Solid State Chemistry*, 217 (2014) 1-8.
- 36 P.G. Menon, J. Prasad, Exposure of Metallic Copper Surface on Cu • Al₂O₃-Carbon Catalysts, *Journal of Catalysis*, 17 (1970) 238-244.
- 37 A. Budiman, M. Ridwan, S.M. Kim, J.-W. Choi, C.W. Yoon, J.-M. Ha, D.J. Suh, Y.-W. Suh, Design and Preparation of High-Surface-Area Cu/ZnO/Al₂O₃ Catalysts Using a Modified Co-Precipitation Method for the Water-Gas Shift Reaction, *Applied Catalysis A: General*, 462 (2013) 220-226.
- 38 Y. Zhao, S. Li, Y. Wang, B. Shan, J. Zhang, S. Wang, X. Ma, Efficient Tuning of Surface Copper Species of Cu/SiO₂ Catalyst for Hydrogenation of Dimethyl Oxalate to Ethylene Glycol, *Chemical Engineering Journal*, 313 (2017) 759-768.
- 39 J.L. Ayastuy, A. Gurbani, M.P. González-Marcos, M.A. Gutiérrez-Ortiz, Effect of Copper Loading on Copper-Ceria Catalysts Performance in Co Selective Oxidation for Fuel Cell Applications, *International Journal of Hydrogen Energy*, 35 (2010) 1232-1244.
- 40 M. Behrens, S. Zander, P. Kurr, N. Jacobsen, J.r. Senker, G. Koch, T. Ressler, R.W. Fischer, R. Schlögl, Performance Improvement of Nanocatalysts by Promoter-Induced Defects in the Support Material: Methanol Synthesis over Cu/ZnO: Al, *Journal of the American Chemical Society*, 135 (2013) 6061-6068.

- 41 Z. Huang, F. Cui, H. Kang, J. Chen, X. Zhang, C. Xia, Highly Dispersed Silica-Supported Copper Nanoparticles Prepared by Precipitation– Gel Method: A Simple but Efficient and Stable Catalyst for Glycerol Hydrogenolysis, *Chemistry of Materials*, 20 (2008) 5090-5099.
- 42 M.L. Dieuzeide, R. de Urriaga, M. Jobbagy, N. Amadeo, Vapor Phase Hydrogenolysis of Glycerol to 1,2-Propanediol at Atmospheric Pressure over Copper Catalysts Supported on Mesoporous Alumina, *Catalysis Today*, 296 (2017) 19-25.
- 43 M.M. Ferrer, G.S.L. Fabris, B.V. de Faria, J.B.L. Martins, M.L. Moreira, J.R. Sambrano, Quantitative Evaluation of the Surface Stability and Morphological Changes of Cu₂o Particles, *Heliyon*, 5 (2019) e02500.
- 44 F. Vila, M. López Granados, M. Ojeda, J.L.G. Fierro, R. Mariscal, Glycerol Hydrogenolysis to 1,2-Propanediol with Cu/Γ-Al₂o₃: Effect of the Activation Process, *Catalysis Today*, 187 (2012) 122-128.
- 45 V. Di Castro, C. Furlani, M. Gargano, N. Ravasio, M. Rossi, Xps Study of Copper Dispersion in Cuo/Al₂o₃ Catalysts, *Journal of Electron Spectroscopy and Related Phenomena*, 52 (1990) 415-422.
- 46 M.C. Biesinger, *Advanced Analysis of Copper X-Ray Photoelectron Spectra*, *Surface and Interface Analysis*, 49 (2017) 1325-1334.
- 47 J. Lee, U.G. Hong, S. Hwang, M.H. Youn, I.K. Song, Catalytic Cracking of C5 Raffinate to Light Olefins over Lanthanum-Containing Phosphorous-Modified Porous Zsm-5: Effect of Lanthanum Content, *Fuel Processing Technology*, 109 (2013) 189-195.
- 48 A. Bouriakova, P.S.F. Mendes, B. Katryniok, J. De Clercq, J.W. Thybaut, Co-Metal Induced Stabilization of Alumina-Supported Copper: Impact on the Hydrogenolysis of Glycerol to 1,2-Propanediol, *Catalysis Communications*, 146 (2020) 106134.
- 49 M.B. Taghavi, G.M. Pajonk, S.J. Teichner, On the Structure-Sensitive and Structure-Insensitive Catalytic Reactions and Their New Characteristics, Demonstrated with Copper-Supported Catalysts, *Journal of Colloid and Interface Science*, 71 (1979) 451-465.
- 50 Z.-P. Liu, P. Hu, General Rules for Predicting Where a Catalytic Reaction Should Occur on Metal Surfaces: A Density Functional Theory Study of C– H and C– O Bond Breaking/Making on Flat, Stepped, and Kinked Metal Surfaces, *Journal of the American Chemical Society*, 125 (2003) 1958-1967.
- 51 J. Gong, H. Yue, Y. Zhao, S. Zhao, L. Zhao, J. Lv, S. Wang, X. Ma, Synthesis of Ethanol Via Syngas on Cu/Sio₂ Catalysts with Balanced Cu⁰–Cu⁺ Sites, *Journal of the American Chemical Society*, 134 (2012) 13922-13925.

Supporting information

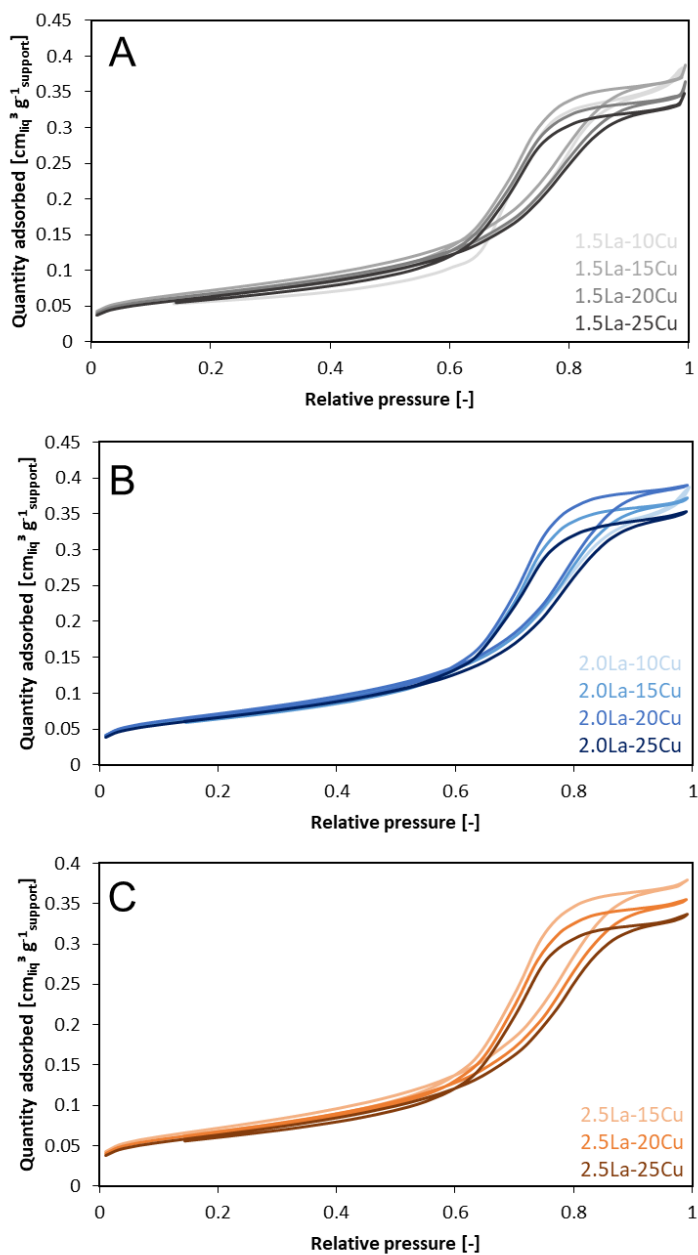


Figure 4.SI.1. N_2 -sorption isotherms and pore size distributions of the (A) 1.5La-yCu, (B) 2.0La-yCu, (C) 2.5La-yCu.

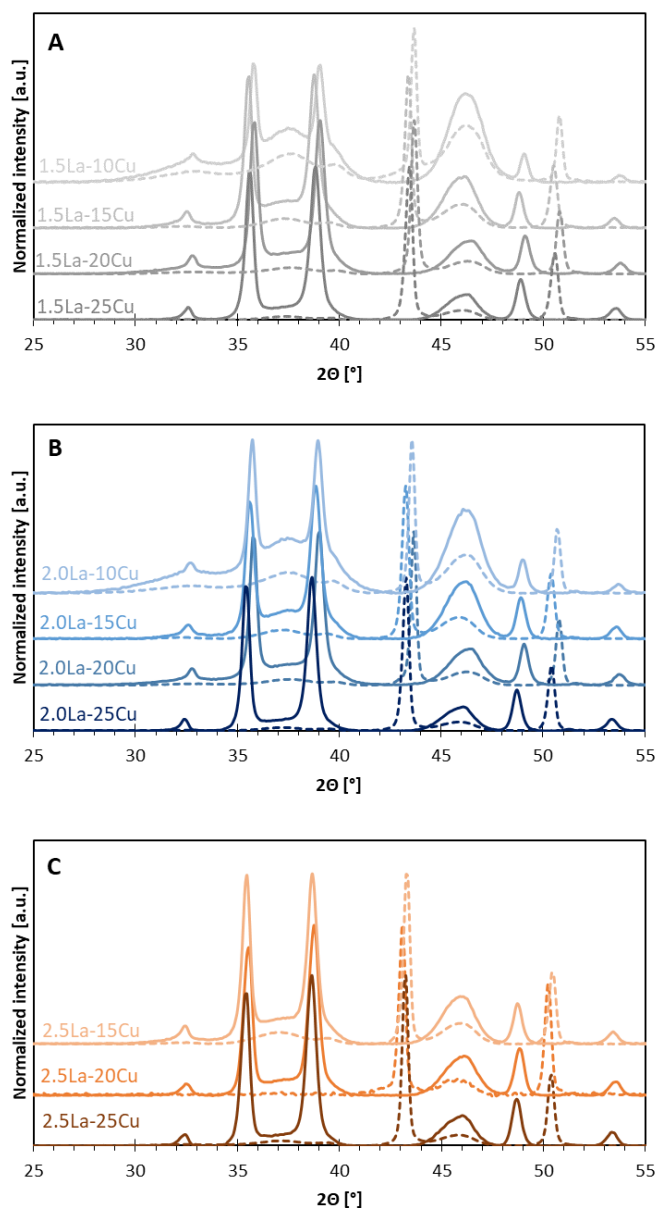


Figure 4.SI.2. XRD patterns of the calcined (full line) and reduced (dashed lines) (A) 1.5La-yCu, (B) 2.0La-yCu, (C) 2.5La-yCu catalysts. The crystalline phases are indicated in Figure 4.2.

Table 4.SI.1. Comparison of the La/Cu and Cu/Al mass ratios calculated from the results obtained by ICP-OES and XPS and the Cu 2p_{3/2} BE and amount of Cu²⁺ of the calcined xLa-γCu catalysts.

	La/Al		Cu/Al		BE [eV]	Cu ²⁺ [%]
	ICP	XPS	ICP	XPS		
10Cu	0.000	0.000	0.202	0.127	934.64	100
1.0La-10Cu	0.013	0.020	0.212	0.124	933.86	92
1.5La-10Cu	0.018	0.016	0.208	0.068	934.44	93
1.5La-15Cu	0.019	0.025	0.212	0.093	934.20	87
1.5La-20Cu	0.018	0.014	0.382	0.076	934.13	91
1.5La-25Cu	0.019	0.026	0.321	0.160	933.44	87
2.0La-10Cu	0.024	0.018	0.19	0.054	934.04	94
2.0La-15Cu	0.025	0.025	0.306	0.084	934.09	86
2.0La-20Cu	0.025	0.018	0.400	0.054	934.17	89
2.0La-25Cu	0.024	0.024	0.531	0.112	933.70	87
2.5La-15Cu	0.029	0.026	0.306	0.160	933.98	86
2.5La-20Cu	0.030	0.035	0.426	0.072	933.68	80
2.5La-25Cu	0.030	0.032	0.514	0.108	933.45	84

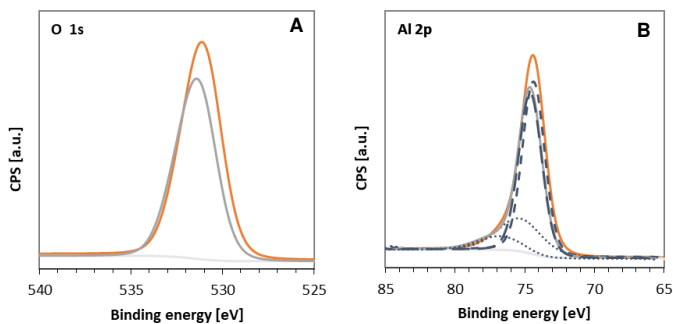


Figure 4.SI.3. The O 1s (A) and Al 2p (B) XPS spectra of the calcined 1.5La-20Cu catalyst (grey) and 2.5La-20Cu (orange), i.e. the lowest and the highest La/Cu ratio, respectively. Dotted and dashed lines in B are the deconvolutions for Al-O and Al-OH.

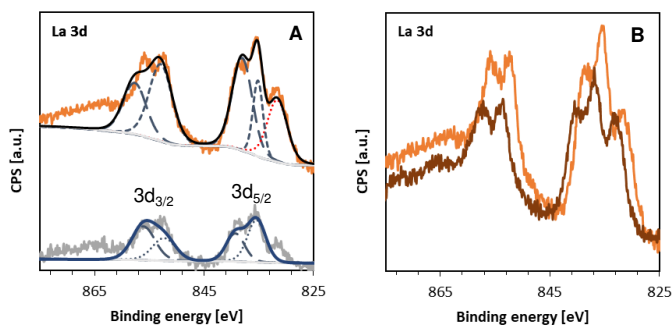


Figure 4.SI.4. La 3d spectrum of (A) the calcined 1.5La-20Cu catalyst (grey) and 2.5La-20Cu (orange), i.e. the lowest and the highest La/Cu ratio, respectively. The dashed and dotted lines correspond to the spin-orbit splitting.

(B) the calcined (orange) and reduced (brown) 2.5La-Cu catalyst. The shoulder in 3d_{5/2} at around 828 eV was assigned to LaF, an impurity in the precursor as it increased with increasing La/Cu ratio.

Table 4.SI.2. The crystallite size of Cu⁰, the metal surface area, average diameter of the Cu⁰ aggregates, dispersion, degree of reduction and total number of acid sites of the reduced xLa-yCu⁰-Al₂O₃ catalysts.

Support	$d_{Cu^0}^a$ [nm]	$MSA_{Cu^0}^b$ [m ² g ⁻¹ _{cat}]	$\Phi_{Cu^0}^b$ [nm]	$D_{Cu^0}^b$ [%]	Degree of reduction ^c [%]	Acid sites ^d [μmol g ⁻¹]
Support	n.a.	n.a.	n.a.	n.a.	n.a.	50
10Cu	75	24	1.8	12	76	60
1.0La-10Cu	52	25	1.7	13	84	55
1.5La-10Cu	50	34	1.3	17	85	61
1.5La-15Cu	48	22	3.1	7.1	85	67
1.5La-20Cu	66	24	3.8	5.7	81	61
1.5La-25Cu	77	18	4.8	4.5	98	58
2.0La-10Cu	42	14	1.1	7.3	89	59
2.0La-15Cu	50	21	2.9	7.6	96	60
2.0La-20Cu	62	18	4.3	5.0	91	53
2.0La-25Cu	66	20	4.4	4.9	97	57
2.5La-15Cu	44	18	3.2	6.9	90	58
2.5La-20Cu	48	18	4.1	5.3	92	51
2.5La-25Cu	56	17	5.4	4.1	93	59

^a determined by XRD patterns using the Scherrer's equation

^b determined via dissociative N₂O adsorption

^c determined from H₂-TPR.

^d determined via NH₃-TPD

Table 4.SI.3. Number of different types of acid sites on the reduced catalysts, determined by NH₃-TPD.

	Total ^a	Total	Weak + moderate	Strong	Weak + moderate Cu ^b	Strong Cu ^c	wt.Al ₂ O ₃ ^d
	[$\mu\text{mol g}^{-1}\text{ sup}$]	[$\mu\text{mol g}^{-1}\text{ cat}$]	[%]				
Support	50	50	37	12	n.a.	n.a.	100
10Cu	66	60	41	23	3	12	90.7
1.0La-10Cu	61	55	42	15	6	4	90.5
1.5La-10Cu	68	61	48	19	8	8	89.4
1.5La-15Cu	79	67	37	20	15	9	84.5
1.5La-20Cu	71	56	43	19	7	9	79.4
1.5La-25Cu	73	58	39	16	12	6	79.5
2.0La-10Cu	67	60	44	21	5	10	89.8
2.0La-15Cu	70	60	37	17	11	6	85.7
2.0La-20Cu	62	51	38	14	6	4	81.7
2.0La-25Cu	72	57	45	19	8	9	79.6
2.5La-15Cu	67	58	38	13	12	3	86.5
2.5La-20Cu	61	51	44	13	6	3	82.8
2.5La-25Cu	75	59	37	15	14	6	78.4

^a determined as total number of acid sites per gram of catalyst divided by the weight percentage of Al₂O₃, i.e. support, in the catalyst

^b estimated as the difference between the number of weak and moderate acid sites in the catalyst and the number of weak and moderate acid sites in the support, corresponding to the weight percentage in the catalyst

^c estimated as the difference between the number of strong acid sites in the catalyst and the number of strong acid sites in the support, corresponding to the weight percentage in the catalyst

^d estimated based on the ICP composition (Table 4.1) of La, assuming to be LaO, and Cu, assuming to be a mixed of CuO and Cu₂O, taking into account the degree of reduction (Table 4.SI.2).

Table 4.SI.4. La/Cu and Cu/Al mass ratios calculated from the results obtained by XPS and XPS characteristics from the Cu 2p_{3/2} region of the xLa-yCu catalysts reduced at 623 K using 100 % H₂ at 0.33 NmL s⁻¹.

	La/Al	Cu/Al	BE [eV]	KE [eV]	Modified Auger parameter [eV]	Cu ⁺ [%]	Cu ⁰ [%]
10Cu	0.000	0.039	932.31	918.41	1850.54	0	100
1.0La-10Cu	0.019	0.066	932.80	916.50	1849.3	60	40
1.5La-10Cu	0.016	0.050	932.84	916.06	1848.9	80	20
1.5La-15Cu	0.023	0.051	932.38	916.57	1849.0	83	17
1.5La-20Cu	0.015	0.049	932.59	916.56	1849.2	65	35
1.5La-25Cu	0.023	0.080	932.52	916.82	1849.3	59	41
2.0La-10Cu	0.015	0.034	932.65	916.34	1849.0	90	10
2.0La-15Cu	0.023	0.043	932.42	916.85	1849.3	85	15
2.0La-20Cu	0.015	0.030	932.81	916.50	1849.3	85	15
2.0La-25Cu	0.021	0.059	932.34	916.95	1849.3	62	38
2.5La-15Cu	0.031	0.050	932.37	916.81	1849.2	83	17
2.5La-20Cu	0.029	0.037	932.24	916.70	1848.9	85	15
2.5La-25Cu	0.030	0.063	932.27	917.02	1849.3	65	35

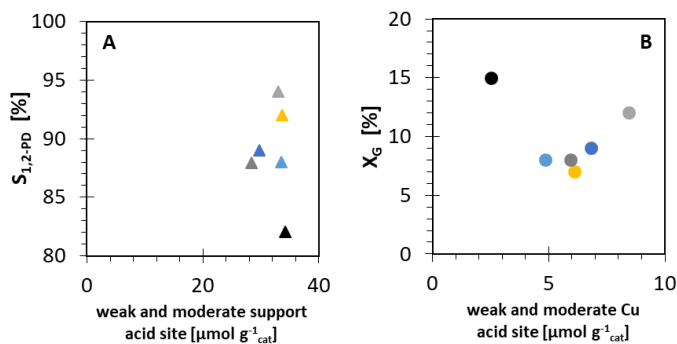


Figure 4.SI.5. (A) Effect of the number of weak and moderate acid sites from the support, on the 1,2-propanediol selectivity. (B) Effect of the number of weak and moderate acid sites from the Cu* on the glycerol conversion. Selectivity and conversion are determined after 12 h time on stream at $135 \text{ kg}_{\text{cat}} \text{ s mol}^{-1}_{\text{glycerol}}$, 473 K, a total H₂ pressure of 7.5 MPa and a molar H₂ to glycerol ratio of 7. Catalysts: 10Cu (black), 1.5La-20Cu (dark grey), 2.0La-20Cu (dark blue), 1.0La-10Cu (yellow), 1.5La-10Cu (light grey) and 2.0La-10Cu (light blue).

Table 4.SI.5. Performance of the undoped Cu/γ-Al₂O₃ catalyst at 473 K, 7.5 MPa, $135 \text{ kg}_{\text{cat}} \text{ s mol}^{-1}_{\text{G}}$ and $7 \text{ mol}_{\text{H}_2} \text{ mol}^{-1}_{\text{G}}$

Total TOS [h]	12-20	36-44	60-68
X _G [%]	15	14	12
Selectivity [%]			
methanol	0	0	0
2-propanol	0	1	1
ethanol	0	0	0
1-propanol	0	1	1
acetol	15	14	16
1,2-propanediol	82	80	77
1,2-ethanediol	1	3	3
1,3-propanediol	1	1	1

Table 4.SI.6. Performance of the 1.0La-10Cu/ γ -Al₂O₃ catalyst at 473 K, 7.5 MPa, 135 kg_{cat} s mol⁻¹_G and 7 molH₂ mol⁻¹_G

Total TOS [h]	12-20	36-44	60-68
X _G [%]	7	7	6
Selectivity [%]			
methanol	0	0	0
2-propanol	0	0	0
ethanol	0	1	2
1-propanol	0	0	0
acetol	2	2	2
1,2-propanediol	93	92	90
1,2-ethanediol	5	4	5
1,3-propanediol	0	0	1

Table 4.SI.7. Performance of the 1.5La-10Cu/ γ -Al₂O₃ catalyst at 473 K, 7.5 MPa, 135 kg_{cat} s mol⁻¹_G and 7 molH₂ mol⁻¹_G

Total TOS [h]	12-20	36-44	60-68
X _G [%]	12	12	10
Selectivity [%]			
methanol	0	0	0
2-propanol	1	0	1
ethanol	0	0	0
1-propanol	0	0	0
acetol	1	2	2
1,2-propanediol	95	94	94
1,2-ethanediol	3	4	3
1,3-propanediol	0	0	0

Table 4.SI.8. Performance of the 1.5La-20Cu/ γ -Al₂O₃ catalyst at 473 K, 7.5 MPa, 135 kg_{cat} s mol⁻¹_G and 7 molH₂ mol⁻¹_G

Total TOS [h]	12-20	36-44	60-68
X _G [%]	9	8	7
Selectivity [%]			
methanol	0	0	0
2-propanol	0	0	0
ethanol	0	0	0
1-propanol	0	0	0
acetol	2	2	2
1,2-propanediol	87	87	90
1,2-ethanediol	8	8	5
1,3-propanediol	3	3	3

Table 4.SI.9. Performance of the 2.0La-10Cu/ γ -Al₂O₃ catalyst at 473 K, 7.5 MPa, 135 kg_{cat} s mol⁻¹G and 7 mol_{H2} mol⁻¹G.

Total TOS [h]	12-20	36-44	60-68
X _G [%]	8	8	7
Selectivity [%]			
methanol	1	1	1
2-propanol	0	0	0
ethanol	1	1	2
1-propanol	1	0	1
acetol	2	2	1
1,2-propanediol	88	87	86
1,2-ethanediol	4	5	6
1,3-propanediol	2	3	3

Table 4.SI.10. Performance of the 2.0La-20Cu/ γ -Al₂O₃ catalyst at 473 K, 7.5 MPa, 135 kg_{cat} s mol⁻¹G and 7 mol_{H2} mol⁻¹G.

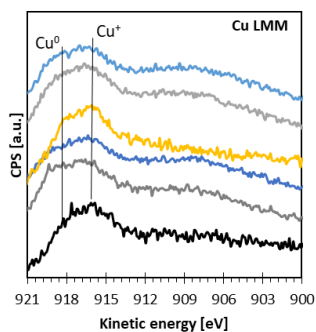
Total TOS [h]	12-20	36-44	60-68
X _G [%]	8	7	6
Selectivity [%]			
methanol	0	0	0
2-propanol	1	1	2
ethanol	1	2	2
1-propanol	0	0	0
acetol	3	3	2
1,2-propanediol	89	88	82
1,2-ethanediol	6	6	11
1,3-propanediol	0	0	0

Table 4.SI.11. Bulk composition and mass ratios calculated from the results obtained by ICP OES of the spent xLa-yCu catalysts.

	La [wt.%]	Cu [wt.%]	La/Al	Cu/Al	La/Cu
10Cu	0.0	5.39	0.0	0.26	0
1.0La-10Cu	0.42	7.47	0.026	0.23	0.11
1.5La-10Cu	0.70	8.07	0.040	0.27	0.086
1.5La-20Cu	0.67	13.98	0.020	0.42	0.047
2.0La-10Cu	0.95	8.34	0.026	0.23	0.113
2.0La-20Cu	0.77	12.10	0.070	0.59	0.063

Table 4.SI.12. La/Cu and Cu/Al mass ratios calculated from the results obtained by XPS and XPS characteristics from the Cu 2p_{3/2} region of the spent xLa-yCu catalysts.

	La/Al	Cu/Al	BE [eV]	KE [eV]	Modified Auger parameter [eV]	Cu ⁺ +Cu ⁰ [%]	Cu ²⁺ [%]	$\frac{Cu^0 + Cu^+}{Cu^{2+}}$
10Cu	0.000	0.087	932.08	916.24	1848.32	21	79	0.27
1.0La-10Cu	0.018	0.102	932.29	916.28	1848.57	46	54	0.85
1.5La-10Cu	0.022	0.056	932.30	916.56	1848.86	80	20	4.00
1.5La-20Cu	0.023	0.062	931.34	917.16	1849.10	41	59	0.69
2.0La-10Cu	0.028	0.049	932.44	916.75	1849.19	77	23	3.35
2.0La-20Cu	0.025	0.051	932.30	916.90	1849.20	49	51	0.95

**Figure 4.SI.6.** Cu LMM spectra of the spent 10Cu (black), 1.5La-20Cu (dark grey), 2.0La-20Cu (dark blue), 1.0La-10Cu (yellow), 1.5La-10Cu (light grey) and 2.0La-10Cu (light blue) catalyst.

CHAPTER 5.
ASSESSMENT OF THE SUPPORT ON
CU AND LA-CU CATALYSTS
FOR GLYCEROL HYDROGENOLYSIS

5.1 Introduction

It was shown in Chapter 4 that catalyst acidity, introduced by the support and Cu^+ species, played a role in the performance of the La-Cu/ $\gamma\text{-Al}_2\text{O}_3$ catalysts in glycerol hydrogenolysis towards 1,2-propanediol. The weak-moderate acid sites were found to enhance the 1,2-propanediol selectivity. By modifying the Al_2O_3 support with SiO_2 , the acidic properties of the catalysts can be modified, with both Lewis and Brønsted acid sites, see Figure 5.1. Lewis acid sites are formed by the substitution of Si^{4+} ions by Al^{3+} ions at tetrahedral lattice sites, while Brønsted acid sites are formed by bridged hydroxy groups, which is reminiscent of zeolites.¹

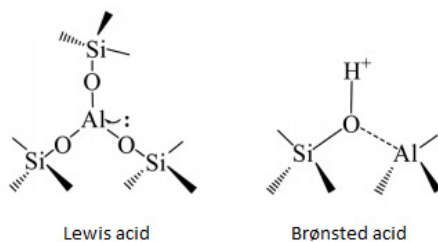


Figure 5.1. Formation of Lewis and Brønsted sites in an $\text{Al}_2\text{O}_3\text{-SiO}_2$ support.

Kim *et al.*² characterized the number and acid site types of various $\text{Al}_2\text{O}_3\text{-SiO}_2$ materials. Pure Al_2O_3 has fewer acid sites than the metal-oxide mixture and pure SiO_2 almost has no acid sites. A maximum total acidity amounting to $450 \mu\text{mol}_{\text{NH}_3} \text{g}^{-1}_{\text{cat}}$ was obtained at 40 mol% (or 53 wt.%) SiO_2 . It was also found that pure alumina contains only Lewis acids¹⁻³, while above 60 mol% (or 47 wt.%) SiO_2 , Brønsted acid sites were the dominant type. Daniell *et al.*¹ identified three surface phases in $\text{Al}_2\text{O}_3\text{-SiO}_2$ catalysts: silica, alumina and aluminosilicate. Figure 5.2A represents pure $\gamma\text{-Al}_2\text{O}_3$. No mixed phases were formed when the SiO_2 was increased up to 5 wt.%, see Figure 5.2B. From CO-FTIR, no large changes with respect to both acid site types were observed at this low SiO_2 content. Further increasing the SiO_2 loading up to 20 wt.%, resulted in the formation of an aluminosilicate phase, see Figure 5.2C, and tetrahedrally unsaturated Al^{3+} ions were observed in the IR-spectrum. This enhanced the strong Brønsted acidity which can be ascribed to bridged OH groups exposed on the aluminosilicate surface phase. Moderate Brønsted acidity is also present, most likely originating from the silica phase. The number of exposed aluminosilicate sites reaches a maximum at 40 wt.% SiO_2 , see Figure 5.2D, where no alumina phase remained on the surface. Further increasing of the SiO_2 content, see Figure 5.2E and F, decreased the acidity and the silica phase encapsulates the aluminosilicate phase until only the SiO_2 phase is present. It was found that the highest acid strength and the maximum number of acid sites is obtained for a SiO_2 content of 40 wt.%.⁴⁻⁶

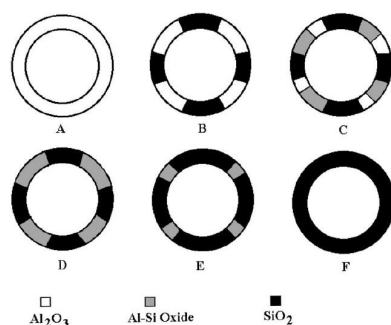


Figure 5.2. Representation of the surface composition of (A) pure γ - Al_2O_3 , (B) γ - Al_2O_3 with 1.5 to 5 wt.% SiO_2 , (C) γ - Al_2O_3 with 10 to 20 wt.% SiO_2 , (D) γ - Al_2O_3 with 30 to 40 wt.% SiO_2 , (E) γ - Al_2O_3 with 40 to 60 wt.% SiO_2 and (F) pure SiO_2 , according to Daniell et al.¹, reproduced with permission of Elsevier.

As stated in section 1.4 (Chapter 1), Lewis acid sites are more selective towards 1,2-propanediol in comparison to Brønsted acid sites which exhibit a more pronounced selectivity towards 1,3-propanediol. To the author's best knowledge, the variation in acid sites of Al_2O_3 - SiO_2 support for glycerol hydrogenolysis is only studied for Pt.⁷ Therefore, it is of utmost interest to investigate the impact of the support, and its acidity, on the performance for (La-)Cu catalysts glycerol hydrogenolysis. To this end, four different commercial supports with varying Al_2O_3 - SiO_2 ratios were used: pure γ - Al_2O_3 (indicated as Al_2O_3), 99 wt.% γ - Al_2O_3 – 1 wt.% SiO_2 (indicated as 99 Al_2O_3), 60 wt.% γ - Al_2O_3 – 40 wt.% SiO_2 (indicated as 60 Al_2O_3) and pure SiO_2 (indicated as SiO_2). The supported 10 wt.% Cu catalyst will be compared to a La doped one (1 wt.%La-10wt.%Cu), to simultaneously assess the effect of the acidity of the support and the La-promotion.

5.2 Results and discussion

5.2.1 Calcined catalyst characterization

N_2 -sorption experiments, were used to determine the textural properties of the catalysts. Evaluating the effect of the Cu loading and La-promotion on these characteristics was done by performing the experiment on the calcined support, the supported Cu and La-Cu supported material. The effect was then deduced from the isotherm type, the BET surface area, the mesopore volume and the pore size distribution. The procedures are discussed in section 2.1.2.1 (Chapter 2).

The sorption isotherms of all catalysts and supports were identified as type IV isotherms according to IUPAC (Figure 5.3), corresponding to porous materials.⁸ For the mixed Al_2O_3 - SiO_2 catalysts, there was an increase in mesopore volume and average mesopore diameter (Table 5.1) compared to the pure Al_2O_3 support as a result of the SiO_2 incorporation. This was evidenced by a wider hysteresis loop. Further, the plateau at high relative pressures became less defined for the 60 Al_2O_3 and SiO_2 supports, indicating the transition to even larger pores. In Figure 5.3A, it can be seen that the SiO_2 support exhibited a very broad pore size distribution with both mesopores (2 – 50 nm) and macro pores (> 50 nm). The hysteresis

curve of Al_2O_3 and $99\text{Al}_2\text{O}_3$ were classified as type H1 indicating cylindrical pores, while $60\text{Al}_2\text{O}_3$ and SiO_2 had type H3 hysteresis curves resulting from slit-shaped pores.⁹ The BET surface area of the supports increased in the order of $\text{SiO}_2 < \text{Al}_2\text{O}_3 < 99\text{Al}_2\text{O}_3 < 60\text{Al}_2\text{O}_3$ (Table 5.1). The surface area was thus higher for the mixed phases than for their bare constituents, with a maximum achieved at 40 wt.% SiO_2 , which is in agreement with literature^{1, 10, 11}. The loading of Cu decreased the BET surface area for about 10 %, compared to the bare support. It can be concluded that the impact of the Cu loading on the textural properties is not more pronounced than one would expect when loading 10 wt.% of non-porous Cu phase. The loading of both La and Cu also resulted in a similar the decrease of the BET surface area compared to the bare support, except for the La-Cu/ SiO_2 where an unexpected increase was observed.

Table 5.1. BET surface area, mesoporous volume, pore diameter, Cu 2p_{3/2} BE and absolute fraction of Cu²⁺ of the calcined supports and catalysts.

	S_{BET} [m ² g ⁻¹] ^a	V_{meso} [cm ³ g ⁻¹] ^b	D_p [nm] ^b	BE [eV]	Cu ²⁺ [%]
Al_2O_3					
Support	185	0.39	7.8	n.a.	n.a.
Cu	164	0.40	6.8	934.64	100
La-Cu	174	0.44	6.5	933.86	92
$99\text{Al}_2\text{O}_3$					
Support	226	0.40	6.2	n.a.	n.a.
Cu	170	0.34	8.3	934.46	92
La-Cu	213	0.45	7.4	933.22	68
$60\text{Al}_2\text{O}_3$					
Support	437	0.68	5.9	n.a.	n.a.
Cu	405	0.67	6.3	933.76	76
La-Cu	371	0.63	6.9	933.21	46
SiO_2					
Support	141	0.01	4.4	n.a.	n.a.
Cu	118	0.05	4.7	933.25	50
La-Cu	224	0.04	4.4	933.45	50

^a determined by BET-method

^b determined by BJH-desorption method

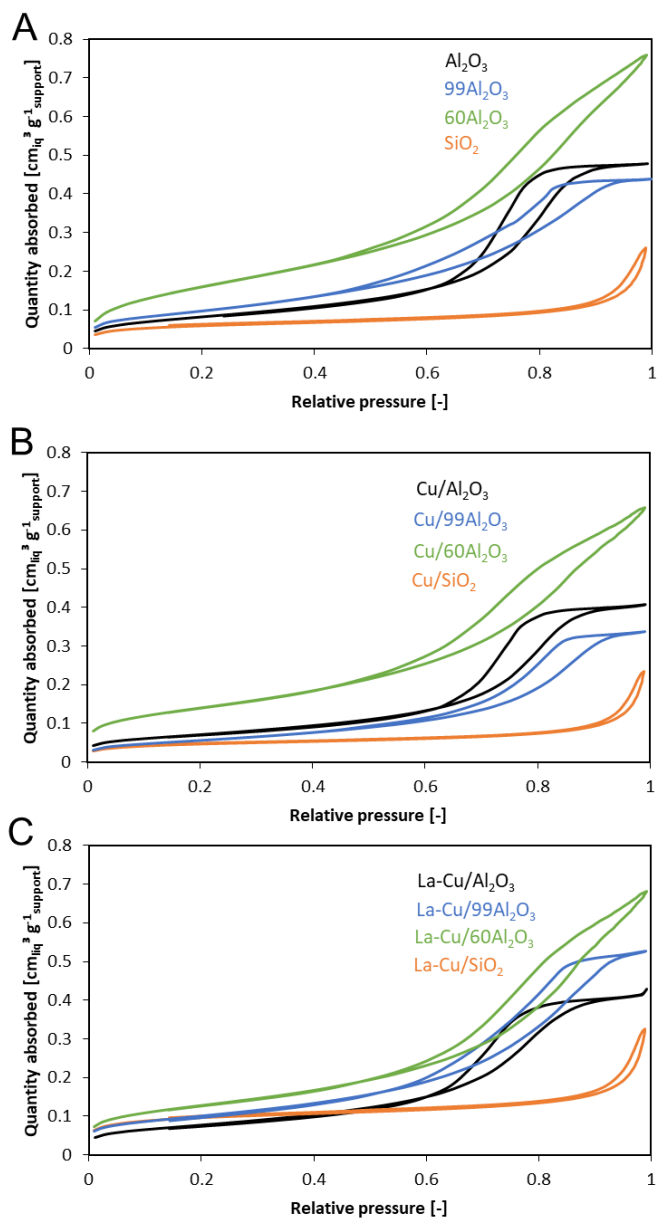


Figure 5.3. N_2 -sorption isotherms and pore size distribution of the calcined (A) supports, (B) supported Cu catalysts (10wt.%) and (C) supported La-Cu catalysts (10wt.% Cu, 1wt.% La).

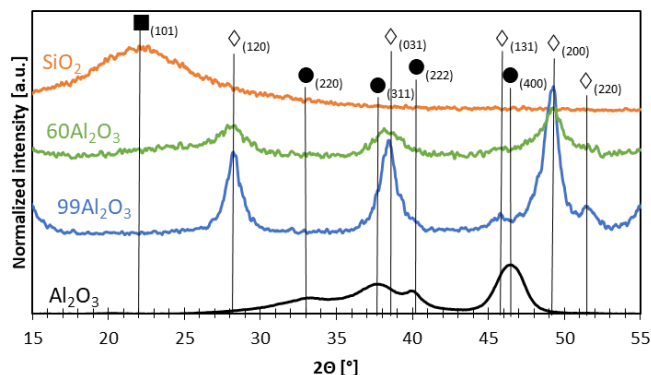


Figure 5.4. XRD pattern of the calcined Al₂O₃ (black), 99Al₂O₃ (blue), 60Al₂O₃ (green) and SiO₂ (orange) with boehmite (◇), γ-Al₂O₃ (●) and SiO₂ (■).

The XRD patterns for the bare supports are shown in Figure 5.4. As discussed in the previous chapters, the γ-Al₂O₃ exhibited diffraction peaks at 31.8°, 37.5°, 39.2°, 45.7° (JCPDS 00-050-0741), respectively corresponding to the Al₂O₃(220), Al₂O₃(311), Al₂O₃(222), Al₂O₃(400) facets. The broad diffraction peak of SiO₂ corresponded to cristobalite SiO₂ (JCPDS 00-0039-1425). For the Al₂O₃-SiO₂ supports, the diffraction peaks at 28.2°, 38.4°, 45.8°, 48.9° and 51.6° corresponded to AlOOH₍₁₂₀₎, AlOOH₍₀₃₁₎, AlOOH₍₁₃₁₎ and AlOOH₍₂₀₀₎. Typically, boehmite transforms into γ-Al₂O₃ at temperatures of 753 – 803 K.¹² As the calcination temperature of the catalysts was 723 K, the mixed Al₂O₃-SiO₂ supports exhibited only boehmite and no γ-Al₂O₃ phases. The diffraction peaks of the boehmite are broadened for increasing SiO₂ content. According to the theory of scattering, as discussed in section 2.1.2.4 (Chapter 2), this was the result of the transition to amorphous phase due to an increase of lattice defects induced by SiO₂.

The calcined catalysts were analyzed by XPS, following the procedures stated in section 2.1.2.6 (Chapter 2), to gain insight in the chemical surface composition and oxidation state, which could be affected on the one hand through the interaction between the support and the Cu species, and on the other hand through the Cu-La interaction. The results of the XPS measurements are shown in Figure 5.5 and listed in Table 5.1. The Cu 2p_{3/2} spectra of the catalyst are displayed in Figure 5.5A. For the Cu/Al₂O₃ catalyst, the peak around 934 eV and the satellite peak (*ca.* 942 eV to *ca.* 948 eV) suggest the presence of Cu²⁺ species. The species were ascribed to CuO (933.5 eV). By increasing the SiO₂ content, the peak shifts to lower BE's, see Figure 5.5B, suggesting the formation of Cu species with a lower oxidation state (Cu⁺). Accordingly, the intensity of the satellite peak decreased indicating a lower amount of Cu²⁺ species, see Figure 5.5C. Next to the effect of the SiO₂ content, the addition of La results in a decrease of the Cu 2p_{3/2} BE, due to the strong La-Cu interactions as discussed in section 4.2.1 (Chapter 5). However, this was only observed for the Al₂O₃-containing supports. For the La doped pure SiO₂ support, the BE shifts to higher values indicating a weaker La-Cu interaction in this case, which is explained by the fact that silica is known for its inert character, whereby no important or only weak

interactions occur with the Cu species.¹³⁻¹⁶ For the Al₂O₃ supported catalyst, the La-promotion decreased the Cu²⁺ content due to the formation of Cu⁺ species, which is in agreement with the results of Chapter 4.

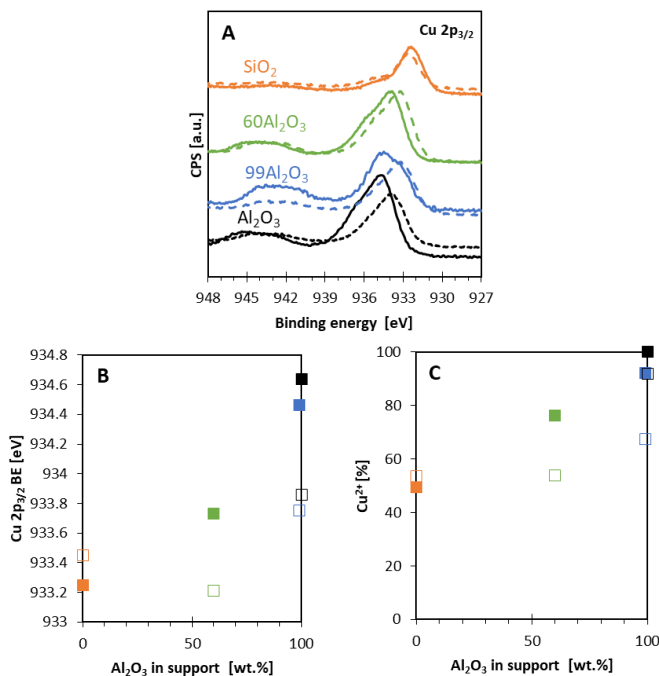


Figure 5.5. (A) Cu 2p_{3/2} spectra of the calcined Cu (full line) and La-Cu (dashed line) catalysts supported on Al₂O₃ (black), 99Al₂O₃ (blue), 60Al₂O₃ (green) and SiO₂ (orange). (B) The corresponding Cu 2p_{3/2} BE and (C) Cu²⁺ fraction for the calcined Cu (■) or La-Cu catalysts (□) supported on Al₂O₃ (black), 99Al₂O₃ (blue), 60Al₂O₃ (green) and SiO₂ (orange).

In summary, the mixed Al₂O₃-SiO₂ supports exhibited larger BET surface areas compared to their constituents and a broader pore size distribution as a result of the incorporation of the highly amorphous SiO₂ with macropores. The Cu-support interaction decreased with increasing SiO₂ content, however, this was counteracted by the addition of La *prior* to the Cu. The stronger the Cu-support interaction, which is strengthened by the presence of La, the higher the Cu²⁺ fraction in the calcined catalysts.

5.2.2 Reduced catalyst characterization

The specific surface area, diameter and dispersion of the reduced Cu species were characterized by means of N₂O adsorption, of which the details are discussed in section 2.1.2.3.2 (Chapter 2). H₂-TPR was used to determine the degree of reduction, see section 2.1.2.3.1 (Chapter 2), and to get insights into the reduction profile. The oxidation state of the surface species was investigated by XPS. The acid characteristics of the supports and catalysts were determined by NH₃-TPD, see section 2.1.2.3.3 (Chapter 2).

The effect of the support on the specific surface area of the Cu aggregates, MSA_{Cu^0} , the average diameter of the aggregates, ϕ_{Cu^0} and the Cu dispersion, D_{Cu^0} , were analyzed by dissociative N_2O adsorption (Table 5.SI.1). The MSA_{Cu^0} decreases from $25 \text{ m}^2 \text{ g}^{-1}_{cat}$ to $6.3 \text{ m}^2 \text{ g}^{-1}_{cat}$ with increasing SiO_2 content (Figure 5.6A). This indicates that Cu was less dispersed, see Figure 5.6C, most probably due to weaker metal-support interactions with SiO_2 compared to Al_2O_3 ,¹³⁻¹⁶ which was already suggested by the XPS results of the calcined catalysts in section 5.2.1. The Cu coverage on the support surface was calculated (Table 5.SI.1) and varied between 0.5 and 3 %, indicating the formation of Cu nanoparticles rather than a monolayer. Correspondingly, the ϕ_{Cu^0} increased almost with a factor four with increasing SiO_2 content, see Figure 5.6B, due to the weaker metal-support interactions. On the Al_2O_3 support, the La-promotion had no significant impact on the MSA_{Cu^0} , as the difference is less than 10 % (which is assumed to be the experimental error). For the $Al_2O_3-SiO_2$, the La-promotion increased the MSA_{Cu^0} , while in case of the SiO_2 support, the MSA_{Cu^0} decreased upon promotion by La. Further, on the Al_2O_3 containing supports, La-promotion decreased the ϕ_{Cu^0} , as expected due to the strong interactions between La and Cu observed in Chapter 4. The effect on the Al_2O_3 is not significant, but it is believed also to be present. No stabilizing effect was observed for the pure SiO_2 supported La-Cu catalyst. As a result, the dispersion decreased with increasing SiO_2 content but increased with La-promotion, with the exception of the pure SiO_2 supported catalyst.

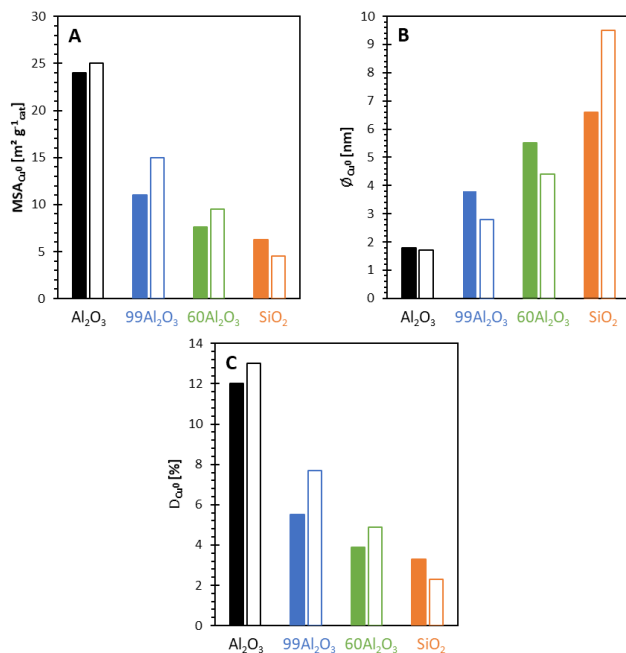


Figure 5.6. Specific surface area of the Cu aggregates, MSA_{Cu^0} (A), average diameter of the Cu aggregates, ϕ_{Cu^0} (B), and Cu dispersion, D_{Cu^0} (C) for the Cu (full bar) and the La-Cu (empty bar) catalysts supported on Al_2O_3 (black), 99 Al_2O_3 (blue), 60 Al_2O_3 (green) and SiO_2 (orange).

Figure 5.7 shows the reduction profile of the Cu species in the considered catalysts. In Chapter 4 section 4.2.2, it was discussed that different reduction temperatures corresponded to different Cu species. Around 450 K, indicated as the α peak, the reduction of highly dispersed CuO^{17} and/or $(\text{Cu-O-Cu})^{2+18}$ species occurred. Bulk CuO , indicated by the γ peak, is reduced around 500 K.^{17, 19, 20} The reduction of Cu^{2+} particles with weak interaction was observed as a shoulder (β) before the γ peak, while Cu^{2+} particles with a strong interaction, such as in CuAl_2O_4 , (β') after the γ peak.²¹⁻²³ Hence, the reduction profile depended on two phenomena: the particle size and the interaction with the support. For the $\text{Cu}/\text{Al}_2\text{O}_3$ catalyst (Figure 5.7A), one can clearly observe that this catalyst has the highest amount of dispersed Cu species (α), in agreement with Figure 5.6B. Adding La, increased the interaction with the support with the formation of the β peak. When a small amount of SiO_2 is introduced (Figure 5.7B), one can clearly observe the weaker interaction with the support due to the presence of the β peak. As observed before, La-promotion decreased the particle size (Figure 5.6B), in these TPR profiles, resulting in a higher α peak. In Figure 5.7C, one can clearly observe the increased particle size from Figure 5.6B, due to the high amount of bulk CuO species (γ peak). On the one hand, the addition of La resulted in Cu species with stronger interactions (β' peak) and smaller particles (peak between α and β). The TPR profile of the SiO_2 supported catalysts (Figure 5.7D) is less complex compared to the catalysts with Al_2O_3 . Only one peak corresponding to Cu species with a weak interaction (β) is observed, which is in agreement with the XPS results in section 5.2.1. For the La-promoted the β peak shifted slightly and a broad β' peak appeared, corresponding to Cu species with a large particle size, as observed in Figure 5.6. The degree of reduction (Table 5.SI.1) increased with SiO_2 content, as Cu^{2+} is easier reduced to Cu^0 due to the weaker metal-support interaction.

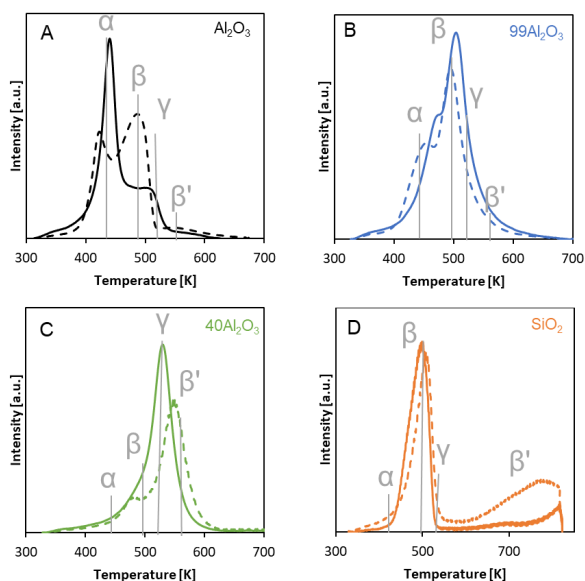


Figure 5.7. TPR profiles for Cu (full line) and La-Cu (dashed line) catalysts, supported on Al_2O_3 (A), $99\text{Al}_2\text{O}_3$ (B), $60\text{Al}_2\text{O}_3$ (C) and SiO_2 (D).

XPS analysis was used to determine the oxidation states and the composition at the surface of the reduced catalysts. Based on the absence of the satellite peaks in Figure 5.8A, one can conclude that most of the Cu^{2+} species were reduced to Cu^+ and/or Cu^0 , in agreement with the calculated degree of reduction (Table 5.SI.1). The shift of the Cu $2p_{3/2}$ BE can be either positive or negative. When the interaction with the support is stronger, the BE generally shifts to lower BE as previously discussed in section 5.2.1. The BE shift can also be caused by the particle size. For a smaller particle size the inter-atomic distance is reduced which results in a shift towards higher BE.^{24, 25} In Figure 5.6 it was shown that the ϕ_{Cu^0} decreased with increasing Al_2O_3 content and with La-addition, with the exception of the La-Cu/ SiO_2 catalyst. So, there is a twofold effect present in the reduced catalysts. On the one hand, with increasing interaction, *i.e.* increasing Al_2O_3 content, the BE will shift to lower values. On the other hand, the smaller ϕ_{Cu^0} as result of the La-promotion or the support interaction, will counteract the shift. This balance results in a maximum Cu $2p_{3/2}$ BE for the $60\text{Al}_2\text{O}_3$ support (Table 5.SI.2). As discussed in Chapter 4, one can distinguish between Cu^+ and Cu^0 by examining the Cu LMM spectra shown in Figure 5.9. The surface of the Cu/ Al_2O_3 catalysts is covered with pure Cu^0 , while all the other catalysts exhibit an asymmetric peak between the KE of Cu^0 and Cu^+ , indicating a coexistence of both species. The concentration of the individual species is shown in Table 5.SI.2. For the unpromoted Cu catalysts, the absolute fraction of Cu^+ increases with ϕ_{Cu^0} . Larger particles (like on SiO_2) are less easy to be reduced in comparison to smaller particles (like on Al_2O_3). As expected, the effect of La-promotion is more complicated, since both - the ϕ_{Cu^0} and the La-Cu interaction - affect the Cu^+ formation.

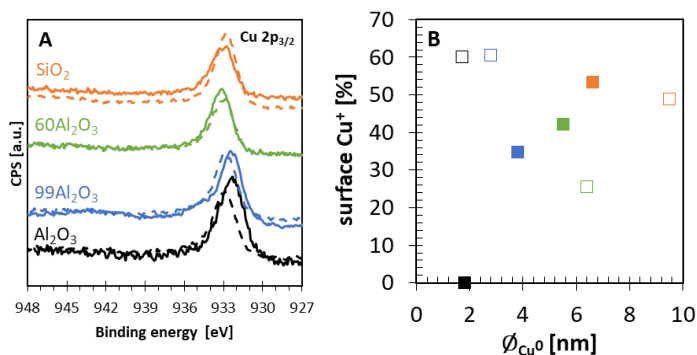


Figure 5.8. (A) Cu 2p_{3/2} spectra of the reduced Cu (full line, ■) and La-Cu (dashed line, □) catalysts supported on Al₂O₃ (black), 99Al₂O₃ (blue), 60Al₂O₃ (green) and SiO₂ (orange). (B) Corresponding fraction of Cu⁺ as function of the ϕ_{Cu^0} .

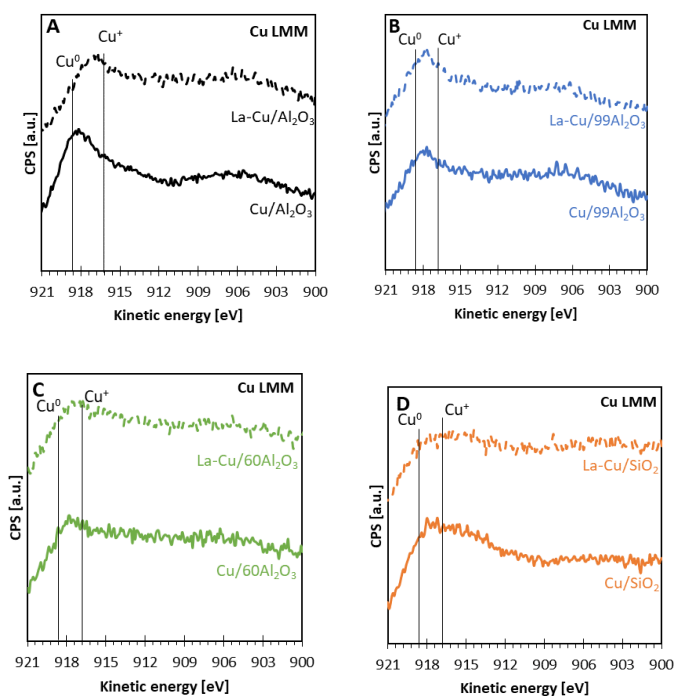


Figure 5.9. Cu LMM spectra of the reduced Cu (full line) and La-Cu (dashed line) catalysts supported on (A) Al₂O₃, (B) 99Al₂O₃, (C) 60Al₂O₃ and (D) SiO₂.

The total acid site concentration, studied by NH₃-TPD, is depicted in Figure 5.10A. The support's total acidity decreased in the order of 60Al₂O₃ ≥ 99Al₂O₃ > Al₂O₃ > SiO₂, in agreement with literature¹⁻³. As stated in the introduction, the incorporation of SiO₂ into Al₂O₃ leads to the formation of bridged hydroxyl groups, with the creation of Brønsted acid sites, or to the substitution of Al³⁺ by Si⁴⁺ by ions, contributing

to the Lewis acidity (Figure 5.1), leading to the formation of an aluminosilicate phase.¹ The increase in acidity was attributed to strong acid sites (Figure 5.10B). A maximum in acidity was observed, as the three phases contributed to the acidity. For the supported Cu catalysts, this trend remained unchanged. The addition of Cu (Figure 5.10C) had almost no effect on the acidity of on the pure supports, whereas for the Cu/99Al₂O₃ and Cu/60Al₂O₃ respectively an increase and decrease was observed. The trends for supported La-Cu catalysts were less coherent. For the La-Cu/99Al₂O₃ catalyst, a significant decrease in the total number of acid sites was observed, compared both to the support and the Cu supported catalyst. For the other catalysts, no significant change was observed in the total number of acid sites. In agreement with Chapter 4, La-addition resulted in an increase of weak-moderate acid sites, but a decrease in strong acid sites (Figure 5.SI.1). To gain more insight into the additional factors affecting the acidity, a more detailed characterization of the type of acid sites, such as pyridine-FTIR or CO-FTIR, is suggested.

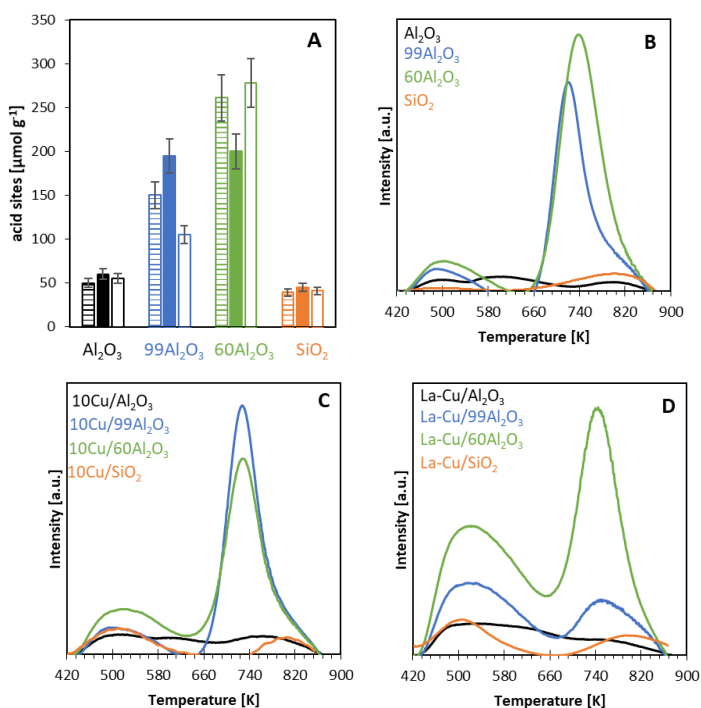


Figure 5.10. (A) Total concentration of acid sites, determined by NH₃-TPD, for the support (striped bar), Cu (full bar) and La-Cu (open bar) catalysts and NH₃-TPD profiles of the support (B), Cu (C) and La-Cu (D) catalysts supported on Al₂O₃ (black), 99Al₂O₃ (blue), 60Al₂O₃ (green) and SiO₂ (orange)

In summary, with increasing SiO₂ content, the Cu-support interaction decreased resulting in a larger ϕ_{Cu^0} and a lower dispersion. On the other hand, the La-Cu interaction caused smaller ϕ_{Cu^0} and higher dispersion. A coexistence of Cu⁰ and Cu⁺, depending on the ϕ_{Cu^0} and the interaction, was observed for the reduced catalysts. Overall, the total acidity decreased in the order of 60Al₂O₃ \geq 99Al₂O₃ > Al₂O₃ >

SiO₂. This trend was related to the introduction of strong acid sites, most probably Brønsted acid sites, when SiO₂ is introduced in the Al₂O₃ framework.

5.2.3 Catalyst performance

Liquid glycerol hydrogenolysis was performed on a fixed-bed reactor operated under trickle-bed regime on the HTK-MI setup. A detail description of the setup can be found in section 2.1.3.1 (Chapter 2). The experimental conditions were chosen within the intrinsic kinetics regime, as described in section 2.1.3.2 (Chapter 2). In this section, the textural properties and acid characteristics of the catalysts were related to their activity in the glycerol hydrogenolysis and the selectivity to 1,2-propanediol.

The stability of the catalyst was verified by returning to the initial reaction conditions, according to the temperature profile in Figure 5.SI.2, after 85 h TOS. The Al₂O₃ and 99Al₂O₃ supported catalysts showed an increase in glycerol conversion (with 57 %, 3 % and 10 %, for respectively Cu/Al₂O₃, Cu/99Al₂O₃ and La-Cu/99Al₂O₃ as listed in Table 5.SI.3, Table 5.SI.5 and Table 5.SI.6), while the glycerol conversion decreased for the supports with the higher SiO₂ content (with 6 %, 4% and 5 %, for respectively Cu/60Al₂O₃, Cu/SiO₂ and La-Cu/SiO₂, see Table 5.SI.7, Table 5.SI.9 and Table 5.SI.10). This rather unexpected observed behavior for the Al₂O₃ and 99Al₂O₃ supported catalysts may be due to differences in the impact of the reaction conditions on the Cu⁰ phase, as the performance of Cu-based catalysts is not only structure sensitive in terms of particle size, but also depends on the exposed facets (as suggested in Chapter 4). Further, the La-promoted catalyst exhibited a more pronounced deactivation than expected, indicating that Cu species are very sensitive to the temperature. A more detailed characterization of the spent catalysts, by means of XPS, N₂O adsorption, XRD and STEM, could provide more insight into the observed phenomena. As the changes on the surface during the temperature profile are unknown, only the results at 473 K are discussed in the next section.

In agreement with Chapter 4, the MSA_{Cu^0} cannot be correlated to the catalytic activity (Figure 5.11A). As stated before, it is assumed that the glycerol hydrogenolysis is catalyzed by acid sites (Chapter 1, section 1.5.1), hence, a higher activity was expected with an increasing number of acid sites. This relationship was observed for the Al₂O₃-containing catalysts in Figure 5.11B. According to the literature²⁶, γ -Al₂O₃-containing supports, and thus the corresponding catalysts, exhibit mostly Lewis acidity. These catalysts showed a relationship between the weak-moderate acid sites and the activity (Figure 5.SI.3A and B), attributed to the presence of Cu⁺ (as discussed in Chapter 4). Additionally, there is a significant increase in Brønsted acidity when increasing the SiO₂ content from 0 wt.% (*i.e.* the Al₂O₃ support) to 40 wt.% (*i.e.* the 60Al₂O₃ support), due to the formation of the bridged hydroxyl groups (as stated in the introduction, see section 5.1). The activity of the Al₂O₃-containing catalysts showed a relationship with the strong acid sites, which are assumed to be Brønsted type (Figure 5.SI.3C). The SiO₂-supported catalysts exhibited a higher TOF, despite the low number of acid sites (Figure 5.10), which is attributed to the structure sensitivity of Cu-based catalysts (Figure 5.11C). As discussed in

section 5.2.1, a higher SiO_2 content resulted in a larger ϕ_{Cu^0} , and as a consequence less active sites will be present on the surface resulting in a higher TOF, despite the similar conversion (Figure 5.12). However, no clear effect of La-promotion on the TOF could be demonstrated. This is most likely the result of the superposition of different aspects, *i.e.* the stronger La-Cu interaction but lower Cu-support interactions with SiO_2 content. Thus, one cannot conclude on the predominant effect, however, it is clear that the catalytic activity is balanced by the ϕ_{Cu^0} and acidity, affected by the fraction of Cu^+ and – probably – the type of acid sites. Therefore, *operando* XAS could afford a great opportunity to understand the mechanism, as it monitors the dynamic behavior of both the geometric structure and the electronic environment of the catalytic sites.

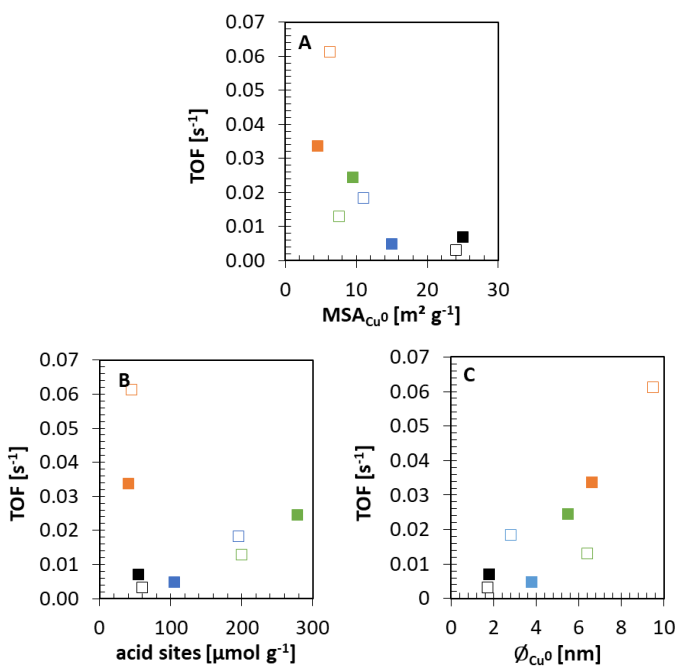


Figure 5.11. TOF as function of (A) the MSA_{Cu^0} , determined by N_2O adsorption, (B) the total number of acid sites, determined by NH_3 -TPD, and (C) the ϕ_{Cu^0} , determined by N_2O adsorption. TOF was calculated at 12 h TOS, $135 \text{ kg}_{\text{cat}} \text{ s mol}^{-1}_{\text{glycerol}}$, 473 K, a total H_2 pressure of 7.5 MPa and a molar H_2 to glycerol ratio of 7 for Cu (■) and La-Cu (□) catalysts supported on Al_2O_3 (black), 99 Al_2O_3 (blue), 60 Al_2O_3 (green) and SiO_2 (orange).

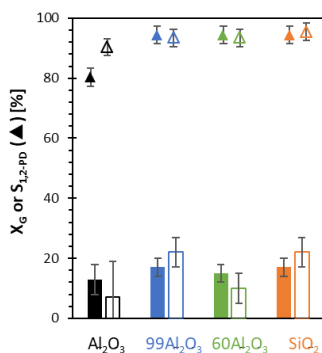


Figure 5.12. Effect of support and La-promotion on the average glycerol conversion (bars) and 1,2-propanediol selectivity (triangle) for the Cu catalysts (full symbols) and La-Cu catalysts (empty symbols) supported on Al₂O₃ (black), 99Al₂O₃ (blue), 60Al₂O₃ (green) and SiO₂ (orange), at 473 K, 135 kg_{cat} s⁻¹ glycerol, a total H₂ pressure of 7.5 MPa and a molar H₂ to glycerol ratio of 7. Error bars are determined as standard deviation.

Cu-based catalysts are very selective for glycerol hydrogenolysis towards 1,2-propanediol (Figure 1.20), with selectivities exceeding 82 % (Figure 5.12). As the amount of Brønsted acid sites are supposed to increase with the SiO₂-content^{1, 26, 27}, it was expected that the catalysts supported on 60Al₂O₃ and 99Al₂O₃ would exhibit a higher selectivity towards 1,3-propanediol and 1,2-ethanediol (as discussed in section 1.4, Chapter 1) compared to the bare Al₂O₃ supported catalysts. This effect was less pronounced as all catalysts showed low selectivity to 1,3-propanediol (*ca.* 0-1%) and 1,2-ethanediol (*ca.* 1-4%), impeding any conclusion. The effect of La-promotion on the 1,2-propanediol selectivity was not significant, except for the Al₂O₃ support. This indicates that the exact ratio of the Lewis and Brønsted acid sites, rather than the total number of acid sites, is acquired for a detailed understanding of the product selectivities.

5.3 Conclusions

The influence of the Al₂O₃-SiO₂ support composition, together with the La-promotion, on the glycerol hydrogenolysis, and more specifically the catalysts activity and selectivity towards 1,2-propanediol has been investigated. Four different Al₂O₃-SiO₂ supports were used to synthesize Cu and La-Cu catalysts.

Characterization, by N₂-sorption and NH₃-TPD, showed that the mixed Al₂O₃-SiO₂ support had an increased specific surface area and total number of acid sites. It was found, by N₂O adsorption, that with increasing SiO₂-content, the Cu-support interaction decreased resulting in a larger ϕ_{Cu^0} , meaning a lower Cu-dispersion, while La-Cu interaction caused smaller ϕ_{Cu^0} and higher Cu-dispersion. The average diameter of the Cu⁰ aggregates was found to be between 1.7 and 9.5 nm, corresponding to a dispersion between 2.3 % and 13 %. In the reduced state, XPS revealed the coexistence of Cu⁰ and Cu⁺, whereby the amount of Cu⁺ species depended not only on the ϕ_{Cu^0} but also on the Cu-support and the La-Cu interaction.

The catalysts were evaluated for liquid phase glycerol hydrogenolysis towards 1,2-propanediol. The structure sensitivity of the Cu particles was one of the dominant factors in the catalytic activity. Further, it was found that the total acidity affected the catalytic activity as well. On the one hand, as the Cu-support interaction decreases, a higher Cu^+ fraction was present on the catalyst prior to the reaction, which facilitated to conversion of glycerol. On the other hand, the $\text{Al}_2\text{O}_3\text{-SiO}_2$ catalysts showed a higher number of strong acid sites, catalyzing the dehydration of glycerol. The prepared Cu-based catalysts are very selective for glycerol hydrogenolysis to 1,2-propanediol, with selectivities exceeding 82%. Unexpectedly, no correlation between the total acidity and the selectivity towards 1,2-propanediol or the other products was found. Therefore, further determination of the exact ratio between Lewis and Brønsted acid sites, by pyridine-FTIR, could lead to new insights on their influence on the catalytic performance and more the product selectivities, *i.e.* the acetol versus 1,2-propanediol selectivity on the one hand and the byproducts on the other hand. A more detailed characterization via *operando* XAS can enlighten the nature of the active catalytic species in glycerol hydrogenolysis. Characterization, such as TGA, STEM, XRD or XPS, of the spent catalysts would also allow to gain further insights into the obtained results.

5.4 References

- 1 W. Daniell, U. Schubert, R. Glöckler, A. Meyer, K. Noweck, H. Knözinger, Enhanced Surface Acidity in Mixed Alumina–Silicas: A Low-Temperature Ftir Study, *Applied Catalysis A: General*, 196 (2000) 247-260.
- 2 Y.T. Kim, K.-D. Jung, E.D. Park, Gas-Phase Dehydration of Glycerol over Silica–Alumina Catalysts, *Applied Catalysis B: Environmental*, 107 (2011) 177-187.
- 3 H. Pines, W.O. Haag, Alumina: Catalyst and Support. I. Alumina, Its Intrinsic Acidity and Catalytic Activity1, *Journal of the American Chemical Society*, 82 (1960) 2471-2483.
- 4 Y. Shinmi, S. Koso, T. Kubota, Y. Nakagawa, K. Tomishige, Modification of Rh/Sio₂ Catalyst for the Hydrogenolysis of Glycerol in Water, *Applied Catalysis B: Environmental*, 94 (2010) 318-326.
- 5 C.W. Chiu, M.A. Dasari, G.J. Suppes, W.R. Sutterlin, Dehydration of Glycerol to Acetol Via Catalytic Reactive Distillation, *AIChE Journal*, 52 (2006) 3543-3548.
- 6 T. Yamaguchi, K. Tanabe, Dehydration of Secondary Alcohols Catalyzed by Solid Acids, *Bulletin of the Chemical Society of Japan*, 47 (1974) 424-429.
- 7 I. Gandarias, P.L. Arias, J. Requies, M.B. Güemez, J.L.G. Fierro, Hydrogenolysis of Glycerol to Propanediols over a Pt/Asa Catalyst: The Role of Acid and Metal Sites on Product Selectivity and the Reaction Mechanism, *Applied Catalysis B: Environmental*, 97 (2010) 248-256.
- 8 K.S. Sing, D. Everett, R. Haul, L. Moscou, R. Pierotti, J. Rouquerol, T. Siemieniowska, Reporting Physisorption Data for Gas/Solid Systems with Special Reference to the Determination of Surface Area and Porosity (Recommendations 1984), *Pure appl. chem.*, 57 (1985) 603-619.
- 9 K.S.W. Sing, R.T. Williams, Physisorption Hysteresis Loops and the Characterization of Nanoporous Materials, *Adsorption Science & Technology*, 22 (2004) 773-782.
- 10 F. Regali, L.F. Liotta, A.M. Venezia, M. Boutonnet, S. Järås, Hydroconversion of N-Hexadecane on Pt/Silica-Alumina Catalysts: Effect of Metal Loading and Support Acidity on Bifunctional and Hydrogenolytic Activity, *Applied Catalysis A: General*, 469 (2014) 328-339.
- 11 S.A. Kishore Kumar, M. John, S.M. Pai, Y. Niwate, B.L. Newalkar, Low Temperature Hydrogenation of Aromatics over Pt–Pd/Sio₂–Al₂O₃ Catalyst, *Fuel Processing Technology*, 128 (2014) 303-309.
- 12 S. Lamouri, M. Hamidouche, N. Bouaouadja, H. Belhouchet, V. Garnier, G. Fantozzi, J.F. Trellat, Control of the γ -Alumina to α -Alumina Phase Transformation for an Optimized Alumina Densification, *Boletín de la Sociedad Española de Cerámica y Vidrio*, 56 (2017) 47-54.
- 13 G. Águila, F. Gracia, J. Cortés, P. Araya, Effect of Copper Species and the Presence of Reaction Products on the Activity of Methane Oxidation on Supported CuO Catalysts, *Applied Catalysis B: Environmental*, 77 (2008) 325-338.
- 14 V.V. Thyssen, T.A. Maia, E.M. Assaf, Cu and Ni Catalysts Supported on γ -Al₂O₃ and SiO₂ Assessed in Glycerol Steam Reforming Reaction, *Journal of the Brazilian Chemical Society*, 26 (2015) 22-31.
- 15 W. Phongsawat, B. Netiworaruksa, K. Suriye, P. Praserttham, J. Panpranot, Effect of SiO₂–Al₂O₃ Composition on the Catalytic Performance of the Re₂O₇/SiO₂–Al₂O₃ Catalysts in the Metathesis of Ethylene and 2-Pentene for Propylene Production, *Catalysis Letters*, 142 (2012) 1141-1149.
- 16 J. Wang, C. Zeng, Al₂O₃ Effect on the Catalytic Activity of Cu–ZnO–Al₂O₃–SiO₂ Catalysts for Dimethyl Ether Synthesis from CO₂ Hydrogenation, *Journal of natural gas Chemistry*, 14 (2005) 156-162.
- 17 C.-Y. Shiau, M. Ma, C. Chuang, Co Oxidation over CeO₂-Promoted Cu/ γ -Al₂O₃ Catalyst: Effect of Preparation Method, *Applied Catalysis A: General*, 301 (2006) 89-95.
- 18 A. Yin, X. Guo, W.-L. Dai, K. Fan, The Nature of Active Copper Species in Cu-Hms Catalyst for Hydrogenation of Dimethyl Oxalate to Ethylene Glycol: New Insights on the Synergetic Effect between Cu⁰ and Cu⁺, *The Journal of Physical Chemistry C*, 113 (2009) 11003-11013.
- 19 M.-F. Luo, Y.-J. Zhong, X.-X. Yuan, X.-M. Zheng, Tpr and Tpd Studies of CuO/CeO₂ Catalysts for Low Temperature CO Oxidation, *Applied Catalysis A: General*, 162 (1997) 121-131.
- 20 J. Xiaoyuan, L. Guanglie, Z. Renxian, M. Jianxin, C. Yu, Z. Xiaoming, Studies of Pore Structure, Temperature-Programmed Reduction Performance, and Micro-Structure of CuO/CeO₂ Catalysts, *Applied Surface Science*, 173 (2001) 208-220.

- 21 Z. Huang, F. Cui, H. Kang, J. Chen, X. Zhang, C. Xia, Highly Dispersed Silica-Supported Copper Nanoparticles Prepared by Precipitation– Gel Method: A Simple but Efficient and Stable Catalyst for Glycerol Hydrogenolysis, *Chemistry of Materials*, 20 (2008) 5090-5099.
- 22 M.L. Dieuzeide, R. de Urriaga, M. Jobbagy, N. Amadeo, Vapor Phase Hydrogenolysis of Glycerol to 1,2-Propanediol at Atmospheric Pressure over Copper Catalysts Supported on Mesoporous Alumina, *Catalysis Today*, 296 (2017) 19-25.
- 23 X. Li, Q. Zhang, H. Xie, X. Gao, Y. Wu, G. Yang, P. Wang, S. Tian, Y. Tan, Facile Preparation of Cu-Al Oxide Catalysts and Their Application in the Direct Synthesis of Ethanol from Syngas, *ChemistrySelect*, 2 (2017) 10365-10370.
- 24 R.J. Isaifan, S. Ntais, E.A. Baranova, Particle Size Effect on Catalytic Activity of Carbon-Supported Pt Nanoparticles for Complete Ethylene Oxidation, *Applied Catalysis A: General*, 464-465 (2013) 87-94.
- 25 M.G. Mason, Electronic Structure of Supported Small Metal Clusters, *Physical Review B*, 27 (1983) 748-762.
- 26 Sasol Performance Chemicals, Doped Aluminas: Silica-Aluminas, Mixed Metal Oxides, Hydrotalcites.
- 27 R.J. Chimentão, P. Hirunsit, C.S. Torres, M.B. Ordoño, A. Urakawa, J.L.G. Fierro, D. Ruiz, Selective Dehydration of Glycerol on Copper Based Catalysts, *Catalysis Today*, (2020).

Supporting information

Table 5.SI.1. The Cu surface coverage, metal surface area, average diameter of the Cu⁰ aggregates, dispersion, degree of reduction and total number of acid sites of the reduced catalysts.

	θ [%] ^a	MSA_{Cu^0} [m ² g ⁻¹ cat] ^b	Φ_{Cu^0} [nm] ^b	D_{Cu^0} [%] ^b	Degree of reduction [%] ^c	Acid sites [μ mol g ⁻¹] ^d
<i>Al₂O₃</i>		n.a.	n.a.	n.a.	n.a.	50
<i>Cu</i>	2.9	24	1.8	12	76	60
<i>La-Cu</i>	2.9	25	1.7	13	84	55
<i>99Al₂O₃</i>		n.a.	n.a.	n.a.	n.a.	150
<i>Cu</i>	1.3	11	3.8	5.6	91	195
<i>La-Cu</i>	1.4	15	2.8	7.7	98	105
<i>60Al₂O₃</i>		n.a.	n.a.	n.a.	n.a.	261
<i>Cu</i>	0.4	7.6	5.5	3.9	100	200
<i>La-Cu</i>	0.5	9.5	4.4	4.9	97	278
<i>SiO₂</i>		n.a.	n.a.	n.a.	n.a.	39
<i>Cu</i>	1.1	6.3	6.6	3.3	100	45
<i>La-Cu</i>	0.4	4.5	9.5	2.3	99	41

^a surface coverage, calculated as the ratio between the 1/5 of the MSA_{Cu^0} to the surface area, assuming a Cu loading of 7.59 wt.% for the supported Cu catalyst and 7.3 wt.% for the supported La-Cu catalysts (according to Table 5.SI.1, as no ICP-OES was performed on the catalysts supported on 99Al₂O₃, 60Al₂O₃ and SiO₂).

^b determined via dissociative N₂O adsorption

^c determined from H₂-TPR.

^d determined via NH₃-TPD

Table 5.SI.2. XPS characteristics from the Cu 2p_{3/2} region of the reduced catalysts.

	BE [eV]	Cu ⁺ [%]	Cu ⁰ [%]
<i>Al₂O₃</i>			
<i>Cu</i>	932.31	0	100
<i>La-Cu</i>	932.80	60	40
<i>99Al₂O₃</i>			
<i>Cu</i>	932.45	41	35
<i>La-Cu</i>	932.93	39	61
<i>60Al₂O₃</i>			
<i>Cu</i>	933.14	58	42
<i>La-Cu</i>	933.07	75	25
<i>SiO₂</i>			
<i>Cu</i>	933.09	47	53
<i>La-Cu</i>	932.84	51	49

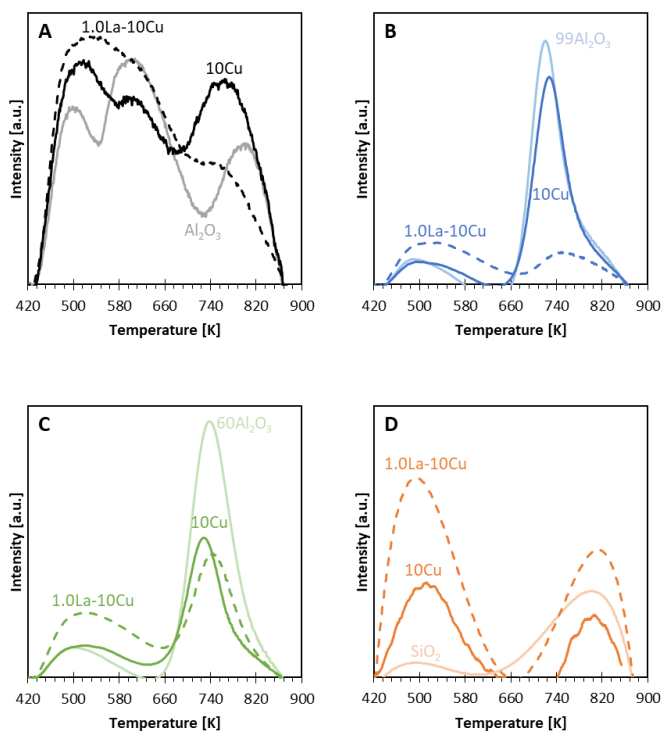


Figure 5.SI.1. NH₃-TPD profiles of the support (lighter color), Cu (full line) and La-Cu (dashed line) catalysts supported on Al₂O₃ (A), 99Al₂O₃ (B), 60Al₂O₃(C) and SiO₂ (D)

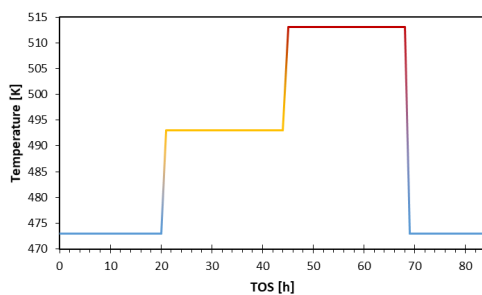


Figure 5.SI.2. Applied temperature profile for the catalysts at 135 kg_{cat} s mol⁻¹_{glycerol}, a total H₂ pressure of 7.5 MPa and a molar H₂ to glycerol ratio of 7.

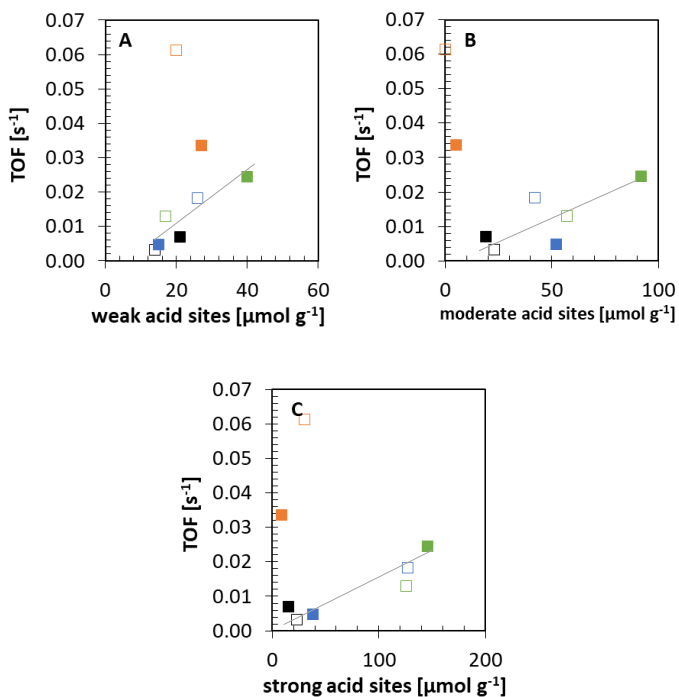


Figure 5.SI.3. The effect of (A) weak, (B) moderate and (C) strong acid sites, determined by NH_3 -TPD on TOF, which was calculated at 12 h TOS, $135 kg_{cat} s mol^{-1}_{glycerol}$, 473 K, a total H_2 pressure of 7.5 MPa and a molar H_2 to glycerol ratio of 7 for Cu (■) and La-Cu (□) catalysts supported on Al_2O_3 (black), $99Al_2O_3$ (blue), $60Al_2O_3$ (green) and SiO_2 (orange).

Table 5.SI.3. Results of the catalytic experiments with the Cu/Al₂O₃ catalyst at 135 kg_{cat} s mol⁻¹, 7.5 MPa and a molar H₂ to glycerol ratio of 7.

Temperature [K]	473	493	513	473
Total TOS [h]	18-20	42-44	66-68	85-88
X _G [%]	13	44	79	70
Selectivity [%]				
methanol	0	0	0	0
2-propanol	0	0	0	0
ethanol	0	0	0	0
1-propanol	0	0	0	0
acetol	15	1	1	2
1,2-propanediol	82	96	95	96
1,2-ethanediol	1	1	2	2
1,3-propanediol	0	0	0	0

Table 5.SI.4. Results of the catalytic experiments with the La-Cu/Al₂O₃ catalyst at 135 kg_{cat} s mol⁻¹, 7.5 MPa and a molar H₂ to glycerol ratio of 7.

Temperature [K]	473	493	513
Total TOS [h]	12-20	n.d.	n.d.
X _G [%]	7	n.d.	n.d.
Selectivity [%]			
methanol	1	n.d.	n.d.
2-propanol	0	n.d.	n.d.
ethanol	1	n.d.	n.d.
1-propanol	0	n.d.	n.d.
acetol	2	n.d.	n.d.
1,2-propanediol	92	n.d.	n.d.
1,2-ethanediol	4	n.d.	n.d.
1,3-propanediol	0	n.d.	n.d.

Table 5.SI.5. Results of the catalytic experiments with the Cu/99Al₂O₃ catalyst at 135 kg_{cat} s mol⁻¹, 7.5 MPa and a molar H₂ to glycerol ratio of 7.

Temperature [K]	473	493	513	473
Total TOS [h]	12-20	37-45	60-68	84-88
X _G [%]	17	26	66	20
Selectivity [%]				
methanol	0	0	0	0
2-propanol	1	1	1	1
ethanol	0	0	0	0
1-propanol	0	0	0	0
acetol	1	1	1	16
1,2-propanediol	95	97	95	77
1,2-ethanediol	2	1	2	2
1,3-propanediol	0	0	0	0
propionic acid	0	0	0	4

Table 5.SI.6. Results of the catalytic experiments with the La-Cu/99Al₂O₃ catalyst at 135 kg_{cat} s mol⁻¹, 7.5 MPa and a molar H₂ to glycerol ratio of 7.

Temperature [K]	473	493	513	473
Total TOS [h]	12-20	37-45	60-68	84-88
X _G [%]	22	37	42	32
Selectivity [%]				
methanol	0	0	0	0
2-propanol	0	0	0	0
ethanol	0	0	0	0
1-propanol	0	0	0	0
acetol	2	2	2	2
1,2-propanediol	95	95	95	95
1,2-ethanediol	2	2	2	2
1,3-propanediol	0	0	0	0
propionic acid	1	1	1	1

Table 5.SI.7. Results of the catalytic experiments with the Cu/60Al₂O₃ catalyst at 135 kg_{cat} s mol⁻¹, 7.5 MPa and a molar H₂ to glycerol ratio of 7.

Temperature [K]	473	493	513	473
Total TOS [h]	12-20	37-45	60-68	84-88
X _G [%]	15	26	48	7
Selectivity [%]				
methanol	0	0	0	0
2-propanol	1	0	0	1
ethanol	0	0	0	0
1-propanol	1	0	5	1
acetol	1	1	3	1
1,2-propanediol	96	95	89	95
1,2-ethanediol	1	2	2	1
1,3-propanediol	0	1	0	1
propionic acid	0	1	1	0

Table 5.SI.8. Results of the catalytic experiments with the La-Cu/60Al₂O₃ catalyst at 135 kg_{cat} s mol⁻¹, 7.5 MPa and a molar H₂ to glycerol ratio of 7.

Temperature [K]	473	493	513
Total TOS [h]	12-20	37-45	n.d.
X _G [%]	10	11	n.d.
Selectivity [%]			
methanol	0	0	n.d.
2-propanol	0	0	n.d.
ethanol	0	0	n.d.
1-propanol	1	1	n.d.
acetol	1	1	n.d.
1,2-propanediol	95	95	n.d.
1,2-ethanediol	1	1	n.d.
1,3-propanediol	1	1	n.d.
propionic acid	0	0	n.d.

Table 5.SI.9. Results of the catalytic experiments with the Cu/SiO₂ catalyst at 135 kg_{cat} s mol⁻¹, 7.5 MPa and a molar H₂ to glycerol ratio of 7.

Temperature [K]	473	493	513	473
Total TOS [h]	12-20	37-45	60-68	84-88
<i>X_G [%]</i>	17	30	55	13
<i>Selectivity [%]</i>				
<i>methanol</i>	0	0	0	0
<i>2-propanol</i>	0	0	0	1
<i>ethanol</i>	0	0	0	1
<i>1-propanol</i>	0	0	0	0
<i>acetol</i>	2	1	1	1
<i>1,2-propanediol</i>	96	97	95	95
<i>1,2-ethanediol</i>	1	1	3	1
<i>1,3-propanediol</i>	0	0	0	0
<i>propionic acid</i>	1	1	1	1

Table 5.SI.10. Results of the catalytic experiments with the La-Cu/SiO₂ catalyst at 135 kg_{cat} s mol⁻¹, 7.5 MPa and a molar H₂ to glycerol ratio of 7.

Temperature [K]	473	493	513	473
Total TOS [h]	12-20	37-45	60-68	84-88
<i>X_G [%]</i>	22	25	31	17
<i>Selectivity [%]</i>				
<i>methanol</i>	0	0	0	0
<i>2-propanol</i>	0	0	0	1
<i>ethanol</i>	0	0	0	0
<i>1-propanol</i>	0	0	0	0
<i>acetol</i>	1	1	0	1
<i>1,2-propanediol</i>	97	97	98	97
<i>1,2-ethanediol</i>	1	1	1	1
<i>1,3-propanediol</i>	0	0	0	0
<i>propionic acid</i>	1	1	1	0

CHAPTER 6. TECHNO-ECONOMIC EVALUATION OF SQUALENE RECOVERY FROM OIL DEODORIZER DISTILLATES

A modified version of this chapter was published as:

Alexandra Bouriakova, Pedro S.F. Mendes, Kathy Elst, Jeriffa De Clercq, Joris W. Thybaut
Techno-economic evaluation of squalene recovery from oil deodorizer distillates
Chemical Engineering Research and Design, 154 (2020), 122-134

6.1 Introduction

As mentioned in Chapter 1, there is an increased interest in vegetal squalene resources, due to consumer and legislative pressures, especially in the cosmetic industry. The squalene concentration in vegetable oils varies between 1-100 ppm for soybean oil and up to 6000 ppm for olive oil.¹ However, the concentration is, in most cases, too small for direct separation to be economically viable. Oil deodorizer distillates (ODD), *i.e.*, a waste stream obtained during the refining of vegetable oils, on the other hand, do represent a promising opportunity for squalene recovery, as they accumulate up to 150 times in the ODD as compared to the original vegetable oil.¹

Deodorization of crude vegetable oils removes several undesirable components for the color, taste and stability by steam stripping.² The obtained deodorizer distillate is a complex mixture of free fatty acids (FFA), fatty acid methyl esters (FAME), triglycerides (TG), diglycerides (DG), monoglycerides (MG), phytosterols and their esters, tocopherols, some aldehydes or ketones and hydrocarbons, *e.g.* squalene.³ As high purity squalene is needed for the food and cosmetic industry, as well as in medical applications, new processes have already been investigated to recover squalene from this sustainable source.¹ Meanwhile, the upgradation of the other valuable substances present in ODD, such as sterols and tocopherols, was investigated as well.¹

The isolation of the ‘minor’ components, *i.e.* not only squalene but also sterols and tocopherols, by molecular distillation⁴, crystallization⁵ and saponification⁶ has been discussed in section 1.7.1 (Chapter 1). The processes developed based on these methodologies have the drawback of being both economically and environmentally expensive, as they make use of organic solvents. Supercritical CO₂ (sc-CO₂) represents an interesting alternative. CO₂ can be considered a “green solvent” as it is nontoxic, nonflammable, inert, renewable and relatively cheap.^{7,8} Moreover, it is supercritical already at moderate pressures (7.4 MPa) and low temperatures (304 K), making it attractive for temperature sensitive components.⁹

Various authors have reported the extraction of squalene with sc-CO₂ from an ODD without prior ODD treatment. Akgün *et al.*¹⁰ attempted such a squalene recovery from olive ODDs. This was, however, not practical nor economically viable as a result of the long extraction time and low squalene purity (66 wt.%). Squalene recoveries up to 95 % *via* sc-CO₂ extraction have been claimed by other authors, but at relatively low extraction yields¹¹⁻¹⁴ or commercially complex process conditions¹⁵⁻¹⁸. This is the result of the comparable solubility of the FFAs and the squalene in sc-CO₂.^{19,20} To isolate squalene more efficiently, a difference in solubility between squalene and the other components in the ODD needs to be induced, *e.g.*, by removing or modifying the FFAs. By modifying the latter *via* esterification with an alcohol, the squalene recovery efficiency can be enhanced as explained in section 1.7.2 (Chapter 1).²¹ ²² Both methanol and ethanol can be used for such esterification, with methanol being favored kinetically as well as economically.²³ However, when ethanol is used for esterification, the produced esters (FAEE)

have a higher added value as biofuel or for technical applications (such as bio-solvents, bio-lubricants, bio-emulsifiers,...) as ethanol is more readily produced in a sustainability context. Even more, it was observed that FAEE are more easily separated from squalene compared to FAME. Simultaneously, the glycerides present in the oil also react with the alcohol. The transesterification of the triglycerides in rapeseed oil^{24, 25}, soybean oil²⁶⁻²⁸, sunflower oil^{25, 29} and linseed oil³⁰ at supercritical conditions was already investigated. At such conditions, the thermophysical properties of all components, such as viscosity, density and polarity, are reducing the impact of mass-transfer limitations of the solute in the supercritical solvent, resulting in higher reaction rates even in the absence of a catalyst.^{24, 25} Esterified ODDs have mainly been investigated for tocopherol and phytosterol isolation through CO₂-extraction.^{19, 31-33} Fornari *et al.*¹⁹ extended the scope towards squalene as a product of extraction of esterified olive ODD (90 wt.% purity, 64 % yield).

Process simulations constitute an alternative to investigate squalene recovery optimization and explore technical and economic viability. However, there are still some challenges in simulating complex mixtures, such as ODD, and supercritical conditions. Firstly, significantly different values can sometimes be obtained for the supercritical properties, *i.e.* the critical temperature, the critical pressure, the critical volume and acentric factor, when using different methods, as incorporated into process modelling software.³⁴ Secondly, there is a shortage of well estimated phase equilibria for supercritical extraction or fractionation for the components in this mixture. This renders the meaningful prediction of equilibrium compositions for multicomponent mixtures, such as ODD, challenging.

In this chapter, the valorization of ODD, is assessed at the process level. First, the kinetic modelling of supercritical ethanol esterification of sunflower ODD is dealt with in section 6.2.1. This step is performed first to reduce the FFA content in the ODD, enhancing the squalene extraction potential by sc-CO₂. The obtained reaction kinetics were used as input in section 6.2.2 for the detailed process simulation for squalene recovery from three different ODDs *via* supercritical ethanol esterification followed by a supercritical CO₂-extraction. To purify the squalene and other valuable by-products from this two-step process, a separation *via* flashing and distillation is included in the simulations and tailored for each of the considered ODDs. A comparison between olive, sunflower and soybean ODD as a vegetal source for squalene, as an alternative for deep shark liver oil, is first established in terms of extraction yield, recovery and purity in section 6.2.3. After the process design, a simplified economic study is performed and technical solutions to improve the process flexibility are explored in section 6.2.4.

6.2 Results and discussion

6.2.1 Thermodynamic and kinetic modelling

One of the most important stages, prior to the design and simulation of a process, is the investigation and identification of suitable thermodynamic and reaction kinetic models. Typically several steps are needed to acquire a model: (i) obtaining the experimental data, (ii) choosing an appropriate thermodynamic or kinetic model, (iii) estimation of the parameters of that model and (iv) selecting the most adequate model, if several models have been proposed. A balanced needs to be made between the (to be acquired) experimental data and the desired level of detail. Hence, a clear understanding of how the resulting model will be applied is required.

As stated in section 2.2.2.2 (Chapter 2), an EOS simulates the (p,V,T)-relationship of a component. A vapor-liquid equilibrium (VLE) describes the distribution of a component between the vapor and the liquid phases at equilibrium at a certain temperature. Experimental VLE data acquired in a wide pressure and temperature range are available in the literature.³⁵⁻⁴² The binary interaction parameters, as discussed in section 2.2.2.2 (Chapter 2), of the RK-ASPEN EOS were regressed to these data using the Data Regression module in the Aspen Plus® software. The regressed binary interaction parameters between CO₂ and every component are listed in Table 6.1.

Table 6.1. Optimized binary interaction coefficients for the RK-ASPEN EOS for system CO₂ (i) and various components (j)

component j	$k_{a,ij}^0$ [-]	$k_{a,ij}^1$ [K ⁻¹]	$k_{b,ij}^0$ [-]	$k_{b,ij}^1$ [K ⁻¹]
oleic acid	0.02 ± 0.21	0.21 ± 0.72	0.31 ± 4.9	-0.82 ± 10.70
triolein	2.08 ± 1.43	-6.44 ± 4.44	7.48 ± 4.5	-22.74 ± 13.90
ethanol	-4.98 ± 2.16	14.73 ± 7.52	6.85 ± 3.64	-28.42 ± 12.05
ethyl oleate	2.20 ± 0.57	-10.26 ± 1.75	11.74 ± 4.24	-56.87 ± 13.08
water	-9.03 ± 3.78	30.15 ± 12.89	-4.52 ± 2.12	15.41 ± 7.24
methyl oleate	0.37 ± 1.44	-0.97 ± 4.56	1.90 ± 5.3	-5.84 ± 16.62
β-sitosterol	9.55 ± 0.12	-15.15 ± 0.35	12.85 ± 0.29	-20.39 ± 0.84
α-tocopherol	-0.81 ± 0.25	2.78 ± 0.80	-5.52 ± 0.91	17.21 ± 2.91
squalene	-1.00 ± 0.83	3.49 ± 2.54	-2.77 ± 2.22	8.65 ± 6.93

The regressed binary interaction between triolein and oleic acid, triolein and sterols, methyl oleate and squalene and ethanol and water are given by equation (2.1), (2.2), (2.3) and (2.4) respectively. Due to the lack of additional experimental equilibrium data, all other interactions are assumed to be ideal, *i.e.* no interaction $k_{a,ij} = k_{b,ij} = 0$.

$$k_{a,TG-FFA} = 2.74(\pm 3.69) - 8.64(\pm 10.27) \frac{T}{1000} \quad (2.1)$$

$$k_{b,TG-FFA} = 2.44(\pm 2.53) - 7.20(\pm 7.9) \frac{T}{1000}$$

$$k_{a,TG-sterol} = 5.39(\pm 0.08) - 4.91(\pm 0.21) \frac{T}{1000} \quad (2.2)$$

$$k_{b,TG-sterol} = 1.95(\pm 0.05) + 1.59(\pm 0.12) \frac{T}{1000}$$

$$k_{a,FAME-squalene} = -0.80(\pm 0.27) + 2.06(\pm 0.86) \frac{T}{1000} \quad (2.3)$$

$$k_{b,FAME-squalene} = -1.96(\pm 0.49) + 5.95(\pm 1.55) \frac{T}{1000}$$

$$k_{a,EtOH-H_2O} = 35.66(\pm 11.31) - 122(\pm 34.99) \frac{T}{1000} \quad (2.4)$$

$$k_{b,EtOH-H_2O} = 32.05(\pm 9.44) - 109(\pm 30.01) \frac{T}{1000}$$

The parity diagram for equilibrium data based on the optimized parameters is shown in Figure 6.1. The parity diagram demonstrates the capability to predict vapor-liquid equilibria in an adequate way, even though some of the parameters were not estimated significantly. That at least one of the interaction parameters is significantly different from zero indicates that interaction effectively has to be accounted for in the model. Indeed, when compared to the prediction of the vapor-liquid equilibria without any interaction (Figure 6.SI.1), it is clear that the inclusion of all (interaction) parameters results in a better prediction of the vapor-liquid equilibrium.

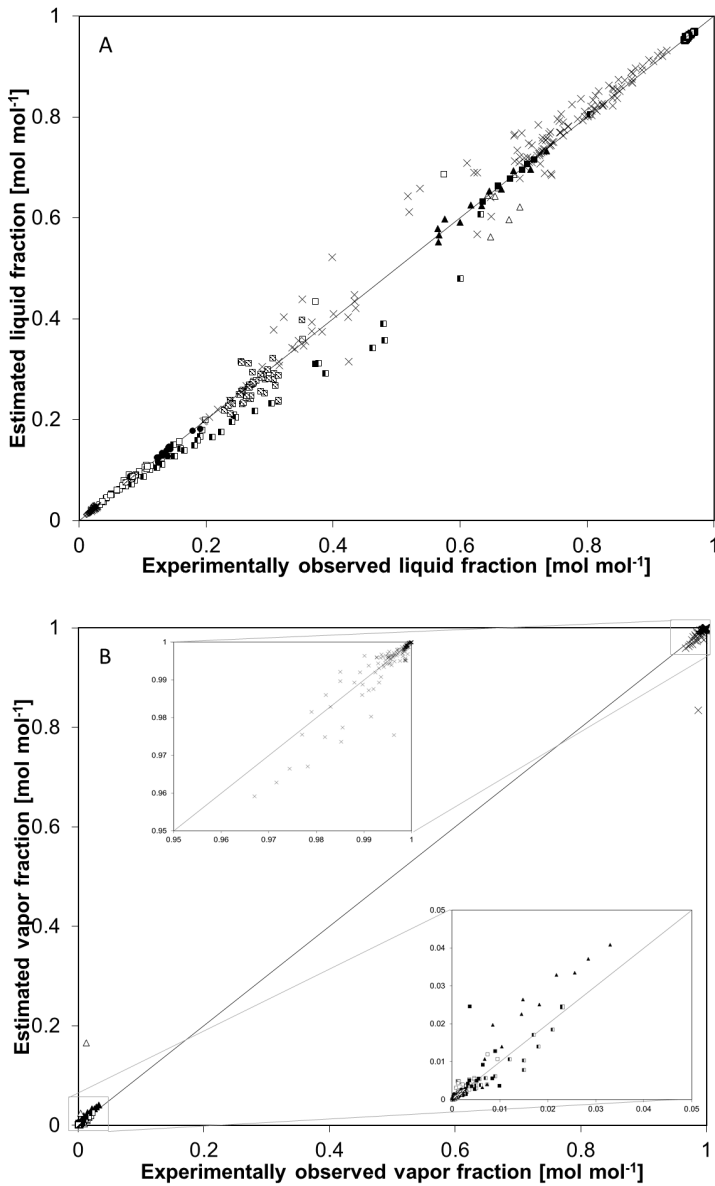


Figure 6.1. Comparison between experimental and estimated liquid (A) and vapor fraction (B) of vapor-liquid equilibria of FFA (\blacktriangle), TG (\blacksquare), EtOH (\diamond), FAEE (\blacksquare), water (\circ), FAME (\square), tocopherol (\boxplus), sterol (\boxminus), squalene (\bullet) and CO₂ (\times) using the RK-ASPEN EOS.

Next, a kinetic model was developed for the esterification of FFAs, reaction (2.18), and the transesterification reactions, reactions (2.19) till (2.21), in ODDs with supercritical ethanol. The experimental data (Appendix B) obtained for the supercritical esterification of sunflower ODD are used

to estimate the four parameters in the kinetic model: the pre-exponential factor and the activation energy of both the transesterification and the esterification reaction. The optimum values of the reaction rates coefficients are shown in Table 6.2.

Table 6.2. Parameter estimates for the pre-exponential factor and activation energy with the corresponding 95% individual confidence interval for the proposed kinetic model.

	$A_{i,T_{avg}} [10^{-8} m^3 mol^{-1} s^{-1}]$	$E_{a,i} [kJ mol^{-1}]$
Esterification reaction	5 ± 1	101 ± 36
Transesterification reaction	37 ± 2	27 ± 8

Tesser *et al.*⁴³ and Alenezi *et al.*⁴⁴ reported an activation energy of 67 kJ mol⁻¹ (for $T_{avg} = 363$ K) and 72 kJ mol⁻¹ (for $T_{avg} = 555$ K), respectively, for the supercritical esterification of FFA (oleic acid) with methanol. Generally, the activation energy for the esterification reaction of FFA is found to be between 50 to 75 kJ mol⁻¹.⁴⁴⁻⁴⁶ The higher activation energy for the esterification reaction can be the result of using ethanol instead of methanol, the latter being kinetically more favored.²³ Most transesterification kinetic models only consider an overall activation energy, *i.e.* for the transesterification of triglyceride with methanol to glycerol, with activation energies varying between 35 and 80 kJ mol⁻¹.^{24, 28, 30, 47, 48} The estimated activation energy is at the lower range compared to the literature, even though ethanol was used and a higher activation energy would be expected.

The reactor outlet composition as function of space time τ is shown in Figure 6.2A. The space time was varied by varying the inlet volumetric flow rate of the mixture. The effect of temperature and ethanol to ODD ratio on the conversion of the FFA and TG is depicted in Figure 6.2B and C respectively. Increasing temperature and ethanol to ODD ratio favored both the conversion of the TGs and FFAs. The FFA conversion was more affected by the increase in temperature as the result of the higher activation energy compared to the transesterification of the TG. Nevertheless, the TG conversion is significantly higher than the FFA conversion, due to the much lower activation energy. The model was better in predicting the effect of temperature on the conversion of the TGs than on the FFAs. This was also the case for the effect of the ethanol to ODD ratio.

The residuals, *i.e.* the differences between the experimentally observed and the estimated values, as function of the investigated process parameters did not reveal any systematic deviation, Figure 6.3. The relative error on the experimentally observed and the estimated values, is shown in Figure 6.SI.2. The F value for the model significance exceeded the tabulated one by six orders of magnitude, providing confidence in the model. Furthermore, the performance curves in Figure 6.2 demonstrate that the model was capable of satisfactorily reproducing the experimental trends. Hence, the obtained kinetic parameters were suited to be used in a process simulation.

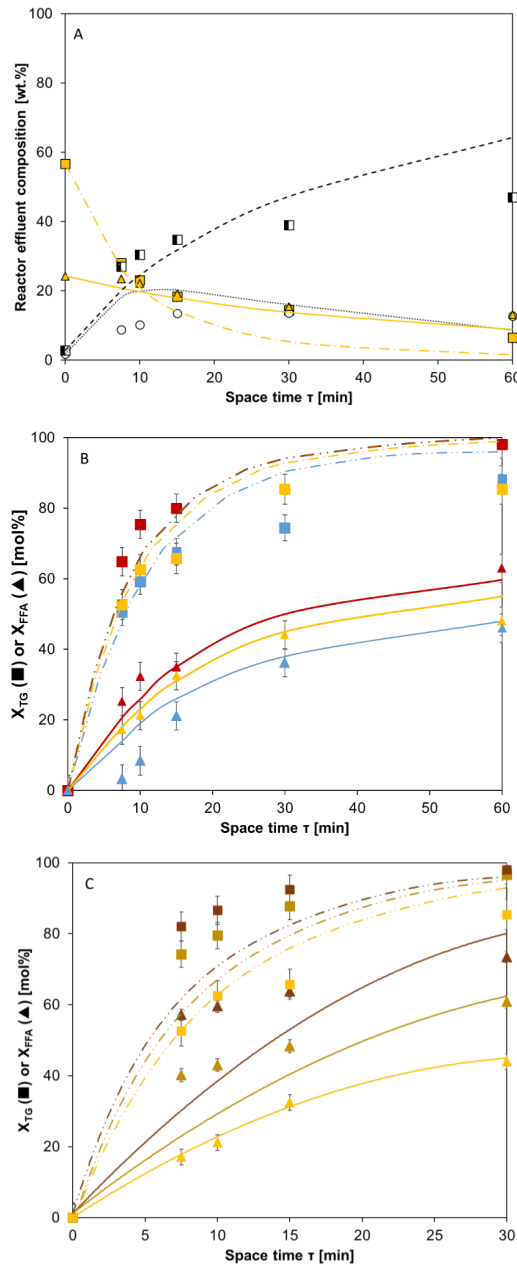


Figure 6.2. Experimental (symbols) and simulated (lines) (A) composition of the reactor effluent of the esterified sunflower ODD as function of the space time at 548 K, 15 MPa and $0.6 \text{ g}_{\text{EIOH}} \text{ g}^{-1}_{\text{ODD}}$ with TG (■, dashed-dotted-dotted line), FFA (▲, full line), FAEE (◼, dashed line) and DG (○, dotted line), (B) conversion of TG (■, dashed-dotted-dotted line) and FFA (▲, full line) as function of the space time at 15 MPa and $0.6 \text{ g}_{\text{EIOH}} \text{ g}^{-1}_{\text{ODD}}$ at 523 K (blue), 548 K (yellow) and 573 K (red) and (C) conversion of TG and FFA as function of the space time at 15 MPa and 548 K at $0.6 \text{ g}_{\text{EIOH}} \text{ g}^{-1}_{\text{ODD}}$ (yellow), $1 \text{ g}_{\text{EIOH}} \text{ g}^{-1}_{\text{ODD}}$ (dark yellow) and $1.5 \text{ g}_{\text{EIOH}} \text{ g}^{-1}_{\text{ODD}}$ (brown).

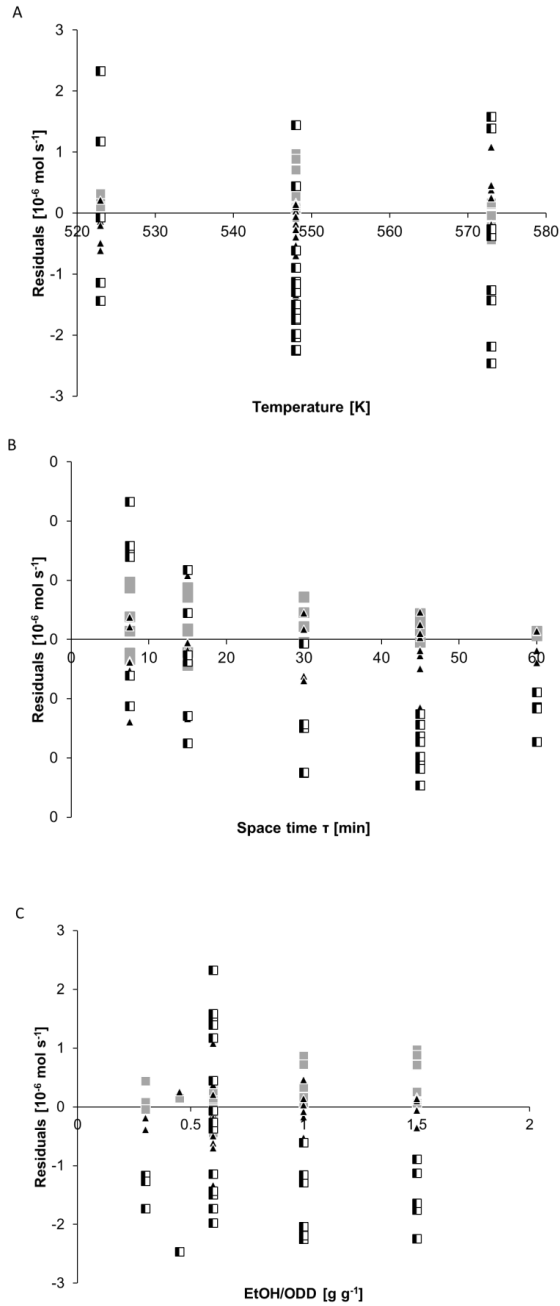


Figure 6.3. Residual plots of the molar flow rate of TG (■), FFA(▲), FAEE (◆) as function of (A) temperature, (B) space time and (C) ethanol to ODD ratio.

6.2.2 Process simulations

It is aimed at the design of a versatile process configuration, as shown in section 6.2.3.2, capable of the valorization of different ODDs. To this end, the considered process scheme for squalene recovery from ODDs with high purity is shown in Figure 6.4. It comprises three sections for which the relevant unit operations are indicated. In the first section, also denoted as the reaction section, the FFA content was reduced by esterification with supercritical ethanol (EtOH). Apart from the FFA esterification the triglycerides present in the ODDs underwent transesterification. Subsequently, squalene was recovered from the obtained mixture in the extraction section. Finally, a more concentrated squalene stream was produced in the purification section. A full description of the process configuration for olive ODD is given in section 6.2.2.2, for sunflower ODD in section 6.2.2.3, and for soybean ODD in section 6.2.2.4. Due to the differences in composition, a different squalene recovery will be achieved (as discussed in section 6.2.3.1).

6.2.2.1 Overall process description

In this section, the general methodology for the design of the unit operations as well as the determination of the operating conditions is discussed.

In the reaction section, the ODD is contacted with supercritical ethanol which is recovered from the effluent and recycled to the reactor. To ensure an efficient squalene extraction in the second step, the conversion of FFAs had to exceed 95 %. The raw materials were assumed to be available at standard conditions (298 K, 0.1 MPa). The ethanol make-up (stream 100-A) was mixed with recycled EtOH (stream 100-B) and pumped into reactor R-100 along with the ODD feed (stream 101). The reaction mixture was heated in E-101 using heating oil. The reactor was selected to be operating isothermally and isobarically (573 K and 15 MPa). The ethanol to ODD mass inlet ratio was set to 1. Slightly higher conversions were observed with a ratio of $1.5 \text{ g}_{\text{EtOH}} \text{ g}^{-1}_{\text{ODD}}$, but the increased operational and equipment (e.g. pump, heat exchangers,...) costs compared to the increase in conversion were considered to be too large. To achieve the desired FFA conversion, *i.e.*, 95 %, the residence time was prolonged by increasing the reactor volume. The reactor effluent (stream 104) was depressurized and cooled down (E-102). These conditions (Table 6.3) were determined such that in the adiabatic separation in F-100, 99 % of the unreacted EtOH is recovered. The gaseous EtOH (stream 107) was cooled down to 348 K to avoid cavitation and 5 % of the stream was purged (stream 109) before being recycled (stream 100-B).

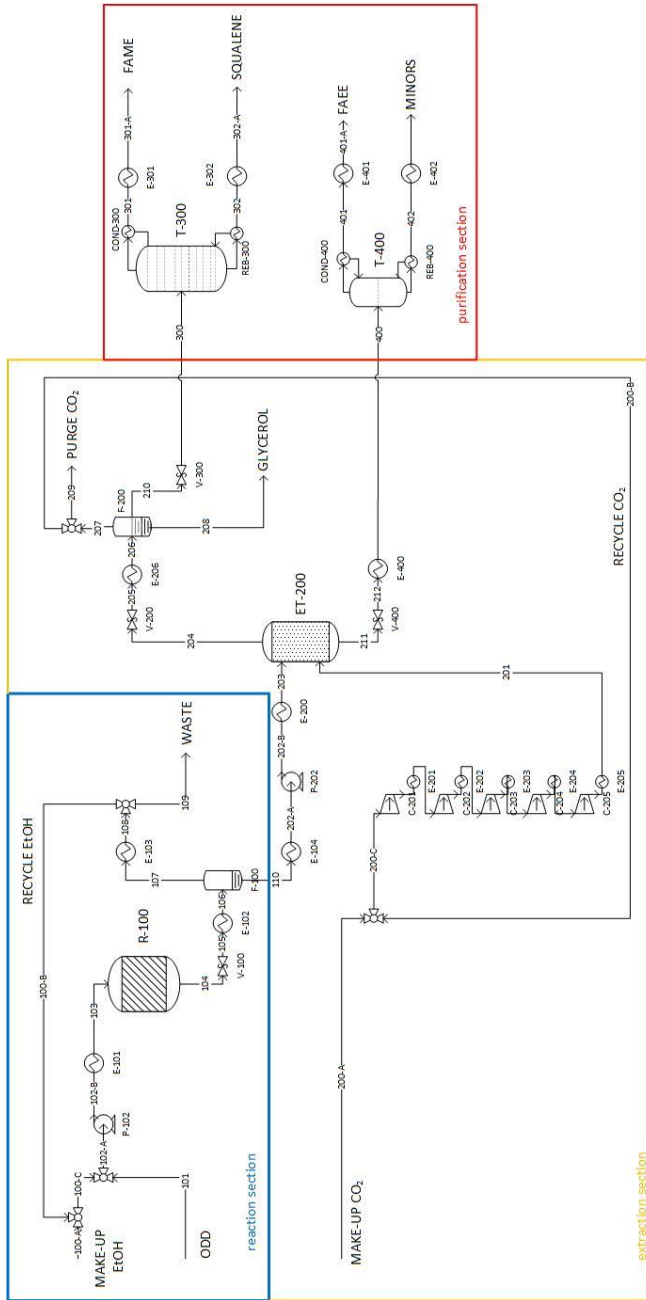


Figure 6.4. Process flow diagram for the supercritical esterification (blue section) and supercritical CO₂-extraction (yellow section) for squalene purification (red section) for the olive, sunflower and soybean ODD.

Table 6.3. Main characteristics of the unit operations for squalene recovery from different ODD feedstocks. For each unit operation, the corresponding Aspen Plus® V10 block is mentioned in parentheses.

	olive ODD	sunflower ODD	soybean ODD
Reactor (RPlug) R-100			
V_{reactor} [m ³]	2.0	1.2	0.75
Residence time* [min]	263	136	136
T [K]	573	573	573
P [MPa]	15	15	15
Adiabatic flash (Flash 2) F-100			
P [MPa]	0.18	0.14	0.10
Extraction tower (Extract) ET-200			
theoretical stages [-]	5	5	5
T [K]	333	333	333
P [MPa]	12	12	12
CO_2 /esterified-ODD [kg kg ⁻¹]	11	15	18
Flash (Flash 3) F-200			
P [MPa]	0.1	0.1	0.1
T [K]	298	298	298
Distillation tower (RadFrac) T-300			
theoretical stages [-]	12	12	12
reflux ratio [mol mol ⁻¹]	1.77	9.8	1.3
distillate to feed ratio [mol mol ⁻¹]	0.3	0.4	0.3
Distillation tower (RadFrac) T-400			
theoretical stages [-]	3	3	3
reflux ratio [mol mol ⁻¹]	0.1	0.1	0.1
distillate to feed ratio [mol mol ⁻¹]	0.97	0.97	0.54

* As Aspen Plus is capable in determining the change in volumetric flowrate throughout the reactor, it is possible to determine the residence time (in stead of the space time τ).

In the extraction section, the squalene was extracted using sc-CO₂ which was recovered by adiabatic separation and recycled to the countercurrent extraction tower. As the solubility is mainly determined by the operating pressure and temperature, a sensitivity analysis was performed to determine the optimal combination of operating conditions.^{49, 50}

Figure 6.5A illustrates the impact of the extraction pressure on the extraction yield of squalene, FFA, FAME and tocopherols from olive ODD at two temperatures for five theoretical stages. The extraction yield of sterols and FAEE are excluded from these figures as those do not have any affinity for the CO₂ and remain as a raffinate. Solubility in sc-CO₂ can be qualitatively assessed employing the solubility parameter theory, *i.e.* the closer the solubility parameters of the solute and the solvent are to each other, the higher the solubility.⁵¹ By increasing the extraction pressure at a constant temperature, the CO₂ density will increase, consequently leading to an enhanced solubility of the components. The temperature effect on the solubility is more complex and depends also on the properties of the components and CO₂. By increasing the temperature at a constant pressure, the reduced CO₂ density will increase the solubility of tocopherols in CO₂, but decrease that of FFA, FAME and squalene.^{22, 31, 52}

The extraction temperature and pressure were set to be 333 K at 12 MPa as at these conditions, more than 99 % of the squalene is extracted, while the FFA and tocopherol entrainment is limited for all ODDs. At these conditions, around 50 % of the FAME is entrained.

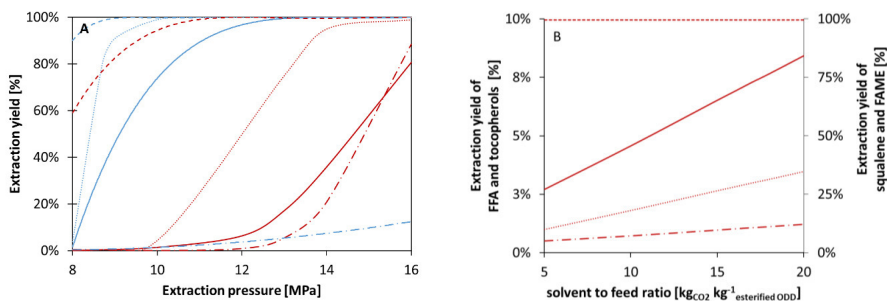


Figure 6.5. Impact of the (A) extraction pressure at 313 K (blue) and 333 K (red) for a solvent to feed ratio of 11 kgCO₂ kg⁻¹ esterified ODD and (B) the solvent to feed ratio for an extraction at 333 K and 12 MPa on the extraction yield of squalene (dashed line), tocopherols (dashed-dotted line), FAME (dotted line) and FFAs (full line) from the esterified olive ODD for five theoretical stages.

Another important operating condition affecting the extraction process, is the solvent to feed ratio, which is shown in Figure 6.5B. To obtain a desired purity of the raffinate, there will be a tradeoff between the solvent to feed inlet ratio and the number of stages. For a given feed rate, the CO₂ flow rate should be sufficiently high to reach the desired extraction yield, but low enough to minimize the operational costs. With increasing solvent to feed inlet ratio, the FFA, the FAME and tocopherol yield increase. The solvent to feed inlet ratio was designed such that more than 99 % of the squalene and less than 5 % of the FFA were entrained to the CO₂ phase, see Table 6.3.

The esterified ODD (stream 110), from the reaction section, was cooled down to 348 K to avoid cavitation in pump P-202 and cooled down (E-200) to the operating conditions of the extraction tower ET-1 (333 K, 12 MPa). The stream was fed countercurrently to the sc-CO₂ (stream 201), for which five compressors (C-201 to C-205) were needed to achieve the operating pressure of 12 MPa. Squalene, FAME and glycerol were entrained in the CO₂, resulting in the extract phase (stream 204). On the other hand, the FAEE and the majority of the sterols and tocopherols were obtained as raffinate (stream 211). The extract phase (stream 204) was first depressurized till atmospheric pressure and cooled down to room temperature (E-206), such that 99 % of the CO₂ (stream 207) was recovered by separation in a vapor/liquid/liquid-separator (F-200). After a purge of 5 % (stream 209), the CO₂ was recycled (stream 200-B) and mixed with the CO₂ make-up (stream 200-A). Glycerol (stream 208) was separated as a first liquid phase in F-200, while a mixture of FAME and squalene was obtained as a second liquid phase (stream 210).

The last step of the process was the purification section. The goal of this section was to concentrate squalene from the extract stream (stream 210), and FAEE from the raffinate stream (stream 211). The

minimum reflux ratio, minimum number of stages, feed stage, distillate to feed ratio and condenser and reboiler duties for the distillation column were obtained by the DSTWU model, while the RadFrac model was used for accurate calculations. The optimization of the reflux ratio and the distillate to feed ratio was performed *via* a sensitivity analysis. As squalene starts to decompose at temperatures exceeding 573 K⁵³, the purification was performed via vacuum distillation⁵⁴⁻⁵⁶ taking the degradation temperature as an upper bound. The purified squalene (stream 302) was achieved as a residue in the squalene purification tower (T-300) with 12 theoretical stages. The distillate of this column was enriched in FAME (stream 301). The tocopherols and sterols also decompose at temperatures above 590 K. Thus, distillation under vacuum was once again required to separate the FAEE from the remaining components. The raffinate of the extraction tower (stream 211) was depressurized and heated using heating oil (E-400). The FAEE purification was done in a three stage distillation tower (T-400), where pure FAEE was obtained (stream 401) and a stream enriched in tocopherol and sterol was produced (stream 402, “minors”).

An overview of the most important equipment data is provided in Table 6.3, the mass balances are given in Table 6.4. Simulation details that were not shown in Table 6.3, can be found in the Supplementary Information. The energy requirements for the full squalene recovery process is shown in Figure 6.6.

Table 6.4. Overall feed and product mass flow rates for squalene recovery from different ODD feedstocks

stream [kg h ⁻¹]	olive ODD	sunflower ODD	soybean ODD
<i>Raw material</i>			
ODD	125	125	125
make-up EtOH	19	23	13
<i>Key products</i>			
squalene	12	3	7
minors ¹	4	14	75
<i>Side products</i>			
FAEE	114	115	49
FAME	2	1	1
glycerol	1	8	3
<i>Consumables</i>			
CO ₂	74	105	119
<i>Waste</i>			
liquid waste ²	10	5	6
CO ₂ emission ³	74	105	119

¹ sterols, tocopherols and some FAEE

² Indicated as the stream 109 “waste” on the flowsheet in Figure 6.4. Main components are EtOH, water, traces of FAEE, glycerol.

³ Indicated as stream 209 “purge” on the flowsheet in Figure 6.4.

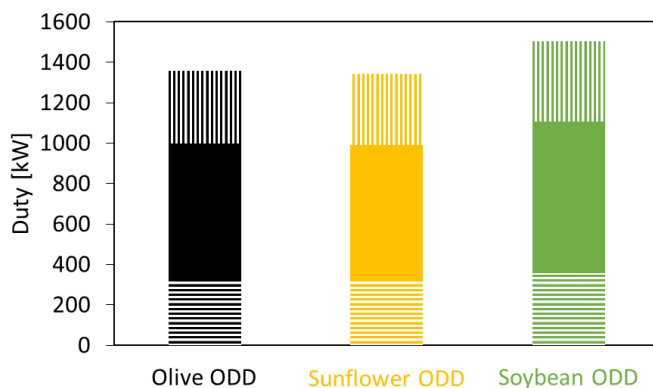


Figure 6.6. Overall heat duty (horizontal lines), cooling duty (full) and electricity (vertical lines) in the squalene recovery process of olive (black), sunflower (yellow) and soybean (green) ODD.

The following sections describe the simulation results and evaluate the process conditions necessary to recover squalene from the different ODDs. Finally, a global discussion of these processes will be provided in section 6.2.3.

6.2.2.2 Squalene recovery from olive ODD

The process had a design capacity amounting to 1 kton_{ODD} year⁻¹, corresponding to 125 kg h⁻¹ of ODD feed. The initial ethanol to ODD inlet ratio of 1 g_{EtOH} g⁻¹_{ODD} was obtained by adding 19 kg h⁻¹ of fresh ethanol. To achieve a 95% FFA and 99 % TG conversion at 15 MPa and 573 K, the reactor volume was determined to amount to 2.0 m³, corresponding to a residence time of 263 min. 99 % recovery of the unreacted EtOH through adiabatic separation could be achieved after depressurization to 0.18 MPa. The gas phase was cooled further to 348 K, before being recycled and mixed with the EtOH make-up. The liquid phase, *i.e.* the esterified ODD, was sent to the supercritical CO₂-extraction section.

As discussed in the general process description, there are three main operating conditions impacting on the extraction capacity at a given number of theoretical stages, *i.e.* the temperature, the pressure and the solvent to feed inlet ratio. The purity of the component can be enhanced by the number of theoretical stages.⁵⁰ Increasing the extraction tower pressure resulted in a higher solubility of the components (Figure 6.5A). A squalene extraction exceeding 99 % was achieved respectively above 12 MPa at the investigated temperatures. At extraction pressures above 12 MPa, less than 10 % of the remaining FFA was entrained with the CO₂ phase. The solvent to feed inlet ratio could be tuned such that this remaining FFA amount further decreased till 5 % (Figure 6.5B). A suitable balance between the squalene extraction (> 99 %) and FFA entrainment (< 5 %) yields was achieved at 333 K, 12 MPa and a solvent to feed inlet ratio of 11 kg_{CO2} kg⁻¹_{esterified ODD}. The extract phase was enriched in squalene to 74 wt.% in the presence of FAME, after glycerol (1 kg h⁻¹, 96 wt.%) and 99 % of the CO₂ were recovered through atmospheric separation at 298 K. 95 % of the CO₂ excess was recycled and mixed with CO₂ make-up (74 kg h⁻¹).

Further purification was achieved through vacuum distillation. For the extract phase (stream 300), the distillation tower (T-300) was operated at $3 \cdot 10^{-3}$ MPa with a molar reflux ratio of 6.56 and a distillate to feed molar ratio of 0.28 to achieve a 99 wt.% pure squalene stream as a residue with a mass flow rate of 12 kg h^{-1} . The distillate stream (2 kg h^{-1}) consisted mainly of the FAME (79 wt.%), which were present in the original ODD, the remaining CO_2 (10 wt.%) and squalene (6 wt.%), and the unreacted and entrained FFA (4 wt.%). The raffinate stream of the ET-100 consisted of FAEE and was enriched with tocopherols and sterols. The distillation tower T-400, which was operated at $5 \cdot 10^{-3}$ MPa, a molar reflux ratio of 0.1 and a distillate to feed molar ratio of 0.97 resulted in a distillate with 90 wt.% FAEE (114 kg h^{-1}). The residue (4 kg h^{-1}) was a mixture enriched in sterols (66 wt.%) in the presence of FAEE (28 wt.%) and tocopherols (3 wt.%).

6.2.2.3 Squalene recovery from sunflower ODD

Sunflower ODDs have a higher TG and a lower FFA content as compared to olive ODDs, but a similar total content in squalene, sterols and tocopherols (Table 2.6). This resulted in an analogous configuration for the squalene recovery from sunflower ODDs. Therefore, at the same operating conditions as for the olive ODD (573 K, 15 MPa) a reactor of 1.2 m^3 and a residence time of 136 min sufficed to convert 95 % of the FFA and 99 % of the TG. The EtOH excess can be adiabatically separated at 0.14 MPa, recycled and mixed with 21 kg h^{-1} of fresh EtOH.

The esterified ODD was fed to the extraction tower at 12 MPa and 333 K. To achieve a 99 % squalene extraction at 5 theoretical stages, a solvent to feed ratio of $15 \text{ kg}_{\text{CO}_2} \text{ kg}^{-1}_{\text{esterified ODD}}$ was used. Glycerol (8 kg h^{-1} , 96 wt.%) was removed by decantation at 298 K and atmospheric pressure (F-200), as well as the excess of CO_2 from the extract phase. The latter was recycled and mixed with 105 kg h^{-1} fresh CO_2 . A residue with 98 wt.% purity squalene (3 kg h^{-1}) was achieved by a 12 stage vacuum distillation tower at $3 \cdot 10^{-3}$ MPa (T 300) with a molar reflux ratio of 9.8 and a distillate to feed molar ratio of 0.41. The distillate (1 kg h^{-1}) of T-300 resulted in a 83 wt.% enriched FAME stream, in the presence of the unreacted and entrained FAA and some squalene.

The raffinate of ET-100 was rich in FAEE, sterols and tocopherols. The FAEE purification, resulting in a 115 kg h^{-1} stream with 95 wt.% FAEE, was performed in a three stage distillation tower (T-400) at $3 \cdot 10^{-3}$ MPa with a molar reflux ratio of 0.1 and a distillate to feed molar ratio of 0.91. The residue was a 14 kg h^{-1} stream enriched in sterols (68 wt.%) and tocopherols (24 wt.%), with the remaining fraction being the FAEE.

6.2.2.4 Squalene recovery from soybean ODD

Soybean ODDs have a significantly lower FFA content as compared to the olive ODDs, and a slightly lower content compared to sunflower ODDs (Table 2.6). Therefore, a reactor of 0.75 m^3 and a residence time of 136 min sufficed to convert 95% of the FFA in the feed at 15 MPa and 573 K. The adiabatic

EtOH separation is performed at atmospheric pressure. After the recycle, only 13 kg h⁻¹ of fresh EtOH is required to achieve a 1 g_{EtOH} g⁻¹_{ODD} ratio at the reactor inlet.

To reach a minimum of 99 % squalene extraction at 12 MPa, 333 K and 5 theoretical stages, a solvent to feed inlet ratio amounting to 18 kg_{CO₂} kg⁻¹_{esterified ODD} was required. At this ratio, less than 5% of the FFA are present in the extract phase. An atmospheric decantation at 298 K separated glycerol (3 kg h⁻¹, 88 wt.%) from the excess of CO₂ and the FAME/squalene mixture. After this separation, the extract phase was enriched up to 85 wt.% squalene. The residue (7 kg h⁻¹) of tower T-300, which operated at a molar reflux ratio of 1.3 and a distillate to feed molar ratio of 0.3, contained 98 wt.% squalene. Traces of FAME, FFA and tocopherols were found in this stream. A FAME rich stream (78 wt.%), in the presence of the unreacted and entrained FFA and some squalene, was obtained as raffinate (2 kg h⁻¹) of T-300.

The raffinate phase of the extraction column, rich in FAEE, sterols and tocopherols, was fed to the three stage tower T-400, which was operated at 3 10⁻³ MPa with a molar reflux ratio of 0.1 and distillate to feed molar ratio of 0.54. The distillate (49 kg h⁻¹) of this column was FAEE with a purity of 88 wt.%. The residue of the distillation tower T-400 was a 75 kg h⁻¹ stream enriched in sterols (56 wt.%) and tocopherols (44 wt.%).

6.2.3 Comparison between different ODDs

Table 6.4 provides an overview of the mass balances for the three different ODDs based on the process schemes presented in Figure 6.4. A very similar squalene yield could be achieved from the three considered ODDs, see Figure 6.7, indicating an optimal extraction tower. Differences arose in the overall squalene recovery, due to the different squalene content in the ODD (Table 2.6). The highest total amount of sterols and tocopherols was obtained with soybean ODD, as the raw material itself was the richest in those components. The highest FAEE production was achieved in the process with sunflower and olive ODD as both ODDs are rich in fatty acids and glycerides, *i.e.* 99 wt.% and 95 wt.% respectively.

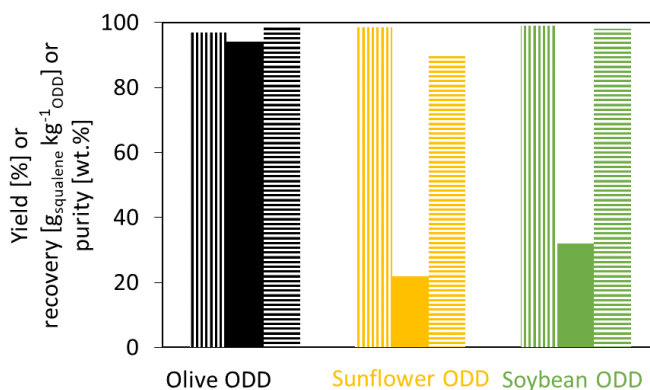


Figure 6.7. Simulated overall squalene extraction yield (vertical lines), recovery (full) and purity (horizontal lines) for squalene recovery process of olive (black), sunflower (yellow) and soybean (green) ODD.

It was possible to process all feedstocks using the same unit operations. The characteristics for these main unit operations are listed in Table 6.3. As a result of the high FFA content, the required reactor volume for the supercritical esterification is the largest for the olive ODD. The opposite is true for soybean ODD. To achieve a squalene extraction of more than 95 %, slight adaptations in the solvent to feed ratio in the extraction were required. In particular, due to the very low squalene content in soybean ODD, a higher solvent to feed ratio was needed to achieve the desired recovery.

The most pronounced differences were situated in the cooling duty and power required. The higher CO₂ to esterified ODD ratio, needed to achieve the desired squalene recovery with soybean ODD, resulted in *ca.* 10 % higher cooling duty and electricity need (for the compressors) compared to the sunflower ODD (Figure 6.6) and around 50 % compared to olive ODD.

6.2.3.1 Squalene recovery

The overall recovery, extraction yield and purity, determined as described in section 2.2.4 (Chapter 2), are given in Figure 6.7, for the configurations described in section 6.2.2.

According to the simulation results, a final squalene product with purity > 98 wt.% and > 95 % squalene recovery can be obtained upon the combination of a supercritical esterification of olive ODD, at 573 K, 15 MPa and an ethanol to ODD mass inlet ratio of 1, followed by a supercritical extraction at 333 K, 12 MPa and a solvent to feed ratio of 11 kg_{CO₂} kg⁻¹_{esterified ODD}.

Akgün *et al.*¹⁰ carried out squalene separation from an olive ODD through methanol esterification followed by supercritical CO₂-extraction at 325 K, 10.5 MPa and a volumetric solvent to feed ratio of 1. This resulted in a squalene purity up to 75 wt.%, the remaining fraction was FAME. Ruivo *et al.*⁵⁷ investigated the squalene extraction from a binary mixture with methyl oleate. At a solvent to feed volume ratio amounting to 20, a squalene recovery of 90% was achieved at 313 K and 11.5 MPa.

Vázquez *et al.*¹⁸ predicted a squalene purity of 91 wt.% and a squalene recovery of 93% from olive ODD (52 wt.% squalene, 34 wt.% methylmyristate, 10 wt.% ethyloleate and 5 wt.% triolein). This was achieved with a 15 stage extraction tower at 18 MPa, 343 K and a solvent to feed mass ratio of 51.

In this work, higher squalene recovery and purity were achieved at milder operating conditions due to removal of the fatty acids by the esterification reaction with ethanol. Compared to the work of Vázquez *et al.*¹⁸, to achieve an analogous quality, the solvent to feed mass ratio and number of theoretical stages were both considerably reduced, in spite of the concentration of squalene being significantly lower in the ODDs considered in our work. The used concentrations in this work resemble as well more closely the real ODD composition.

Sunflower and soybean ODDs are mainly used for the recovery of sterols and tocopherols.^{5, 58} However, our work reveals that both sunflower and soybean ODD can be a good alternative source of pure squalene. After supercritical esterification and extraction at 333 K, 12 MPa and a solvent to feed mass ratio of 15 kg_{CO₂} kg⁻¹_{esterified ODD}, a 98 wt.% squalene product can be achieved with 100 % yield (Figure 6.7), according to the simulations. A 96 % squalene yield was achieved with soybean ODD. The obtained squalene product was 98 wt.% pure.

6.2.3.2 A versatile process configuration for different feedstocks

It is of strategic advantage to develop a single process configuration allowing squalene recovery from different ODDs. Due to the similarities in the esterification step, a single set of unit operations can be used by selecting the largest reactor volume (*i.e.* 2.0 m³). For the supercritical CO₂-extraction, three units should be revised in more detail: the extraction tower ET-200 and the two distillation towers T-300 and T-400. An extraction tower with the same number of theoretical stages was capable of extracting more than 95 % of the squalene for the three feedstocks. Due to the differences in solvent to feed ratio, the column diameter would be different. The diameter for the olive and sunflower ODD was estimated to be 0.34 m, while it was 0.60 m in the case of soybean ODD. However, the differences in the diameter could be counteracted by selecting a suitable packing which would result in the use of the same extraction tower.¹³

In the purification step, there was a small difference between the feedstocks. As reported in Table 6.4, the feed flow rates towards T-400 are comparable for the different ODDs (*i.e.* 119, 129 and 124 kg h⁻¹ for respectively olive, sunflower and soybean ODD), but that was not the case for T-300 (*i.e.* 15, 4 and 5 kg h⁻¹ for respectively olive, sunflower and soybean ODD). Nevertheless, the distillation towers T-300 and T-400 had an identical number of theoretical stages for processing the different feedstocks, the only expected difference would be the diameter as a result of the difference in the flow rates. According to simulations, the two distillation towers can be designed with a diameter of 0.46 m, but with respectively a height of 4.9 m and 12.8 m for T-400 and T-300.

To proceed towards industrial implementation, other equipment, such as pumps and heat-exchangers, should be sized such that they are applicable for the three feedstocks. In summary, our feasibility study pointed to possible design of one process scheme with same unit operations for all three ODD, which gives rise to a versatile process.

6.2.4 Economic analysis

Estimating manufacturing costs of a new process can provide a good indication of its economic viability. Although potentially compromised because some information may be missing, these early estimates are often sufficiently accurate to shed light on long-term viability.

The capital costs for the complete valorization unit, *i.e.* the esterification, the extraction and the purification section, were estimated using the Aspen Process Economic Analyzer to amount to 4,98 M€. A detailed cost per equipment is reported in Table 6.5. An estimation of the operating costs is given in Table 6.SI.13. The fixed operating costs are estimated at 1,98 M€ for the complete valorization unit. The most important difference in the variable operating costs is situated in the raw materials cost.

Table 6.5. Estimation of capital cost for the valorization unit, existing out of the supercritical esterification, the supercritical CO₂-extraction and the purification section

	Cost [k€]
<i>Esterification section</i>	
<i>Pump P-102</i>	480
<i>Burner E-101</i>	135
<i>Reactor R-100</i>	250
<i>Heat exchangers</i>	90
<i>Flash F-100</i>	96
<i>Extraction section</i>	
<i>Compressors</i>	1 900
<i>Pump P-202</i>	670
<i>Extraction tower ET-200</i>	179
<i>Heat exchangers</i>	165
<i>Flash F-200</i>	120
<i>Purification section</i>	
<i>Distillation tower T-300</i>	325
<i>Distillation tower T-400</i>	315
<i>Heat exchangers</i>	255
<i>Total CAPEX</i>	4 980

The estimation of the yearly revenue and variable production costs are summarized in Table 6.6. The soybean ODD had the highest yearly revenue of 15.6 M€, followed by the olive ODD (3.1 M€) and the sunflower ODD (2.2 M€). The soybean ODD has a significantly higher revenue due to the higher amount of the minor-products, which have also a higher purity compared to olive and sunflower ODD.

Nevertheless, the GMR and the contribution margin ratio (CMR) were the lowest due the high raw material price of the ODD itself. The difference arising in the revenue between olive and sunflower ODD, can be mainly attributed to the difference is the minor concentration, *i.e.* squalene vs. mixture of tocopherols and sterols, and their price.

Table 6.6. Estimation of revenues and variable production costs for different ODD

[k€ year ⁻¹]	olive ODD	sunflower ODD	soybean ODD
<i>Raw material</i>			
<i>ODD</i>	551	551	3 342
<i>make-up EtOH</i>	126	153	86
<i>Key products</i>			
<i>squalene</i>	3 084	771	1 028
<i>minors</i>	53	1 482	14 558
<i>Side products</i>			
<i>FAEE</i>	659	665	283
<i>FAME</i>	0	0	0
<i>glycerol</i>	0	0	0
<i>Consumables</i>			
<i>CO₂</i>	6	8	9
<i>Waste</i>			
<i>liquid waste</i>	83	42	50
<i>CO₂ emission</i>	12	17	19
<i>Utilities</i>			
<i>heating</i>	48	45	51
<i>cooling</i>	6	7	8
<i>electricity</i>	40	58	64
<i>Revenue [k€ year⁻¹]</i>	3 137	2 253	15 586
<i>GMR [%]</i>	96	96	79
<i>CMR [%]</i>	93	90	79

A versatile chemical feedstock is the one leading to products with a wide variety of applications. These feedstocks can provide more economic security, as they are less sensitive to changes in a single product market. In that respect, one can conclude that the sunflower ODD is the most versatile feedstock: 54 % of the revenue of the main and side products is achieved from the minors and 23 % from squalene and 23 % from FAEE (Figure 6.8). Olive ODD obtains most of its revenue from squalene, while soybean ODD is a good resource for mixtures containing sterols and tocopherols (minors). This result is not unexpected as olive ODD is rich in squalene (9.97 wt.%, Table 2.8) compared to the other ODDs, while soybean ODD has the highest concentration of sterols and tocopherols (60,7 wt.%, Table 2.8). Thus, if only one of the minors (squalene, sterols or tocopherols) would be targeted, it could be beneficial to select the proper ODD feedstock (olive ODD and soybean ODD, respectively).

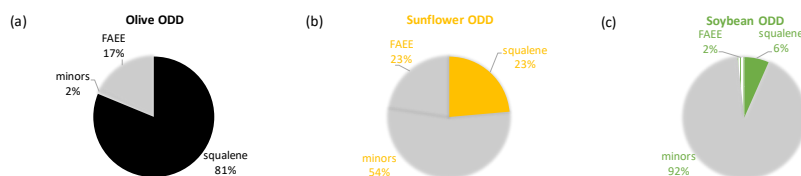


Figure 6.8. Percentage of the revenues from the key products, i.e. squalene (full) and minors (horizontal lines), and the side products, i.e. FAEE (vertical lines), for olive (black), sunflower (yellow) and soybean (green) ODD.

Although the economic evaluation of the base case for the various feedstocks is essential, a sensitivity analysis on the revenues and the economic viability towards price variations is also important to anticipate possible market changes. On the short-term, the prices of vegetable oils and their derivatives are mostly driven by weather conditions and exchange rates, as those have an impact on the import and export of goods.⁵⁹ Long-term factors for vegetable oils prices are the impact of climate change on the agricultural yields and the effect of urbanization on the land and water resources.⁶⁰ The bio-ethanol price is driven by technology and national legislation (e.g. policy support).⁶¹ The prices for FAEE and squalene are mainly affected by supply and demand. Though, unstable crude oil markets can make biofuels more profitable when the FAEE manufacturing is cheaper than that of conventional fuels. The CO₂ price depends very much on its origin. The average CO₂ price from CO₂ capturing process amounts to € 0.03 kg⁻¹CO₂⁷, while CO₂-supercritical processes take up to € 0.36 kg⁻¹CO₂^{62, 63}. As prices can be strongly affected by supply and demand over the years, a sensitivity analysis was performed on the GMR and CMR by varying the price of raw materials and products at a constant price of the utilities. The price variation (-50 % to 50 % relative to the nominal price) for both raw materials, the key product squalene and the side product FAEE are considered in Figure 6.9A to E. Figure 6.9F shows the effect of the CO₂ price on the CMR as the utilities are only taken into account in the CMR and not the GMR. For the investigated ODD, a 50 % decrease in feedstock price resulted in up to 14 % increase for both GMR and CMR. A decrease in the squalene selling price has a significant effect on both the margin ratios of olive ODD, as squalene ensures up to 81 % of the revenue of the main and side products. This trend is also observed for the selling price of the minor-products in the case of soybean ODD, as respectively 92 % of the revenue of the key and side products is achieved by the minors (Figure 6.8). The benefit of a versatile feedstock, such as sunflower ODD, is the lower sensitivity to price variations of a single product, e.g. squalene or the minors. For a high squalene demand, one should select olive ODD. In case of a drop in demand, one could easily switch to sunflower ODD as they have not only revenue from squalene but also from FAEE. Depending on the feedstock price, a change could be made using the same versatile process.

In the worst case scenario, i.e. the highest prices (+ 50 %) for the raw materials and consumables (€ 0.36 kg⁻¹), and the lowest (- 50 %) ones for the main and side products, the GMR of olive, sunflower and soybean ODDs would be respectively 50 %, 31 % and 35 %, while the CMRs are 31 %, - 6 % and

29 %. Obviously, the GMR and CMR would decrease sharply. The negative CMR for sunflower ODD indicates that the variable costs in that process exceed the revenues, *i.e.* the process is economically unviable.

Overall, one can conclude that, thanks to its versatility, this process shows a very high flexibility for both the feedstocks supply and products demand. To increase the economic viability of the process, the unit could be built on an edible oil production site. This way, some of the operating costs could be decreased as they would become part of the whole site and not only the valorization unit.

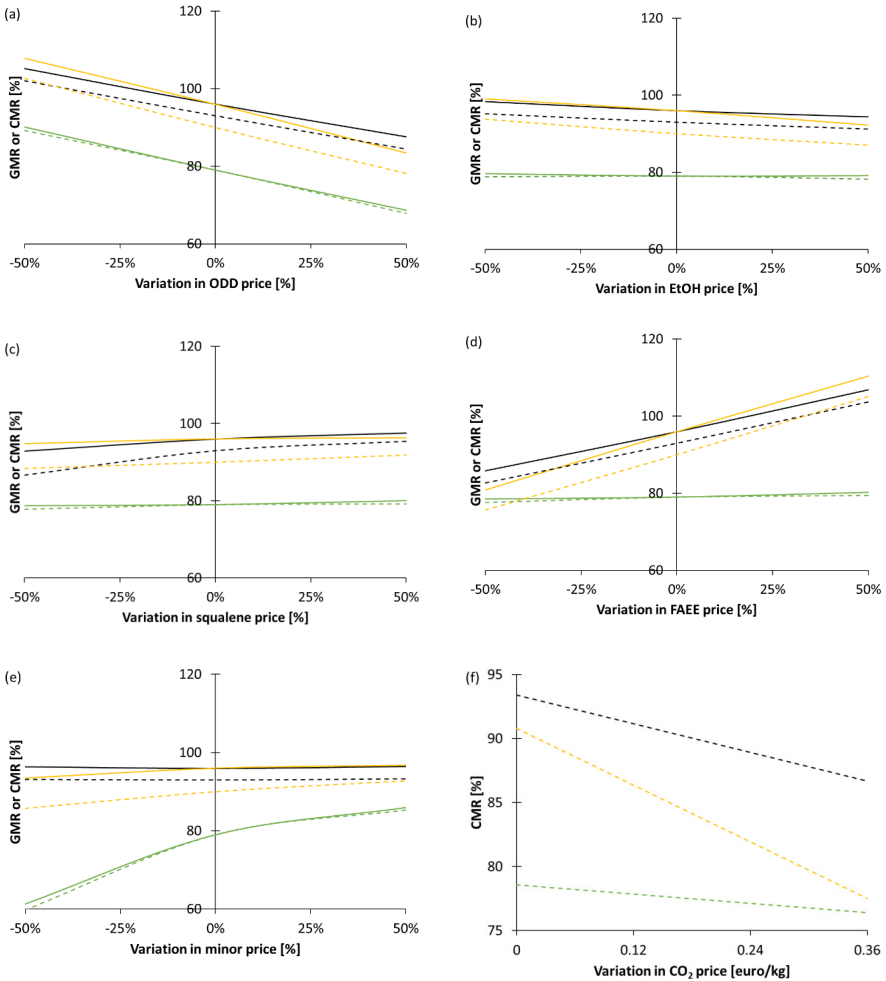


Figure 6.9. Influence of the price variation of (A) ODD, (B) EtOH, (C) squalene, (D) FAEE, (E) minors and (F) CO₂ on the GMR (full line) and CMR (dashed line) of squalene recovery from olive (black), sunflower (yellow) and soybean (green) ODD.

6.3 Conclusions

The recovery of squalene from sunflower, soybean and olive ODD, which is a waste stream in the edible oil production, was assessed as a sustainable alternative for its recovery from deep shark liver oil. A three-step process was simulated to obtain squalene with purities exceeding 98 wt.%. The complexity of the ODDs was assessed by the instruction of eight component families for which a model component was selected. Further, equilibrium data in sc-CO₂ were used to estimate all binary interactions between CO₂ and all the components and between triolein and oleic acid, triolein and β -sitosterol, methyl oleate and squalene, and ethanol and water. The estimated interaction binary interaction coefficients were found to be significant, except for triolein. First, a reactive pre-treatment of the ODD with supercritical ethanol was performed. In this step, the concentration of FFA, which exhibits a similar solubility in CO₂ as squalene, is reduced. Significant kinetic parameters for the reactions were regressed based on experimental data and were used for the detailed simulation. Next, a supercritical CO₂-extraction is performed to recover squalene from the esterified ODD. Thanks to the prior FFA esterification, this extraction could be performed at milder operating conditions as compared to conventional squalene recovery technologies. Finally, a purification step is required to achieve high purity squalene.

The three-step process results in an overall extraction yield exceeding 95 % ($89 \text{ g}_{\text{squalene}} \text{ kg}^{-1}_{\text{ODD}}$) with final squalene purity up to 99 wt.% for olive ODD. A full extraction yield was achieved with the other feedstocks, yet the total squalene recovery was lower. Furthermore, our work demonstrated that a single, but versatile process configuration is capable of handling those different feedstocks. In combination with the economic analysis, it becomes clear that the feedstock that can be labeled as the most ‘profitable’ one depends on the market price of the raw materials and the products, *i.e.* squalene, FAEE and the ‘minors’ tocopherol and sterols. The process flexibility for handling different ODD can be a key factor to ensure its profitability, allowing fast adaptation to the market, with co-feeding being also an option.

6.4 References

- 1 O. Popa, N.E. Băbeanu, I. Popa, S. Niță, C.E. Dinu-Pârvu, Methods for Obtaining and Determination of Squalene from Natural Sources, *BioMed Research International*, 2015 (2015) 16.
- 2 F.A. Dudrow, Deodorization of Edible Oil, *Journal of the American Oil Chemists' Society*, 60 (1983) 272-274.
- 3 D.S. Laoretani, O.A. Iribarren, Procedure for the Selection among Technologies. Treatment of Deodorizer Distillate Oil, *Industrial & Engineering Chemistry Research*, 53 (2014) 16803-16812.
- 4 L.R. Posada, J. Shi, Y. Kakuda, S.J. Xue, Extraction of Tocotrienols from Palm Fatty Acid Distillates Using Molecular Distillation, Separation and Purification Technology, 57 (2007) 220-229.
- 5 E.A. Moreira, M.A. Baltanás, Recovery of Phytosterols from Sunflower Oil Deodorizer Distillates, *Journal of the American Oil Chemists' Society*, 81 (2004) 161-167.
- 6 D. Copeland, W.M. Belcher, Methods for Treating Deodorizer Distillate, P Holdings LLC 2001.
- 7 H. Naims, Economics of Carbon Dioxide Capture and Utilization—a Supply and Demand Perspective, *Environmental Science and Pollution Research*, 23 (2016) 22226-22241.
- 8 A.P. Sánchez-Camargo, J.A. Mendiola, E. Ibáñez, M. Herrero, *Supercritical Fluid Extraction, Chemistry, Molecular Sciences and Chemical Engineering*, Elsevier 2014.
- 9 F. Temelli, Perspectives on Supercritical Fluid Processing of Fats and Oils, *The Journal of Supercritical Fluids*, 47 (2009) 583-590.
- 10 N.A. Akgün, Separation of Squalene from Olive Oil Deodorizer Distillate Using Supercritical Fluids, *European Journal of Lipid Science and Technology*, 113 (2011) 1558-1565.
- 11 C.J. Chang, Y.-F. Chang, H.-z. Lee, J.-q. Lin, P.-W. Yang, Supercritical Carbon Dioxide Extraction of High-Value Substances from Soybean Oil Deodorizer Distillate, *Industrial & Engineering Chemistry Research*, 39 (2000) 4521-4525.
- 12 Ö. Güçlü-Üstündağ, F. Temelli, Column Fractionation of Canola Oil Deodorizer Distillate Using Supercritical Carbon Dioxide, *Journal of the American Oil Chemists' Society*, 84 (2007) 953-961.
- 13 A. M. Hurtado Benavides, P. J. Martín-Álvarez, L. Vázquez, G. Reglero, F. J. Señoráns, E. Ibáñez, Optimization of Countercurrent Supercritical Fluid Extraction of Minor Components from Olive Oil, *Current Analytical Chemistry*, 10 (2014) 78-85.
- 14 S. Gunawan, N.S. Kasim, Y.-H. Ju, Separation and Purification of Squalene from Soybean Oil Deodorizer Distillate, Separation and Purification Technology, 60 (2008) 128-135.
- 15 N. Al-Darmaki, T. Lu, B. Al-Duri, J. Harris, T. Favre, K. Bhaggan, R. Santos, Isothermal and Temperature Gradient Supercritical Fluid Extraction and Fractionation of Squalene from Palm Fatty Acid Distillate Using Compressed Carbon Dioxide, *The Journal of Supercritical Fluids*, 61 (2012) 108-114.
- 16 N. Sugihara, A. Kanda, T. Nakano, T. Nakamura, H. Igusa, S. Hara, Novel Fractionation Method for Squalene and Phytosterols Contained in the Deodorization Distillate of Rice Bran Oil, *Journal of oleo science*, 59 (2010) 65-70.
- 17 M. Mendes, F. Pessoa, G. Coelho, A. Uller, Recovery of the High Aggregated Compounds Present in the Deodorizer Distillate of the Vegetable Oils Using Supercritical Fluids, *The Journal of Supercritical Fluids*, 34 (2005) 157-162.
- 18 L. Vázquez, C.F. Torres, T. Fornari, F.J. Señoráns, G. Reglero, Recovery of Squalene from Vegetable Oil Sources Using Countercurrent Supercritical Carbon Dioxide Extraction, *The Journal of Supercritical Fluids*, 40 (2007) 59-66.
- 19 T. Fornari, L. Vázquez, C.F. Torres, E. Ibáñez, F.J. Señoráns, G. Reglero, Countercurrent Supercritical Fluid Extraction of Different Lipid-Type Materials: Experimental and Thermodynamic Modeling, *The Journal of Supercritical Fluids*, 45 (2008) 206-212.
- 20 C.F. Torres, G. Reglero, G. Torreló, Extraction and Enzymatic Modification of Functional Lipids from Soybean Oil Deodorizer Distillate, *Recent Trends for Enhancing the Diversity and Quality of Soybean Products*, Intech 2011, pp. 447-482.
- 21 W.B. Nilsson, E.J. Gauglitz, J.K. Hudson, Solubilities of Methyl Oleate, Oleic Acid, Oleyl Glycerols, and Oleyl Glycerol Mixtures in Supercritical Carbon Dioxide, *Journal of the American Oil Chemists Society*, 68 (1991) 87-91.
- 22 M.D.L. de Castro, M. Valcarcel, M.T. Tena, *Analytical Supercritical Fluid Extraction*, Springer Berlin Heidelberg 2012.

- 23 A. Santana, J. Maçaira, M.A. Larrayoz, Continuous Production of Biodiesel Using Supercritical Fluids: A Comparative Study between Methanol and Ethanol, *Fuel Processing Technology*, 102 (2012) 110-115.
- 24 D. Kusdiana, S. Saka, Kinetics of Transesterification in Rapeseed Oil to Biodiesel Fuel as Treated in Supercritical Methanol, *Fuel*, 80 (2001) 693-698.
- 25 A. Demirbaş, Biodiesel from Vegetable Oils Via Transesterification in Supercritical Methanol, *Energy Conversion and Management*, 43 (2002) 2349-2356.
- 26 C. Bertoldi, C. da Silva, J.P. Bernardon, M.L. Corazza, L.C. Filho, J.V. Oliveira, F.C. Corazza, Continuous Production of Biodiesel from Soybean Oil in Supercritical Ethanol and Carbon Dioxide as Cosolvent, *Energy & Fuels*, 23 (2009) 5165-5172.
- 27 M. Diasakou, A. Louloudi, N. Papayannakos, Kinetics of the Non-Catalytic Transesterification of Soybean Oil, *Fuel*, 77 (1998) 1297-1302.
- 28 H. He, S. Sun, T. Wang, S. Zhu, Transesterification Kinetics of Soybean Oil for Production of Biodiesel in Supercritical Methanol, *Journal of the American Oil Chemists' Society*, 84 (2007) 399-404.
- 29 G. Madras, C. Kolluru, R. Kumar, Synthesis of Biodiesel in Supercritical Fluids, *Fuel*, 83 (2004) 2029-2033.
- 30 M.N. Varma, G. Madras, Synthesis of Biodiesel from Castor Oil and Linseed Oil in Supercritical Fluids, *Industrial & Engineering Chemistry Research*, 46 (2007) 1-6.
- 31 G.K. Nagesha, B. Manohar, K. Udaya Sankar, Enrichment of Tocopherols in Modified Soy Deodorizer Distillate Using Supercritical Carbon Dioxide Extraction, *European Food Research and Technology*, 217 (2003) 427-433.
- 32 T. Fang, M. Goto, X. Wang, X. Ding, J. Geng, M. Sasaki, T. Hirose, Separation of Natural Tocopherols from Soybean Oil Byproduct with Supercritical Carbon Dioxide, *The Journal of Supercritical Fluids*, 40 (2007) 50-58.
- 33 V.M. Ito, P.F. Martins, C.B. Batistella, M.R. Wolf Maciel, Tocopherols and Phytosterols Concentration from Soybean Oil Deodorizer Distillate, ENPROMER 2005 Rio de Janeiro, 2005.
- 34 S. Lee, D. Posarac, N. Ellis, Process Simulation and Economic Analysis of Biodiesel Production Processes Using Fresh and Waste Vegetable Oil and Supercritical Methanol, *Chemical Engineering Research and Design*, 89 (2011) 2626-2642.
- 35 T. Fang, M. Goto, M. Sasaki, T. Hirose, Phase Equilibria for the Ternary System Methyl Oleate+Tocopherol+ Supercritical Co₂, *Journal of Chemical & Engineering Data*, 50 (2005) 390-397.
- 36 T. Fang, M. Goto, Z. Yun, X.-I. Ding, T. Hirose, Phase Equilibria for Binary Systems of Methyl Oleate–Supercritical Co₂ and A-Tocopherol–Supercritical Co₂, *The Journal of Supercritical Fluids*, 30 (2004) 1-16.
- 37 R. Bharath, H. Inomata, T. Adschiri, K. Arai, Phase Equilibrium Study for the Separation and Fractionation of Fatty Oil Components Using Supercritical Carbon Dioxide, *Fluid Phase Equilibria*, 81 (1992) 307-320.
- 38 R. Bharath, H. Inomata, K. Arai, K. Shoji, Y. Noguchi, Vapor-Liquid Equilibria for Binary Mixtures of Carbon Dioxide and Fatty Acid Ethyl Esters, *Fluid Phase Equilibria*, 50 (1989) 315-327.
- 39 Z.-R. Yu, S.S. Rizvi, J.A. Zollweg, Phase Equilibria of Oleic Acid, Methyl Oleate, and Anhydrous Milk Fat in Supercritical Carbon Dioxide, *The Journal of Supercritical Fluids*, 5 (1992) 114-122.
- 40 P.J. Pereira, M. Goncalves, B. Coto, E.G. de Azevedo, M.N. da Ponte, Phase Equilibria of Co₂ + Dl-A-Tocopherol at Temperatures from 292 K to 333 K and Pressures up to 26 Mpa, *Fluid Phase Equilibria*, 91 (1993) 133-143.
- 41 R. Ruivo, A. Paiva, P. Simões, Phase Equilibria of the Ternary System Methyl Oleate/Squalene/Carbon Dioxide at High Pressure Conditions, *The Journal of Supercritical Fluids*, 29 (2004) 77-85.
- 42 J. Stoldt, G. Brunner, Phase Equilibrium Measurements in Complex Systems of Fats, Fat Compounds and Supercritical Carbon Dioxide, *Fluid Phase Equilibria*, 146 (1998) 269-295.
- 43 R. Tesser, L. Casale, D. Verde, M. Di Serio, E. Santacesaria, Kinetics of Free Fatty Acids Esterification: Batch and Loop Reactor Modeling, *Chemical Engineering Journal*, 154 (2009) 25-33.
- 44 R. Alenezi, G.A. Leeke, J.M. Winterbottom, R.C.D. Santos, A.R. Khan, Esterification Kinetics of Free Fatty Acids with Supercritical Methanol for Biodiesel Production, *Energy Conversion and Management*, 51 (2010) 1055-1059.

- 45 T. Jin, B. Wang, J. Zeng, C. Yang, Y. Wang, T. Fang, Esterification of Free Fatty Acids with Supercritical Methanol for Biodiesel Production and Related Kinetic Study, *RSC Advances*, 5 (2015) 52072-52078.
- 46 M. Chai, Q. Tu, M. Lu, Y.J. Yang, Esterification Pretreatment of Free Fatty Acid in Biodiesel Production, from Laboratory to Industry, *Fuel Processing Technology*, 125 (2014) 106-113.
- 47 A. Permsuwan, N. Tippayawong, T. Kiatsiriroat, C. Thararux, S. Wangkarn, Reaction Kinetics of Transesterification between Palm Oil and Methanol under Subcritical Conditions, *Energy Science and Technology*, 2 (2011) 35-42.
- 48 C.-S. Choi, J.-W. Kim, C.-J. Jeong, H. Kim, K.-P. Yoo, Transesterification Kinetics of Palm Olein Oil Using Supercritical Methanol, *The Journal of Supercritical Fluids*, 58 (2011) 365-370.
- 49 A.d.P. Sanchez-Camargo, J.A. Mendiola, E. Ibáñez, M. Herrero, Supercritical Fluid Extraction, Reference Module in Chemistry, Molecular Sciences and Chemical Engineering, (2014).
- 50 J.L. Humphrey, *Separation Process Technology*, McGraw-Hill (Canada)1997.
- 51 X. Lou, H.-G. Janssen, C.A. Cramers, Temperature and Pressure Effects on Solubility in Supercritical Carbon Dioxide and Retention in Supercritical Fluid Chromatography, *Journal of Chromatography A*, 785 (1997) 57-64.
- 52 N.A. Akgün, G. Gece, E. Tekneci, Strategies to Obtain Tocopherols, Phytosterols and Squalene from Deodorizer Distillates and Acid Oils Using Supercritical Fluids, *Recent Research Developments in Lipids*, 9 (2013) 67-84.
- 53 J. Busch, Safety Assessment of Squalene and Squalene, *International Journal of Toxicology*, 1 (1990) 37-56.
- 54 H. Wang, M. Goto, M. Sasaki, T. Hirose, Separation of A-Tocopherol and Squalene by Pressure Swing Adsorption in Supercritical Carbon Dioxide, *Industrial & Engineering Chemistry Research*, 43 (2004) 2753-2758.
- 55 H. Sun, D. Wiesenborn, K. Tostenson, J. Gillespie, P. Rayas-Duarte, Fractionation of Squalene from Amaranth Seed Oil, *Journal of the American Oil Chemists' Society*, 74 (1997) 413-418.
- 56 C. Lyon, R. Becker, Extraction and Refining of Oil from Amaranth Seed, *Journal of the American Oil Chemists' Society*, 64 (1987) 233-236.
- 57 R. Ruivo, M.J. Cebola, P.C. Simões, M. Nunes da Ponte, Fractionation of Edible Oil Model Mixtures by Supercritical Carbon Dioxide in a Packed Column. Part I: Experimental Results, *Industrial & Engineering Chemistry Research*, 40 (2001) 1706-1711.
- 58 S.T. Sherazi, S. Mahesar, S. Uddin, Vegetable Oil Deodorizer Distillate: A Rich Source of the Natural Bioactive Components, 2016.
- 59 A. Harri, L. Nalley, D. Hudson, The Relationship between Oil, Exchange Rates, and Commodity Prices, *Journal of Agricultural and Applied Economics*, 41 (2015) 501-510.
- 60 A.D. Owen, K. Chowdhury, J.R.R. Garrido, Price Interrelationships in the Vegetable and Tropical Oils Market, *Applied Economics*, 29 (1997) 119-124.
- 61 J. Littlewood, M. Guo, W. Boerjan, R.J. Murphy, Bioethanol from Poplar: A Commercially Viable Alternative to Fossil Fuel in the European Union, *Biotechnology for biofuels*, 7 (2014) 113-113.
- 62 M. Eisenmenger, N.T. Dunford, F. Eller, S. Taylor, J. Martinez, Pilot-Scale Supercritical Carbon Dioxide Extraction and Fractionation of Wheat Germ Oil, *Journal of the American Oil Chemists' Society*, 83 (2006) 863-868.
- 63 N. Mezzomo, J. Martínez, S.R.S. Ferreira, Economical Viability of Sfe from Peach Almond, Spearmint and Marigold, *Journal of Food Engineering*, 103 (2011) 473-479.
- 64 J. Anderson, Determining Manufacturing Costs, *CEP*, (2009) 27-31.
- 65 Economic Evaluation, *Chemical Process Design and Simulation*2018, pp. 263-281.

Supporting information

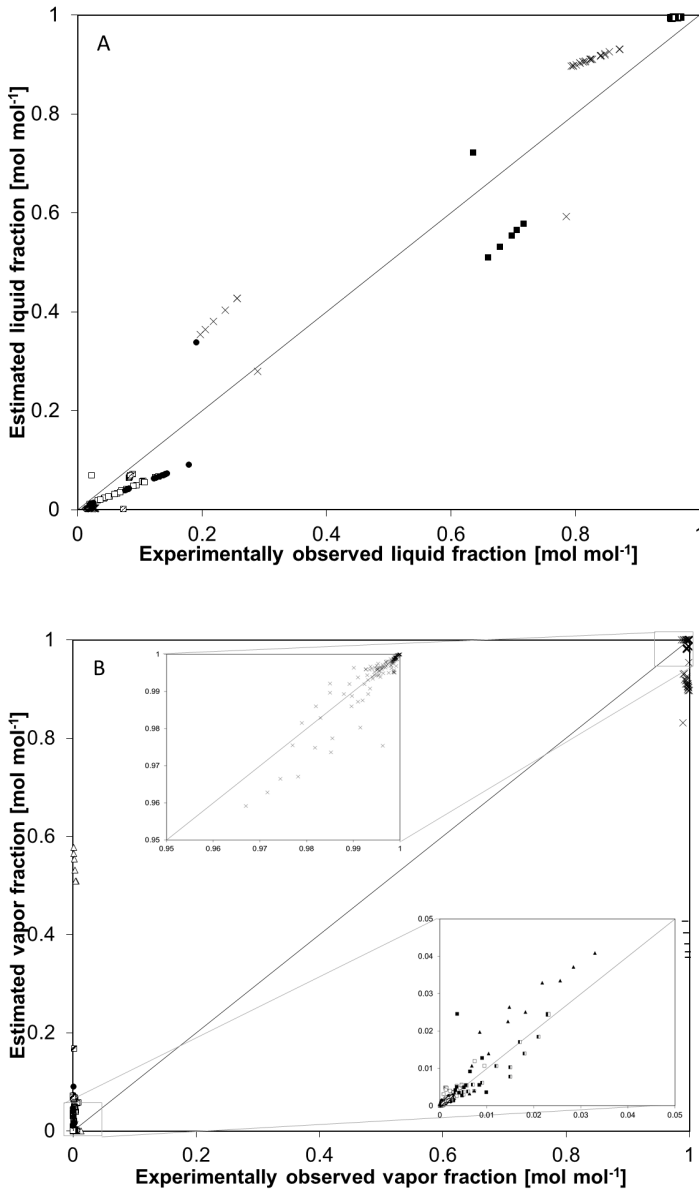


Figure 6.SI.1. Comparison between experimental and estimated liquid (A) and vapor fraction (B) of vapor-liquid equilibria of FFA (\blacktriangle), TG (\blacksquare), EtOH (\diamond), FAEE (\blacklozenge), water (\blacklozenge), FAME (\square), tocopherol (\boxplus), sterol (\boxminus), squalene (\bullet) and CO₂ (\times) without the implementation of the binary interaction coefficients.

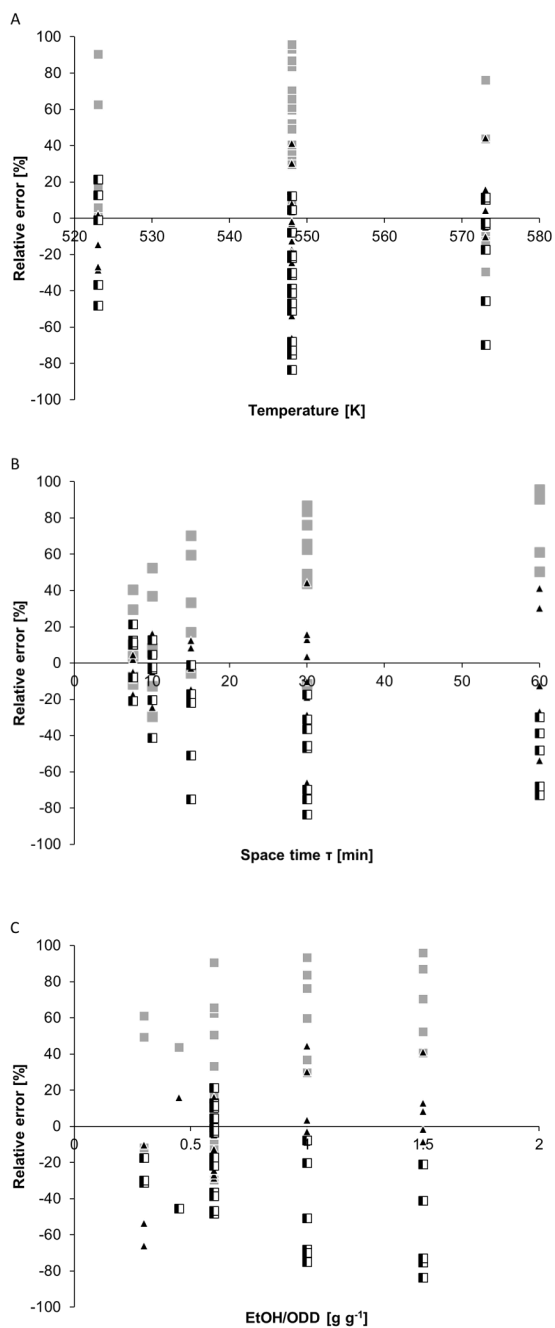


Figure 6.SI.2. Relative error of the molar flow rate of TG (■), FFA (▲), FAEE (◆) as function of (A) temperature, (B) space time and (C) ethanol to ODD ratio.

Main characteristics of relevant units in the valorization of olive ODD

Table 6.SI.1. Main characteristics of the distillation units for olive ODD

Distillation tower	T-300	T-400
Number of stages	12	3
Feed stage	6	2
Condenser pressure	kPa 3	5
Condenser temperature	K 482	514
Condenser duty	kW -2	-3
Molar reflux ratio	- 6.5	0.1
Reboiler pressure	kPa 14	7
Reboiler temperature	K 574	547
Reboiler duty	kW 5	14
Molar boilup ratio	- 8.3	32

Table 6.SI.2. Main characteristics of the heat exchangers for olive ODD

Heat exchangers	E-101	E-102	E-103	E-104	E-200	E-206
Pressure	kPa 15 000	180	180	180	12 000	100
Outlet temperature	K 573	458	348	348	313	298
Outlet vapor fraction	- 0.81	0.90	0	0	0	0.99
Heat duty	kW 58	-6	-52	-10	-11	48
Heat exchangers	E-301	E-302	E-400	E-401	E-402	
Pressure	kPa 100	100	100	100	100	
Outlet temperature	K 298	298	631	298	298	
Outlet vapor fraction	- 0.12	0	0.79	0	0	
Heat duty	kW -0.5	-2	11	-23	-1	
Heat exchangers	E-201	E-202	E-203	E-204	E-205	
Pressure	kPa 260	679	177	461	12 000	
Outlet temperature	K 373	373	373	373	313	
Outlet vapor fraction	- 1	1	1	1	1	
Heat duty	kW -11	-38	-45	-48	-103	

Table 6.SI.3. Main characteristics of the pumps for olive ODD

<i>Pumps</i>		<i>P-102</i>	<i>P-202</i>
<i>Discharge pressure</i>	kPa	15 000	12 000
<i>Pressure change</i>	kPa	14 900	11 800
<i>Duty</i>	kW	2	1

Table 6.SI.4. Main characteristics of the compressors for olive ODD

<i>Compressors</i>		<i>C-201</i>	<i>C-202</i>	<i>C-203</i>	<i>C-204</i>	<i>C-205</i>
<i>Discharge pressure</i>	kPa	260	679	1 770	4 610	12 000
<i>Compression ratio</i>		2.6	2.6	2.6	2.6	2.6
<i>Duty</i>	kW	34	41	42	41	39

Main characteristics of relevant units in the valorization of sunflower ODD

Table 6.SI.5. Main characteristics of the distillation units for sunflower ODD

<i>Distillation tower</i>		<i>T-300</i>	<i>T-400</i>
<i>Number of stages</i>		12	3
<i>Feed stage</i>		2	2
<i>Condenser pressure</i>	kPa	3	3
<i>Condenser temperature</i>	K	498	503
<i>Condenser duty</i>	kW	-1	-2
<i>Molar reflux ratio</i>	-	9.8	0.1
<i>Reboiler pressure</i>	k Pa	14	5
<i>Reboiler temperature</i>	K	573	573
<i>Reboiler duty</i>	kW	2	410
<i>Molar boilup ratio</i>	-	14	1.1

Table 6.SI.6. Main characteristics of the heat exchangers for sunflower ODD

Heat exchangers		E-101	E-102	E-103	E-104	E-200	E-206
Pressure	kPa	15 000	141	141	141	12 000	100
Outlet temperature	K	573	441	348	348	313	298
Outlet vapor fraction	-	0.96	0.86	0	0	0	0.99
Heat duty	kW	59	-7	-44	-8	-1	70
<hr/>							
Heat exchangers		E-301	E-302	E-400	E-401	E-402	
Pressure	kPa	100	100	100	100	100	
Outlet temperature	K	298	298	631	298	298	
Outlet vapor fraction	-	0	0	0.54	0	0	
Heat duty	kW	-0.2	-0.5	23	-22	-2	
<hr/>							
Heat exchangers		E-201	E-202	E-203	E-204	E-205	
Pressure	kPa	260	679	1 770	4 610	12 000	
Outlet temperature	K	373	373	373	373	313	
Outlet vapor fraction	-	1	1	1	1	1	
Heat duty	kW	-16	-55	-14	-70	-147	

Table 6.SI.7. Main characteristics of the pumps for sunflower ODD

Pumps		P-102	P-202
Discharge pressure	kPa	15 000	12 000
Pressure change	kPa	14 900	11 800
Duty	kW	2	1

Table 6.SI.8. Main characteristics of the compressors for sunflower ODD

Compressors		C-201	C-202	C-203	C-204	C-205
Discharge pressure	105 Pa	2.60	6.79	17.7	46.1	120
Compression ratio		2.6	2.6	2.6	2.6	2.6
Duty	kW	48	58	60	58	56

Main characteristics of relevant units in the valorization of soybean ODD

Table 6.SI.9. Main characteristics of the distillation units for soybean ODD

Distillation tower		T-300	T-400
Number of stages		12	3
Feed stage		6	2
Condenser pressure	kPa	3	3
Condenser temperature	K	484	626
Condenser duty	kW	-0.2	-2
Molar reflux ratio	-	1.3	0.1
Reboiler pressure	k Pa	14	5
Reboiler temperature	K	573	573
Reboiler duty	kW	1	16
Molar boilup ratio	-	5.4	1.4

Table 6.SI.10. Main characteristics of the heat exchangers for soybean ODD

Heat exchangers		E-101	E-102	E-103	E-104	E-200	E-206
Pressure	k Pa	15 000	100	100	100	12 000	100
Outlet temperature	K	573	422	348	348	313	298
Outlet vapor fraction	-	0.87	0.88	0	0	0	0.99
Heat duty	kW	54	-15	-42	-6	-3	81
<hr/>							
Heat exchangers		E-301	E-302	E-400	E-401	E-402	
Pressure	k Pa	100	100	100	100	100	
Outlet temperature	K	298	298	498	298	298	
Outlet vapor fraction	-	0	0	0.02	0	0	
Heat duty	kW	-1	-1	11	-10	-17	
<hr/>							
Heat exchangers		E-201	E-202	E-203	E-204	E-205	
Pressure	k Pa	260	679	1 770	4 610	12 000	
Outlet temperature	K	373	373	373	373	313	
Outlet vapor fraction	-	1	1	1	1	1	
Heat duty	kW	-18	-62	-72	-79	-168	

Table 6.SI.11. Main characteristics of the pumps for soybean ODD

Pumps		P-102	P-202
Discharge pressure	kPa	15 000	12 000
Pressure change	kPa	14 900	11 800
Duty	kW	1	1

Table 6.SI.12. Main characteristics of the compressors for soybean ODD

Compressors		C-201	C-202	C-203	C-204	C-205
Discharge pressure	kPa	260	679	1 770	4 610	12 000
Compression ratio		2.6	2.6	2.6	2.6	2.6
Duty	kW	55	66	68	66	63

Side note in the economic evaluation

Next to the CAPEX, which was estimated to be 4,98 M€ (Table 6.5), the operating costs need to be considered when looking at the economic evaluation of a process.

The operating costs (OPEX) are divided into manufacturing costs and general expenses. Manufacturing costs are further divided into variable costs (*i.e.* raw material, utilities, operating labor, direct supervision, supplies, maintenance and repairs,...), fixed costs (*i.e.* insurances, taxes,..) and plant overheads. General expenses are costs related to administration, distribution and marketing. The following guidelines⁶⁴ were used for estimating fixed costs as a function of the capital or operating cost:

- Operating labor cost is estimated as 3 persons per shift, 3 shifts per day at a cost of € 65 000 per person per year.
- Non-operating labor is estimated as 60 % of the operating labor cost.
- Supplies are estimated as 30 % of the operating labor cost.
- Administration is estimated as 90 % of the operating labor cost.
- Maintenance is estimated as 5 % of the capital costs.
- Yearly taxes and insurances are estimated as 2 % of the capital costs.

An estimation of the operating costs is given in Table 6.SI.13. The fixed operating costs are estimated at 1,98 M€ for the complete valorization unit. The most important difference in the variable operating costs is situated in the raw materials cost. The overview of the income per feedstock, is given in Table 6.SI.14.

Table 6.SI.13. Estimation of variable and fixed operating costs for different ODD.

[k€ year ⁻¹]	olive ODD	sunflower ODD	soybean ODD
<i>Variable costs</i>			
<i>Raw material</i>			
<i>ODD</i>	551	551	3 342
<i>make-up EtOH</i>	126	153	86
<i>Consumables</i>			
<i>CO₂</i>	6	8	9
<i>Waste</i>			
<i>liquid waste</i>	83	42	50
<i>CO₂ emission</i>	12	17	19
<i>Utilities</i>			
<i>heating</i>	48	45	51
<i>cooling</i>	6	7	8
<i>electricity</i>	40	58	64
<i>Fixed operating costs</i>			
<i>Operating labor cost</i>	585	585	585
<i>Non-operating labor cos</i>	351	351	351
<i>Supplies</i>	175	175	175
<i>Administration</i>	527	527	527
<i>Maintenance</i>	250	250	250
<i>Taxes, insurances</i>	100	100	100
<i>Total operating cost</i>	2 850	2 869	5 617

Table 6.SI.14. Estimation of incomes per feedstock.

[k€ year ⁻¹]	olive ODD	sunflower ODD	soybean ODD
<i>Key products = REV</i>			
<i>squalene</i>	3 084	771	1 028
<i>minors</i>	53	1 482	14 558
<i>Side products = SP</i>			
<i>FAEE</i>	659	665	283
<i>FAME</i>	0	0	0
<i>glycerol</i>	0	0	0

The profitability of a process can be evaluated by the return on investment (ROI). To calculate ROI, the annual net profit, which is calculated as the difference from the total income (REV+SP) and all the expenses (fixed and variable), is divided by the capital costs⁶⁵.

$$ROI = \frac{\text{net gain}}{CAPEX} \times 100\% \quad (6.1)$$

The payback time (PBT) refers to the time (in years) it takes to recover the costs of an investment, i.e. the CAPEX, and is defined according to equation (6.2)⁶⁵.

$$\text{Payback time (PBT)} = \frac{\text{CAPEX}}{\text{net gain}} \quad (6.2)$$

The estimation of the different profitability parameters is summarized in Table 6.SI.15. The soybean ODD gives the highest yearly net income amounting to 15.9 M€, followed by the olive ODD (3.7 M€) and the sunflower ODD (2.9 M€). The net gain, which is the difference between the net income and the operating costs, is the highest for the soybean ODD and the lowest for the sunflower ODD. The highest ROI is achieved with soybean ODD. For sunflower ODD, the ROI reveals that the process is not really viable, although it is the most versatile feedstock (Figure 6.8). The PBT is 0.5 years for soybean ODD and 5.8 years for olive ODD. The soybean ODD has a significantly higher revenue and lower PBT due to the higher amount of the minor-products, which have also a higher purity compared to olive ODD.

Table 6.SI.15. Estimation of the parameters for different ODD

	<i>olive ODD</i>	<i>sunflower ODD</i>	<i>soybean ODD</i>
<i>Net Income [k€ year⁻¹] = REV + SP</i>	3 706	2 913	15 869
<i>Expenses [k€ year⁻¹]</i>	2 850	2 869	5 617
<i>Net gain [k€ year⁻¹]</i>	856	44	10 252
<i>CAPEX [k€]</i>	4 980	4980	4980
<i>ROI [%]</i>	17	< 1	> 200
<i>PBT [years]</i>	5.8	> 100	0.48



CHAPTER 7.
CONCLUSIONS AND PERSPECTIVES

This thesis focused on the valorization of side streams in natural oil processing with an, at present, low economic value. As a biomass resource, such side streams are expected to contribute to a green and sustainable economy. First, conclusions are presented with respect to doped Cu based catalysts for the production of ‘green’ 1,2-propanediol from glycerol, as a side product in the biodiesel production. Next, the conclusions are given for the valorization of Oil Deodorizer Distillates (ODD), for which a versatile conceptual process configuration was designed, simulated and optimized for the recovery of squalene from ODDs. Finally, generic conclusions and perspectives for future research related to these valorization processes are presented.

7.1 Understanding the factors controlling the catalyst performance for glycerol hydrogenolysis

Copper based catalysts give high selectivity to 1,2-propanediol from glycerol hydrogenolysis, which is a more sustainable route compared to the conventional one via petroleum derived propylene oxide. However, these catalysts exhibit moderate activity and, more particularly, low stability due to Cu sintering. Commercial catalysts typically contain various promoters, in different amounts, precluding a clear understanding of their individual roles on the catalytic performance, *i.e.* stability, activity and selectivity. The aim of this thesis was to perform a systematic investigation on the role of dopants on Cu-based catalysts, for glycerol hydrogenolysis at industry-like conditions.

7.1.1 Catalyst characterization

Detailed characterization was performed to understand the catalysts’ overall appearance, and not just from a single perspective or property point of view. The characterization techniques can be divided into morphological and physical properties (*e.g.* N₂-sorption and STEM), surface composition and surface properties (*e.g.* XPS, NH₃-TPD, N₂O-chemisorption) and bulk properties (*e.g.* ICP, XRD, H₂-TPR, TGA). It is advisable to understand the limitations and strengths of the different techniques, in order to combine them in a complementary way. The catalysts were characterized in three stages: (i) after calcination *via* ICP, N₂-sorption, XRD, XPS and STEM, (ii) after reduction *via* XRD, N₂O-chemisorption, H₂-TPR, XPS, STEM and NH₃-TPD, (iii) after reaction, *i.e.* the spent catalyst, *via* XRD, N₂O-chemisorption, XPS and STEM.

The actual, bulk metal loadings were lower than the nominal ones, which was attributed to the hygroscopic nature of the precursors. The supports showed broad diffraction peaks, indicating an amorphous phase (especially in the case of SiO₂). For all calcined catalysts, the main characteristic diffraction peaks of CuO were detected. After reduction, the CuO diffraction peak disappeared with the appearance of the Cu⁰ diffraction peaks. No characteristic peaks for Cu₂O nor the dopants, of which the loading was close to the detection limit of XRD (1 wt.%), nor mixed phases were identified. For the La-Cu catalysts, XPS revealed the coexistence of Cu²⁺ and Cu⁺ in the calcined catalysts, and that of Cu⁺ and Cu⁰ in the reduced catalysts. Based on the Cu Binding Energy (BE), and the fraction of Cu⁺,

calculated from the Cu LMM spectra, it was found that the La-Cu interaction in both the calcined and the reduced catalysts, increased with promotion ratio. On the other hand, with increasing SiO₂-content in the support, the Cu-support interaction decreased both in the calcined and reduced state, as evidenced by the shift in the Cu BE, resulting in more surface Cu⁺ species.

The reduction behavior of the catalysts was investigated by means of H₂-TPR. In general, several Cu species could be identified: highly dispersed CuO and/or Cu²⁺-O-Cu²⁺ species, CuO particles with weak support interactions, bulk CuO and CuO particles with a strong support interaction. The evolution of the CuO during the reduction was investigated more in depth by *in situ* XRD for a La-Cu catalysts. A small amount of highly dispersed Cu₂O was identified after reduction, in agreement with the XPS analysis.

The Cu particle size was analyzed by various techniques: XRD, dissociative N₂O-sorption and STEM. While, XRD is a widely applied technique, resulting in statistically representative, volume-averaged values, its main disadvantage is that it is not suitable for amorphous materials or particles with a crystallite size below 5 nm.¹ The XRD-derived sizes are typically higher than the chemisorption-derived sizes, as the presence of some large crystallites in the sample will create more intense XRD peaks. On the contrary, STEM-derived sizes are number based and, hence, the presence of a few larger particles will not give rise to a larger average TEM-derived size. For TEM, particles as small as 5 nm can be identified.² For smaller particles sizes, HR-TEM is recommended (up to 0.1 nm).³ The dispersion of the surface Cu⁰ was determined by dissociative N₂O-chemisorption, as the population of all the smaller Cu⁰ particles, is then also considered. HR-TEM could provide an alternative as it is more accurate than STEM and accounts for all small particles. The Cu loading, rather than the promotion ratio, proved to be the key factor in determining Cu⁰ particle size and, hence, dispersion. The average diameter as determined by dissociative N₂O-chemisorption varied between 1.1 and 9.5 nm, with corresponding dispersions of 17% to 2%. STEM-EDX confirmed the presence of well dispersed metals for the La-Cu catalysts. It was found that Ba-, Ce- and La-doped catalysts stabilized the Cu⁰ particle size during the reaction, inhibiting sintering. Therefore, Ba, Ce and La act both as structural promoters. For the La-Cu/ γ -Al₂O₃ catalysts, it was found that the La promotion inhibited the sintering of the Cu⁰ particles as a result of the stronger La-Cu interaction. The mechanism behind this stabilization remains unclear, however.

It seemed that a simple preparation method, such as impregnation, led to the formation of both very small (as evidenced by STEM-EDX and dissociative N₂O-chemisorption) and larger (as detected by XRD) Cu particles. The determination of the fractions of both populations and the factors controlling it, remain to be clarified. A more homogenous population could potentially be achieved by using a small amount of a complexing agent. Cyclodextrins, which are oligosaccharides, could be used during the catalyst preparation. They possess a cavity, of which the size depends on the exact type of cyclodextrin, which can attract a wide range of molecules, such as metallic anions. This enables the stabilization and

anchoring of the metallic nanoparticles, up to a certain size, onto the support. During the calcination the cyclodextrins will decompose, leaving well dispersed metals on the catalyst surface. The increased metal dispersion are expected to result in a higher catalytic activity.⁴

Concerning the impact of the dopants on the acidity, it was found that Ba, Ce and La slightly increased the total acidity of the catalysts. For the La-Cu/ γ -Al₂O₃ catalysts, the increase in weak to moderate acidity was found to be related to the presence of Cu⁺ introduced by the La-Cu interaction. With respect to the effect of the SiO₂-content in the support, the total acidity for the supported Cu and La-Cu catalyst decreased in the order of 60Al₂O₃ \geq 99Al₂O₃ > Al₂O₃ > SiO₂. This trend was ascribed to the generation of strong acid sites, most probably Brønsted acid sites, when SiO₂ is introduced in the Al₂O₃ framework. Further determination of the exact ratio between Lewis and Brønsted acid sites, by pyridine-FTIR, could lead to new insights about the factors controlling the acid site distribution.

The catalyst characterization indicated that the bulk of the calcined and reduced catalysts had respectively homogeneously dispersed Cu²⁺ and Cu⁰ species. A fraction of Cu⁺, which depended both on the interaction between the support and the Cu and the interaction between the dopant and Cu, was also detected on the catalyst surface. However, it is uncertain whether the Cu⁺ species are located on top of Cu⁰ or Cu²⁺ particles, as assumed from the XPS results, or exist on their own. HR-TEM could provide insights into this missing information by determining the interplanar distances and compare them to the facets in Cu crystals.

It is clear that some insights were gained by the characterization, despite the fact it remained sometimes incomplete or the differences between the catalysts were limited, *i.e.*, not significant. The fundamental research of the catalysts under relevant conditions by *in situ* techniques, such as XRD or TPR/TPD, give little information of the atom by atom characterization of the surface, while the surface sensitive techniques, such as XPS or STEM, can only be applied under vacuum, which is a point of concern. Another point of concern is the difference in *in situ* characterization of the reduced catalyst and the *in situ* activation of the catalyst prior to the reaction. While it is possible to mimic the temperature profile and gas composition quite easily, this is practically impossible for the H₂ partial pressure, the contact and space time. Thus, it is good to realize that, although many techniques reveal useful information on the catalyst, the information from the real catalyst surface during the reaction often remains disguised.

7.1.2 The role of Cu⁰ and Cu⁺

It was revealed that the Cu catalysts exhibited a structure sensitivity, *i.e.* a relationship between the Cu⁰ particle size and the TOF, for the glycerol hydrogenolysis. To understand this relationship, all investigated catalysts are visualized in Figure 7.1. The obtained activity of the catalysts was at the lower limit for industrially relevant applications (10⁻² – 10² s⁻¹)⁵. The structure sensitivity is not only related to the Φ_{Cu^0} , as two different relationships were identified. Hence, other factors among which the coordination number of the Cu species play a role in the catalytic activity.^{6,7}

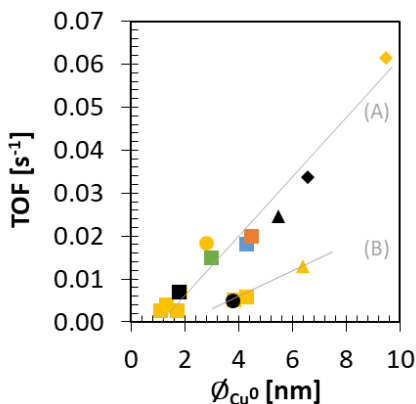


Figure 7.1. TOF at 12 h TOS, $125 \text{ kg}_{\text{cat}} \text{ s mol}^{-1}_{\text{glycerol}}$, 473 K, a total H_2 pressure of 7.5 MPa and a molar H_2 to glycerol ratio of 7 as function of the average diameter of the Cu^0 aggregates, ϕ_{Cu^0} , for pure glycerol hydrogenolysis for the Cu (black), Ba-Cu (blue), Ce-Cu (orange), Cs-Cu (green) and La-Cu (yellow) catalysts supported on Al_2O_3 (■), $99\text{Al}_2\text{O}_3$ (◆), $60\text{Al}_2\text{O}_3$ (▲) and SiO_2 (♦).

On the one hand, defects are known to vary the coordination number. Step sites have a higher number of nearest neighbors compared to kink sites, *i.e.* respectively four and three, resulting in a higher activity.⁶ On the other hand, the different facets in a Cu particle, such as (110), (100) or (111), result in different coordination numbers of the surface layer atoms, respectively seven, eight and nine. The lower the coordination number, the lower the electron density and the higher the adsorption strength.⁷ It is known that dissociation reactions, such as hydrogenation, are favored on sites with lower coordination numbers.⁷ Therefore, the strongly adsorbed H_2 will compete with the active sites for the adsorption of glycerol on the catalytic surface, resulting in a lower activity. Based on this knowledge and the observations in Figure 7.1, it is assumed that the catalysts following relationship (A) have Cu^0 species with a higher coordination number and, hence a higher activity, compared to the catalysts following relationship (B). To verify this assumption, atomic-scale information could be obtained from HR-TEM which would enhance the understanding of the catalyst surface. Alternatively, this could be done by Density-Functional Theory calculations.

As the differences between the various La-Cu/ γ - Al_2O_3 catalysts in terms of total acidity and catalytic activity were rather small, a more pronounced variation of the acidic properties of the catalysts, and correspondingly, their performance, is achieved by introducing SiO_2 into the support. It was found that with increasing SiO_2 -content, the Cu-support interaction decreased resulting in a lower Cu-dispersion and a higher Cu^+ surface fraction. It was not possible to conclude on the dominant effect, however, it is clear that both the particle size of Cu^0 and the acidity, affected by the fraction of Cu^+ enhanced the catalytic activity.

7.1.3 Factors controlling the selectivity

Based on the observed products, two main reaction pathways were identified: the dehydration of glycerol leads to the formation of acetol, which can be hydrogenated to 1,2-propanediol, while 1,2-ethanediol was formed by direct hydrogenation (Figure 4.7). The Ba-, Ce- and La-doped catalysts increased the selectivity (at 473 K, 7.5 MPa, $125 \text{ kg}_{\text{cat}} \text{ s mol}^{-1}_{\text{glycerol}}$ and $7 \text{ mol}_{\text{H}_2} \text{ mol}_{\text{G}}^{-1}$) towards 1,2-propanediol to 92 % compared to the Cu catalyst (82 %) and, hence, these dopants act as a textural promoter.

It was found that the La/Cu ratio increased the La-Cu interaction leading to a higher ratio of surface Cu^+ species and a coexistence of Cu^0 and Cu^+ . The presence of Cu^+ , which is considered to be a weak-moderate Lewis acid, increased the total acidity of the catalysts and, hence, resulted in an increased 1,2-propanediol (> 86 %) selectivity compared to the bare Cu catalyst (82 %). The maximum 1,2-propanediol selectivity (94 %) at $125 \text{ kg}_{\text{cat}} \text{ s mol}^{-1}_{\text{glycerol}}$, 473 K, 7.5 MPa H_2 pressure and a molar H_2 to glycerol ratio of 7 was obtained for a catalyst with a La/Cu ratio of 0.088, with 1,2-ethanediol as major side product. It was found that glycerol hydrogenolysis to 1,2-ethanediol also requires a synergy between metal and acid sites. The undesired products require stronger acid sites, mostly provided by the support.

Unexpectedly, no significant effect of the total acidity was found on the selectivity towards 1,2-propanediol or the side products. Whereas NH_3 -TPD provided information about the total acidity and the acidic strength, additional pyridine-FTIR can be used to quantify the nature (Lewis vs. Brønsted) of the acid sites. This could lead to new insights about their respective influence on the catalytic performance.

7.1.4 Perspectives

This work has shown that metal catalysis shows more complexity and brings more challenges in identifying the unequivocal effect of parameters than anticipated. For the development of high performing catalysts, a kinetic model will be needed to gain fundamental insights as the experimental observations have their limitations. The use of a kinetic model to gain insight into a reaction has already proven its value for acid catalyzed processes⁸⁻¹¹ or metal catalysis¹²⁻¹⁴, for the determination of optimal reaction conditions aiming at the minimization of undesired products. The interaction between the reactants and the catalytic surface is often described by the chemisorption enthalpy as catalytic descriptor. It is well known, that a too strongly adsorbed reactant will slow the reaction by “poisoning” the surface, while a too weakly adsorbed one will not react with the surface. While the chemisorption enthalpy is a measurable property, its fine tuning is less evident. Often, the relationship between the catalyst properties and its impact on the kinetics is missing. Therefore it would be advisable to work with more directly accessible catalytic descriptors for the support, primary metal, in this case Cu, and dopant, as those contain a large amount of information as well. For the support, the calcination method

is a key parameter as this impacts on the pore volume and surface area.¹⁵⁻¹⁷ For the primary metal, *c.g.*, Cu, at least the loading weight and binding energy should be accounted for. From the characterization it was pointed out that the former impacts on the particle size of the Cu⁰, while the latter affected the formation of Cu⁺. For the dopant, the loading should be considered as it affected the catalytic properties. Even more, additional understanding in the catalytic performance could be achieved by investigating the change in the Cu binding energy and oxidation state in the Ba- and Ce-doped catalysts. As glycerol hydrogenolysis is enhanced by acid sites, an additional descriptor for the acidity should be identified. Hence, further catalytic characterization, *via* pyridine-FTIR for the determination of acid types, should focus on acquiring information about measurable or tunable properties. Spent catalyst characterization should be performed to investigate the change of the catalyst surface on the different supports. Additional performance testing at higher temperatures and various space times, but equal time on stream, will be necessary to relate the catalysts performance by means of various catalytic descriptors in the kinetic model. The retrieved insights will provide a strategic advantage in the design of novel, high performing catalyst.

7.2 Valorization of oil deodorizer distillates

Process simulations constitute a powerful technique in the optimization of existing and the design of new processes. One of the most important stages in the design is the investigation and identification of suitable models such as those for the reaction kinetics and the thermodynamics.

Experimental insights into the reaction mechanism and kinetics of supercritical esterification of oil deodorizer distillates were obtained by performing supercritical esterification of sunflower ODD with ethanol at 15 MPa at varying space time (0 – 60 min), temperature (523 K - 573 K) and ethanol to ODD ratio (0.3 g_{EIOH} g⁻¹_{ODD} - 1.5 g_{EIOH} g⁻¹_{ODD}). The modelling of such reactions has not only experimental but also specific simulation challenges. On the one hand, the complexity to achieve accurate effluent analysis increases when a complex mixture such as ODD is used. On the other hand, describing the phenomena which are happening at supercritical conditions is potentially challenging and the regression of a limited number of data points may rather easily leads to overfitting. The reactions considered are the esterification of the Free Fatty Acids (FFA) and the transesterification of the glycerides, the latter comprising three consecutive steps. The kinetic model is simplified by assuming the reactions to be irreversible and considering the chemical similarity, if not equivalence, of the consecutive transesterification reactions, leading to a kinetic model with only four kinetic parameters. The regression resulted in a model with statistically significant and physically meaningful values. The activation energies for the esterification and transesterification reaction amounted to, respectively, 101 ± 36 kJ mol⁻¹ and 27 ± 8 kJ mol⁻¹. The former is higher compared to literature reported values¹⁸⁻²⁰ (50-75 kJ mol⁻¹), which can be the result of using ethanol instead of methanol. The latter is lower compared to the typical values of 35 to 80 kJ mol⁻¹.²¹⁻²⁵ This simplified model showed a good fit for the

temperature dependence at a given mixture composition of $0.6 g_{\text{EtOH}} g_{\text{ODD}}^{-1}$, but failed at other ratios, most likely due to the limited number of data points. Nonetheless, adequate information about the mixture composition is required as the change in composition, and the consequent change of mixture properties may strongly affect the reactor design and its configuration. Therefore, one should be careful when the model is used to predict the performance far beyond the experimental conditions.

Another key factor is the proper selection of the models to calculate the thermodynamic properties of each pure component and the mixture. These models enable the calculation of thermophysical properties (such as density, compressibility factor, enthalpy, entropy, heat capacity, critical temperature, pressure and volume,...), and phase equilibria. Additionally, interactions between the components may not be neglected. Errors in the properties or interactions can lead to major problems in the process configuration, sizing and evaluation. Here again, the level of detail is a crucial point. When simulating the complexity of ODD by a limited number of key components, crucial information will likely be missing. Including all components would require the knowledge of a huge number of parameters, *e.g.*, interaction coefficients, such that the simulations' accuracy would be undermined. This is, among others, a consequence of a lack of for high pressure data bases, compared to the low-pressure ones. Therefore, it was more effective to represent the mixture by a lumped approach, where for each component family one component was selected for the representation of all components within the family. The ODDs were described in terms of eight component families, *i.e.*, lumps, for which a model component was selected, *i.e.* for FFA (oleic acid), TG (triolein), DG (diolein), MG (monoolein), FAEE (ethyl oleate), phytosterols (β -sitosterol), tocopherols (α -tocopherol) and squalene. As the process configuration consisted of both, low (purification and reaction) and high pressure (extraction) sections, an appropriate thermodynamic model was selected for each of these. For the reaction section, an ideal property method was selected as it is assumed that non-idealities are accounted for via the estimated kinetic parameters. For the extraction section, the Redlich-Kwong-Aspen equation of state was selected as it has been found to perform well at supercritical conditions with light gases such as CO_2 . The binary interactions coefficients between sc- CO_2 and each model component of ODD were regressed to literature reported experimental data. Additionally, the binary interaction between TG and FFA, TG and sterols, FAME and squalene and ethanol and water were regressed as well to literature reported experimental data. For the purification section, which is a low pressure section, the activity coefficient model UNIQUAC-Redlich-Kwong was used. All the missing parameters in the model were estimated based on experimental data.

The design of a versatile process configuration was aimed at, capable of the valorization of different ODDs, *i.e.* olive, sunflower and soybean ODD. The configuration existed of three sections: the reaction section, the extraction section and the purification section. In the reaction section, an FFA conversion exceeding 95 % was aimed to achieve a good extraction of the minor components in the following section. This could be achieved by operating the reactor at 573 K and 15 MPa with a volume of 2.0 m³.

An extraction tower with five theoretical stages at operating at 333 K and 12 MPa was capable of extracting more than 95 % squalene of the esterified ODD. Due to the differences in the solvent to feed ratio, the optimal diameter of the tower for the olive and sunflower ODD was determined to be 0.34 m and 0.60 m in the case of soybean ODD. However, the differences in the diameter could be counteracted by selecting a suitable packing. The purification section consisted of two vacuum distillation towers, to prevent degradation of the minor components, able to process various ODDs. A first one with 12 theoretical stages, to purify squalene from FAME. A second one was designed to increase the economic viability of the process, by separating FAEE from mixed stream of the sterols and tocopherols in three stages. According to the simulations, the two distillation towers can be designed with a diameter of 0.46 m, but with different heights of 12.8 m and 4.9 m.

In this thesis, it was demonstrated that the recovery of squalene from ODD not only contributed to the valorization of this waste stream, but also demonstrated to be a sustainable alternative for its recovery from deep sea shark liver oil. The overall extraction yield exceeded 95 % with a squalene purity up to 99 wt.% for olive ODD, which is higher than what is reported in the literature^{26, 27} (90 % yield and purity around 90 wt.%). Furthermore, it was demonstrated that a single, but versatile process configuration is capable of handling different ODD feedstocks, with varying compositions, at milder conditions than typically reported. The economic evaluation pointed out that the process is economically feasible, but the profitability strongly depends on the market price of the raw materials and the products. Correspondingly, the process configuration's flexibility is the key factor to ensure its profitability, allowing fast adaptation to the market.

The process simulation could be further improved by determining the experimental VL(L)E-data between FFA or TG and each minor component, for regression of the binary interaction coefficients between the major component families and the minors. In this manner, the process simulation of the extraction section will be described even more accurately.

7.3 Generic conclusions on valorization of natural oil and fats derived side streams

The transition towards a green and sustainable economy is coming stepwise, through interdisciplinary research and innovational technologies. The use of side streams from the processing of natural oils and fats can contribute to this future, but the availability of these streams, the knowledge and experience within a company and the governmental context will determine which valorization is most suited and successful.

It was demonstrated that even for a capacity of 1 % of the European produced ODDs, the recovery of squalene from various ODDs was profitable. Although this promising result focused on the recovery of squalene, further research could be performed in optimizing the recovery and separation of the other

minor components, such as sterols and tocopherols. In order to bring this closer to industrialization, a better understanding and description of the reaction mechanism and physicochemical properties will be essential.

Even by performing a systematic research of the role of dopants in Cu-catalyst for glycerol hydrogenolysis, it was found that unequivocal relationship between measurable properties and catalytic performance was not possible. The limited variation in the performance between Cu^+ and Cu^0 made it difficult to elucidate their individual roles. A more elaborated catalytic evaluation will improve the understanding of the catalyst structure and the effect of Cu species on the reaction mechanism. This could be attributed to a too narrow range of dopant loading and the interdependence between various interactions of the metals, the dopant and the support. A larger range could be covered by applying steps of 1 wt.% in promoter loading, instead of 0.5 wt.%, and use a loading up to 5 wt.%. This way, the differences could be more pronounced assuming the effect behaves linearly. However, a large number of different catalysts will not be the only solution, as the experimental workload will be too intensive. Machine learning could contribute in the investigation of large experimental data sets from literature, indicating the most interesting catalysts descriptors to be tested.

Chemical engineering, a marriage between science and industry, has a pioneering role in establishing technological solutions to the environmental issues and global climate change. As the chemical industry is indispensable to modern life necessities, it plays a key role in the transition to a more sustainable economy. This research has shown that environmental (*e.g.* reduce of waste, protecting sea life), social (*e.g.* by improving safety and health, through the use of less toxic components or explosive processes, lower CO_2 footprint) and economical (*e.g.* by the reduction of cost and energy use) responsibilities go hand-in hand to find the best possible scale-tailored solutions for a more sustainable future

7.4 References

- 1 C.F. Holder, R.E. Schaak, Tutorial on Powder X-Ray Diffraction for Characterizing Nanoscale Materials, *ACS Nano*, 13 (2019) 7359-7365.
- 2 M.H. Loretto, Introduction to Electron Beam Instruments, in: M.H. Loretto (Ed.) *Electron Beam Analysis of Materials*, Springer Netherlands, Dordrecht, 1984, pp. 1-18.
- 3 M. Haider, H. Rose, S. Uhlemann, B. Kabius, K. Urban, Towards 0.1 Nm Resolution with the First Spherically Corrected Transmission Electron Microscope, *Journal of Electron Microscopy*, 47 (1998) 395-405.
- 4 A. Jean-Marie, A. Griboval-Constant, A.Y. Khodakov, E. Monflier, F. Diehl, B-Cyclodextrin for Design of Alumina Supported Cobalt Catalysts Efficient in Fischer–Tropsch Synthesis, *Chemical Communications*, 47 (2011) 10767-10769.
- 5 J. Hagen, *Industrial Catalysis*, 2005.
- 6 R. Beerthuis, J.W. de Rijk, J.M.S. Deeley, G.J. Sunley, K.P. de Jong, P.E. de Jongh, Particle Size Effects in Copper-Catalyzed Hydrogenation of Ethyl Acetate, *Journal of Catalysis*, 388 (2020) 30-37.
- 7 Z.-P. Liu, P. Hu, General Rules for Predicting Where a Catalytic Reaction Should Occur on Metal Surfaces: A Density Functional Theory Study of C–H and C–O Bond Breaking/Making on Flat, Stepped, and Kinked Metal Surfaces, *Journal of the American Chemical Society*, 125 (2003) 1958-1967.
- 8 J.W. Thybaut, G.B. Marin, Single-Event Microkinetics: Catalyst Design for Complex Reaction Networks, *Journal of Catalysis*, 308 (2013) 352-362.
- 9 K. Toch, J.W. Thybaut, G.B. Marin, A Systematic Methodology for Kinetic Modeling of Chemical Reactions Applied to N-Hexane Hydroisomerization, *AIChE Journal*, 61 (2015) 880-892.
- 10 K.S. Wong, J.W. Thybaut, E. Tangstad, M.W. Stöcker, G.B. Marin, Methane Aromatisation Based Upon Elementary Steps: Kinetic and Catalyst Descriptors, *Microporous and Mesoporous Materials*, 164 (2012) 302-312.
- 11 J.W. Thybaut, I.R. Choudhury, J.F. Denayer, G.V. Baron, P.A. Jacobs, J.A. Martens, G.B. Marin, Design of Optimum Zeolite Pore System for Central Hydrocracking of Long-Chain N-Alkanes Based on a Single-Event Microkinetic Model, *Topics in Catalysis*, 52 (2009) 1251-1260.
- 12 G. Lozano-Blanco, J.W. Thybaut, K. Surla, P. Galtier, G.B. Marin, Single-Event Microkinetic Model for Fischer–Tropsch Synthesis on Iron-Based Catalysts, *Industrial & Engineering Chemistry Research*, 47 (2008) 5879-5891.
- 13 J. Van Belleghem, C. Ledesma, J. Yang, K. Toch, D. Chen, J.W. Thybaut, G.B. Marin, A Single-Event Microkinetic Model for the Cobalt Catalyzed Fischer-Tropsch Synthesis, *Applied Catalysis A: General*, 524 (2016) 149-162.
- 14 A. Chakkingal, L. Pirro, A.R. Costa da Cruz, A.J. Barrios, M. Virginie, A.Y. Khodakov, J.W. Thybaut, Unravelling the Influence of Catalyst Properties on Light Olefin Production Via Fischer–Tropsch Synthesis: A Descriptor Space Investigation Using Single-Event Microkinetics, *Chemical Engineering Journal*, 419 (2021).
- 15 L. Samain, A. Jaworski, M. Edén, D.M. Ladd, D.-K. Seo, F. Javier Garcia-Garcia, U. Häussermann, Structural Analysis of Highly Porous γ -Al₂O₃, *Journal of Solid State Chemistry*, 217 (2014) 1-8.
- 16 F. Vila, M. López Granados, M. Ojeda, J.L.G. Fierro, R. Mariscal, Glycerol Hydrogenolysis to 1,2-Propanediol with Cu/ γ -Al₂O₃: Effect of the Activation Process, *Catalysis Today*, 187 (2012) 122-128.
- 17 E.S. Vasiliadou, T.M. Eggenhuisen, P. Munnik, P.E. de Jongh, K.P. de Jong, A.A. Lemonidou, Synthesis and Performance of Highly Dispersed Cu/SiO₂ Catalysts for the Hydrogenolysis of Glycerol, *Applied Catalysis B: Environmental*, 145 (2014) 108-119.
- 18 R. Alenezi, G.A. Leeke, J.M. Winterbottom, R.C.D. Santos, A.R. Khan, Esterification Kinetics of Free Fatty Acids with Supercritical Methanol for Biodiesel Production, *Energy Conversion and Management*, 51 (2010) 1055-1059.
- 19 T. Jin, B. Wang, J. Zeng, C. Yang, Y. Wang, T. Fang, Esterification of Free Fatty Acids with Supercritical Methanol for Biodiesel Production and Related Kinetic Study, *RSC Advances*, 5 (2015) 52072-52078.

- 20 M. Chai, Q. Tu, M. Lu, Y.J. Yang, Esterification Pretreatment of Free Fatty Acid in Biodiesel Production, from Laboratory to Industry, *Fuel Processing Technology*, 125 (2014) 106-113.
- 21 H. He, S. Sun, T. Wang, S. Zhu, Transesterification Kinetics of Soybean Oil for Production of Biodiesel in Supercritical Methanol, *Journal of the American Oil Chemists' Society*, 84 (2007) 399-404.
- 22 M.N. Varma, G. Madras, Synthesis of Biodiesel from Castor Oil and Linseed Oil in Supercritical Fluids, *Industrial & Engineering Chemistry Research*, 46 (2007) 1-6.
- 23 D. Kusdiana, S. Saka, Kinetics of Transesterification in Rapeseed Oil to Biodiesel Fuel as Treated in Supercritical Methanol, *Fuel*, 80 (2001) 693-698.
- 24 A. Permsuwan, N. Tippayawong, T. Kiatsiriroat, C. Thararux, S. Wangkarn, Reaction Kinetics of Transesterification between Palm Oil and Methanol under Subcritical Conditions, *Energy Science and Technology*, 2 (2011) 35-42.
- 25 C.-S. Choi, J.-W. Kim, C.-J. Jeong, H. Kim, K.-P. Yoo, Transesterification Kinetics of Palm Olein Oil Using Supercritical Methanol, *The Journal of Supercritical Fluids*, 58 (2011) 365-370.
- 26 P. Bondioli, C. Mariani, A. Lanzani, E. Fedeli, A. Muller, Squalene Recovery from Olive Oil Deodorizer Distillates, *Journal of the American Oil Chemists' Society*, 70 (1993) 763-766.
- 27 N.A. Akgün, Separation of Squalene from Olive Oil Deodorizer Distillate Using Supercritical Fluids, *European Journal of Lipid Science and Technology*, 113 (2011) 1558-1565.

APPENDIX A.
ASSESSMENT OF TRANSPORT
LIMITATIONS

This appendix contains, for the completeness of the work, the theoretical background for the determination of the intrinsic kinetics in a trickle-bed reactor.

A.1 Transport effects on reactor scale

In a trickle-bed reactor a liquid and a gas phase flow co-currently through a fixed bed of catalyst particles. Some of the well-known applications in the chemical industry are hydrodesulfurization of petroleum fractions and selective hydrogenation of alkynes. In comparison with packed-bed absorption columns the trickle-bed reactors are operated with low gas and liquid velocities and contain active catalyst particles that could be in various shapes (*e.g.* of spherical, cylindrical pellets, cubes, ...). Although the reactor geometry is relatively simple (*i.e.* a tubular reactor), the hydrodynamics are extremely complex.¹⁴

The catalyst particles are often diluted with inert particles of typically 100-300 μm as this reduces the axial dispersion, improves the mass transport and isothermicity of the bed.

A.1.1 Pressure drop over the reactor

A pressure drop occurs when frictional forces, caused by the resistance to flow, act on a fluid (gas or liquid) as it flows through the reactor tube. Additionally, due to the presence of solid particles (the catalyst particle), a pressure drop will occur. Since the pressure drop influences the total pressure in the reactor and, hence, the component's partial pressures and the kinetics, it should remain limited. When criterion (A.1) is satisfied, under the operating conditions discussed in Table 2.4, the effect of the pressure drop on the kinetics is negligible.

$$\Delta P < \frac{0.2P_{tot}}{n} \quad (\text{A.1})$$

With ΔP : the pressure drop over the catalyst bed [Pa]

P_{tot} : the feed pressure [Pa]

n : the total reaction order [-]

The pressure drop over the reactor follows from the application of the laws of conservation of momentum for the fluidum F (thus, gas or liquid).

$$\Delta P = \frac{f_m \rho_F u_s^2 h_{bed}}{d_{h,bed}} \quad (\text{A.2})$$

With f_m : the modified friction factor [-]

ρ_F : the fluidum density [kg m^{-3}],

u_s : the superficial gas velocity [$\text{m}^3 \text{m}_{\text{reactor}}^{-2} \text{s}^{-1}$], defined as the ratio of the volumetric flow rate to the cross-sectional area of the reactor

h_{bed} : the height of the catalyst bed [m], calculated $h_{bed} = \frac{V_{bed}}{\frac{\pi}{4}d_t^2}$

in which d_t : the internal diameter of the reactor [m],

V_{bed} : the total bed volume [m³], calculated as

$$V_{bed} = \frac{m_{cat}}{\rho_{cat}(1-\varepsilon_b)} + \frac{m_{dil}}{\rho_{dil}(1-\varepsilon_b)}$$

with ρ the density and amount of the catalyst (cat) or diluent (dil)

m the amount of the catalyst (cat) or diluent (dil)

ε_b the bed porosity [m_{void}³ m_{bed}⁻³], typically in the range 0.2-0.4

$d_{h,bed}$: the hydraulic diameter of the catalyst bed [m], which is directly proportional with the

$$\text{ratio of the "wetted" volume to the "wetted" surface } d_{h,bed} = \frac{4\varepsilon_b}{a_{LS}} = \frac{2}{3} d_{pe} \frac{\varepsilon_b}{(1-\varepsilon_b)}$$

in which a_{LS} : the ratio of the external catalyst pellet surface area to its volume

[m² m⁻³_{bed}], calculated from the equivalent pellet diameter d_{pe} ,

$$\text{calculated as } d_{pe} = \frac{6V_p}{S_p} = \frac{6(1-\varepsilon_b)}{a_{LS}}$$

with d_{pe} : diameter of the of inert particle [m] when a diluents is used

Several empirical correlations exist for the estimation of the friction factor of the reactor, depending on fluidum, flow regime, geometry of the catalyst,... A correlation for the friction factor follows from the widely applied Ergun equation. This correlation is valid in the range of $0.1 < Re_F < 1000$.

$$f_m = \frac{(1-\varepsilon_b)}{\varepsilon_b^3} \left(1.75 + 150 \frac{(1-\varepsilon_b)}{Re_F} \right) \quad (\text{A.3})$$

With Re_F : the Reynolds number of the fluidum [-], the ratio of inertial forces to viscous forces,

$$\text{calculated as: } Re_F = \frac{d_{pe} \rho_F u_s}{\mu_F}$$

in which μ_F : the fluidum viscosity [kg m⁻¹ s⁻¹]

A.1.2 Axial and radial dispersion

It is desired to have a uniform liquid velocity along the radial direction in the reactor. Due to the variation in catalyst packing, caused by looser packing near the wall, an undesired radial velocity profile may result. The deviation from radial uniformity is given by the effective radial diffusion coefficient $D_{r,eff}$, using the Péclet number $Pe'_{p,F}$ of the fluidum based on the particle size d_p . Since the radial dispersion for gas is typically better than for liquid, the criteria are only applied for the liquid phase.

$$Pe'_{p,F} = \frac{u d_p}{D_{r,eff}} \quad (\text{A.4})$$

With u_L : the liquid velocity [m s⁻¹]

$D_{r,eff}$: the effective radial diffusion coefficient [m_{fluid}³ m_{reactor}⁻¹ s⁻¹]

Froment¹⁵ was able to take the wall effects into account with a correction factor on the Péclet number, where d_t is diameter of the reactor [m].

$$\frac{Pe'_{p,L}}{1 + 19.4 \left(\frac{d_p}{d_t}\right)^2} = \frac{ud_p}{D_{r,eff}} \quad (\text{A.5})$$

The wall effects can be neglected when the denominator is close to unity. As a rule of thumb, which is valid based under the operating conditions discussed in Table 2.4, criterion (A.6) is chosen to neglect the wall effects.

$$\frac{d_t}{d_p} > 10 \quad (\text{A.6})$$

In addition to radial diffusion, axial diffusion is also unwanted. The criterion, which is valid under the operating conditions discussed in Table 2.4, used for neglecting axial diffusion is developed by Fu and Tan¹⁶ specifically for trickle flow regimes. In their approach a minimum required ratio of catalyst bed height to catalyst particle diameter is calculated for both gas and liquid. The minimum ratios are determined *via* Eq. (A.7). The ratio of bed height to particle diameter used during experiments must be higher than both minima. The axial dispersion in the gas is only important if a mixed gas is used. As pure hydrogen is used as a reactant, the equation is only calculated for the liquid.

$$\left(\frac{h_{bed}}{d_p}\right)_{\min A} = 8 \left(\frac{n_A}{Pe_{p,L}}\right) \ln\left(\frac{1}{1 - 0.01X_A}\right) \quad (\text{A.7})$$

With n_A : the reaction order for component A, *i.e.* glycerol (=1) [-]

X_A : the (expected) molar conversion for component A [%], at the most severe reaction conditions

$Pe_{p,L}$: the Péclet number as defined as $Pe_{p,L} = \max\left(0.04; \frac{0.00014}{d_h^{0.75} \varepsilon_b}\right)$

in which d_h is the hydraulic diameter [m]. It is directly proportional to the

“wetted” volume to the area and calculated as $d_h = d_p \left(\frac{16\varepsilon_b^3}{9\pi(1-\varepsilon_b)^2}\right)^{1/3}$

A.2 Mass transport

As the fixed-bed reactor is operated in trickle bed regime, the mass transfer between the gas phase (H₂), the liquid phase (glycerol) and the solid phase (catalyst) needs to be considered. The overall mass transport limitations consist of a contribution of four possible limitations, as indicated in Figure A.1:

- (1) The mass transport from the bulk gas phase to the gas-liquid interface
- (2) The mass transport from the gas-liquid interface to the bulk liquid phase
- (3) The mass transport from the bulk liquid phase to the liquid-solid interface
- (4) The mass transport in the pores of the catalyst particle

It should be noted that limitations (1) and (2) only apply for the gaseous reactant, while limitations (3) and (4) apply for both gaseous and liquid reactants.

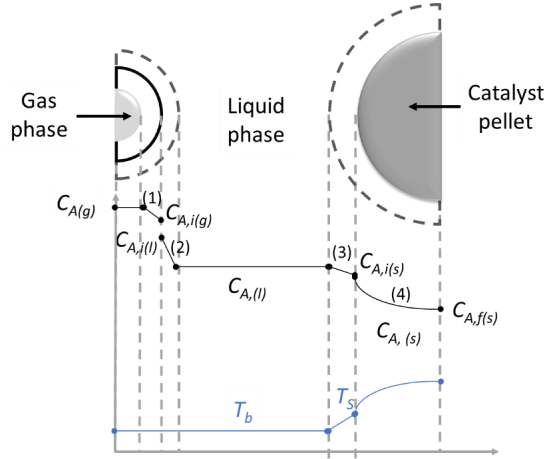


Figure A.1. General representation of the concentration of reactant A and temperature profile in a three-phase exothermal reaction.

A.2.1 From the bulk gas phase to the G-L interface

The relative impact of gas-side G-L mass transfer on the observations can be expressed via the Carberry number (Ca) which should be smaller than $0.05/n$ for this impact to be negligible. The calculation of the Carberry number requires the reaction rate, R^{obs} , expressed per unit of volume. The criterion expresses that the resistance due to external mass transfer is less than 5 % of the resistance due to chemical reaction.

$$Ca_G = \frac{C_{A(g)} - C_{A,i(g)}}{C_{A(g)}} = \frac{R_{v,A}^{obs}}{k_G a_{GL} C_{A(g)}} < 0.05 \quad (A.8)$$

With Ca_G : the gas Carberry number [-]

$C_{A(g)}$: the concentration of reactant A in the gas phase [mol m^{-3}_G]

$C_{A,i(g)}$: the concentration of reactant A in the gas phase at the G-L interface [mol m^{-3}_G]

$R_{v,A}^{obs}$: the observed reaction rate [$\text{mol m}^{-3}_{\text{reactor}} \text{s}^{-1}$], for diluted catalyst beds calculated

$$\text{as } R_{v,A}^{obs} = R_{w,A}^{obs} \rho_{cat} \frac{\varepsilon_{cat}}{1 - \varepsilon_{cat}}$$

in which, ε_{cat} is the volume fraction of the catalyst in the bed [$\text{m}^3_{\text{cat}} \text{m}^{-3}_{\text{reactor}}$],

$$\text{calculated as } \varepsilon_{cat} = \frac{m_{cat}}{\rho_{cat} V_{bed}}$$

k_G : the mass transfer coefficient between the gas bulk and the G-L interface [$\text{m}^3_G \text{m}^{-2} \text{s}^{-1}$]

a_{GL} : the G-L interfacial area [$\text{m}^2_G \text{m}^{-3}_{\text{reactor}}$]

There are several correlations for estimating the product $k_G a_{GL}$, depending on the flow regime and reactor configuration.¹⁷⁻²¹ Typical values of $k_G a_{GL}$ lie in a broad range (0.01 up to 70 s^{-1}).²² Most of these correlations rely on the Sherwood number, the ratio of convective to diffusive transport.

As a pure H₂ is used as feed, the Ca_G is not applicable.

A.2.2 The mass transport from the G-L interface to the bulk liquid phase

Similar to the mass transfer from the bulk gas phase to the G-L interface, the Carberry number can be used to assess the relevance of the resistance due to the G-L mass transfer on the liquid side.

$$Ca_L = \frac{C_{A,i(l)} - C_{A,(l)}}{C_{A,(l)}} = \frac{R_{v,A}^{obs}}{k_L a_{GL} C_{A,(l)}} < 0.05 \quad (A.9)$$

With Ca_L: the liquid Carberry number [-]

C_{A,(l)}: the concentration of reactant A in the liquid phase [mol m⁻³_L]

C_{A,i(l)}: the concentration of reactant A in the liquid phase at the G-L interface [mol m⁻³_L]

k_L: the mass transfer coefficient for transfer from G-L interface into bulk liquid [m³_L m⁻² s⁻¹]

Again, correlations exist to estimate the product k_La_{GL}.^{18, 23-28} Typical values for k_La_{GL} in trickle bed are 0.01 to 0.3 s⁻¹.²² Under the reaction conditions in Table 2.4, the mass transfer for H₂ on the liquid side is negligible, as the Carberry number was calculated to be 0.03.

A.2.3 From the bulk liquid phase to the L-S interface

The effect of the L-S mass transfer limitations is expressed *via* a Carberry number. Since both glycerol and hydrogen are consumed at the active site on the catalyst surface, this criterion must be satisfied for both reactants.

$$Ca = \frac{C_{A,(l)} - C_{A,i(s)}}{C_{A,(l)}} = \frac{R_{v,A}^{obs}}{f_e k_{LS} a_{LS} C_{A,(l)}} < 0.05 \quad (A.10)$$

With C_{A,(l)}: the bulk concentration of reactant A in the liquid phase [mol m³_L]

C_{A,i(s)}: the concentration of reactant A in the liquid phase at the external pellet surface [mol m³_L]

f_e: the wetting efficiency [-]

k_{LS}: the mass transfer coefficient for transfer from bulk liquid to L-S interface [m³_L m⁻² s⁻¹]

a_{LS}: the L-S interfacial area [m²_L m⁻³_{cat-bed}], , for spherical particles it equals 6/d_p

Typical values for f_ek_{LS}a_{LS} in trickle bed are 0.005-0.2 s⁻¹.²⁹ Under the reaction conditions in Table 2.4, mass transport is not limiting for glycerol (Ca = 0.04), however, some transport limitations could be present for hydrogen (Ca = 0.21).

A.2.4 Internal gradients inside the catalyst particle

Inside the catalyst pellet, a concentration profile may develop due to the occurrence of diffusion limitations. The mass transport through the catalyst particle cannot be separated from the chemical reaction, *i.e.*, both occur in parallel and not in series. The combined effect is assessed *via* the Thiele modulus, φ:

$$\varphi = \frac{1}{a_{LS}} \sqrt{\frac{k_v}{D_{A,eff}}} \quad (\text{A.11})$$

With k_v : the volumetric rate constant in the absence of transport limitations

$D_{A,eff}$: the effective diffusion coefficient of component A, which is corrected for the porosity and tortuosity of the pellet [$\text{m}^2 \text{s}^{-1}$].

When the Thiele modulus is approaching zero, in other words, the diffusion coefficient is high compared to the rate coefficient, the concentration across the catalyst is uniform and almost equal to the surface concentration. On the other hand, a high value of the Thiele modulus corresponds to fast reaction compared to diffusion, resulting in a concentration profile and thus intraparticle mass transfer limitations. For the calculation of the Thiele modulus, the intrinsic kinetics of the reactions have to be known. Therefore, it is more convenient to make use of the Weisz modulus¹², since it is based on the measured production rate. The definition of the Weisz modulus Φ is given by:

$$\Phi = \left(\frac{n+1}{2}\right) \frac{R_{v,A}^{obs}}{a_{LS}^2 D_{A,eff} C_{A,(s)}} \quad (\text{A.12})$$

To avoid intraparticle limitations, the Weisz modulus has to be lower than 0.14.

A.3 Heat transport

To measure intrinsic kinetics, not only radial and axial temperature gradients on reactor scale must be avoided but also those around and in catalyst pellets. The occurrence of heat transport limitations between the liquid and the gas is assumed to be limited as the heat capacity of liquids is three orders of magnitude larger than that of gasses. The thermocouple will mainly measure the liquid temperature and not the gas temperature. In literature³⁰ correlations are found to investigate the occurrence of heat transport limitations. The temperature gradients are, under the operating conditions discussed in Table 2.4, negligible and also much less pronounced than the concentration gradients, which are typical in trickle bed reactors.

A.3.1 Axial and radial isothermicity

A reactor is considered isothermal if the temperature non-uniformities are sufficiently small such that there is no significant impact on the observed net production rate.

$$0.95 < \frac{R_A(T)}{R_A(T + \Delta T)} < 1.05 \quad (\text{A.13})$$

One can distinguish between isothermicity in the axial and in the radial direction. An axial temperature profile may occur in the reactor, *i.e.* a higher temperature at the outlet than at the inlet, due to the heat produced during reaction. To improve the axial isothermicity, the catalyst bed can be diluted with inert material, e.g. α -alumina. By diluting the catalyst bed, the heat production per unit volume will decrease,

enhancing the heat dissipation and, hence, isothermicity. Nevertheless, the dilution may affect the conversion. When the dilution is too pronounced, the reactants have a smaller probability to interact with the catalyst. Therefore, Berger *et al.*³¹ proposed a maximum dilution degree b [$\text{m}_{\text{inert}}^3 \text{m}_{\text{inert+cat}}^{-3}$] at which a conversion X_{dil} will be obtained.

$$b < \frac{1}{1 + 10X_{\text{dil}}(d_p/L_{\text{bed}})} \quad (\text{A.14})$$

From criterion (A.14), it is clear that a longer catalyst bed and a lower pellet diameter allow a larger dilution.

Radial temperature gradients are difficult to measure compared to those in the axial direction. The Mears criterion³² assesses the radial isothermicity inside a tubular reactor assuming a maximum deviation of 5 % to the intrinsic production rate:

$$\Delta T_{\text{rad}} = \frac{R_{v,A}^{\text{obs}} |\Delta_r H| (1 - \varepsilon_b) d_t^2}{32 \lambda_{r,e}} < \frac{0.05 R T_w^2}{E_a} \quad (\text{A.15})$$

With $R_{v,A}^{\text{obs}}$: the observed volumetric reaction rate [$\text{mol m}^{-3} \text{s}^{-1}$]

ΔT_{rad} : the radial temperature difference [K]

$\Delta_r H$: the reaction enthalpy [J mol^{-1}]

$1 - \varepsilon_b$: the fraction of the reactor volume occupied by the catalyst bed [$\text{m}_{\text{bed}}^3 \text{m}_{\text{reactor}}^{-3}$]

$\lambda_{r,e}$: the effective radial heat conductivity of the catalyst bed [$\text{W m}_{\text{reactor}}^{-1} \text{K}^{-1}$]

T_w : the temperature near the wall [K]

For this criterion, the effective radial heat conductivity of the catalyst bed $\lambda_{r,e}$ should be known, for which correlations can be found in literature.^{18, 33-35}

A.3.2 External temperature gradients

In case of an exothermic reaction, such as glycerol hydrogenolysis, a temperature gradient can occur when the bulk temperature is different from the temperature at the surface of the catalyst pellet. A linear temperature profile is assumed in the boundary layer around the pellet (Figure A.1). External heat transfer can be described based on the energy balance:

$$R_{v,A}^{\text{obs}} (-\Delta_r H) \left(\frac{\pi}{6} d_p^3 \right) = \alpha_{LS} (T_s - T_b) (\pi d_p^2) \quad (\text{A.16})$$

With α_{LS} : the convection coefficient between solid, *i.e.*, the catalyst pellet and the liquid,

i.e. glycerol [$\text{W m}_{\text{cat}}^{-2} \text{K}^{-1}$]

T_s : the external surface temperature [K]

T_b : the bulk liquid temperature [K]

The observed volumetric production rate is temperature dependent according to the Arrhenius law. Substitution yields a criterion for the temperature difference over the boundary layer, $\Delta T_{boundary\ layer}$, with only observable or calculable quantities.

$$\Delta T_{boundary\ layer} = (T_s - T_b) = \frac{R_{v,A}^{obs} |\Delta_r H| d_p}{6\alpha_{LS}} < \frac{0.05RT_b^2}{E_a} \quad (A.17)$$

The heat transfer coefficient between the catalyst pellet and the liquid, is defined by:

$$\alpha_{LS} = \frac{Nu_{LS}\lambda_L}{d_p} \quad (A.18)$$

With λ_L : the thermal conductivity of the liquid, *i.e.* glycerol [J s⁻¹ m⁻¹ K⁻¹]

Nu_{LS} : the Nusselt number [-], the ratio of convective to conductive heat transfer according to the Chilton-)colburn J-factor analogy:

$$Nu_{LS} = f_e Sh_{LS} \left(\frac{Pr_L}{Sc_L} \right)^{1/3} \quad (A.19)$$

Sh_{LS} : the Sherwood number for mass transport of the liquid into the solid:

$$Sh_{LS} = \frac{k_{LS}d_p}{D_L} \quad (A.20)$$

Pr_L : the liquid Prandtl number [-], the ratio of momentum diffusivity to thermal diffusivity:

$$Pr_L = \frac{\mu_L c_{p,L}}{\lambda_L} \quad (A.21)$$

Sc_L the liquid Schmidt number [-], the ratio of momentum diffusivity to mass diffusivity:

$$Sc_L = \frac{\mu_L}{\rho_L D_L} \quad (A.22)$$

With k_{LS} : the mass transfer coefficient for transport from the liquid surface towards the catalyst surface [m³_{liq} m⁻² s⁻¹]

D_L : the molar diffusion coefficient of the liquid, *i.e.* glycerol [m² s⁻¹]

μ_L : the viscosity of the liquid, *i.e.* glycerol [kg s⁻¹ m⁻¹]

$c_{p,L}$: the heat capacity of the liquid, *i.e.* glycerol [J kg⁻¹ K⁻¹]

ρ_L : the density of the liquid, *i.e.* glycerol [kg m⁻³]

A.3.3 Internal temperature gradients

Heat transport limitations can cause a temperature gradient inside the catalyst pellet. For exothermic reactions, the temperature in the center of the catalyst will be higher than at the external surface of the

pellet (Figure A.1). A criterion for the maximum internal temperature difference between the external surface and the average in the particle, ΔT_{int} , can be obtained by applying a Taylor series expansion on the production rate around T_s .

$$\Delta T_{int} = \frac{R_{v,A}^{obs} |\Delta_r H| d_p^2}{60 \lambda_p} < \frac{0.05 R T_s^2}{E_a} \quad (\text{A.23})$$

APPENDIX B.
EXPERIMENTAL DATASET FOR
ESTERIFICATION OF SUNFLOWER
ODD WITH SUPERCRITICAL ETOH

Experimental dataset for esterification of sunflower ODD with supercritical EtOH

Table B.1. Reaction conditions for the esterification of sunflower ODD with supercritical EtOH at 15 MPa in a reactor of 20.48 cm³. (1/2)

Exp.	T [K]	t [s]	F_{TG}^0 [mol s ⁻¹]	F_{DG}^0 [mol s ⁻¹]	F_{MG}^0 [mol s ⁻¹]	F_{FFA}^0 [mol s ⁻¹]	F_{FAEE}^0 [mol s ⁻¹]	F_{EtOH}^0 [mol s ⁻¹]	$F_{H_2O}^0$ [mol s ⁻¹]	F_G^0 [mol s ⁻¹]
1	523	450	8.01·10 ⁻⁶	3.80·10 ⁻⁷	4.38·10 ⁻⁷	1.08·10 ⁻⁵	1.16·10 ⁻⁶	1.70·10 ⁻⁴	0	0
2	523	600	6.01·10 ⁻⁶	2.85·10 ⁻⁷	3.29·10 ⁻⁷	8.07·10 ⁻⁶	8.70·10 ⁻⁷	1.28·10 ⁻⁴	0	0
3	523	900	4.00·10 ⁻⁶	1.90·10 ⁻⁷	2.19·10 ⁻⁷	5.38·10 ⁻⁶	5.80·10 ⁻⁷	8.51·10 ⁻⁵	0	0
4	523	1800	2.00·10 ⁻⁶	9.49·10 ⁻⁸	1.10·10 ⁻⁷	2.69·10 ⁻⁶	2.90·10 ⁻⁷	4.26·10 ⁻⁵	0	0
5	523	3600	1.00·10 ⁻⁶	4.75·10 ⁻⁸	5.48·10 ⁻⁸	1.34·10 ⁻⁶	1.45·10 ⁻⁷	2.13·10 ⁻⁵	0	0
6	548	450	8.01·10 ⁻⁶	3.80·10 ⁻⁷	4.38·10 ⁻⁷	1.08·10 ⁻⁵	1.16·10 ⁻⁶	1.70·10 ⁻⁴	0	0
7	548	600	6.01·10 ⁻⁶	2.85·10 ⁻⁷	3.29·10 ⁻⁷	8.07·10 ⁻⁶	8.70·10 ⁻⁷	1.28·10 ⁻⁴	0	0
8	548	900	4.00·10 ⁻⁶	1.90·10 ⁻⁷	2.19·10 ⁻⁷	5.38·10 ⁻⁶	5.80·10 ⁻⁷	8.51·10 ⁻⁵	0	0
9	548	1800	2.00·10 ⁻⁶	9.49·10 ⁻⁸	1.10·10 ⁻⁷	2.69·10 ⁻⁶	2.90·10 ⁻⁷	4.26·10 ⁻⁵	0	0
10	548	450	5.61·10 ⁻⁶	2.66·10 ⁻⁷	3.07·10 ⁻⁷	7.54·10 ⁻⁶	8.12·10 ⁻⁷	1.99·10 ⁻⁴	0	0
11	548	600	4.21·10 ⁻⁶	1.99·10 ⁻⁷	2.30·10 ⁻⁷	5.65·10 ⁻⁶	6.09·10 ⁻⁷	1.49·10 ⁻⁴	0	0
12	548	900	2.80·10 ⁻⁶	1.33·10 ⁻⁷	1.54·10 ⁻⁷	3.77·10 ⁻⁶	4.06·10 ⁻⁷	9.94·10 ⁻⁵	0	0
13	548	1800	1.40·10 ⁻⁶	6.65·10 ⁻⁸	7.68·10 ⁻⁸	1.88·10 ⁻⁶	2.03·10 ⁻⁷	4.97·10 ⁻⁵	0	0
14	548	3600	7.01·10 ⁻⁷	3.32·10 ⁻⁸	3.84·10 ⁻⁸	9.42·10 ⁻⁷	1.02·10 ⁻⁷	2.48·10 ⁻⁵	0	0
15	548	450	4.08·10 ⁻⁶	1.94·10 ⁻⁷	2.23·10 ⁻⁷	5.48·10 ⁻⁶	5.91·10 ⁻⁷	2.17·10 ⁻⁴	0	0
16	548	600	3.06·10 ⁻⁶	1.45·10 ⁻⁷	1.68·10 ⁻⁷	4.11·10 ⁻⁶	4.43·10 ⁻⁷	1.63·10 ⁻⁴	0	0
17	548	900	2.04·10 ⁻⁶	9.68·10 ⁻⁸	1.12·10 ⁻⁷	2.74·10 ⁻⁶	2.95·10 ⁻⁷	1.08·10 ⁻⁴	0	0
18	548	1800	1.02·10 ⁻⁶	4.84·10 ⁻⁸	5.58·10 ⁻⁸	1.37·10 ⁻⁶	1.48·10 ⁻⁷	5.42·10 ⁻⁵	0	0
19	548	3600	5.10·10 ⁻⁷	2.42·10 ⁻⁸	2.79·10 ⁻⁸	6.85·10 ⁻⁷	7.39·10 ⁻⁸	2.71·10 ⁻⁵	0	0
20	548	1800	2.95·10 ⁻⁶	1.40·10 ⁻⁷	1.61·10 ⁻⁷	3.96·10 ⁻⁶	4.27·10 ⁻⁷	3.13·10 ⁻⁵	0	0

Table B.2. Reaction conditions for the esterification of sunflower ODD with supercritical EtOH at 15 MPa in a reactor of 20.48 cm³. (2/2)

Exp.	T [K]	t [s]	F_{FG}^0 [mol s ⁻¹]	F_{DG}^0 [mol s ⁻¹]	F_{MG}^0 [mol s ⁻¹]	F_{FFA}^0 [mol s ⁻¹]	F_{FAEE}^0 [mol s ⁻¹]	F_{EtOH}^0 [mol s ⁻¹]	$F_{H_2O}^0$ [mol s ⁻¹]	F_G^0 [mol s ⁻¹]
21	548	3600	1.47·10 ⁻⁶	6.99·10 ⁻⁸	8.07·10 ⁻⁸	1.98·10 ⁻⁶	2.13·10 ⁻⁷	1.57·10 ⁻⁵	0	0
22	548	1800	2.00·10 ⁻⁶	9.49·10 ⁻⁸	1.10·10 ⁻⁷	2.69·10 ⁻⁶	2.90·10 ⁻⁷	4.26·10 ⁻⁵	0	0
23	573	450	8.01·10 ⁻⁶	3.80·10 ⁻⁷	4.38·10 ⁻⁷	1.08·10 ⁻⁵	1.16·10 ⁻⁶	1.70·10 ⁻⁴	0	0
24	573	600	6.01·10 ⁻⁶	2.85·10 ⁻⁷	3.29·10 ⁻⁷	8.07·10 ⁻⁶	8.70·10 ⁻⁷	1.28·10 ⁻⁴	0	0
25	573	900	4.00·10 ⁻⁶	1.90·10 ⁻⁷	2.19·10 ⁻⁷	5.38·10 ⁻⁶	5.80·10 ⁻⁷	8.51·10 ⁻⁵	0	0
26	573	1800	2.95·10 ⁻⁶	1.40·10 ⁻⁷	1.61·10 ⁻⁷	3.96·10 ⁻⁶	4.27·10 ⁻⁷	3.13·10 ⁻⁵	0	0
27	573	1800	2.38·10 ⁻⁶	1.13·10 ⁻⁷	1.31·10 ⁻⁷	3.20·10 ⁻⁶	3.45·10 ⁻⁷	3.80·10 ⁻⁵	0	0
28	573	1800	1.40·10 ⁻⁶	6.65·10 ⁻⁸	7.68·10 ⁻⁸	1.88·10 ⁻⁶	2.03·10 ⁻⁷	4.97·10 ⁻⁵	0	0
29	573	450	8.01·10 ⁻⁶	3.80·10 ⁻⁷	4.38·10 ⁻⁷	1.08·10 ⁻⁵	1.16·10 ⁻⁶	1.70·10 ⁻⁴	0	0
30	573	600	6.01·10 ⁻⁶	2.85·10 ⁻⁷	3.29·10 ⁻⁷	8.07·10 ⁻⁶	8.70·10 ⁻⁷	1.28·10 ⁻⁴	0	0

Table B.3. Reactor effluent composition the esterification of sunflower ODD with supercritical EtOH at 15 MPa in a reactor of 20.48 cm³. (1/2)

Exp.	F_{FG} [mol s ⁻¹]	F_{DG} [mol s ⁻¹]	F_{MG} [mol s ⁻¹]	F_{FFA} [mol s ⁻¹]	F_{FAEE} [mol s ⁻¹]	F_{EtOH} [mol s ⁻¹]	F_{H_2O} [mol s ⁻¹]	F_G [mol s ⁻¹]
1	3.97·10 ⁻⁶	1.77·10 ⁻⁶	2.72·10 ⁻⁷	1.04·10 ⁻⁵	1.09·10 ⁻⁵	1.60·10 ⁻⁴	3.42·10 ⁻⁷	2.82·10 ⁻⁶
2	2.45·10 ⁻⁶	1.55·10 ⁻⁶	3.29·10 ⁻⁷	7.39·10 ⁻⁶	9.20·10 ⁻⁶	1.19·10 ⁻⁴	6.75·10 ⁻⁷	2.29·10 ⁻⁶
3	1.30·10 ⁻⁶	1.36·10 ⁻⁶	3.65·10 ⁻⁷	4.24·10 ⁻⁶	7.02·10 ⁻⁶	7.84·10 ⁻⁵	1.14·10 ⁻⁶	1.39·10 ⁻⁶
4	5.12·10 ⁻⁷	6.88·10 ⁻⁷	2.97·10 ⁻⁷	1.72·10 ⁻⁶	3.93·10 ⁻⁶	3.85·10 ⁻⁵	9.72·10 ⁻⁷	7.08·10 ⁻⁷
5	1.16·10 ⁻⁷	3.23·10 ⁻⁷	2.34·10 ⁻⁷	7.26·10 ⁻⁷	2.37·10 ⁻⁶	1.87·10 ⁻⁵	6.18·10 ⁻⁷	4.30·10 ⁻⁷
6	3.79·10 ⁻⁶	2.16·10 ⁻⁶	5.86·10 ⁻⁷	8.05·10 ⁻⁶	1.17·10 ⁻⁵	1.59·10 ⁻⁴	2.71·10 ⁻⁶	2.29·10 ⁻⁶
7	2.25·10 ⁻⁶	1.97·10 ⁻⁶	6.35·10 ⁻⁷	5.47·10 ⁻⁶	9.93·10 ⁻⁶	1.18·10 ⁻⁴	2.60·10 ⁻⁶	1.77·10 ⁻⁶
8	1.37·10 ⁻⁶	1.32·10 ⁻⁶	5.12·10 ⁻⁷	3.50·10 ⁻⁶	6.86·10 ⁻⁶	7.79·10 ⁻⁵	1.88·10 ⁻⁶	1.22·10 ⁻⁶
9	2.92·10 ⁻⁷	5.68·10 ⁻⁷	4.32·10 ⁻⁷	1.49·10 ⁻⁶	4.47·10 ⁻⁶	3.75·10 ⁻⁵	1.20·10 ⁻⁶	9.15·10 ⁻⁷
10	2.93·10 ⁻⁶	1.35·10 ⁻⁶	3.32·10 ⁻⁷	5.91·10 ⁻⁶	7.74·10 ⁻⁶	1.91·10 ⁻⁴	1.62·10 ⁻⁶	1.56·10 ⁻⁶

Experimental dataset for esterification of sunflower ODD with supercritical EtOH

Table B.4. Reactor effluent composition the esterification of sunflower ODD with supercritical EtOH at 15 MPa in a reactor of 20.48 cm³. (2/2)

Exp.	F_{TG} [mol s ⁻¹]	F_{DG} [mol s ⁻¹]	F_{MG} [mol s ⁻¹]	F_{FFA} [mol s ⁻¹]	F_{FAEE} [mol s ⁻¹]	F_{EtOH} [mol s ⁻¹]	F_{H_2O} [mol s ⁻¹]	F_G [mol s ⁻¹]
11	1.95·10 ⁻⁶	1.09·10 ⁻⁶	2.67·10 ⁻⁷	4.43·10 ⁻⁶	6.35·10 ⁻⁶	0.000143	1.23·10 ⁻⁵	1.33·10 ⁻⁶
12	1.22·10 ⁻⁶	8.38·10 ⁻⁷	2.28·10 ⁻⁷	2.71·10 ⁻⁶	4.43·10 ⁻⁶	9.51·10 ⁻⁵	1.06·10 ⁻⁶	8.08·10 ⁻⁷
13	4.00·10 ⁻⁷	4.84·10 ⁻⁷	2.20·10 ⁻⁷	1.09·10 ⁻⁶	2.71·10 ⁻⁶	4.69·10 ⁻⁵	7.92·10 ⁻⁷	4.41·10 ⁻⁷
14	8.16·10 ⁻⁸	1.92·10 ⁻⁷	1.76·10 ⁻⁷	4.62·10 ⁻⁷	1.70·10 ⁻⁶	2.30·10 ⁻⁵	4.80·10 ⁻⁷	3.23·10 ⁻⁷
15	2.41·10 ⁻⁶	8.86·10 ⁻⁷	1.65·10 ⁻⁷	4.25·10 ⁻⁶	5.39·10 ⁻⁶	2.12·10 ⁻⁴	1.24·10 ⁻⁶	1.03·10 ⁻⁶
16	1.69·10 ⁻⁶	6.87·10 ⁻⁷	1.36·10 ⁻⁷	3.21·10 ⁻⁶	4.25·10 ⁻⁶	1.59·10 ⁻⁴	9.00·10 ⁻⁷	8.62·10 ⁻⁷
17	1.01·10 ⁻⁶	5.09·10 ⁻⁷	1.15·10 ⁻⁷	2.13·10 ⁻⁶	2.98·10 ⁻⁶	1.06·10 ⁻⁴	6.14·10 ⁻⁷	6.12·10 ⁻⁷
18	2.99·10 ⁻⁷	3.44·10 ⁻⁷	1.37·10 ⁻⁷	8.22·10 ⁻⁷	1.95·10 ⁻⁶	5.22·10 ⁻⁵	5.49·10 ⁻⁷	3.45·10 ⁻⁷
19	7.28·10 ⁻⁸	1.62·10 ⁻⁷	1.14·10 ⁻⁷	3.54·10 ⁻⁷	1.22·10 ⁻⁶	2.58·10 ⁻⁵	3.32·10 ⁻⁷	2.13·10 ⁻⁷
20	8.98·10 ⁻⁷	1.10·10 ⁻⁶	5.57·10 ⁻⁷	1.74·10 ⁻⁶	5.55·10 ⁻⁶	2.53·10 ⁻⁵	2.22·10 ⁻⁶	6.89·10 ⁻⁷
21	1.33·10 ⁻⁷	3.76·10 ⁻⁷	4.82·10 ⁻⁷	7.23·10 ⁻⁷	3.88·10 ⁻⁶	1.14·10 ⁻⁵	1.26·10 ⁻⁶	6.33·10 ⁻⁷
22	4.20·10 ⁻⁷	7.04·10 ⁻⁷	4.02·10 ⁻⁷	1.41·10 ⁻⁶	4.22·10 ⁻⁶	3.81·10 ⁻⁵	1.28·10 ⁻⁶	6.80·10 ⁻⁷
23	2.81·10 ⁻⁶	2.44·10 ⁻⁶	7.84·10 ⁻⁷	8.48·10 ⁻⁶	1.36·10 ⁻⁵	1.57·10 ⁻⁴	2.28·10 ⁻⁶	2.78·10 ⁻⁶
24	1.48·10 ⁻⁶	2.06·10 ⁻⁶	8.73·10 ⁻⁷	6.69·10 ⁻⁶	1.08·10 ⁻⁵	1.17·10 ⁻⁴	1.38·10 ⁻⁶	2.21·10 ⁻⁶
25	7.77·10 ⁻⁷	1.27·10 ⁻⁶	7.64·10 ⁻⁷	3.63·10 ⁻⁶	8.33·10 ⁻⁶	7.64·10 ⁻⁵	1.75·10 ⁻⁶	1.61·10 ⁻⁶
26	3.40·10 ⁻⁷	8.65·10 ⁻⁷	9.06·10 ⁻⁷	1.82·10 ⁻⁶	7.27·10 ⁻⁶	2.36·10 ⁻⁵	2.14·10 ⁻⁶	1.14·10 ⁻⁶
27	3.41·10 ⁻⁷	8.42·10 ⁻⁷	6.56·10 ⁻⁷	1.61·10 ⁻⁶	5.41·10 ⁻⁶	3.23·10 ⁻⁵	1.59·10 ⁻⁶	7.89·10 ⁻⁷
28	2.18·10 ⁻⁷	5.27·10 ⁻⁷	3.53·10 ⁻⁷	1.04·10 ⁻⁶	3.13·10 ⁻⁶	4.65·10 ⁻⁵	8.42·10 ⁻⁷	4.48·10 ⁻⁷
29	2.92·10 ⁻⁶	2.43·10 ⁻⁶	7.44·10 ⁻⁷	7.72·10 ⁻⁶	1.38·10 ⁻⁵	1.56·10 ⁻⁴	3.04·10 ⁻⁶	2.73·10 ⁻⁶
30	1.70·10 ⁻⁶	2.04·10 ⁻⁶	7.90·10 ⁻⁷	5.35·10 ⁻⁶	1.09·10 ⁻⁵	1.16·10 ⁻⁴	2.72·10 ⁻⁶	2.09·10 ⁻⁶

APPENDIX C.
PARAMETER ESTIMATION IN THE
ESTERIFICATION OF SUNFLOWER
OIL WITH SUPERCRITICAL ETOH


```

Global Temp As Real
Global Press As Real
Global Vreactor As Real
Global time As Real
Global Tgas As Real
Global Rgas As Real
! There are nine components
Global MFI(8) As Real ! molar inlet flow rate - experimental data [mol/s]
Global rho(8) As Real ! density [kg/m³]
Global MM(8) As Real ! molar mass [kg/mol]
Global flow(8) As Real ! molar flow in reactor [mol/s]
Global C(8) As Real ! molar concentration in reactor [mol/m³]
Global rate(8) As Real ! reaction rate [mol/(m³*s)]
Global NROF(8) As Real ! net component production rate [mol/(m³*s)]
! There are only two reaction rate coefficients so four parameters to be estimated
Global I(2) As Real ! pre-exponential factor [m³/(mol*s)]
Global Ea(2) As Real ! Activation energy [J/mol]
Global k(2) As Real ! reaction rate coefficient [m³/(mol*s)]

@Connect Parameters and Settings
!reaction conditions (read from input)
Temp=Xu(1) ! [K]
Press=Xu(2) ! [Pa]
Vreactor=Xu(3) ! [m³]
time=Xu(4) ! [s]

!molar inlet flow rate [mol/s] of all components (read from input)
MFI(1)=Xu(5) ! TG
MFI(2)=Xu(6) ! DG
MFI(3)=Xu(7) ! MG
MFI(4)=Xu(8) ! FFA
MFI(5)=Xu(9) ! EE
MFI(6)=Xu(10) ! EtOH
MFI(7)=Xu(11) ! H2O
MFI(8)=Xu(12) ! GLY

!read initial estimates from input
! [L] = m³/(mol*s) and [Ea] = J/mol.
I(1)=Par(1) ! pre-exponential factor of FFA + EtOH --> EE + H2O
I(2)=Par(2) ! pre-exponential factor of TG + EtOH --> DG + EE, of DG + EtOH --> MG + EE and of MG + EtOH --> GLY + EE

Ea(1)=Par(3) ! activation energy of FFA + EtOH --> EE + H2O
Ea(2)=Par(4) ! activation energy of TG + EtOH --> DG + EE, of DG + EtOH --> MG + EE and of MG + EtOH --> GLY + EE

@Initial Conditions
!molar inlet flow rate of all components (link with read data)
U(1)=MFI(1) ! TG
U(2)=MFI(2) ! DG
U(3)=MFI(3) ! MG
U(4)=MFI(4) ! FFA
U(5)=MFI(5) ! EE
U(6)=MFI(6) ! EtOH
U(7)=MFI(7) ! water
U(8)=MFI(8) ! glycerol

!temperature dependency of density [kg/m³]
rho(1)=-0.3358*Temp+1010.1 ! TG
rho(2)=-0.3522*Temp+1033.0 ! DG
rho(3)=-0.7354*Temp+1185.6 ! MG
rho(4)=-0.8702*Temp+1175.5 ! FFA
rho(5)=-0.904*Temp+1170.3 ! EE
rho(6)=-0.0018*Temp**2+0.3735*Temp+679.96 ! EtOH
rho(7)=-0.0041*Temp**2+2.8242*Temp+378.3 ! H2O
rho(8)=-1.0098*Temp+1605.3 ! Gly

!molar mass of the components [kg/mol]
MM(1)=0.885432 ! TG
MM(2)=0.62099 ! DG
MM(3)=0.356547 ! MG
MM(4)=0.28247 ! FFA
MM(5)=0.31052 ! EE
MM(6)=0.044068 ! EtOH
MM(7)=0.018015 ! H2O
MM(8)=0.092094 ! GLY

!constants
Rgas=8.31451 ! [J/(mol*K)]
Tgas=550.1 ! [K]

@Model Equations
!definition molar flow rates [mol/s] of all components
flow(1)=U(1) ! TG
flow(2)=U(2) ! DG
flow(3)=U(3) ! MG
flow(4)=U(4) ! FFA
flow(5)=U(5) ! EE
flow(6)=U(6) ! EtOH
flow(7)=U(7) ! H2O
flow(8)=U(8) ! GLY
    
```

Appendix C

```
'determination of the concentrations [mol/m^3]
C(1)=0(1)/(0(1)/rho(1)*M(1)+0(2)/rho(2)*M(2)+0(3)/rho(3)*M(3)+0(4)/rho(4)*M(4)+0(5)/rho(5)*M(5)+0(6)/rho(6)*M(6)+0(7)/rho(7)*M(7)+0(8)/rho(8)*M(8) ! TG
C(2)=0(2)/(0(1)/rho(1)*M(1)+0(2)/rho(2)*M(2)+0(3)/rho(3)*M(3)+0(4)/rho(4)*M(4)+0(5)/rho(5)*M(5)+0(6)/rho(6)*M(6)+0(7)/rho(7)*M(7)+0(8)/rho(8)*M(8) ! DG
C(3)=0(3)/(0(1)/rho(1)*M(1)+0(2)/rho(2)*M(2)+0(3)/rho(3)*M(3)+0(4)/rho(4)*M(4)+0(5)/rho(5)*M(5)+0(6)/rho(6)*M(6)+0(7)/rho(7)*M(7)+0(8)/rho(8)*M(8) ! MG
C(4)=0(4)/(0(1)/rho(1)*M(1)+0(2)/rho(2)*M(2)+0(3)/rho(3)*M(3)+0(4)/rho(4)*M(4)+0(5)/rho(5)*M(5)+0(6)/rho(6)*M(6)+0(7)/rho(7)*M(7)+0(8)/rho(8)*M(8) ! FFA
C(5)=0(5)/(0(1)/rho(1)*M(1)+0(2)/rho(2)*M(2)+0(3)/rho(3)*M(3)+0(4)/rho(4)*M(4)+0(5)/rho(5)*M(5)+0(6)/rho(6)*M(6)+0(7)/rho(7)*M(7)+0(8)/rho(8)*M(8) ! EE
C(6)=0(6)/(0(1)/rho(1)*M(1)+0(2)/rho(2)*M(2)+0(3)/rho(3)*M(3)+0(4)/rho(4)*M(4)+0(5)/rho(5)*M(5)+0(6)/rho(6)*M(6)+0(7)/rho(7)*M(7)+0(8)/rho(8)*M(8) ! EtOH
C(7)=0(7)/(0(1)/rho(1)*M(1)+0(2)/rho(2)*M(2)+0(3)/rho(3)*M(3)+0(4)/rho(4)*M(4)+0(5)/rho(5)*M(5)+0(6)/rho(6)*M(6)+0(7)/rho(7)*M(7)+0(8)/rho(8)*M(8) ! H2O
C(8)=0(8)/(0(1)/rho(1)*M(1)+0(2)/rho(2)*M(2)+0(3)/rho(3)*M(3)+0(4)/rho(4)*M(4)+0(5)/rho(5)*M(5)+0(6)/rho(6)*M(6)+0(7)/rho(7)*M(7)+0(8)/rho(8)*M(8) ! GLY

'definition of the reaction rate coefficients [m^3/(mol*s)]
k(1)=I(1)*exp(-Ea(1)/Rgas*(1/(Temp)-1/(Tgem)))
k(2)=I(2)*exp(-Ea(2)/Rgas*(1/(Temp)-1/(Tgem)))

'definition of reaction rates [mol/(m^3*s)]
rate(1)=k(1)*C(4)*C(6) !FFA + EtOH --> EE + H2O
rate(2)=k(2)*C(1)*C(6) !TG + EtOH --> DG + EE
rate(3)=k(2)*C(2)*C(6) !DG + EtOH --> MG + EE
rate(4)=k(2)*C(3)*C(6) !MG + EtOH --> GLY + EE

'definition of net production rates of the components [mol/(m^3*s)]
NROF(1)=-rate(2) !TG
NROF(2)=-rate(3)+rate(2) !DG
NROF(3)=rate(3)-rate(4) !MG
NROF(4)=-rate(1) !FFA
NROF(5)=rate(1)+rate(2)+rate(3)+rate(4) !EE
NROF(6)=-rate(1)-rate(2)-rate(3)-rate(4) !EtOH
NROF(7)=rate(1) !H2O
NROF(8)=rate(4) !GLY

'differential equations to be solved
F(1)=NROF(1) ! TG
F(2)=NROF(2) ! DG
F(3)=NROF(3) ! MG
F(4)=NROF(4) ! FFA
F(5)=NROF(5) ! EE
F(6)=NROF(6) ! EtOH
F(7)=NROF(7) ! H2O
F(8)=NROF(8) ! GLY

@Response Model
'calculation of molar outflow rate of the components [mol/s]
Y(1)=0(1) !TG
Y(2)=0(2) !DG
Y(3)=0(3) !MG
Y(4)=0(4) !FFA
Y(5)=0(5) !EE
Y(6)=0(6) !EtOH
Y(7)=0(7) !H2O
Y(8)=0(8) !GLY
```

APPENDIX D.
LIST OF PUBLICATIONS

D.1 A1 publications

D.1.1 Published

Techno-economic evaluation of squalene recovery from oil deodorizer distillates

Bouriakova, A.; Mendes, P.S.F.; Elst, K.; Thybaut, J.W.; De Clercq, J.

Chemical Engineering Research and Design

February 2020, Volume 154, Pages 122-134

Co-metal induced stabilization of alumina supported copper – impact on the catalytic performance in the hydrogenolysis of glycerol to 1,2-propanediol

Bouriakova, A.; Mendes, P.S.F.; Katryniok, B.; De Clercq, J.; Thybaut, J.W.

Catalysis Communications

November 2020, Volume 146, Article 106134

D.1.2 Submitted

Insight into the mechanism of glycerol hydrogenolysis to 1,2-propanediol: benefits of Cu promotion by La

Bouriakova, A.; Mendes, P.S.F.; Wojcieszak, R.; Detavernier, C.; Katryniok, B.; De Clercq, J.; Thybaut, J.W.

Applied Catalysis B: Environmental

Under review since August 29, 2021

D.2 C3 contributions

D.2.1 Oral presentations

Improving Cu-alumina catalyst stability for glycerol hydrogenolysis by incorporation of lanthanum

Bouriakova, A.; Lauwaert, J.; Katryniok, B.; De Clercq, J.; Thybaut, J.W.

Europacat 2017

Florence, Italy, August 27 to September 1, 2017

From fundamental insights to economic viability: valorization of minors from deodorizer distillates

Bouriakova, A.; Elst, K.; Benats, H.; De Clercq, J.; De Schepper, S.; De Weirde, W.; D'Hondt, E.; Geuens, J.; Congry, P.; Schatteman, K.; Tavenier, S.; Thybaut, J.W.

RRB-14

Ghent, Belgium, May 30 to June 1, 2018

D.2.2 Poster presentations

Fast pyrolysis oil hydrodeoxygenation kinetics using lignin-derived model compounds

Bouriakova, A.; Otyuskaya D.; Thybaut, J.W.; Marin, G.B.

IAP Annual Meeting

Hasselt, Belgium, September 11, 2015

Driving on wood! Wood waste valorization for biofuel production

Bouriakova, A.; Otyuskaya D.; Thybaut, J.W.; Marin, G.B.

FEA Research Symposium

Ghent, Belgium, December 9, 2015

From fundamental insights to economic viability: recovering natural products from deodorizer distillates

Bouriakova, A.; De Clercq, J.; Thybaut, J.W.

CatBior 2017

Lyon, France, December 11 to December 15, 2017

Effect of La in copper-alumina catalysis for “green” propylene glycol production

Bouriakova, A.; Mendes, P.S.F.; Katryniok, B.; De Clercq, J.; Thybaut, J.W.

PREPA12

Louvain-La-Neuve, Belgium, July 8 to July 12, 2018

Improving Cu-alumina catalyst stability for glycerol hydrogenolysis by incorporation of lanthanum

Bouriakova, A.; Mendes, P.S.F.; Katryniok, B.; De Clercq, J.; Thybaut, J.W.

CatPrep Summer School

Vogüé, France, June 16 to June 21, 2019



Abstract representation of natural ("green") oil.